Nonlinear Behaviour of Ferromagnetic Steel

by

O.C.O. Baas

to obtain the degree of Master of Science
at the Delft University of Technology,
to be defended publicly on Thursday November 29, 2018 at 14:30 PM.

Student number:	4151208	
Project duration:	March 1, 2018 - November 29, 2018	
Thesis committee:	Prof. dr. ir. M. L. Kaminski	Delft University of Technology
	Dr. ir. P. Th. L. M. van Woerkom	Delft University of Technology
	Dr. ir. G. H. Keetels	Delft University of Technology
	Dr. ir. L. Pahlavan	Delft University of Technology
	Ir. A. R. P. J. Vijn	Delft University of Technology
	Dr. ir. E. S. A. M. Lepelaars	TNO

An electronic version of this thesis is available at http://repository.tudelft.nl/.

TU Delft

Abstract

In order to monitor elliptical fatigue crack growth in ferromagnetic steel using magnetic methods, an alternative to the self magnetic flux leakage method must be derived as elliptical cracks can grow to significant sizes before they reach through the thickness of the plate material. An approach is sought by translating subtle changes in magnetisation back to the Villari effect, a phenomenon which depicts how applied stress induces changes in magnetisation in ferromagnetic objects. Since the magnitude of these changes in magnetisation is small, other nonlinear effects of similar order such as magnetic relaxation and hysteresis are identified, measured and quantified preliminarily.

The magnetic behaviour in this project is assumed to be quasi-static, and derivations of the expressions for the magnetic field around simple geometric shapes are provided in order to understand magnetic behaviour and verify the outcome of the numerical simulations. It is shown that the numerical simulations produce identical magnetostatic induction fields as the analytically derived expressions when using a sufficiently refined mesh.

An attempt is made to measure long-term magnetic relaxation by subjecting a solid prolate spheroid to a continuous uniform background field for periods of an hour while trying to measure differences in the induction field at a fixed distance. Short-term relaxation, the time it takes for an object to reach a certain magnetisation when the background field is abruptly changed, is also investigated. It is concluded that both effects could not be successfully measured using the current setup. In order to draw proper conclusions, further research into this topic should be conducted using more accurate equipment for extended periods of time.

Upon investigation it is discovered that it can not be assumed that the steel specimens exhibit a uniform permanent magnetisation. A self-developed method is introduced through which non-uniform magnetisation in three directions can be calculated by means of inversion using a set of magnetic induction field measurements in a plane below the specimen when the background field is zero. These measurements are translated to magnetisation using a set of higher order square Gaussian distribution functions that are spaced in a grid over the domain of the test specimen in order to vary the magnetisation locally. Literature that shows comparable results regarding description of non-uniform permanent magnetisation using an array of induction field measurements has not been found.

The concept of hysteresis is introduced and a method is presented through which the parameters of the Jiles-Atherton hysteresis model can be determined using parameter fitting in combination with a forward numerical model created in COMSOL. Closure of minor loops require modifications to the original JA equations which are implemented in the forward model. The numerical model is encapsulated within the Shuffled Leaping Frog parameter optimisation algorithm in order to compute the correct hysteresis parameters. It is found that it is possible to successfully determine the parameters of multiple specimens using weak magnetic fields, and therefore minor loops, which is unparalleled in literature.

Eventually, the Villari effect is introduced and an attempt is made to measure and model the effect using an extension of the Jiles-Atherton model proposed by Naus. Experiments have shown that using this methodology the magnetostriction parameters can be succesfully obtained. A recommendation is provided into how these results can be implemented in crack-propagation models in future research.

Preface

The thesis that lies before you was written by me, Olivier Baas, as the final stage in the process of obtaining my degree as Master of Science in the field of Offshore & Dredging Engineering at the faculty of Mechanical, Maritime and Materials Engineering at the Delft University of Technology. This graduation project was realised in a cooperation between TU Delft and TNO.

First, I would like to sincerely thank my daily supervisor at TNO, Eugène Lepelaars, for the enormous support that he provided to me over the past nine months. What started out as one-sided lectures on a topic that was previously completely unknown to me, evolved into meaningful and exciting discussions as the project progressed. His tremendous mathematical capabilities were something that intimidated me slightly initially, but eventually taught me a great deal. To me, it feels like I have grown significantly in aspects like terminology, correct use of symbols, and proper mathematical writing compared to when I started nine months ago. In the months preceding my internship he constructed and programmed a Helmholtz-cage and an array of magnetometers from scratch by himself, which is a daunting task that he executed extremely well. These tools enabled me to perform the unique and intriguing experiments that are the foundation of this master's thesis, and for this I am very grateful.

I would also like to express gratitude to Aad Vijn, who is well on his way to obtaining his PhD title in this equally challenging and intriguing field. Even though he was initially not officially assigned as my supervisor from TU Delft he did act like one from the start by spending a great deal of time reviewing my work, modeling and discussing results with me. His well-trained mathematical brain was always willing, ready and able to help out with any problems that occured while trying to fit real-world measurements to physical models. Even outside of regular working hours he was always swift to reply, for which I am thankful.

I would like to thank my professor, Mirek Kaminski, as well as my supervisors from the university, Menno van der Horst and Pooriah Pahlavan, for the engaging progress meetings we held every six weeks. The feedback, ideas exchanged, and mutual excitement that flowed during these meetings energised and inspired me every time. I hope that the findings of my thesis may provide a good foundation for the next phase of the CrackGuard joint industry project.

Finally, I would like to thank my family, friends, and in particular my girlfriend Nika for providing continuous support during the past nine months, especially in those weeks when progress was slow.

Olivier Baas
The Hague, November 2018

Contents

Nomenclature

Terminology

Accommodation	Non-physical aspect of the JA-model which prevents minor hysteresis loops from closing properly
Annealing	Heating metal up to a point that any residual stresses due to production processes disappear
Condition number	Measure of how the output of a function changes for a small change in the input argument
COMSOL	A cross-platform FEA, solver and multiphysics simulation software developed by `COMSOL` Inc.
Eddy current	Loops of electrical current within a conducting material induced by a changing magnetic field
FEM / FEA	Finite element method / analysis
Helmholtz cage	A domain in which the magnetic field in three directions can be controlled
Homogeneous	Material parameters do not vary over the domain
Hysteresis	The dependence of the state of a system on its history
Inversion	Process of calculating from a set of observations the causal factors that produced these observations
Inverse magnetostriction	Changes in magnetisation due to applied stress
Isotropic	Directional independence
JA(N)	Jiles-Atherton(-Naus) Model
Uniform	Magnetisation does not vary over the domain
Magnetic after-effect	See *Relaxation*
Magnetostriction	A property of ferromagnetic materials that causes them to change dimensions during the process of magnetisation
Magnetostatics	The study of magnetic fields when the electric currents are steady (not changing over time)
Magnetomechanical effect	See *inverse magnetostriction*
MATLAB	A numerical computing environment and proprietary programming language developed by MathWorks
Prolate spheroid	A spheroid with one long axis and two smaller axes of equal length
Relaxation	The accumulation of magnetisation in a ferromagnetic object subjected to a constant background field
Regularisation	The process of introducing additional information in order to solve ill-posed problems or to prevent overfitting
RMSE	Root-mean-square error
Villari effect	See *inverse magnetostriction*
(Quasi-)static	Neglecting any time-dependent effects
Zero measurement	Measurement performed without a specimen present for comparative purposes

Mathematical symbols

α	Inter-domain coupling parameter	-
a	Domain wall density	A/m
B	Magnetic induction field	T
B_a	Applied magnetic induction field	T
c	Reversibility	-
ϵ	Strain	%
E	Young's modulus of elasticity	N/m^2
η	Relative error	%
f	focal length	m
H	Magnetic field	A/m
H_a	Applied magnetic field	A/m
H_c	Coercive force	A/m
H_e	Effective magnetic field	A/m
H_r	Resulting magnetic field	A/m
H_σ	Stress-induced magnetic field	A/m
k	Pinning parameter	A/m
k_m	Boltzmann's constant	J/K
λ	Magnetostriction	-
μ_0	Permeability of vaccum (air)	N/A^2
μ_r	Relative permeability	-
m	Length to width ratio spheroid	-
m	Dipole moment	A·m^2
M	Magnetisation	A/m
M_0	Initial /starting magnetisation	A/m
M_{an}	Anhysteretic magnetisation	A/m
M_{irr}	Irreversible magnetisation	A/m
M_s	Saturation magnetisation	A/m
M_r	Remnant magnetisation	A/m
N	Demagnetisation factor	-
$\underline{\underline{M}}$	Parameter sensitivity matrix	T
R	Dissipative irreversible magnetisation factor	-
σ	Stress	N/m^2
σ_y	Yield stress	N/m^2
s	Standard deviation	-
u	Unit vector	-
V_{m0}	Magnetic scalar potential	A
w	Specimen width	m
ξ, η, ϕ	Spherical coordinates	-

1 Introduction

1.1. Motivation

To guarantee structural integrity of marine structures, methods are developed to detect and monitor cracks in steel structures. Be it a drilling rig, vessel or bridge, eventually all structures made from steel beams will develop cracks after long periods of continuous cyclic loading below the global yield stress which is a phenomenon known as fatigue damage. The horrendous accident in which a bridge collapsed in Genoa, Italy, in September 2018 demonstrates the importance of operating an adequate fatigue detection and monitoring system [16].

Detecting and monitoring cracks can be subdivided into destructive- and non-destructive tests. Since the integrity of structures is analysed, destructive testing is not suitable as the goal is to monitor cracks while the target structure is in-service. Some of the prevalent ways of non-destructive evaluation (NDE) are strain monitoring, ultrasonic testing, radiographic testing and magnetic testing which are analysed and compared by Van der Horst [54]. In his paper it was concluded that, while each of these options have shown merit, a solution which is wireless, cheap, robust and conveniently implemented should be sought by means of the Self Magnetic Flux Leakage method (SMFL). The SMFL method is based on the principle of differences in magnetic permeability μ between steel (the structure) and air (the crack). As the magnetic permeability of air is much lower than that of ferromagnetic steel this causes the magnetic flux lines to flow a different route when encountering a pocket of air. Some of this flux will leave the material which is therefore defined as *flux leakage*, see Sophian [47]. A visualisation of magnetic flux leakage is given in figure 1.1.

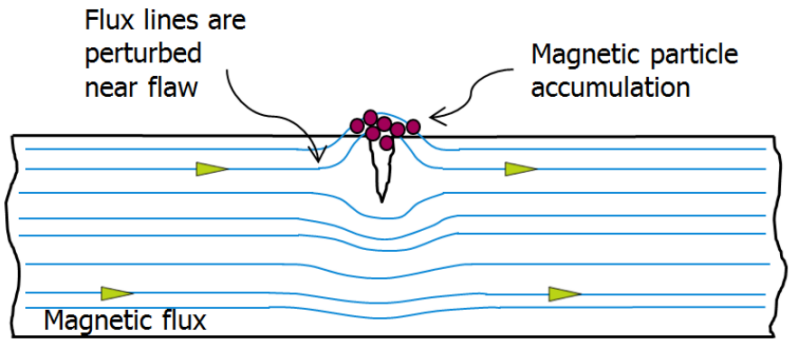

Figure 1.1: Plate (top view) with a through-thickness crack and magnetic flux leakage, from [53].

In order to use this concept to detect cracks, the specimen must be actively magnetised which means that an applied magnetic field needs to be generated using an external power source. This method has shown to be robust and reliable but it does depend on human inspection and the fact that a background

field must be generated rendering the application not wireless. SMFL is based on the same principle as ordinary magnetic flux leakage, but through theorising that the applied background field is represented by the Earth's magnetic field. Although this field is much weaker, it has shown to influence the distribution of the magnetic induction field on the surface of ferromagnetic materials, see Dong [13]. The application of this concept to fatigue cracks has been studied extensively by Van der Horst [52][54].

The fatigue cracks studied by Van der Horst only consider so-called through-thickness cracks. This implies that, as the name suggests, the material has disappeared over the entire depth of the crack. In fatigue-sensitive locations, for instance near weld seams, cracks can grow at the steel's surface in a semi-elliptical shape, possibly reaching large sizes before eventually becoming a through-thickness crack. Monitoring the growth of these cracks before they reach a substantial size is not possible with the leakage method since the de-routing of magnetic induction field lines does not occur as apparently as for through thickness cracks. A schematic drawing of a semi-elliptical crack is given in figure 1.2. Please note that figure 1.2 depicts a cross section of a metal plate opposed to a top view in figure 1.1.

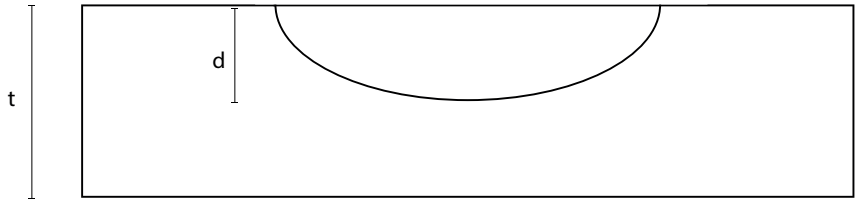

Figure 1.2: Plate (cross section) with a semi-elliptical surface crack. t = thickness of the plate, d = depth of the crack.

Even so, the possibility remains that magnetic flux can be used as a measure for the severity of crack propagation such as drawn in figure 1.2. This requires a crack monitoring system which analyses magnetic induction field changes of an even smaller magnitude than while using the SMFL method. In this order of magnitude the significance of different, smaller and highly nonlinear effects which could previously be neglected increases. This thesis aims to identify, measure, model and quantify these nonlinear effects.

1.2. Objective

From an introductory point of view the magnetisation of a ferromagnetic object can be split into two parts: permanent and induced magnetisation, as described by Holmes [19]. The former describes the magnetisation that is apparent within a ferromagnetic object when there is no background field present, whereas the latter depicts the additional magnetisation that an object accumulates when exposed to a certain magnetic background field. Gradual changes in permanent magnetisation over extended time periods have been observed in steel structures which are expected to occur due to a combination of ferromagnetic mechanics. Describing these gradual changes provides a challenge since they are governed by effects that are relatively small, highly nonlinear, and sometimes poorly documented. This thesis aims to provide better understanding into how these nonlinear changes in permanent magnetisation occur in ferromagnetic steel. A number of separate effects have been identified up to date, of which the stress-induced component, known as the magneto-mechanical- or Villari effect, is beforehand expected to be the largest contributor within the testcase that will be analysed during this research project. Proper quantification and modelling of this effect can then be implemented in sensoring equipment used for elliptical crack monitoring systems in the future.

1.2.1. Research question

The main research question is defined as:

- Is it possible to model the magnetic behaviour of a ferromagnetic object regarding the nonlinear effects (relaxation, hysteresis and Villari) and non-uniform distribution of the magnetisation?

Which corresponds with the set of subquestions that need to be answered preliminary:

- What is the effect of magnetic relaxation, or the magnetic after-effect, on the permanent magnetisation of ferromagnetic steel and can it be quantified?
- Are the test specimens uniformly magnetised, and if not, is it possible to describe a non-uniform distribution using inversion?
- How does magnetic hysteresis influence the permanent magnetisation of ferromagnetic steel?
- What is the significance of the magneto-mechanical or Villari effect when investigating changes in the permanent magnetisation of ferromagnetic steel?

1.2.2. Methodology

Rrelaxation has not been studied extensively, so an attempt is made to measure and quantify this effect. Magnetic hysteresis normally only occurs due to changes in positioning of the observed object within the Earth's magnetic field. This field has a strength of around 50 µT, from which follows that when a ferromagnetic object is rotated in the Earth's magnetic field, for instance a vessel that changes its course, the amplitude of the change in applied magnetic field is in the order of 50 µT. Besides this effect, structural steel is also subjected to high amounts of tensile and compressive stress, and even though its effect on permanent magnetisation compared to magnetic hysteresis is currently unclear, for now it is expected that the majority of the changes in permanent magnetisation over time, or *perm*, originate as a consequence of this magneto-mechanical effect. For this project, the choice was made to use a hysteresis model that could be conveniently modified to include a stress-induced magnetisation component. Since this model is an extension of an ordinary magnetic hysteresis model, magnetic hysteresis itself is initially described without stress in order to expand with a stress-induced component at a later stage.

The magnetic behaviour of a ferromagnetic object is dependent on three factors:

1. Material properties;
2. Geometry;
3. External factors (stress, applied background field, temperature).

Since the goal is to find the correct material parameters, it is essential that the other factors are known and controlled. Using the right test setup, both the stress and the background field can be controlled. Geometry is controlled by testing specimens consisting of different geometric shapes for which analytical (approximate) expressions of the magnetic field can be derived. Generic descriptions of stationary magnetic fields in matter are given for a certain range of objects. These are the objects that will be tested during experiments, and an explanation is provided as to why these objects are selected for the scope of this research. After describing the magnetic field of these objects using the magnetostatic field equations, a three-dimensional numerical model that is created using finite element analysis (FEA) software is presented which is used to validate the analytical solutions.

Up front it is not anticipated that specimens subjected to constant background fields show significant changes in magnetisation due to magnetic relaxation. To verify this, an attempt is made to measure and describe magnetic relaxation in the laboratory setup. Then, the permanent magnetisation of the test specimens is analysed by describing the non-uniform magnetisation of these specimens using a self-derived methodology. Following this, an explanation of the concept of magnetic hysteresis is provided and a comparison of existing models that are widely used to capture this effect is given. An approach is presented in which multiple hysteresis experiments are conducted on various specimens. These experiments are then recreated and compared using FEA which uses the earlier derived non-uniform magnetisation description to describe the starting point of the hysteresis curve.

The hysteresis model is extended with two additional parameters in order to accommodate a stress-induced magnetisation component. Laboratory tests are performed by means of tensioning a rectangular steel plate in a custom setup made from aluminium which uses titanium bolts in order to apply tension. The resulting changes in induction field measurements below the specimen due to the tensioning are

measured and an attempt is be made to translate this to magnetisational changes using FEA. This is followed by several conclusion as well as future recommendations and a discussion regarding the implementation of the knowledge acquired during this project.

1.3. Outline

The contents of each chapter are summarised here.

Chapter 2 provides the analytical derivation of expressions for the magnetostatic field around a sphere, spheroid, and a square plate. It explains why these objects are chosen and why the derivation of these equations is relevant for the scope of this research.

Chapter 3 includes an investigation into the significance of magnetic relaxation or the magnetic after-effect.

Chapter 4 shows that the specimens can not be treated as exhibiting uniform permanent magnetisation. This is followed by a self-developed method through which the non-uniform magnetisation can be calculated using inversion.

Chapter 5 introduces the concept of magnetic hysteresis and provides insight into the prevalent hysteresis models. Hysteresis is measured and successfully recreated using the Jiles-Atherton model in combination with FEA, which uses the methodlogy from chapter 4 to define a starting magnetisation.

Chapter 6 introduces the Villari effect, and how the model used to describe magnetic hysteresis in chapter 5 can be extended in order to incorporate stress-induced magnetisation. The Villari effect is measured and reproduced using FEA, which uses the methodlogy from chapter 4 to define a starting magnetisation.

Chapter 7 contains conclusions drawn from chapters 3-6 including some recommendationds and insight into further research and application of the acquired knowledge in ellipsoidal crack detection methods.

2

Magnetostatics

2.1. Magnetostatic field equations

As explained in section 1.2.2, the goal of this thesis is to describe changes in permanent magnetisation of steel using experiments and numerical simulations. A problem that arises while trying to measure magnetisation during experiments is that magnetisation is impossibly measured directly, i.e. it is not possible to 'open up' a test specimen and directly measure its magnetisation. In order to describe magnetisation within a specimen a method known as *inversion* is adopted. Expressions for the magnetic field can be derived given that the objects' magnetisation is known. Inversion entails, as the name suggest, that the opposite is done: measurements are conducted at a distance from the material and translated back to magnetisation using the inverse of these field equations.

Analytical expressions of the magnetic field of uniformly magnetised objects can be derived from the magnetic field equations formulated by Maxwell. These analytical expressions can only be derived, with relative ease, for simple geometric shapes. These shapes include spheres, spheroids and thin metal plates. Since this is rather fundamental research, it is prefered to compare numerical and analytical solutions which limits the test specimen geometries to these shapes.

The experiments in this research project are restricted to a quasi-static magnetic domain in which there are no external electric currents present. This physical state is known as *magnetostatics*. In order to describe magnetic fields, a system of three field equations, known as Maxwell's equations, is governing. These equations use the following physical quantities, as introduced by Jackson [21]

$\mathbf{H}$ = magnetic field [A/m]
$\mathbf{B}$ = magnetic induction field [T]
$\mathbf{M}$ = magnetisation [A/m]

and the constant μ_0 = magnetic permeability in vacuum (air) = $4\pi 10^{-7}$[H/m] .

H, **B**, and **M** are vector fields. This implicates that for every point in three-dimensional space there is a vector describing the magnetic field in that point, with its own three-dimensional direction and magnitude. Characters that represent vectors are from here on printed in bold and vector fields are printed in bold capital letters.

It is assumed that there are no electrical currents on the ferromagnetic material's surface, hence **J = 0**. The first field equation then states that the curl of **H** is **0**. This implies that given a certain ferromagnetic object in space, the vector describing the magnetisation in any point (x,y,z) does not change over time, the magnetisation is static

$$\nabla \times \mathbf{H} = \mathbf{J} = \mathbf{0} \,. \tag{2.1}$$

The second field equation states that the magnetic induction field **B** is divergence-free. This implicates that there are no sources or sinks of magnetism within the observed domain, ensuring zero net magnetisation, i.e. magnetism is conserved

$$\nabla \cdot \mathbf{B} = 0 \, . \tag{2.2}$$

The third and final field equation describes the relation between the magnetisation, the magnetic field, and the magnetic induction field as

$$\mathbf{B} = \mu_0(\mathbf{H} + \mathbf{M}) \, . \tag{2.3}$$

Magnetisation may only exist in matter, whereas **B** and **H** exist both in matter and air. From this it follows that the magnetic induction field and the magnetic field outside of the object, in air, are linearly correlated by

$$\mathbf{B} = \mu_0 \mathbf{H} \tag{2.4}$$

as described by Coey [9].

2.2. Sphere

2.2.1. Uniformly magnetised

As described in the previous section there is a limited number of geometries for which an analytical expression for the magnetic field can be provided. The geometry with the most straightforward derivation is a sphere. Even though a sphere is not one of the objects that will be subjected to experiments, a good understanding of the derivation of the analytical expression for the magnetic field around a uniformly magnetised sphere provide an excellent starting point for the derivations of the analytical expressions for the spheroid and thin plate that will be subjected to experiments in the laboratory setup. Because of its relatively simple derivation, the sphere serves as a good method of verifying correct implementation in the FEA-package.

Presented in this section is a summarised version of the derivation of the magnetic field **H** of a sphere with radius a which is uniformly magnetised in z-direction with magnetisation **M**. The full extent of this derivation can be found in appendix A.1. In figure 2.1, a two-dimensional sketch of the magnetised sphere is presented with the y-axis pointing out of the paper.

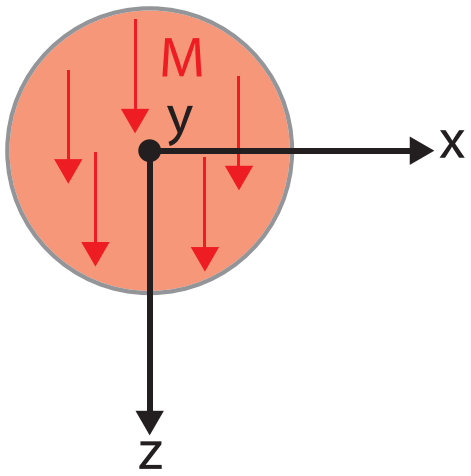

Figure 2.1: Two-dimensional view of a uniformly magnetised sphere.

Uniform magnetisation in z-direction implies that for every point within the sphere the magnetisation is given by the vector

$$\mathbf{M} = M \begin{bmatrix} 0 \\ 0 \\ 1 \end{bmatrix} \tag{2.5}$$

assuming no magnetisation in x and y-directions. In order to calculate the magnetic field **H** it can be stated that based on equation (2.1), a magnetic scalar potential Φ can be introduced (see Jackson [21] and Griffiths [18]) such that

$$\mathbf{H} = -\nabla\Phi \, . \tag{2.6}$$

In this equation, $\Phi(\mathbf{r})$ is given by

$$\Phi(\mathbf{r}) = \frac{-1}{4\pi} \iiint_{\Omega} \frac{(\nabla' \cdot \mathbf{M})(\mathbf{r}')}{|\mathbf{r} - \mathbf{r}'|} \, d^3r \tag{2.7}$$

in which Ω is the infinite air domain. In order to further simplify this solution to the potential equation it is necessary to define an expression for $\nabla \cdot \mathbf{M}$. The vector **r** is considered in a spherical coordinate system as shown in figure 2.2. Only the coordinate system is shown here, the magnetised sphere has its centre at the origin as shown in figure 2.1.

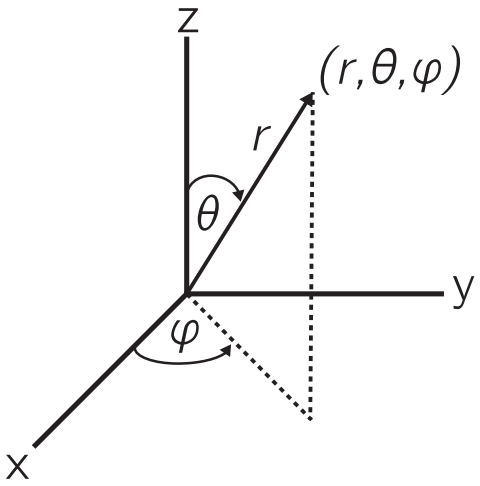

Figure 2.2: Spherical coordinate system.

After rewriting, see appendix A.1, the **H**-field is given by

$$\mathbf{H} = \begin{cases} -\nabla\Phi = \frac{M_0 \cdot r}{3}(\cos\theta \mathbf{u}_r - \sin\theta \mathbf{u}_\theta) = -\frac{M_0}{3}\mathbf{u}_z & \text{if } r < a, \\ -\nabla\Phi = \frac{M_0 \cdot a^3}{3r^3}(2\cos\theta \mathbf{u}_\mathbf{r} + \sin\theta \mathbf{u}_\theta) = \frac{M_0 a^3}{3r^3}(3\sin\theta \mathbf{u}_\theta + 2\mathbf{u}_z) & \text{if } r > a \end{cases} \tag{2.8}$$

in which $\mathbf{u}_z = \cos\theta \mathbf{u}_r - \sin\theta \mathbf{u}_\theta$. Using the fact that a sphere's volume is given by $V_{\text{sphere}} = \frac{4}{3}\pi a^3$, for $r > a$ it is possible to write **H** as

$$\mathbf{H} = \frac{V_{\text{sphere}} M_0}{4\pi r^3}(2\cos\theta \mathbf{u}_r + \sin\theta \mathbf{u}_\theta) \, . \tag{2.9}$$

Visualising a magnetic field provides a challenge since a vector field implies that for every point in three-dimensional space, a vector can be constructed which has three components. A way of visualising a vector field is using a two-dimensional approach by taking a cut plane out of the data by fixing one of the three coordinates, and plotting the size of the B_x, B_y, B_z and B_{tot} components individually at each location in this plane. For the case of the magnetic field around a uniformly magnetised sphere, an arbitrary sphere with its centre at the origin, radius $a = 100$ mm and a uniform magnetisation pointing downwards in z-direction of 1000 A/m was modelled analytically using `MATLAB`. The plane observed is the xy-plane directly below the sphere at $z = 200$ mm, which is shown in figure 2.3. The analytically calculated magnetic induction field components B_x, B_y and B_z as well as the norm B_{tot} in this plane are shown in figure 2.4.

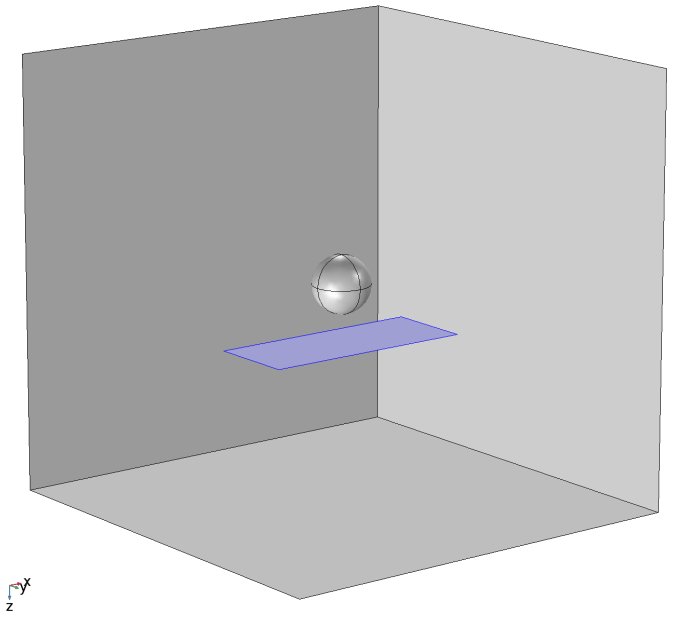

Figure 2.3: Sphere with origin at (0,0,0) and a xy-plane at z = 200 mm.

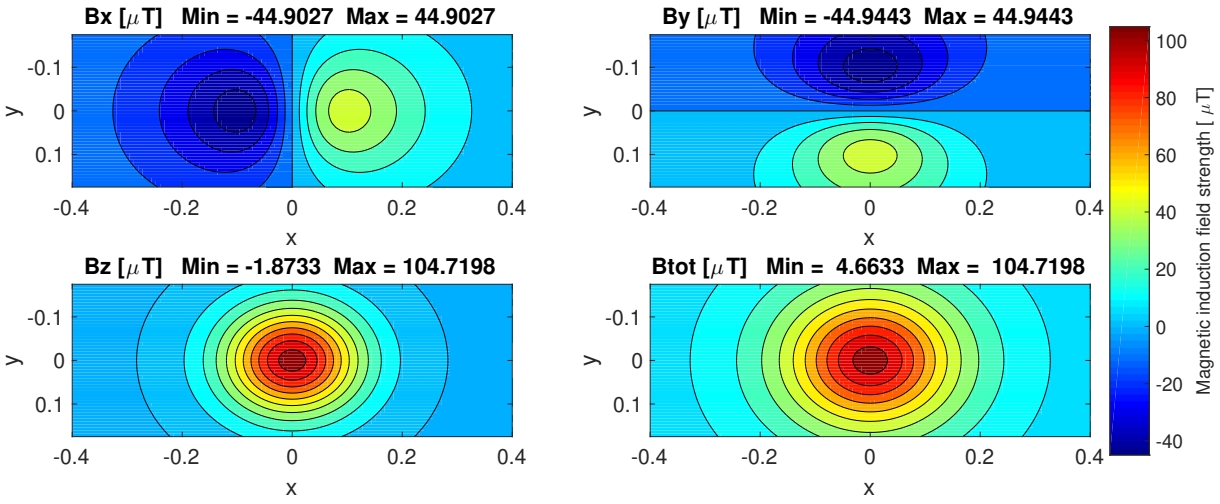

Figure 2.4: Magnetic induction field of a magnetised sphere (a = 100 mm, M_z = 1000 A/m), in the xy-plane at z = 200 mm.

From equation (2.8) it can be observed that the magnetic field **H** within the sphere points in a direction opposite to the direction of the magnetisation. Equation (2.8) can be rewritten in such a way that a

demagnetisation factor N_z can be defined as

$$H_z = -N_z M_{0z} \tag{2.10}$$

from which follows that $N_z = 1/3$. Because of radial symmetry it can be stated that $N_x = N_y = N_z = 1/3$ for a sphere. The demagnetisation factors serve as a parameter that provides insight into the relation of the magnetisation within the object and the strength of the magnetic field, within the object, that works in the opposite direction due to this magnetisation. A low demagnetisation factor implies that the object prefers to be magnetised into that direction. As shown in the derivation, this factor is defined by geometry of the specimen only. The importance of this property will be explained further in section 2.3 when the magnetic field equations derivation for spheroid is presented.

2.2.2. Linearly reacting material

Section 2.2 and appendix A.1 show the derivation of the equations describing the magnetic field due to a magnetised sphere without a background field. However, in practice there is usually a background field present, for example the Earth's magnetic field. A ferromagnetic object in this case amplifies the background field. It is relevant to see how this magnetisation differs from the derivation presented in section 2.2, since in practice the magnetic field around an object can be best represented by a combination of internal magnetisation and linear dependence on a certain background field. Please note that in this section a summarised version of the derivation is given. The full derivation is presented in appendix A.2 and is taken from Morse and Fesbach [38].

The sphere from section 2.2 is placed in a uniform background field $\mathbf{H} = H_0\mathbf{u}_z$, and it is stated that the magnetisation inside the sphere is no longer a fixed constant but rather scales linearly with the background field with a relative permeability μ_r. The relative permeability μ_r describes the magnetic permeability of the material as a multiplication of the magnetic permeability in free space, μ_0. The equation describing the magnetisation within the sphere becomes, as described by Jackson [21] and Griffiths [18]:

$$\mathbf{M} = (\mu_r - 1)\mathbf{H}\,. \tag{2.11}$$

From equation (2.11) it can be seen that for μ_r = 1 the magnetisation completely vanishes since the permeability of the object is identical to μ_0 which is present outside the object. In (2.11), **H** inside the sphere is defined as the sum of $\mathbf{H}_o$ due to the background field, and $\mathbf{H}_i$ due to the magnetisation of the sphere itself:

$$\mathbf{H} = \mathbf{H}_o + \mathbf{H}_i\,. \tag{2.12}$$

Please note that for this example it has been assumed that the magnetic background field points uniformly downward in the z-direction. Combining equations (2.11) and (2.12) returns the following expression for **M**:

$$\mathbf{M} = (\mu_r - 1)(\mathbf{H}_o + \mathbf{H}_i)\,. \tag{2.13}$$

Rewriting, see appendix A.2, and substituting into equation (2.9) yields

$$\mathbf{H} = \mathbf{H}_o + \mathbf{H}_i = H_0\mathbf{u}_z + \frac{V_{\text{sphere}}}{4\pi r^3}(2\cos\theta\mathbf{u}_r + \sin\theta\mathbf{u}_\theta)\left[\frac{\mu_r - 1}{1 + \frac{1}{3}(\mu_r - 1)}\right]H_0\,. \tag{2.14}$$

This can be rewritten using spherical unit vectors and the knowledge that the magnetic dipole moment is given by

$$\mathbf{m} = \int_\Omega \mathbf{M}(\mathbf{r})\mathrm{d}(\mathbf{r}) = \mathrm{V}_{\text{sphere}}\mathbf{M} = \mathrm{V}_{\text{sphere}}\mathrm{M}_0\mathbf{u}_z\,. \tag{2.15}$$

This leads to the following equation describing the magnetic field outside a sphere which has a magnetisation that scales linearly with the applied background field:

$$\mathbf{H}(\mathbf{r}) = H_0\mathbf{u}_z + \frac{3H_0(\mu_r - 1)}{4\pi r^3(\mu_r + 2)}\left(\frac{3\mathbf{r}(\mathbf{m}\cdot\mathbf{r})}{r^2} - \mathbf{m}\right). \tag{2.16}$$

A linearly reacting sphere with radius a = 100 mm and relative permeability μ_r = 100 is subjected to a background field of 100 µT which points downward in z-direction. The components of the magnetic induction field in the xy-plane at z = 200 mm (see figure 2.3) are plotted in figure 2.5.

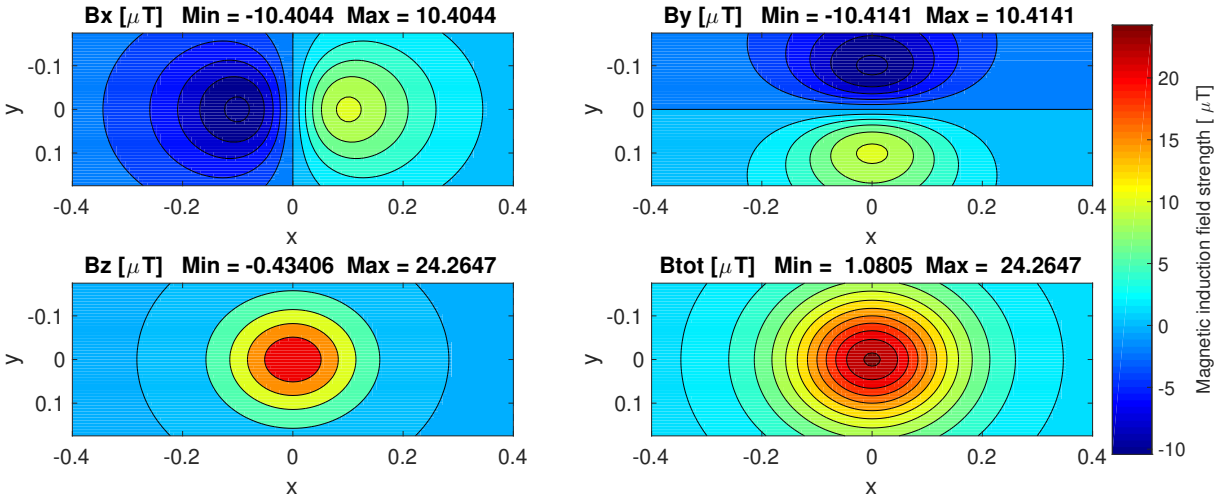

Figure 2.5: Magnetic induction field of a magnetisable sphere (a = 100 mm, μ_r = 100), subjected to a background field $B_{0,z}$ = 100 µT, in the xy-plane at z = 200 mm.

2.3. Prolate spheroid

2.3.1. Uniformly magnetised

An analytical solution for the magnetic field around a solid, uniformly magnetised sphere was presented in section 2.2. Besides spheres, another shape for which an analytical solution exists is the prolate spheroid. This will be one of the objects that will be used in laboratory experiments. A spheroid is created by spinning a two-dimensional ellipse around one of its axes as shown in figure 2.6. Assume an ellipse with major axis a and minor axis b such that $a > b$. In order to turn this into a three-dimensional object, one can revolve this ellipse around either of these axes. When rotated around its major axis, a cigar-shaped three-dimensional volume is created with one major and two identical minor axes, which is known as a prolate spheroid. Revolving around the minor axis will yield a pancake-shaped volume with two major and one minor axis which is known as an oblate spheroid. In mathematical terms:

$$\begin{aligned} &\text{if } \ a > b = c \ : \text{ prolate spheroid;} \\ &\text{if } \ a = c > b \ : \text{ oblate spheroid.} \end{aligned} \tag{2.17}$$

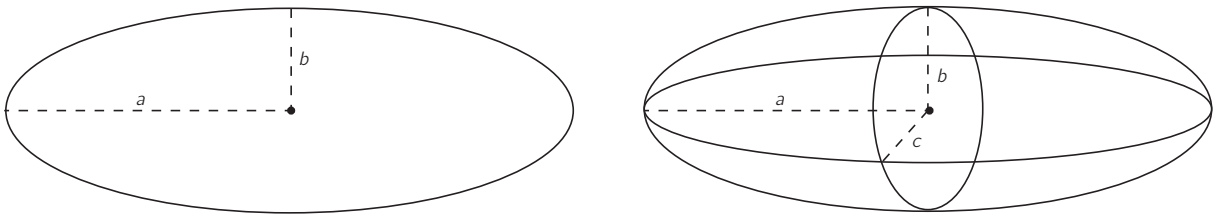

Figure 2.6: Ellipse (2D) and spheroid (3D).

The main reason that the analytical solution to the magnetic field of a prolate spheroid is derived here involves the demagnetisation factors that were introduced at the end of section 2.2. For a sphere it was found that in the xyz-directions the demagnetisation factors were all equal to 1/3. This can be interpreted as that for a certain magnetisation in a given direction, the magnetic field within the material points in a direction opposite to this magnetisation at a third of the strength of the magnetisation. For spheroids it is known that these demagnetisation factors are different, depending on the length to width ratio as derived by Osborn [42]. At the end of this section it will be found that for prolate spheroids the demagnetisation factor in the longitudinal direction becomes much smaller than in the transverse directions for increasing length to width ratio. This implicates that when a certain field is applied in line with the major axis of a prolate spheroid (from here on the x-axis), the magnetisation within the material in that direction will change by a greater amount than if a field with identical strength is applied in y or z-directions. This property will come in very useful when measuring hysteresis in a laboratory setup, since larger changes in magnetisation cause the hysteretic effect to become increasingly detectable when applying a certain external magnetic field along the prolate spheroid's longitudinal direction. On top of that, it is known that for both solid spheres and spheroids the magnetisation and the corresponding magnetic field within the material are uniform when a linearly reacting material is subjected to a uniform field, as described by Osborn [42]. The introduction of spheroidal coordinates is given by Morse and Feshbach [38] and the full derivation of the equations below is presented in appendix A.3.

In order to describe a spheroid a new coordinate system will be introduced using prolate spheroidal coordinates (ξ, η, ϕ). This is explained further below and illustrated in figure 2.7.

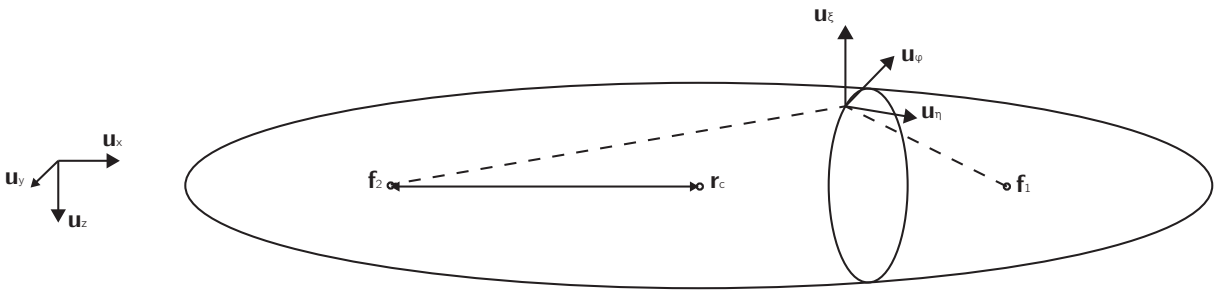

Figure 2.7: Prolate spheroid in spheroidal coordinates.

The centre point of the spheroid is described in Cartesian coordinates by

$$\mathbf{r}_c = \begin{pmatrix} x_0 \\ y_0 \\ z_0 \end{pmatrix} . \tag{2.18}$$

The focal length $2f$ is introduced as the distance (in x-direction) from the centre towards the two focal points:

$$\begin{aligned} \mathbf{f1} &= \mathbf{r}_c + f\mathbf{u}_x , \\ \mathbf{f2} &= \mathbf{r}_c - f\mathbf{u}_x . \end{aligned} \tag{2.19}$$

A position vector $\mathbf{r} = (x, y, z)^T$ can now be defined in terms of (ξ, η, ϕ), while using that $r_1 = |\mathbf{r} - \mathbf{f_1}|$ and

$r_2 = |\mathbf{r} - \mathbf{f_2}|$:

$$\begin{aligned} \xi &= \frac{r_1 + r_2}{2f} \\ \eta &= \frac{r_1 - r_2}{2f} \\ \cos(\phi) &= \frac{y - y_0}{\sqrt{(y - y_0)^2 + (z - z_0)^2}} \\ \sin(\phi) &= \frac{z - z_0}{\sqrt{(y - y_0)^2 + (z - z_0)^2}} \,. \end{aligned} \tag{2.20}$$

The surface of the spheroid is given by $\xi = \xi_0$. It then follows that $\xi < \xi_0$ lies within the spheroid and $\xi > \xi_0$ lies in free space. The uniform magnetisation is then described by

$$\mathbf{M} = \begin{cases} M_x \mathbf{u}_x + M_y \mathbf{u}_y + M_z \mathbf{u}_z & \text{for} \quad \xi < \xi_0 \\ \mathbf{0} & \text{for} \quad \xi > \xi_0 \end{cases} . \tag{2.21}$$

Similar to section 2.2, the following solution to the potential equation must be worked out in order to find the magnetic field:

$$\Phi(\mathbf{r}) = \frac{-1}{4\pi} \iiint_{\Omega} \frac{(\nabla' \cdot \mathbf{M})(\mathbf{r}')}{|\mathbf{r} - \mathbf{r}'|} d^3\mathbf{r}' \,. \tag{2.22}$$

The solution to equation (2.22) is once more found using (associated) Legendre functions which is further described in Appendix A.3 and follows from Morse and Feshbach [38]. The magnetic field **H** inside the spheroid is given by

$$\mathbf{H}(\mathbf{r}) = -N_x M_{0x} \mathbf{u}_x - N_y M_{0y} \mathbf{u}_y - N_z M_{0z} \mathbf{u}_z \tag{2.23}$$

with demagnetisation factors

$$N_x = \frac{1}{m^2 - 1} \left[\frac{m}{\sqrt{m^2 - 1}} \ln\left(m + \sqrt{m - 1}\right) - 1 \right] \tag{2.24}$$

$$N_y = N_z = \frac{m}{2(m^2 - 1)} \left[m - \frac{1}{\sqrt{m^2 - 1}} \ln\left(m + \sqrt{m - 1}\right) \right] \tag{2.25}$$

in which m is the ratio of the spheroid's length to diameter, $m = a/b$. From figure 2.8 it can be seen that for m = 1 the demagnetisation factors are all 1/3, as derived earlier for the sphere. Upon elongation in x-direction, the ratio between length and diameter increases, causing the demagnetisation factor longitudinal direction to decrease. This shows that a prolate spheroid accumulates magnetisation more easily in the longitudinal direction.

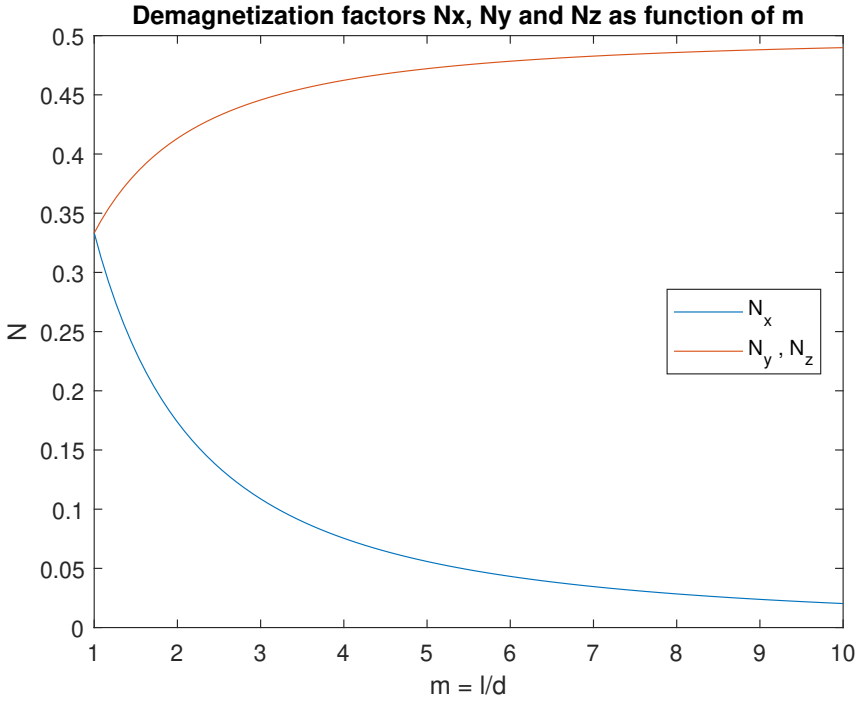

Figure 2.8: Demagnetisation factors of a prolate spheroid as a function of m.

The solution to the magnetic induction field outside of the spheroid is given by

$$\mathbf{B} = \mu_0 \xi_0 (\xi_0^2 - 1) \underline{\underline{A}} \mathbf{M} \tag{2.26}$$

in which

$$\underline{\underline{A}} = \begin{pmatrix} A_{xx} & A_{xy} & A_{xz} \\ A_{yx} & A_{yy} & A_{yz} \\ A_{zx} & A_{zy} & A_{zz} \end{pmatrix} \tag{2.27}$$

with

$$A_{xx} = -\frac{1}{2} \ln\left(\frac{\xi + 1}{\xi - 1}\right) + \frac{\xi}{\xi^2 - \eta^2} \tag{2.28a}$$

$$A_{xy} = -\frac{\eta \cos\phi}{\xi^2 - \eta^2} \sqrt{\frac{1 - \eta^2}{\xi^2 - 1}} \tag{2.28b}$$

$$A_{xz} = -\frac{\eta \sin\phi}{\xi^2 - \eta^2} \sqrt{\frac{1 - \eta^2}{\xi^2 - 1}} \tag{2.28c}$$

$$A_{yx} = A_{xy} \tag{2.28d}$$

$$A_{yy} = -\frac{1}{4} \ln\left(\frac{\xi + 1}{\xi - 1}\right) + \frac{\xi}{\xi^2 - 1} \left[\frac{1 - \eta^2}{\xi^2 - \eta^2} \cos^2\phi - \frac{1}{2}\right] \tag{2.28e}$$

$$A_{yz} = \frac{\xi(1 - \eta^2)}{(\xi^2 - 1)(\xi^2 - \eta^2)} \sin\phi \cos\phi \tag{2.28f}$$

$$A_{zx} = A_{xz} \tag{2.28g}$$

$$A_{zy} = A_{yz} \tag{2.28h}$$

$$A_{zz} = \frac{1}{4}\ln\left(\frac{\xi+1}{\xi-1}\right) + \frac{\xi}{\xi^2-1}\left[\frac{1-\eta^2}{\xi^2-\eta^2}\sin^2\phi - \frac{1}{2}\right] . \tag{2.28i}$$

In order to visualise the magnetic field around a spheroid, a prolate spheroid is modelled with length 560 mm and diameter 95 mm, or $a = 280$ mm and $b = 47.5$ mm. These dimensions are identical to the spheroid that will be tested during laboratory experiments. These dimensions result in $\xi_0 = 1.01$, $m = 5.89$, $N_x = 0.0442$, $N_y = N_z = 0.4778$, and $V = 2.65\times10^{-3}$ m^3. The spheroid is assumed to be uniformly magnetised in x-direction with a magnetisation of 1000 A/m. The magnetic field is observed is the xy-plane at $z = 200$ mm below the origin of the spheroid. The different components of the magnetic induction field are computed using MATLAB and presented in figure 2.9.

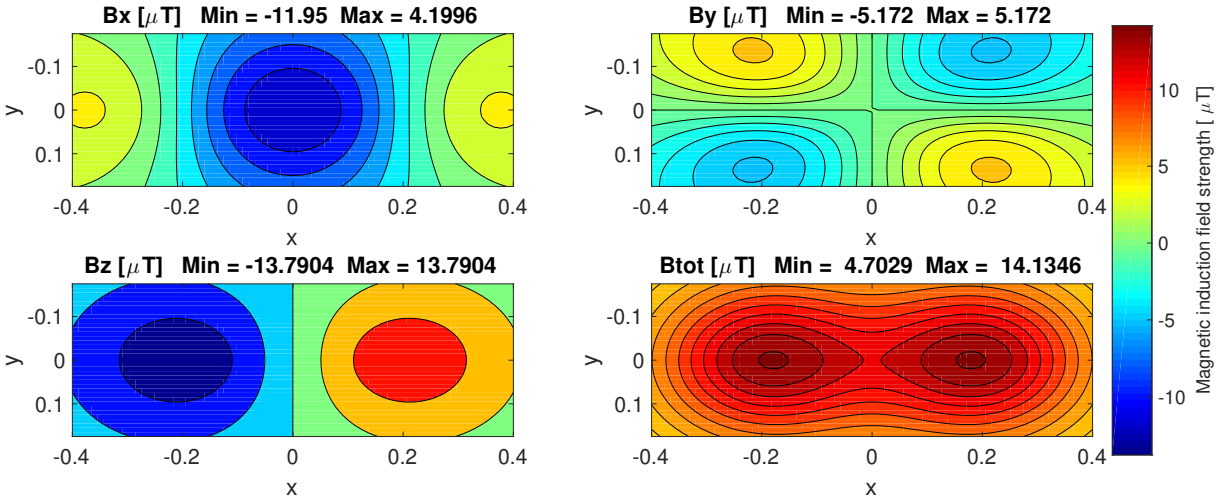

Figure 2.9: Magnetic induction field of a magnetised prolate spheroid with its centre at the origin (length 560 mm, diameter 95 mm, $M_x = 1000$ A/m), in the xy-plane at $z = 200$ mm.

2.3.2. Linearly reacting material

In the same manner as the sphere, the magnetic induction field of the spheroid can be calculated when the material supposedly reacts linearly to a uniform background field. The complete derivation shows large similarities to sections 2.2.2 and 2.3.1 and is therefore not presented here. It can be found in a document by Lepelaars [33]. The expression describing the magnetic field inside the spheroid is given by

$$\mathbf{H}_i = \frac{H_{0x}\mathbf{u}_x}{1+(\mu_r-1)N_x} + \frac{H_{0y}\mathbf{u}_y}{1+(\mu_r-1)N_y} + \frac{H_{0z}\mathbf{u}_z}{1+(\mu_r-1)N_z} \tag{2.29}$$

in which N_x, N_y and N_z represent the demagnetisation factors derived in section 2.3. Since the magnetic induction field inside the spheroid can be written as

$$\mathbf{B}_i = \mu_0(\mathbf{H}_i + \mathbf{M}) , \tag{2.30}$$

and from the fact that the magnetisation is uniform inside the spheroid, it follows that the magnetisation $\mathbf{M}$ and dipole moment $\mathbf{m}$ can be written as

$$\mathbf{M} = (\mu_r - 1)\mathbf{H}_i, \qquad \mathbf{m} = V_{\text{spheroid}}\mathbf{M} = \frac{4}{3}\pi f^3 \xi_0(\xi_0^2 - 1)\mathbf{M} . \tag{2.31}$$

The magnetic induction field outside of the spheroid follows from the result found in section 2.2 to which the background field is added. This returns

$$\mathbf{B}_o = \mathbf{B}_0 + \mu_0 \xi_0 (\xi_0^2 - 1) \underline{\underline{A}} \mathbf{M} \tag{2.32}$$

in which the matrix $\underline{\underline{A}}$ is identical to the matrix derived in section 2.3.1. The magnetic induction field in an xy-plane 200 mm below the centre of a linearly reacting spheroid with length 560 mm, diameter 95 mm and μ_r of 100 which is subjected to a uniform background field of 100 µT pointing in x-direction is presented in figure 2.10.

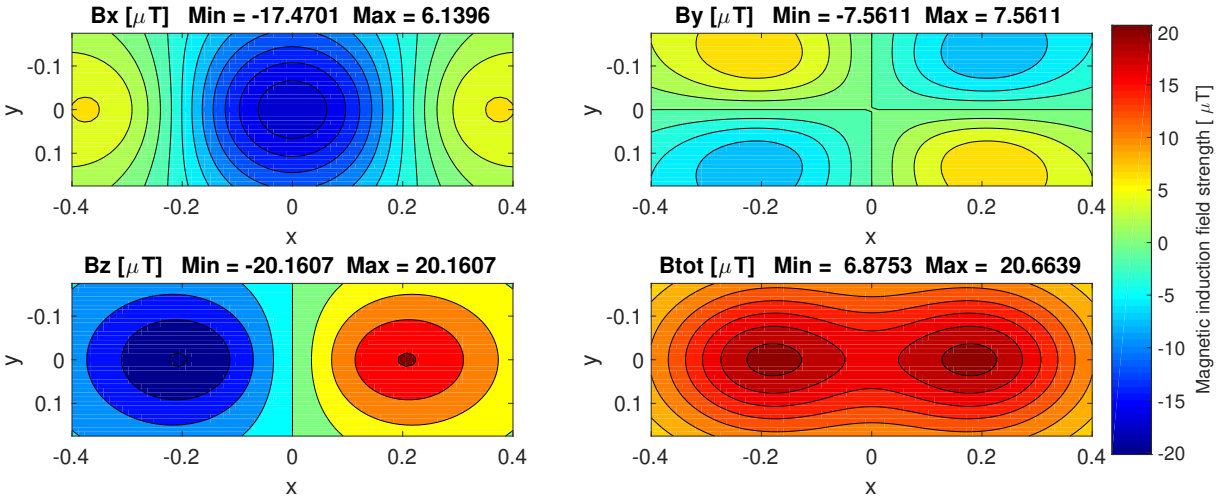

Figure 2.10: Magnetic induction field of a magnetisable prolate spheroid (length 560 mm, diameter 95 mm, μ_r = 100), subjected to a background field $B_{0,x}$ = 100 µT, in the xy-plane at z = 200 mm.

2.4. Metal plate

2.4.1. Uniformly magnetised

Previously, the magnetic field properties of spheres and spheroids have been derived. However, in practice, the material that is used in the construction of marine applications consists mainly of sheet metal plates. In order to get a better understanding of hysteresis in these types of steel, measurements are performed on pieces of construction-grade sheet metal. These are widely available in different dimensions and provide a good addition to the experiments since they are easily subjected to tension tests, unlike spheroids or spheres. A perfect analytical solution for thin plates exists in a rather complex form, so an adequate approximation is presented here. This derivation is taken from [54].

A plate with width w, length ℓ, and thickness t in respectively x, y and z-direction exhibits a uniform magnetisation in x-direction, M_0. Making use of the Heaviside step function H, the magnetisation can be written as

$$\begin{aligned}\mathbf{M} = M_0 \cdot &\left[H\left(x + \tfrac{w}{2}\right) - H\left(x - \tfrac{w}{2}\right)\right] \cdot \left[H\left(y + \tfrac{\ell}{2}\right) - H\left(y - \tfrac{\ell}{2}\right)\right] \cdot \\ &\left[H\left(z + \tfrac{t}{2}\right) - H\left(z - \tfrac{t}{2}\right)\right] \mathbf{u}_x \,.\end{aligned} \tag{2.33}$$

The three magnetostatic field equations are independent of geometry and identical to the sphere and spheroid

$$\nabla \times \mathbf{H} = \mathbf{0} \,, \tag{2.34}$$

$$\nabla \cdot \mathbf{B} = 0 \,, \tag{2.35}$$

$$\mathbf{B} = \mu_0(\mathbf{H} + \mathbf{M}) \,. \tag{2.36}$$

It follows that the potential equation has the shape of

$$\begin{aligned} \nabla^2\Phi = \quad & \nabla \cdot \nabla\Phi = -\nabla \cdot \mathbf{H} = \nabla \cdot \mathbf{M} \\ \nabla^2\Phi = M_0 \cdot & \left[\delta\left(x + \tfrac{w}{2}\right) - \delta\left(x - \tfrac{w}{2}\right)\right] \cdot \left[H\left(y + \tfrac{\ell}{2}\right) - H\left(y - \tfrac{\ell}{2}\right)\right] \cdot \\ & \left[H\left(z + \tfrac{t}{2}\right) - H\left(z - \tfrac{t}{2}\right)\right] \,. \end{aligned} \tag{2.37}$$

The corresponding magnetic field is given by equation (2.38) below. For the full derivation, please view appendix A.4.

$$\begin{aligned} \mathbf{H}(\mathbf{r}) = -\nabla\Phi = \frac{M_0 t}{4\pi} \Bigg\{ & \frac{1}{D^{--}}\mathbf{u}_y + \frac{1}{(x-\frac{w}{2})^2+z^2}\left(1 - \frac{y-\frac{\ell}{2}}{D^{--}}\right)\left[\left(x - \tfrac{w}{2}\right)\mathbf{u}_x + z\mathbf{u}_z\right] - \\ & \frac{1}{D^{-+}}\mathbf{u}_y + \frac{1}{(x-\frac{w}{2})^2+z^2}\left(1 - \frac{y+\frac{\ell}{2}}{D^{-+}}\right)\left[\left(x - \tfrac{w}{2}\right)\mathbf{u}_x + z\mathbf{u}_z\right] - \\ & \frac{1}{D^{+-}}\mathbf{u}_y + \frac{1}{(x+\frac{w}{2})^2+z^2}\left(1 - \frac{y-\frac{\ell}{2}}{D^{+-}}\right)\left[\left(x + \tfrac{w}{2}\right)\mathbf{u}_x + z\mathbf{u}_z\right] + \\ & \frac{1}{D^{++}}\mathbf{u}_y + \frac{1}{(x+\frac{w}{2})^2+z^2}\left(1 - \frac{y+\frac{\ell}{2}}{D^{++}}\right)\left[\left(x + \tfrac{w}{2}\right)\mathbf{u}_x + z\mathbf{u}_z\right] \Bigg\} \,. \end{aligned} \tag{2.38}$$

In the middle of the plate, where $\mathbf{r} = \mathbf{0}$, it follows that

$$D^{++} = D^{+-} = D^{-+} = D^{--} = \sqrt{\left(\frac{w}{2}\right)^2 + \left(\frac{\ell}{2}\right)^2} \,. \tag{2.39}$$

The magnetic field in the centre of the plate then simplifies to

$$\mathbf{H}(\mathbf{r} = \mathbf{0}) = -M_0 K \mathbf{u}_x \qquad \text{with} \qquad K = \frac{2t\ell}{\pi w\sqrt{w^2 + \ell^2}} \,. \tag{2.40}$$

It can be observed that the magnetic field inside the plate due to the magnetisation points in a direction opposite to the direction of the magnetisation from equation (2.40), which is also observed in the sphere and spheroid. The magnetic field increases with magnetisation M_0, thickness t and length ℓ, but reduces with increasing width w. This is due to the fact that the edges of the plate at $x = \pm w/2$ can be seen as the sources of the magnetic field, since this is where $\nabla \cdot \mathbf{M} \neq 0$. As the plate becomes wider, these sources are separated further, decreasing the strength of the magnetic field. Source strength does increase for larger values of M_0, t and ℓ.

A metal plate with its centre at the origin, $w \times l \times t$ = 300×300×5 mm and a uniform magnetisation in x-direction of 1000 A/m was modelled analytically using `MATLAB`. The magnetic flux density components in the xy-plane below the plate at $z = 200$ mm are shown in figure 2.11.

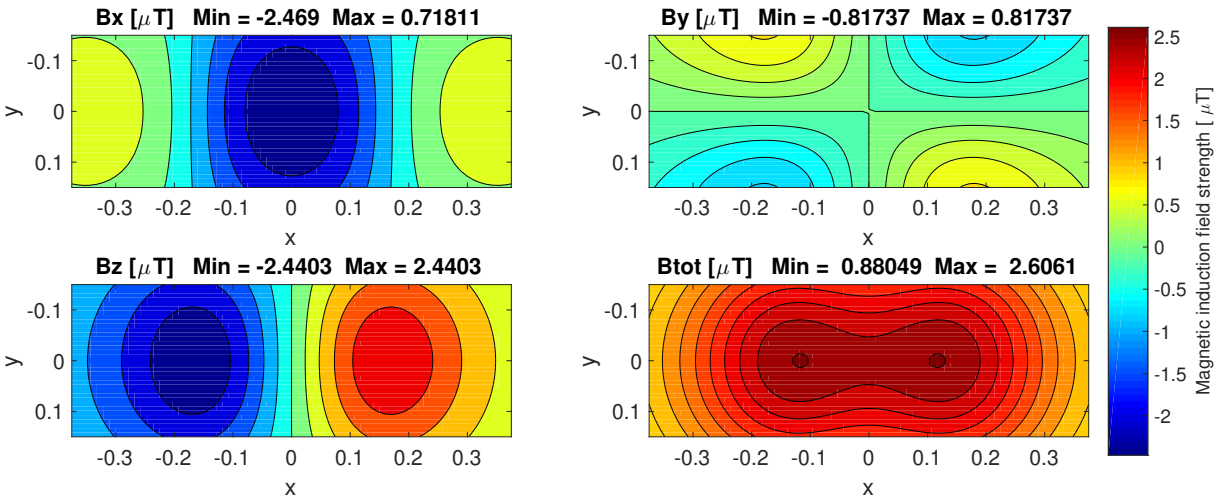

Figure 2.11: Magnetic induction field of a magnetised plate $w \times l \times t$ = 300×300×5 mm, $M_x = 1000$ A/m), in the xy-plane at z = 200 mm.

2.4.2. Linearly reacting material

In the same manner as previous examples, the magnetic induction field of a thin plate can be calculated when the material reacts linearly to a uniform background field. Assume a uniform background field

$$\mathbf{B}_0 = B_0\mathbf{u}_x = \mu_0\mathbf{H}_e = \mu_0 H_0\mathbf{u}_x \, . \tag{2.41}$$

If the plate reacts linearly with a relative permeability μ_r, a magnetisation is introduced when the plate is placed in the background field. It is for now assumed that this magnetisation is uniform throughout the plate. It is known that this property holds for spheres and spheroids, but for thin plates this is not the case, so a small error is made which can be observed when compared with FEA computations later on. The solution for the magnetic field from section 2.4.1 can be used and the total magnetic field within the plate becomes, using the centre-point of the plate:

$$\mathbf{H}(\mathbf{r} = \mathbf{0}) = (H_0 - M_0 K)\mathbf{u}_x \, . \tag{2.42}$$

The magnetic induction field is given by

$$\mathbf{B}(\mathbf{r} = \mathbf{0}) = \mu_0(M_0 - M_0 K + H_0)\mathbf{u}_x \, . \tag{2.43}$$

Furthermore, the following relation holds within the plate:

$$\mathbf{B} = \mu_0\mu_r\mathbf{H} \, . \tag{2.44}$$

Combining these three equations yields

$$\mu_0(M_0 - M_0 K + H_0) = \mu_0\mu_r(H_0 - M_0 K) \tag{2.45}$$

from which a new expression for M_0 can be computed, which is directly related to the background field H_0 and the relative permeability μ_r:

$$M_0 = \frac{(\mu_r - 1)H_0}{1 + (\mu_r - 1)K}. \tag{2.46}$$

This expression for M_0 can be substituted in the equation that is derived earlier, describing the magnetic field for the magnetised plate (equation 2.38). This is shown in figure 2.12

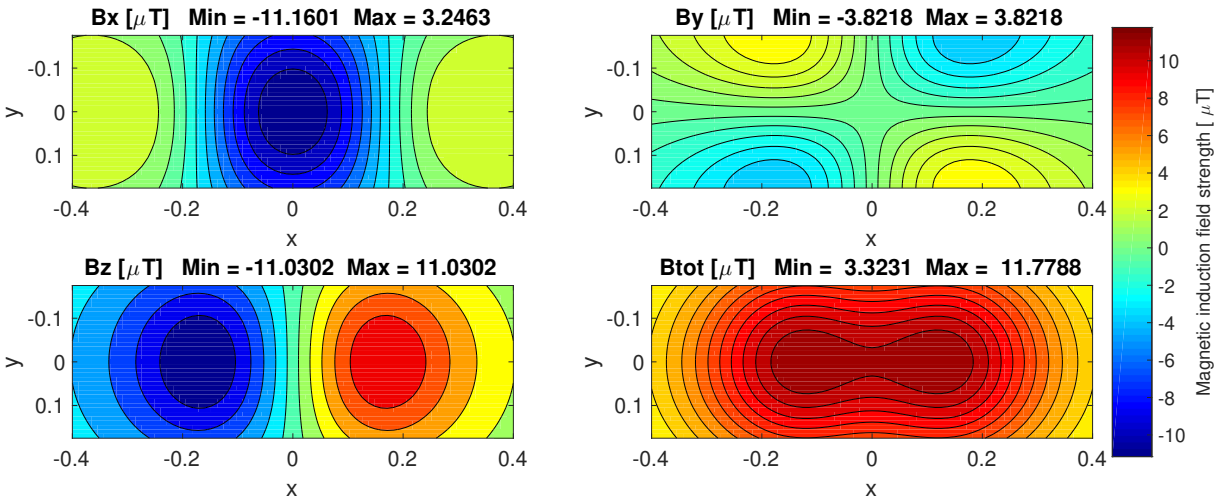

Figure 2.12: Magnetic induction field of a magnetisable plate ($w \times l \times t$ = 300×300×5 mm, μ_r = 100), subjected to a background field $B_{0,x}$ = 100 μT, in the xy-plane at z = 200 mm.

2.5. Finite Element Analysis

Analytical solutions to the magnetostatic field equations for various objects presented in the previous sections provide an elegant insight into the distribution of magnetic fields around ferromagnetic objects. However, major drawbacks include that these formulations only hold for certain specific geometric cases. For more complex geometries, varying time-signals, or highly nonlinear hysteretic behaviour, such direct analytical formulations might simply not exist. The most common way around this problem which is widely adopted by scientists and engineers globally is known as the Finite Element Method, *FEM*, or Finite Element Analysis, *FEA*. Where analytical solutions require the solution to boundary value problems for partial differential equations over the entire domain, the FEM solves a set of algebraic equations which result in approximate solutions at a discrete number of points on a given domain. The problem is solved by subdividing the area under investigation into multiple small and finite elements for which the physical equations that one wishes to solve for are computed. This section simulates step-by-step how `COMSOL Multiphysics`, a FEA package, is used to calculate the magnetostatic fields numerically.

Besides the fact that `COMSOL` suits itself very well for complex problems, another major advantage of using FEM simultaneously with analytical formulations is the property of validation. When the analytical derivation and the FEM implementation are done correctly, they should provide identical results with increasing mesh refinement. At this point, `COMSOL` serves as a perfect tool for validating if the implementation of the field equations is done correctly, and vice versa. Eventually, this powerful software is used to model hysteresis and stress-induced magnetic components on more complex geometries for which the analytical expressions become too complex to solve for altogether.

`COMSOL` provides different sets of physics to work with. In order to create an appropriate environment for the magnetostatic computations that will be conducted, a stationary study is used in combination with the physics-package ”Magnetic Fields, No Currents” which is part of the ”AC/DC” module.

2.5.1. Sphere

Uniformly magnetised:
The first thing that must be defined in order to perform magnetic computations within `COMSOL` is the analysis domain. From equation (A.34) it can be observed that the gradient of the potential, which defines the strength of the magnetic field, decreases as $1/r^3$ when moving away from the sphere. Theoretically, the strength of this field keeps decaying when moving further away from the sphere but never reaches 0. This asymptotic behaviour can not be modelled as such within FEM software, because a discrete domain has to be determined for which the solution is calculated. In order to provide `COMSOL` with a starting point, a box is drawn at a distance which is sufficiently far away from the sphere such that $-\nabla\Phi \approx 0$. Because of the third power term it can be calculated that at a distance of $10 \cdot a$ the field strength has decayed to

an insignificant amount of $\approx 1/1000$ of the field strength at the edge.

In order to calculate the magnetic field around a sphere with radius $a = 100$ mm, a cube with an edge length of 2000 mm is modelled which represent the air domain. The constitutive relation that holds in this domain is given by

$$\mathbf{B} = \mu_0 \mu_r \mathbf{H} \,. \tag{2.47}$$

This air domain has the property that its *relative permeability* μ_r is set to 1. This means that for this volume $\mu_{air} = \mu_0 \cdot \mu_r = \mu_0$. The edges of this box are subject to a boundary condition which is defined in COMSOL as magnetic insulation, which states that on all boundaries

$$\mathbf{n} \cdot \mathbf{B} = 0 \,. \tag{2.48}$$

This ensures that no magnetic field leaks from this box, i.e. that the magnetic field is conserved. At the centre of the box, a sphere is placed with a radius of 100 mm. Within this sphere, magnetism is conserved using the magnetisation constitutive relation

$$\mathbf{B} = \mu_0(\mathbf{H} + \mathbf{M}) \,. \tag{2.49}$$

In order to compare this with the analytical solution as presented in figure 2.4, the same cut plane is investigated: an xy-plane at z = 200 mm below the sphere, shown in figure 2.3. The results of the numerical computation are presented in figure 2.13 below. Comparisons with figure 2.4 show a relative error of less than 1%, verifying that the COMSOL implementation and the analytical derivations are executed correctly.

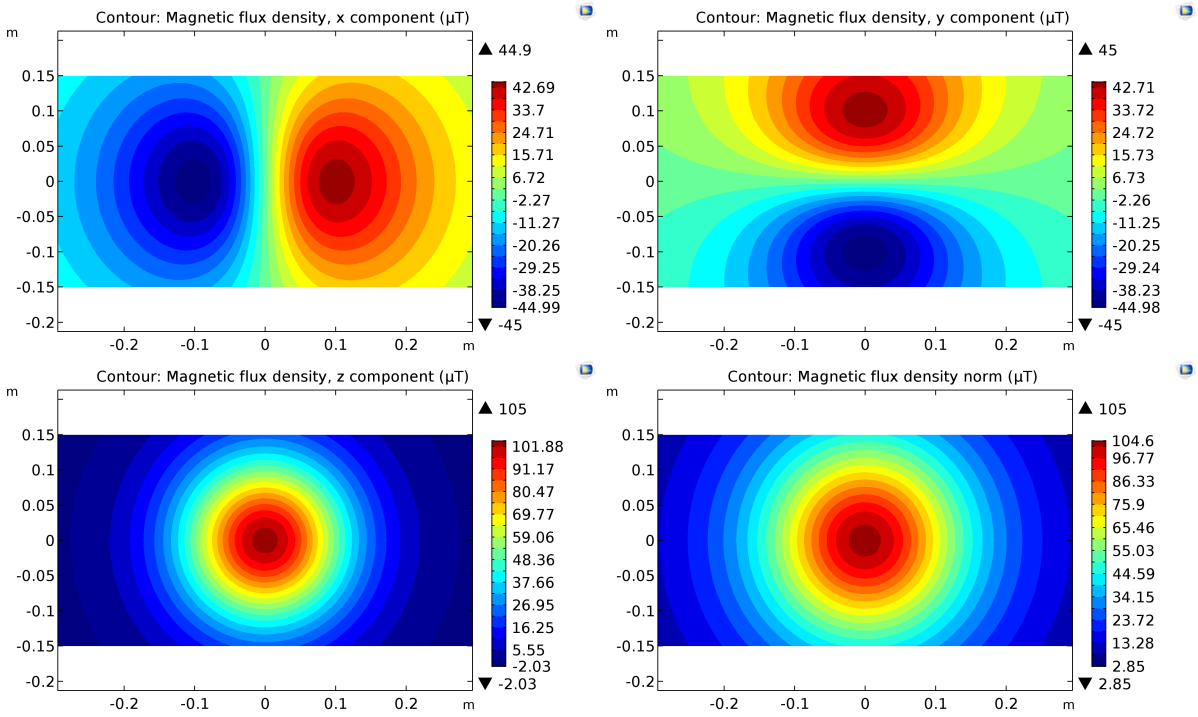

Figure 2.13: B-components of magnetised sphere with radius a = 100 mm and M_z = 1000 A/m in an xy-plane at z = 200 mm.

Linearly reacting material:
For the magnetisable sphere in a uniform background field the same model is used as for the magnetised

sphere. A uniform background field within the entire domain is applied in z-direction:

$$\mathbf{B}_0 = \begin{pmatrix} 0 \\ 0 \\ 100 \end{pmatrix} \mu\mathrm{T}\,. \tag{2.50}$$

Furthermore, the constitutive relations inside and outside the material are now identical and given by

$$\mathbf{B} = \mu_0 \mu_r \mathbf{H_0} \tag{2.51}$$

in which the μ_r within the sphere is set to 100. The results of this numerical computation are shown in figure 2.14 below. Comparisons with figure 2.5 show a relative error of less than 1%, verifying that the COMSOL implementation as well as the analytical derivations are correct.

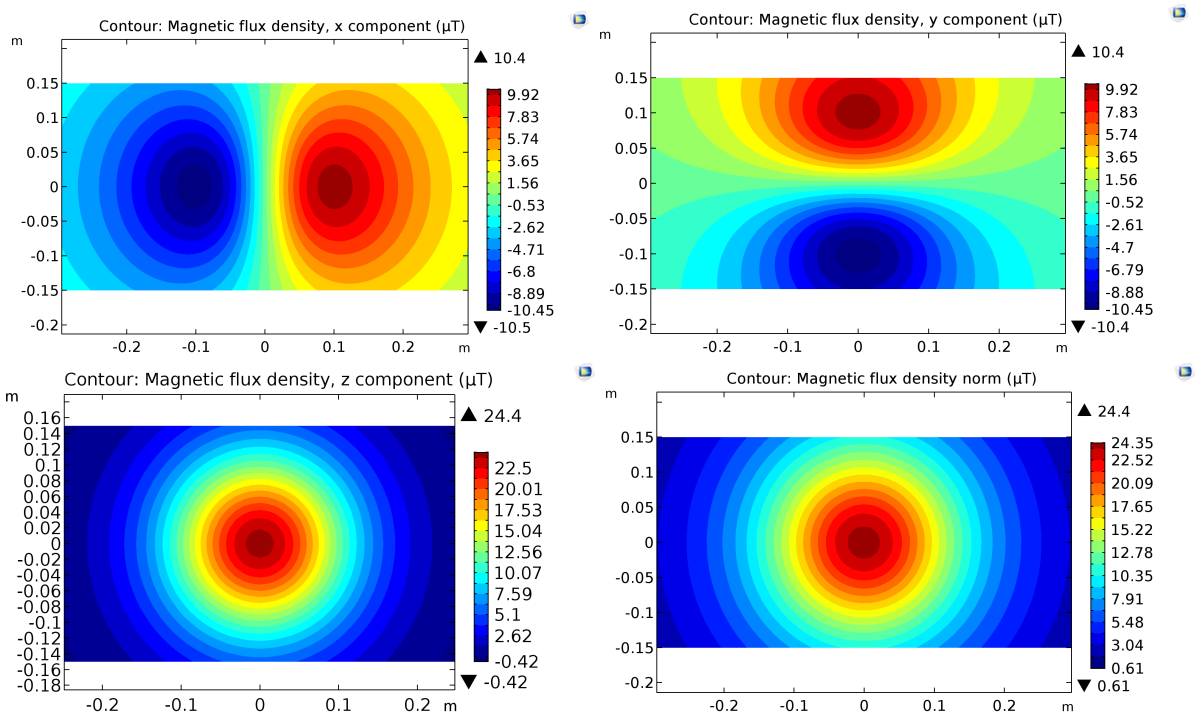

Figure 2.14: B-components of magnetisable sphere with radius a = 100 mm and μ_r = 100 subjected to a background field of 100 μT in z-direction in an xy-plane z = 200 mm.

2.5.2. Spheroid

Uniformly magnetised:
The numerical implementation of the solid uniformly magnetised spheroid is performed analogous to the solid sphere, with equations (2.47) and (2.49) describing the constitutive relations in respectively the air domain and the spheroid. Figure 2.15 shows the B_x, B_y, B_z and B_{tot} components in an xy-plane 200 mm below the centre of a spheroid with length 560 mm, diameter 95 mm and magnetisation of 1000 A/m in x-direction. The error with the analytical solution is less than 1%.

Linearly reacting material:
The numerical validation of the linearly reacting magnetisable spheroid in a uniform background field is done analogous to the linearly reacting sphere, with merely the geometry changing and the constitutive relation within the entire domain equal to equation (2.47). The magnetic induction field components in an xy-plane 200 mm below the centre of a spheroid with length 560 mm, diameter 95 mm, μ_r = 100,

subjected to a background field in x-direction of 100 µT is given in figure 2.16. The error with the analytical solution is less than 1%.

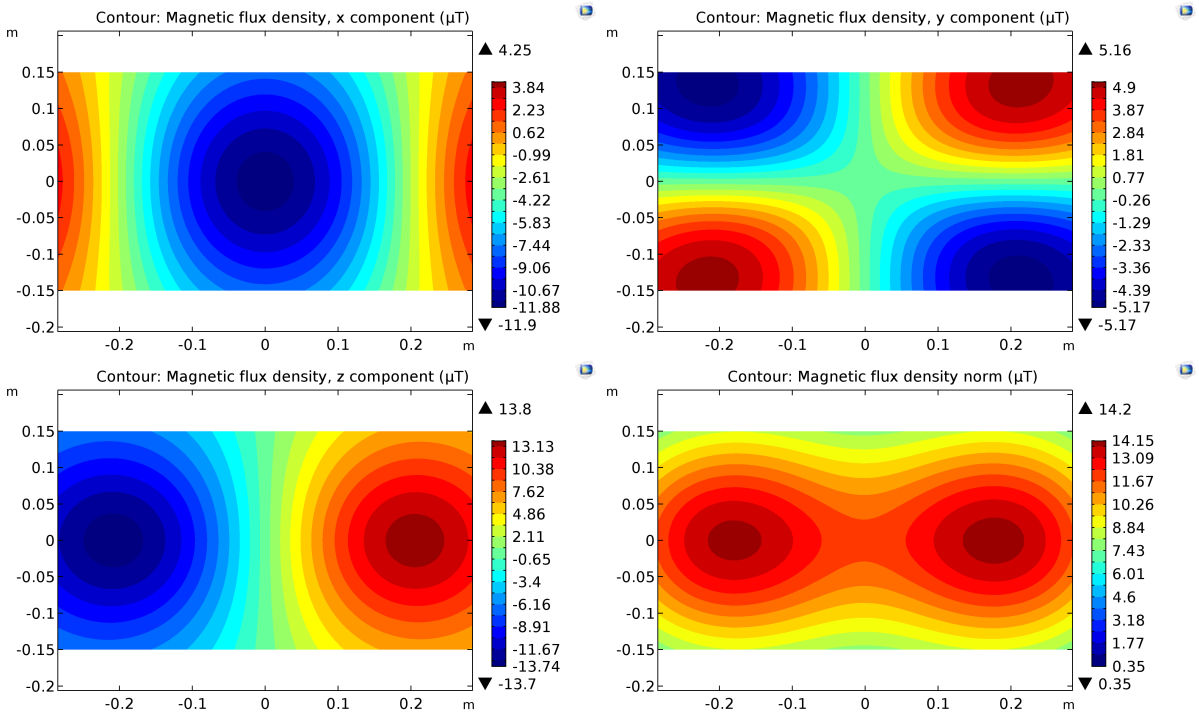

Figure 2.15: B-components of a magnetised spheroid ($l \times d$ = 560×95 mm) and M_x = 1000 A/m in an xy-plane at z = 200 mm.

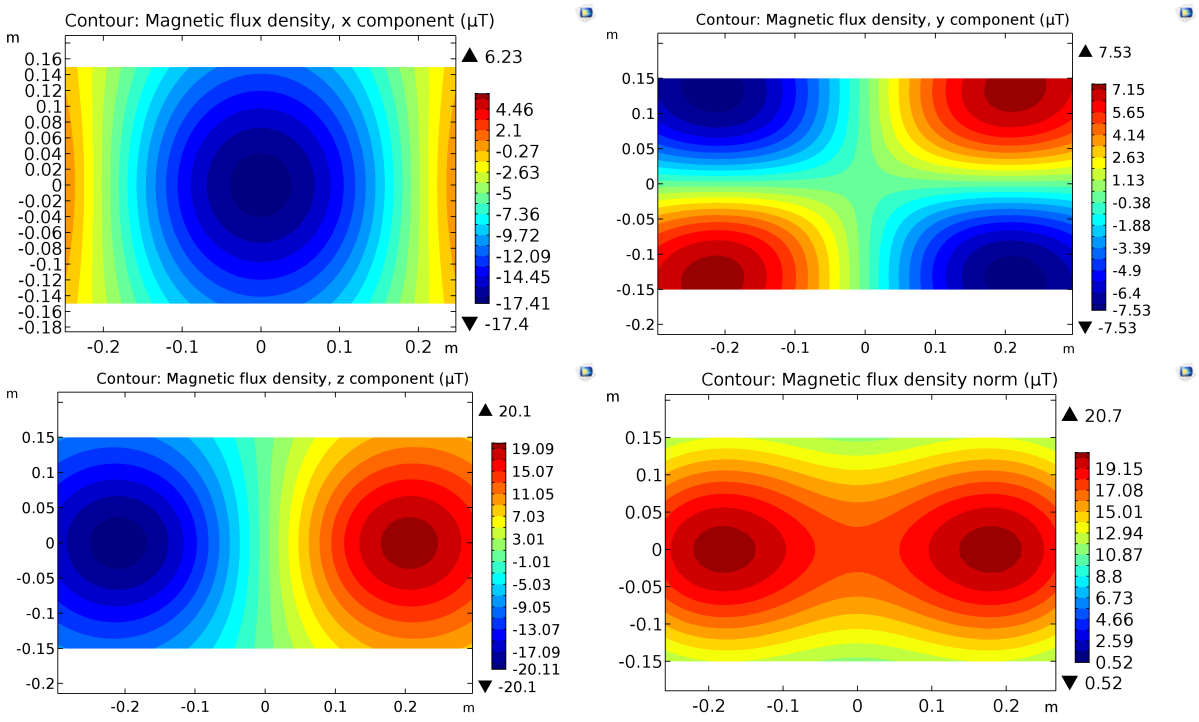

Figure 2.16: B-components of a magnetisable spheroid ($l \times d$ = 560×95 mm) with μ_r = 100 subjected to a background field of 100 µT in x-direction in an xy-plane at z = 200 mm.

2.5.3. Plate

Uniformly magnetised:
The numerical implementation of the magnetised plate is performed analogous to the solid sphere and spheroid, with equations (2.47) and (2.49) describing the constitutive relations in respectively the air domain and the plate. Figure 2.17 shows the B- components in an xy-plane 200 mm below the centre of a plate with length 300 mm, width 300 mm, thickness 5 mm and M of 1000 A/m in x-direction. The error between the numerical and analytical solution is less than 1%.

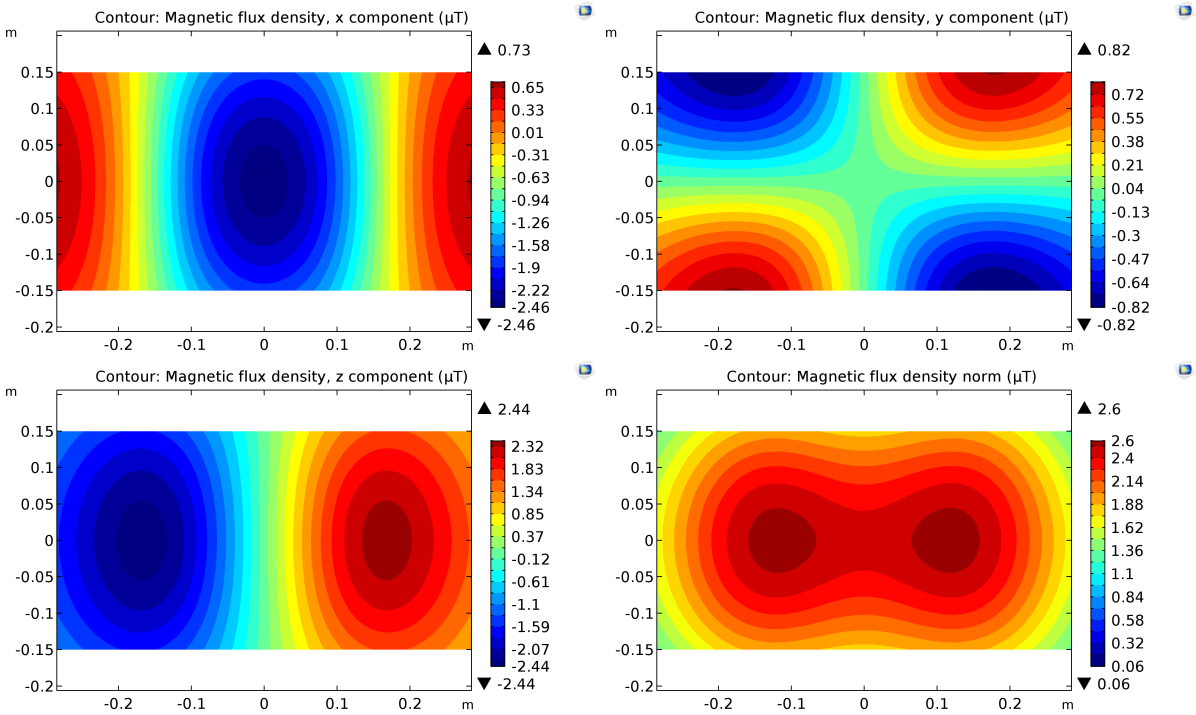

Figure 2.17: B-components of a magnetised plate ($l \times w \times t$ = 300×300×5 mm) with M_x = 1000 A/m in an xy-plane at z = 200 mm.

Linearly reacting material:
The numerical validation of the magnetisable plate in a uniform background field is done analogous to previous examples. The magnetic induction field components in an xy-plane 200 mm below a plate ($l \times w \times t$ = 300×300×5 mm and μ_r = 100) subjected to a background field in x-direction of 100 μT is given in figure 2.18.

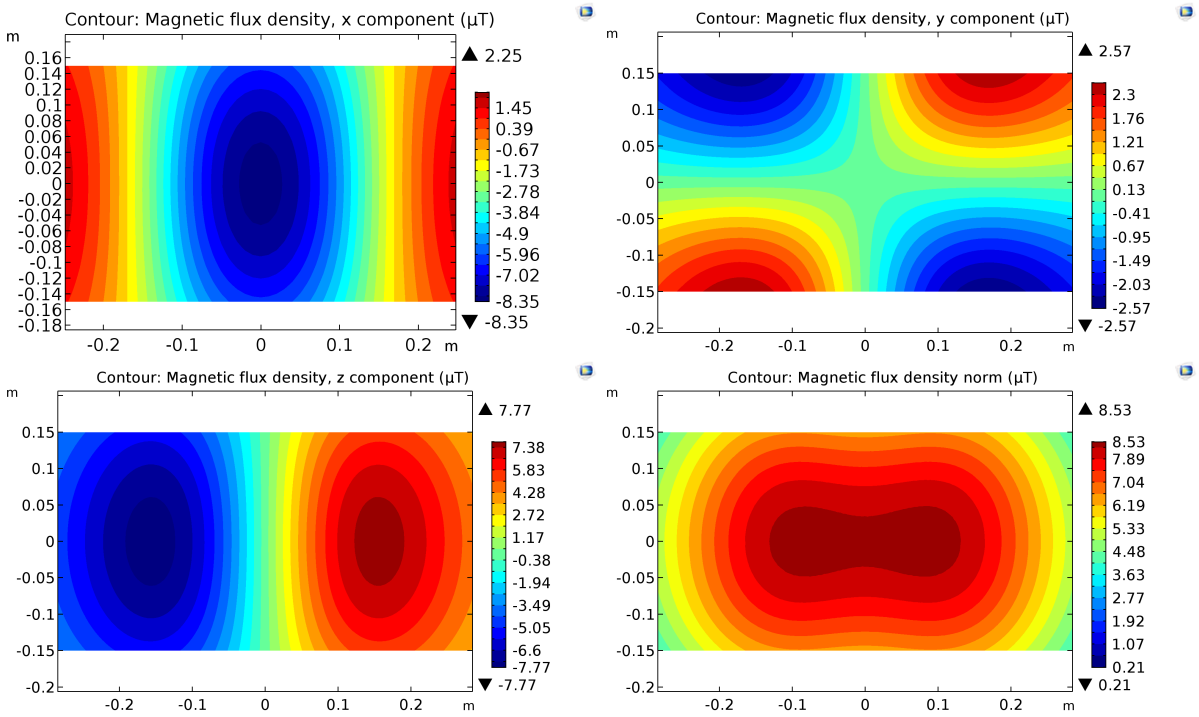

Figure 2.18: B-components of a magnetisable plate (($l \times w \times t$ = 300×300×5 mm) with $\mu_r = 100$ subjected to a background field of 100 μT in x-direction in an xy-plane at z = 200 mm.

In this final example, there is a significant error visible in the extreme values between the numerical and analytical solutions of roughly 20%. This can be explained by the fact that in the analytical solution the assumption is made that the magnetisation within the plate is constant over the entire domain of the plate. In practice this is the case for spheres and spheroids, but not for plates, which is what makes spheroids and spheres ideal testing objects. A small over-estimation is made of the magnetisation in the analytical solution because the sides of the plate get less magnetised than the centre. The numerically calculated magnetisation distribution of the magnetisable plate mentioned above is shown in figure 2.19.

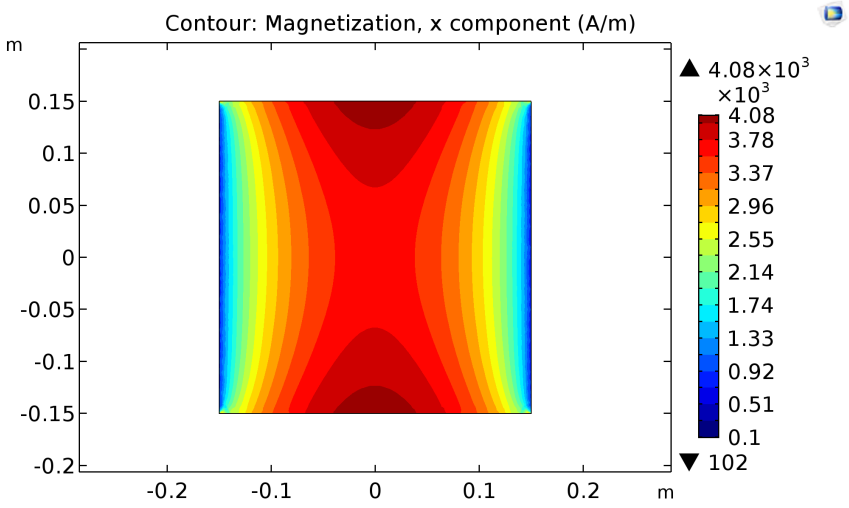

Figure 2.19: Numerically calculated magnetisation distribution of a magnetisable plate (Top view, $l \times w \times t$ = 300×300×5 mm) subjected to a background field of 100 μT in x-direction with μ_r = 100.

3

Relaxation

3.1. Introduction

The concept of *relaxation*, also known as the *magnetic after-effect*, deals with changes in magnetisation in ferromagnets due to time-dependent effects. An example of relaxation is the fact that when a ferromagnetic object is subjected to a constant magnetic field for a large amount of time, the magnetic orientation of the domains rotates slightly into the direction of the background field. Looking at relaxation on a much smaller timescale, it can also be said that it takes a certain amount of time for an object to be magnetised when the background field is abruptly changed. In this research project the assumption is made that relaxational effects are neglibily small when compared to hysteresis and the Villari effect. This also implies that time-dependent factors are negligible, and that the effects measured are identical independent of the time frame in which these tests are conducted. In order to verify this hypothesis, an attempt to capture magnetic relaxation is made by measuring changes in induction field over time and comparing those with *zero measurements*, which are experiments conducted without a specimen present for comparative purposes.

In the original paper by Ferenc Preisach from 1935 [43], the question is raised whether the magnetisation of ferromagnetic materials follows changes in the background field instantaneously or if a defined amount of time can be defined that is required to reach a certain level of magnetisation. In order to test this, numerous experiments have been concluded with varying results. Overall, it has been found that energy losses due to these time-dependent effects, much like hysteresis, start to become apparent under high frequencies [60] (losses due to eddy currents and hysteresis) and high temperatures [36]. Since no rapid changes in background field will take place and tests are conducted at constant room temperature, it is expected that these effects will have negligible disruptive effect on the measurements conducted in the laboratory setup. Regarding the changes in magnetisation in the longer term it is expected that these changes, if observable, are negligible as well compared to the range of data that is observed during hysteresis and Villari experiments. In summary, two types of time-dependent changes in magnetisation can be defined:

1. The short-term magnetic after-effect, which looks at the time needed for the material to come to a constant magnetisation after the background field is abruptly increased;
2. The long-term magnetic after-effect, which shows the gradual change in magnetisation of a ferromagnetic object in a constant background field for a longer period of time.

3.2. Test setup

In order to measure magnetic relaxation, the solid prolate spheroid (appendix B.4) is placed within the Helmholtz cage (appendix B.1). The fluxgate sensor (appendix B.2.2) is placed 145 mm below the centre of the spheroid. In order to capture both the short and long-term magnetic after-effect in one setting, a so-called switch test is performed which consists of the following four phases:

1. In the first phase, the Earth's magnetic field is lifted within the Helmholtz cage resulting in net zero background field in three directions. This phase lasts for an hour without conducting measurements in order to create a stable starting condition for the experiment;
2. After an hour the fluxgate sensor starts taking measurements at a sampling frequency of around 5 Hz. The background field is kept constant during this hour;
3. After two hours, the background field in x-direction is instantaneously increased to +250 µT for another hour;
4. After three hours the background field is reverted back to 0, and measurements are taken for another full hour.

At the end of the experiment, four hours have elapsed. The applied time-signal is shown in figure 3.1 (phase 1 excluded).

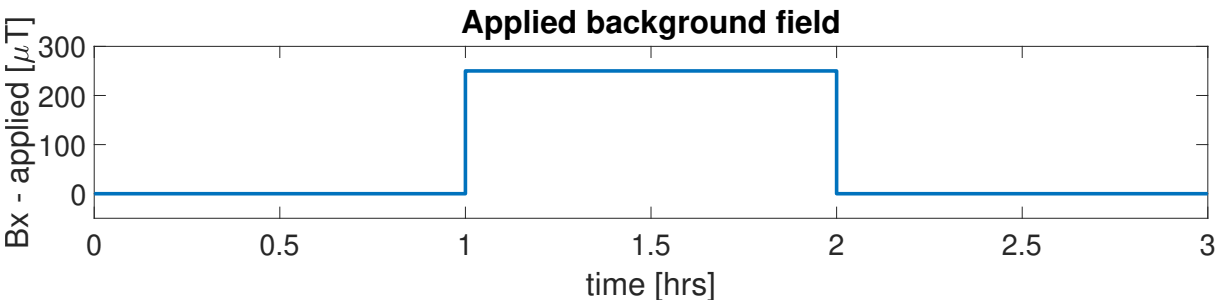

Figure 3.1: Applied background field during relaxation testing.

In order to verify that any measured effects can indeed be contributed to changes in the magnetisation of the spheroid, the same test was performed without an object present, a zero measurement. The tests conducted on the spheroid are then compared with the zero measurements in order to form an opinion on the magnitude of magnetic relaxation.

3.3. Results

The relaxation experiment described in section 3.2 was performed twice with the same object, the solid prolate spheroid. These experiments are named R1 and R2. An identical experiment was performed without an object present, a zero measurement R0. The applied background magnetic field is shown in figure 3.1. The measured signal in both experiment R1 and R2 is shown in figure 3.2 and 3.3. The zero measurement R0 is plotted in figure 3.4. As expected, the shape of these graphs is identical to the applied time signal when observing the entire graph with a timescale of three hours and a bandwidth of 400 µT. During phase 2 it can be seen that the measured B_x signal is roughly 100 µT lower than the applied background field. This is in line with the results found while deriving the expressions for the magnetic field around a prolate spheroid that is magnetised in x-direction in chapter 2.

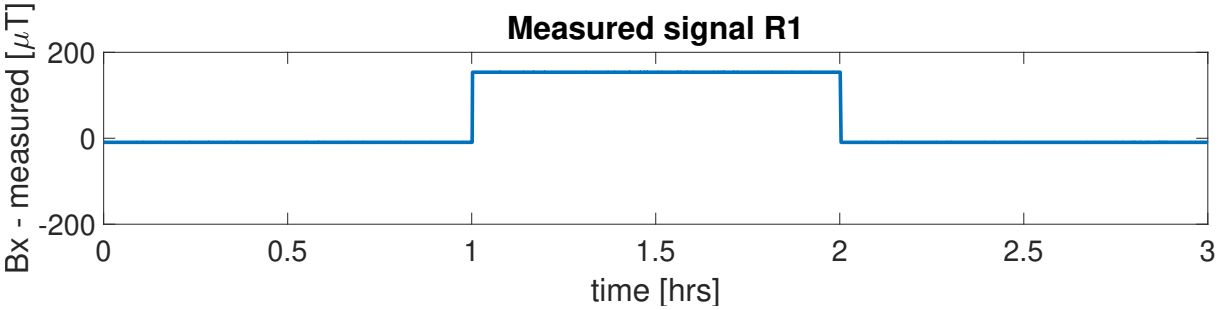

Figure 3.2: Measured signal R1.

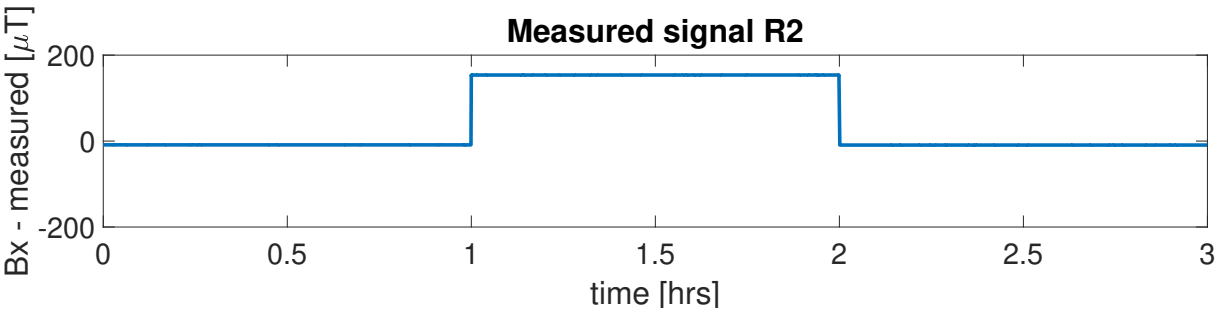

Figure 3.3: Measured signal R2.

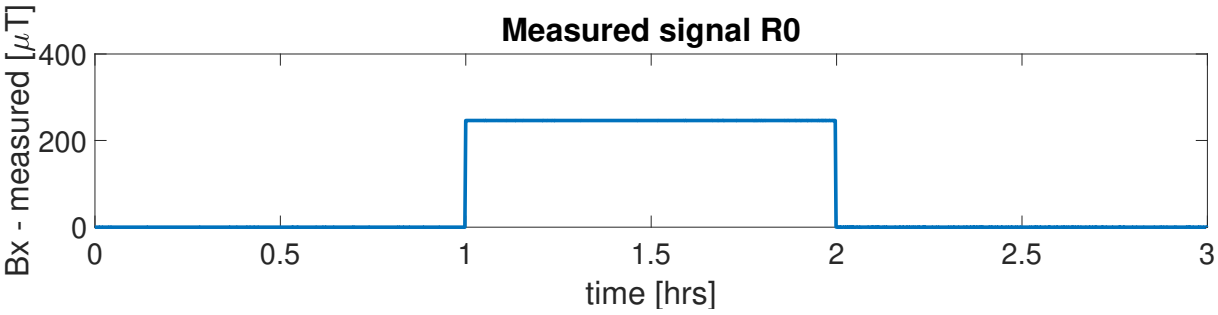

Figure 3.4: Measured signal R0.

The following sections discuss specific parts of the figures above in more detail, in order to provide more insight into the short and long-term relaxation effects separately.

3.3.1. Short-term

With respect to short-term relaxation, the vertical sections at t = 1 hour and t = 2 hours are shown in figures 3.5-3.10. For convenience, t_0 iss taken as the moment just before the abrupt change in background field. In figures 3.5-3.7 the effect of short time relaxation at t = 1 hour is shown.

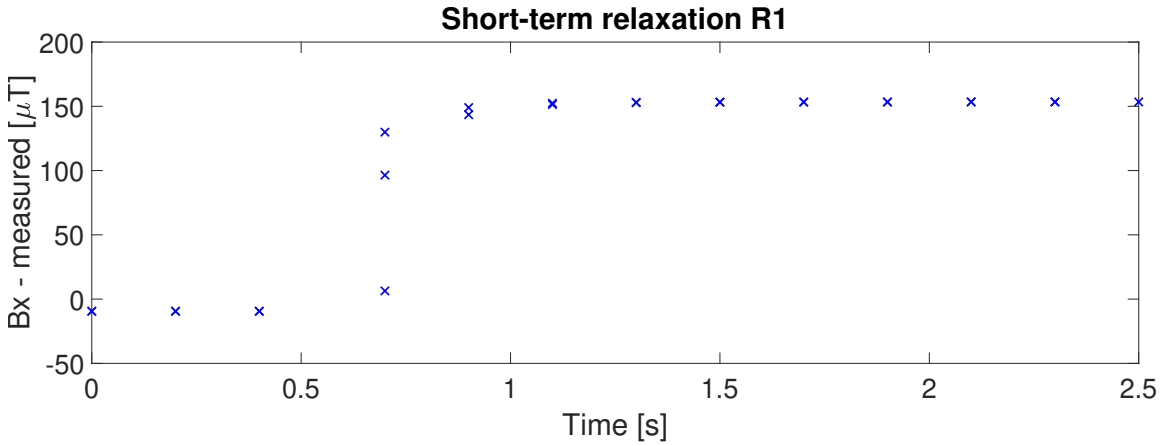

Figure 3.5: Short-term relaxation R1, at t = 1 hour.

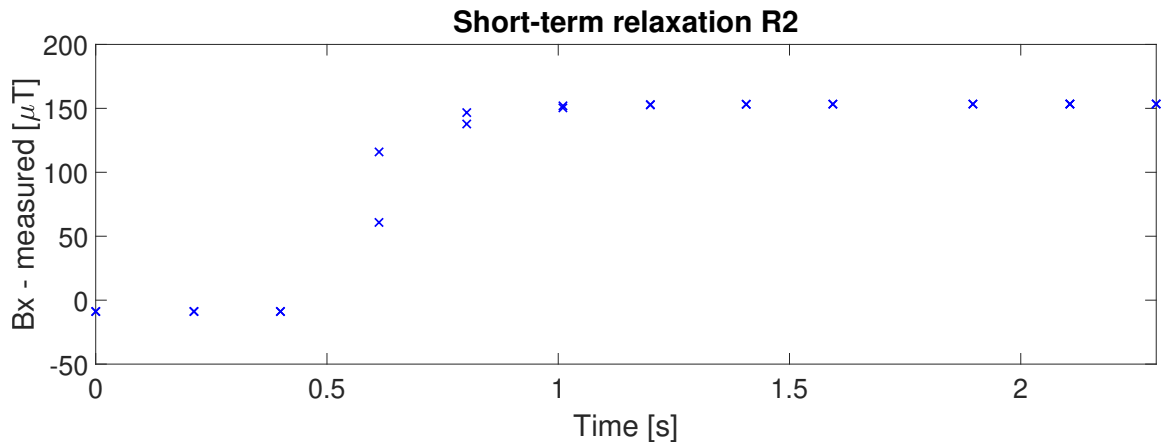

Figure 3.6: Short-term relaxation R2, at t = 1 hour.

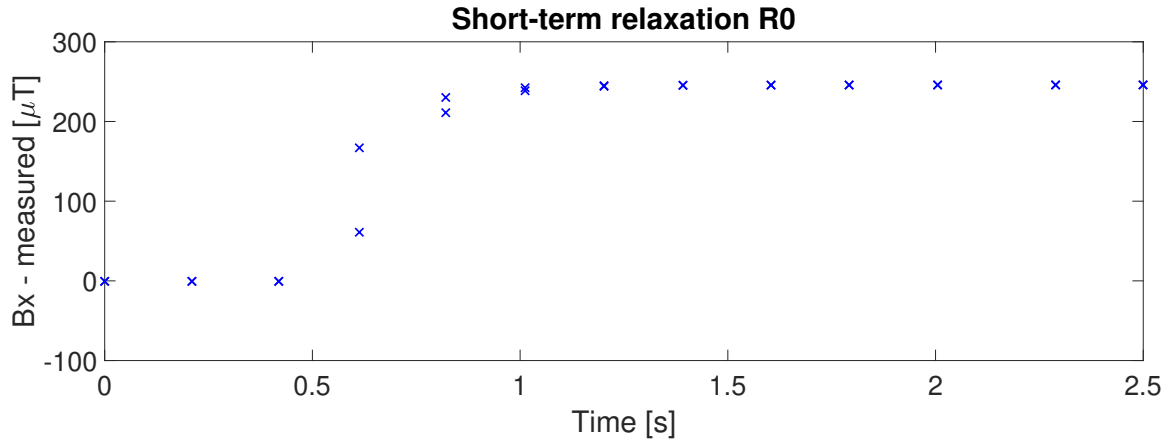

Figure 3.7: Short-term relaxation R0, at t = 1 hour.

The figures below show a similar effect which occurs at t = 2 hours when the background field as abruptly dropped back to 0.

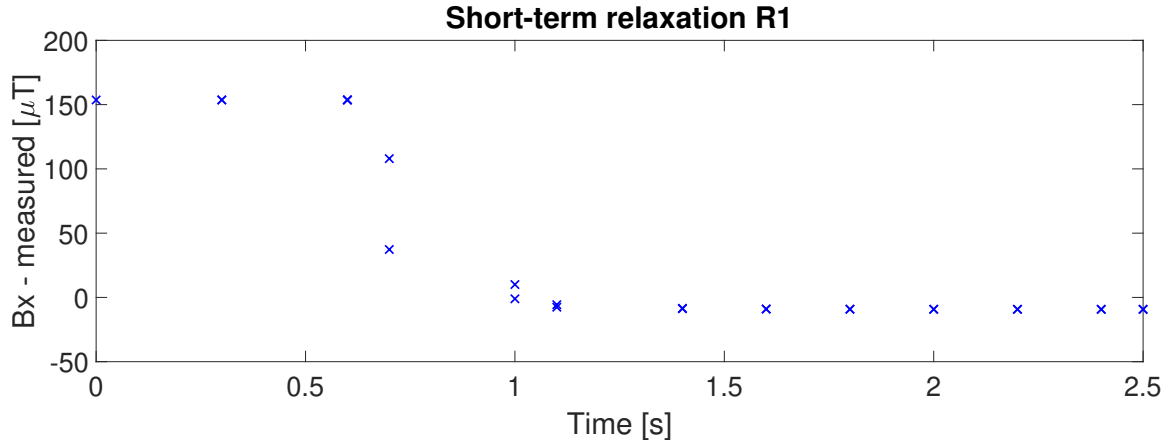

Figure 3.8: Short-term relaxation R1, at t = 2 hours.

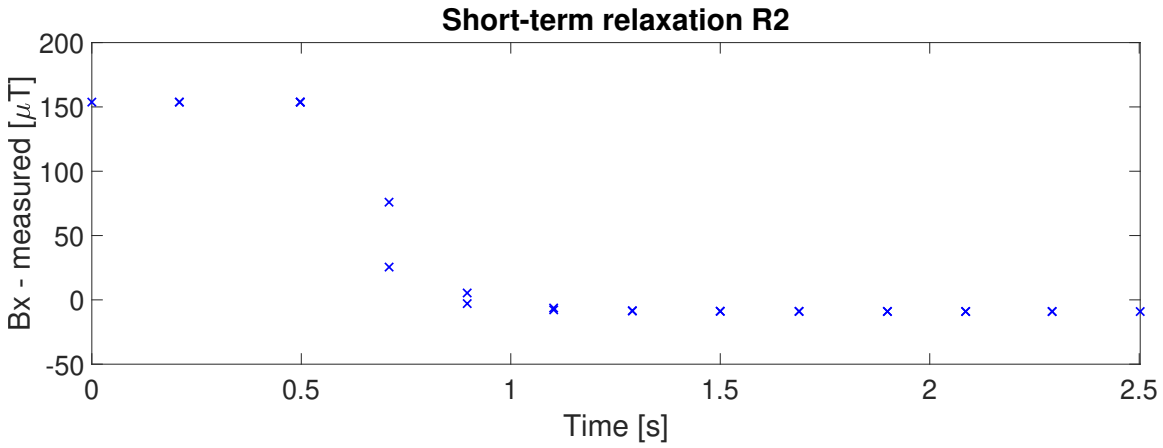

Figure 3.9: Short-term relaxation R2, at t = 2 hours.

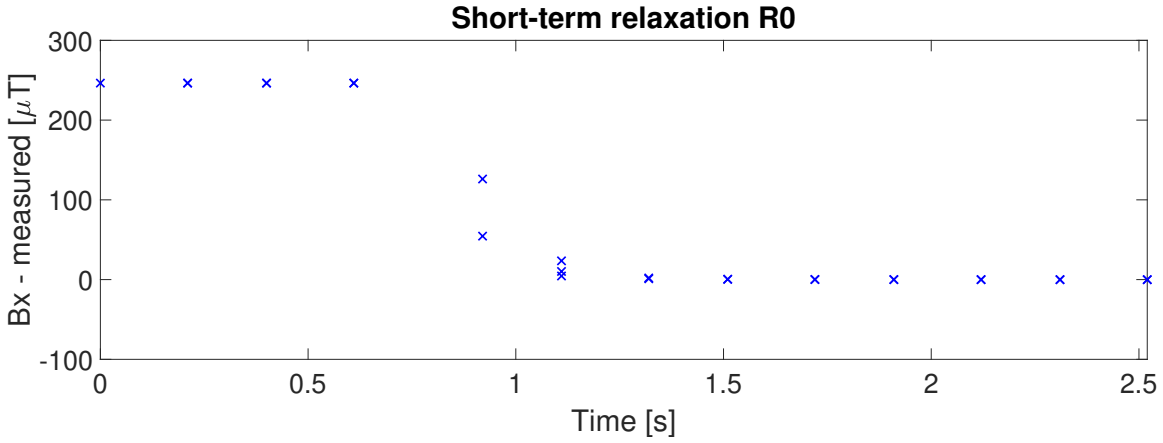

Figure 3.10: Short-term relaxation R0, at t = 2 hours.

When investigating the right-hand side of figures 3.5-3.10 it can be seen that on a smaller scale, the measured signal shows asymptotically in- or decreasing behaviour. In figures 3.11-3.16 the same t = 0 is adopted, but now the signal from t = 2.5 s to t = 20 s is shown which is from here on called the medium-term.

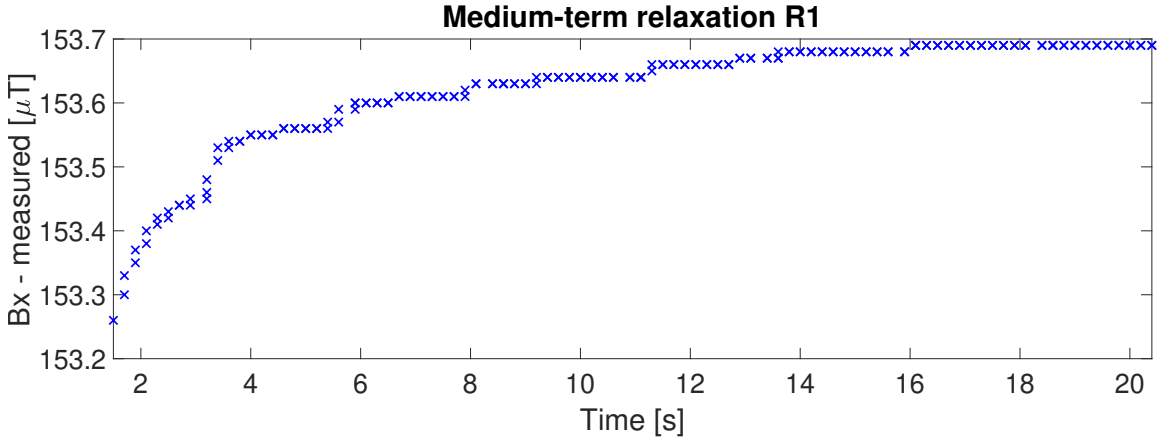

Figure 3.11: Medium-term relaxation R1, beyond t = 1 hour.

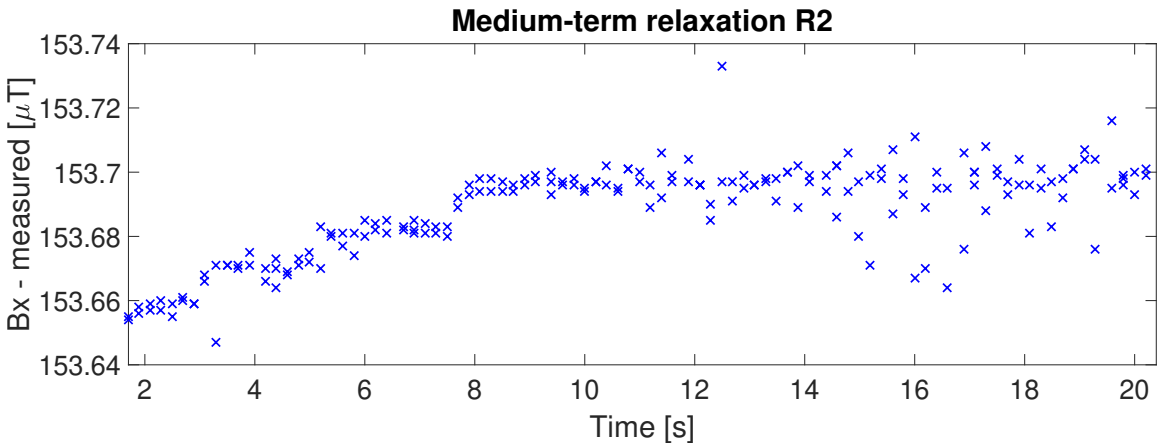

Figure 3.12: Medium-term relaxation R2, beyond t = 1 hour.

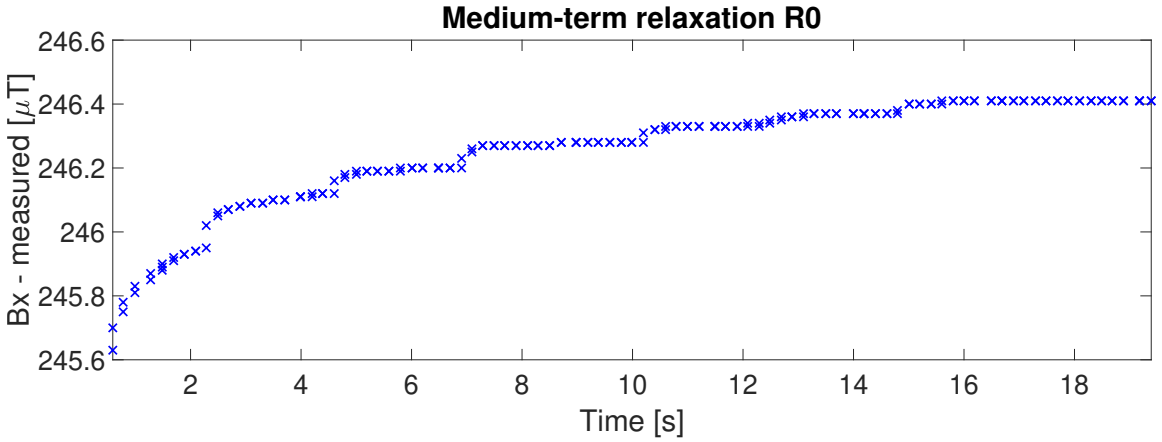

Figure 3.13: Medium-term relaxation R0, beyond t = 1 hour.

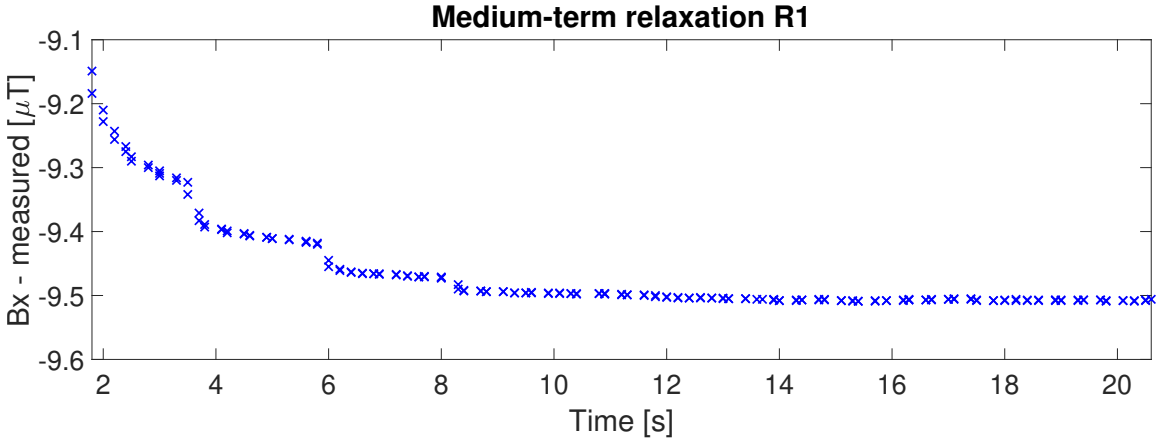

Figure 3.14: Medium-term relaxation R1, beyond t = 2 hours.

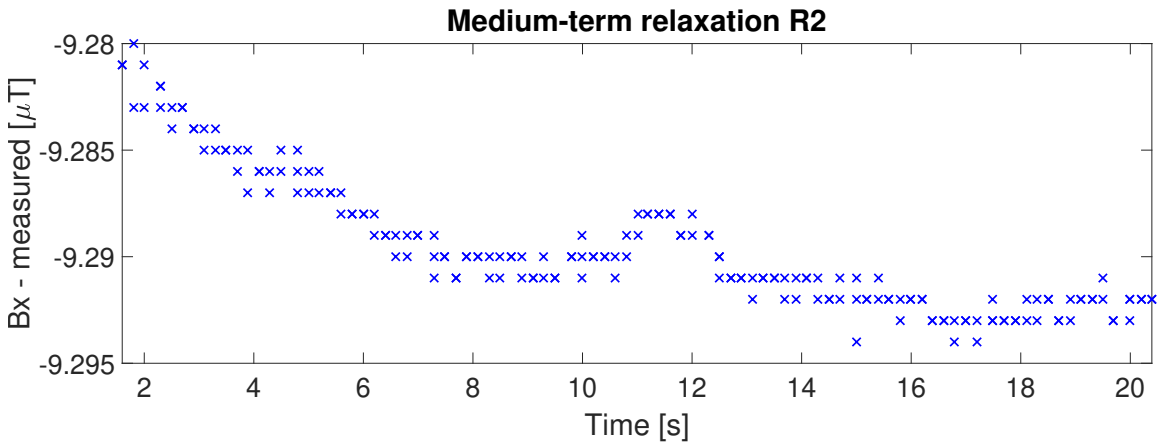

Figure 3.15: Medium-term relaxation R2, beyond t = 2 hours.

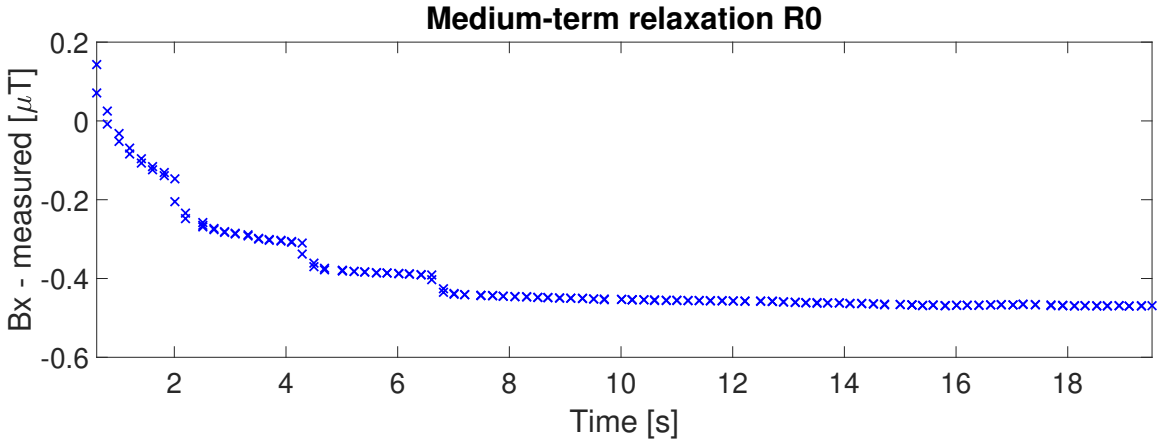

Figure 3.16: Medium-term relaxation R0, beyond t = 2 hours.

As for the medium-term, it can be seen that the measured signal keeps de- or increasing slightly for around 30 seconds after the background field is changed. But, as can be seen from the zero measurement, this effect can not be contributed to the magnetic relaxation. This can be explained by the fact that the computer sends a desired current to the Helmholtz coils. The amplifier then starts varying the voltage until the desired amperage is reached. This varying of the voltage causes changes in the magnetic field and therefore changes in the measured signal.

3.3.2. Long-term

As for long-term relaxation, a closer look is taken at the horizontal sections from figures 3.2 & 3.3. Three horizontal sections, or phases, can be observed:

Phase 1 : 0 < t < 1 hr;

Phase 2 : 1 hr < t < 2 hrs;

Phase 3 : 2 hrs < t < 3 hrs.

For each phase separately, the effect of the long-term relaxation is shown in figures 3.17-3.25 below. Please note that for $t_0 \approx 1$ hour for phase 2 and $t_0 \approx 2$ hours for phase 3.

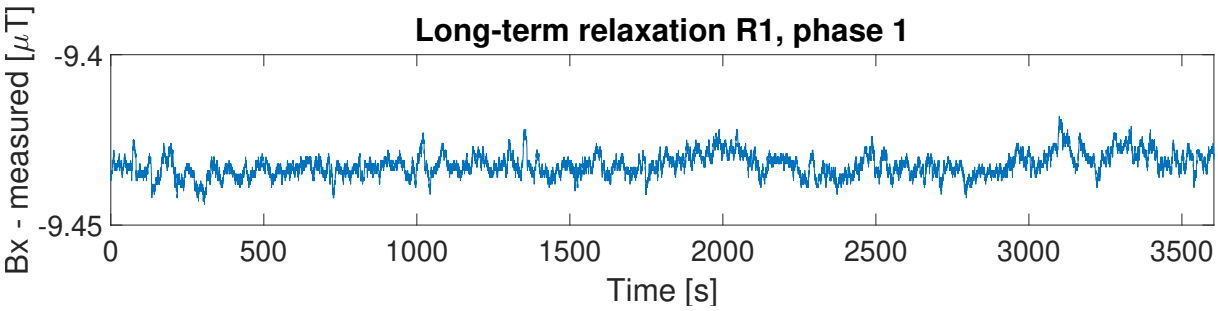

Figure 3.17: Long-term relaxation R1, phase 1.

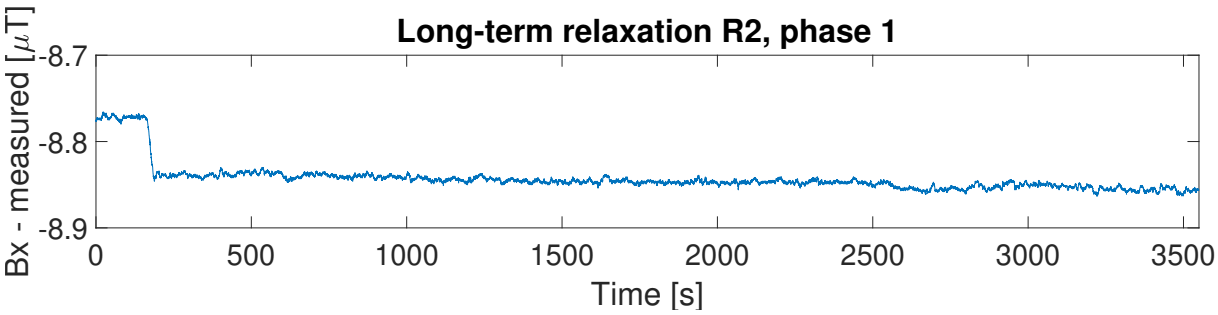

Figure 3.18: Long-term relaxation R2, phase 1.

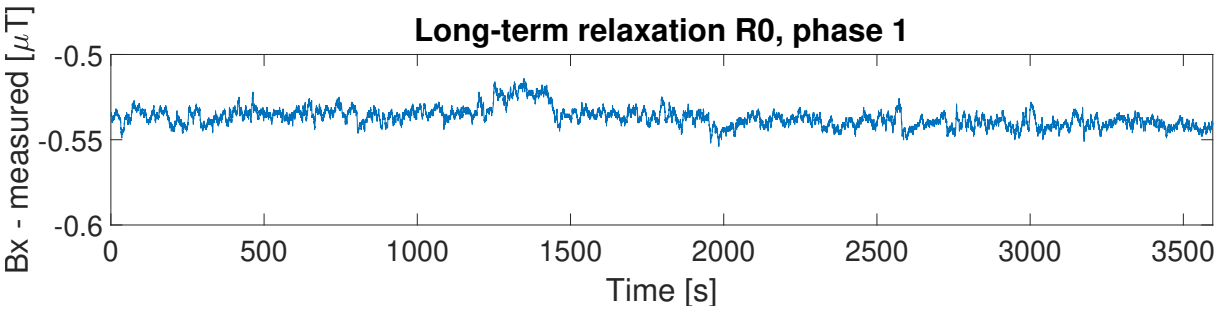

Figure 3.19: Long-term relaxation R0, phase 1.

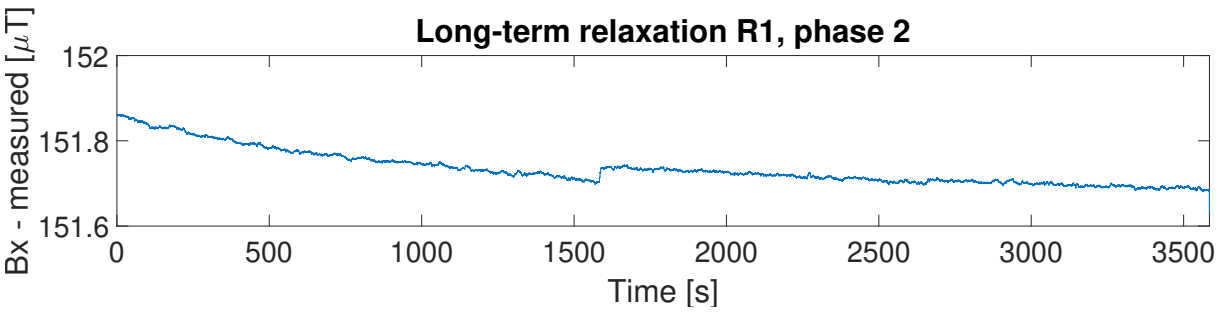

Figure 3.20: Long-term relaxation R1, phase 2.

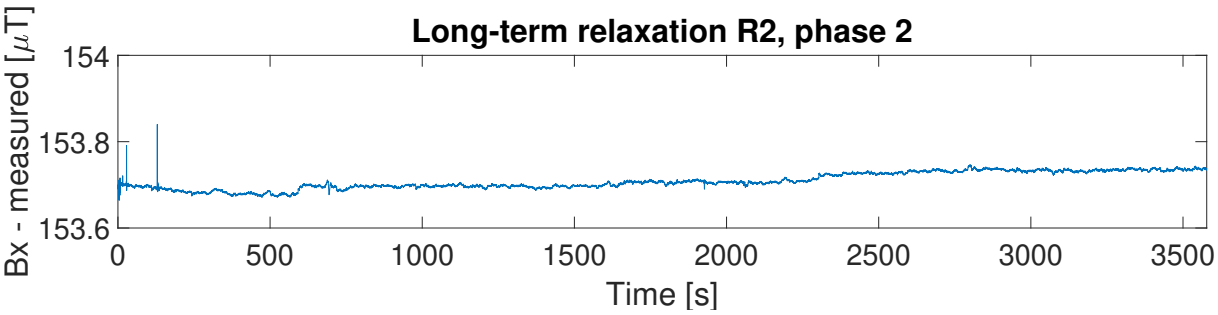

Figure 3.21: Long-term relaxation R2, phase 2.

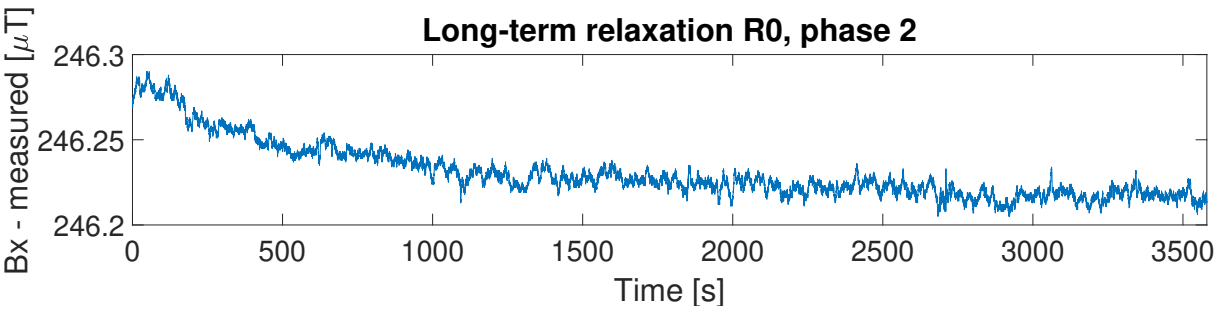

Figure 3.22: Long-term relaxation R0, phase 2.

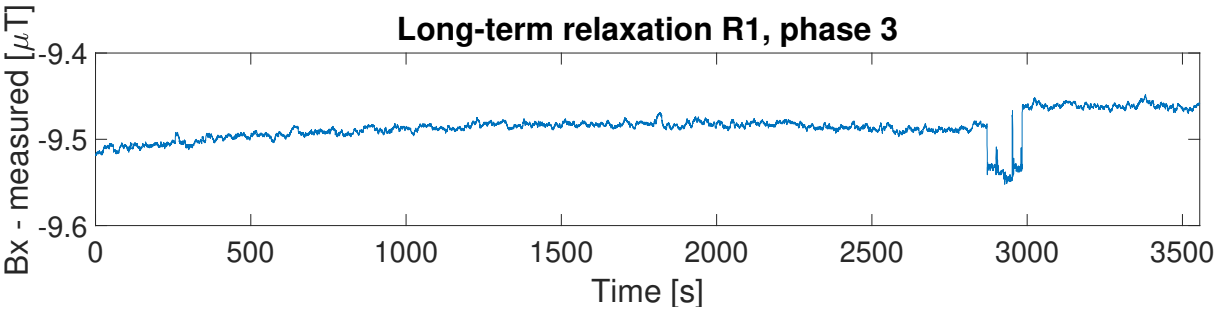

Figure 3.23: Long-term relaxation R1, phase 3.

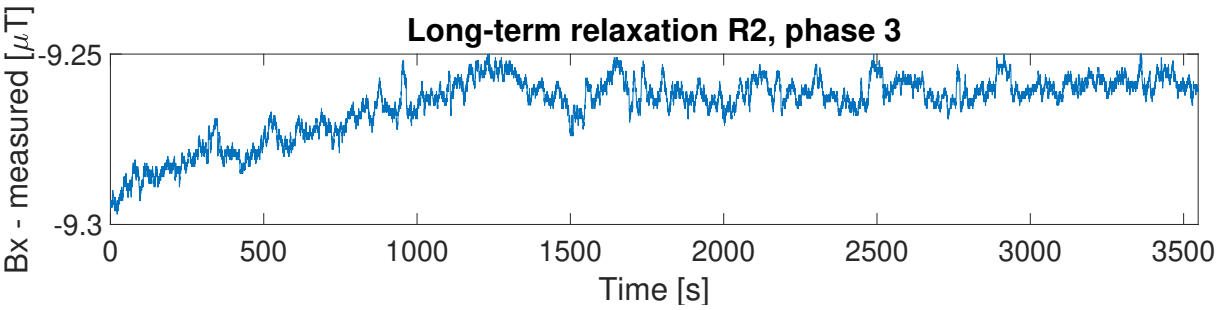

Figure 3.24: Long-term relaxation R2, phase 3.

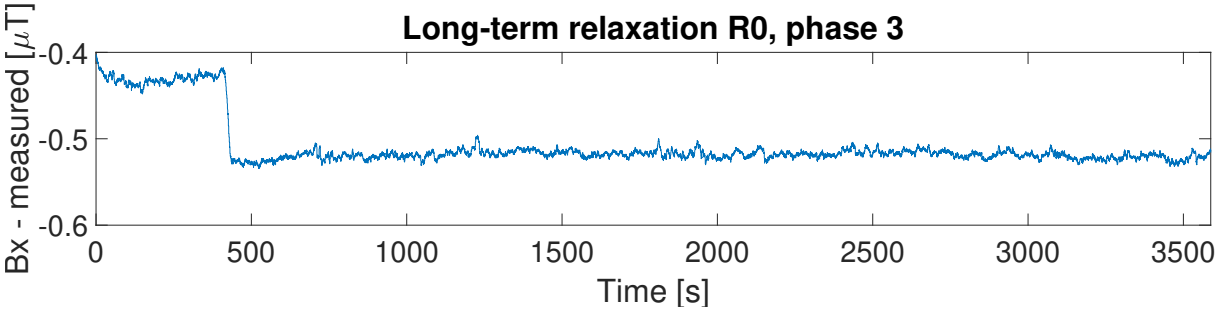

Figure 3.25: Long-term relaxation R0, phase 3.

When looking at all long-term relaxation figures above it can only be concluded that long-term magnetic relaxation is not succesfully measured using this setup. Some gradual changes can be observed, but nothing that a clear difference with the zero measurements. In order to capture the effect it might be necessary to measure for longer periods of time. An idea is to store a specimen in a certain fixed position with respect to the magnetic field of the Earth, and then measure the magnetic flux at a fixed distance for multiple days, weeks, or even months to observe gradual changes in magnetic flux.

4

Uniformity

4.1. Introduction

An important assumption through which the expressions formulated in chapter 2 are derived is the fact that the objects are magnetised uniformly. Magnetic uniformity implies that the vector describing the magnetisation within an object does not vary within the domain of the object. Without uniform magnetisation, the inverse problem becomes more complicated.

In order to see if an object is uniformly magnetised, multiple magnetic induction field measurements are taken around a specimen which is subjected to a uniform and constant background field. Following the theory provided in chapter 2, inversion performed at different locations leads to identical vectors describing the three-dimensional uniform magnetisation within the object. The difference in the inversely calculated magnetisation at different locations can be seen as a qualitative indication of the amount of non-uniformity in the material.

4.2. Initial test setup

The magnetic uniformity is initially investigated for two specimens, see appendix B.4:

- A solid prolate steel spheroid (580×95×95 mm);
- Steel plate specimen 1 (300×300×5 mm).

Five locations are marked around each specimen along their symmetry axes. For the spheroid, the locations of these sensors are numbered and given in table 4.1.

Table 4.1: Sensor locations with respect to the spheroid's centrepoint.

Sensor	x [mm]	y [mm]	z [mm]
1	0	0	145
2	150	0	74
3	-150	0	74
4	0	150	74
5	0	-150	74

Please refer to figures 4.1 and 4.2 for a schematic top and side view of the solid spheroid and the sensor locations. Please note that the z-direction points downwards.

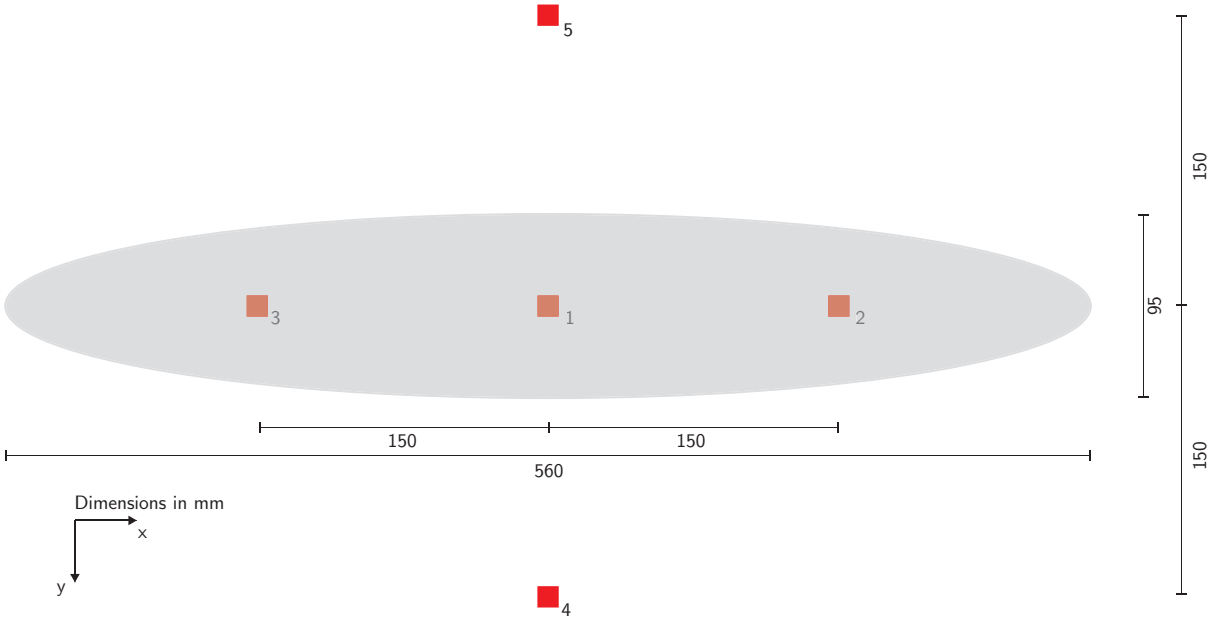

Figure 4.1: Spheroid sensor locations (top view).

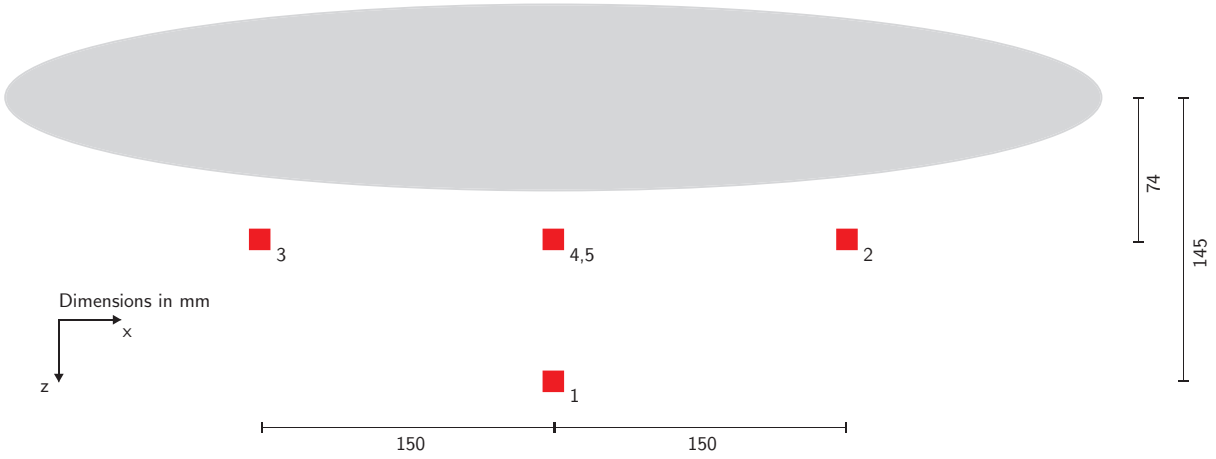

Figure 4.2: Spheroid sensor locations (side view).

For the steel plate the locations of the sensors are given in table 4.2.

Table 4.2: Sensor locations with respect to the centre point of the metal plate.

Sensor	x [mm]	y [mm]	z [mm]
1	0	0	50
2	166	0	-12
3	-166	0	-12
4	0	185	-12
5	0	-185	-12

Please refer to figures 4.3 & 4.4 for a schematic top and side view of the spheroid and the sensor locations. The z-direction points downwards.

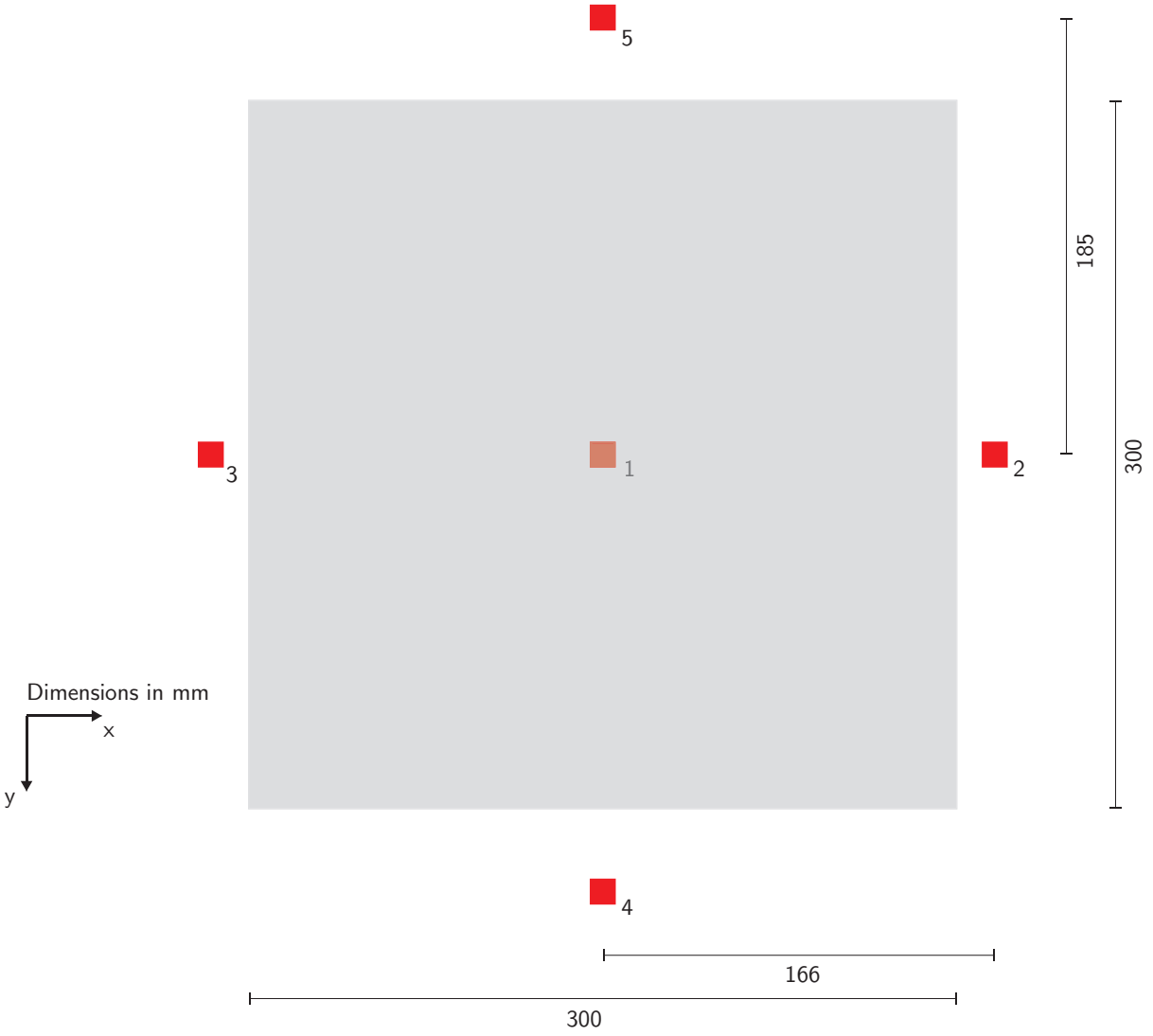

Figure 4.3: Plate sensor locations (top view).

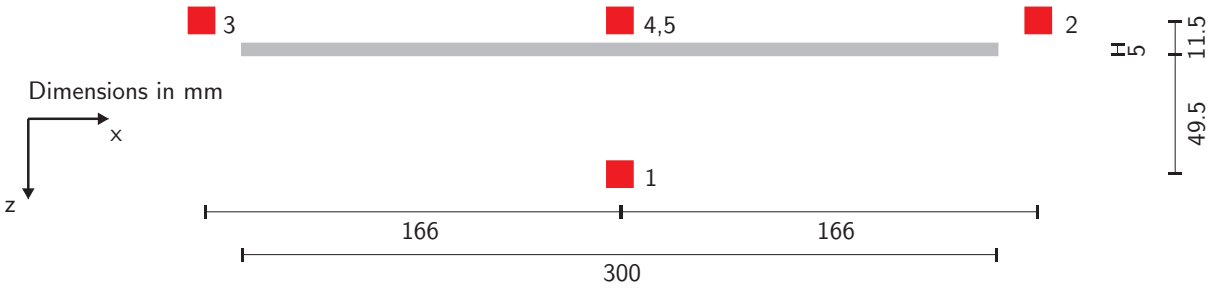

Figure 4.4: Plate sensor locations (side view).

The individual measurements are provided as input for the inversion at different locations and the results are compared. The variance in inversely calculated magnetisation can be used as a qualitative measure of uniformity.

Three test cases are defined for the spheroid:

- Case 1: With the Earth's magnetic field present;
- Case 2: With background field 0 in all directions;
- Case 3: With background field +200 µT in x-direction.

The calculation of the magnetisation through inversion at each sensor location yields a vector with three components. This implies that for each test case, a table can be constructed with the inversely calculated 'uniform' M_{xyz}-magnetisations corresponding to measurements at that location. The results are presented in table 4.3.

Table 4.3: Spheroid magnetisation [A/m].

Case 1					
Sensor	1	2	3	4	5
M_x	167	1335	1003	-73	366
M_y	119	-99	97	65	41
M_z	-84	-464	-71	28	-96
Case 2					
Sensor	1	2	3	4	5
M_x	483	1616	1313	223	659
M_y	114	-94	123	71	51
M_z	-154	-519	-131	-44	-152
Case 3					
Sensor	1	2	3	4	5
M_x	4188	4919	4547	3626	4030
M_y	178	-111	64	98	13
M_z	-142	-429	-146	-58	-151

For the metal plate, four cases are defined:

- Case 1: With background field 0 in all directions;
- Case 2: With background field +200 µT in x-direction;
- Case 3: Demagnetised, background field 0 in all directions;
- Case 4: Demagnetised, background field +200 µT in x-direction.

The expression used for inverse calculations derived in section 2.4 only deals with one-dimensional magnetisation, meaning that inversion can only be applied for one direction (in this case the x-direction). This means that applying inversion in the x-direction theoretically only works when using the B_x-component at locations 1, 4 and 5 where the magnetic field due to a possible *uniform* magnetisation in y and z-directions is zero (the contributions to B_x due to uniform magnetisation in y and z-directions are zero in the yz-plane at $x = 0$, see chapter 2). After the measurements are taken, the specimen is demagnetised using the demagnetising unit described in appendix B.3. The process is repeated under case 3 & 4. The results are presented in table 4.4.

Table 4.4: Metal plate specimen 1 magnetisation [A/m].

Sensor	1	2	3	4	5
M_x, case 1	1340	349	364	2114	1196
M_x, case 2	13005	4279	4338	16544	15510
M_x, case 3	191	118	143	773	700
M_x, case 4	12262	4096	4135	15136	14980

In an ideal situation with uniform magnetisation, the M_x, M_y and M_z components in table 4.3 would not change for different sensor locations. For the metal plate the same can be said for the M_x component

of the magnetisation at locations 1, 4 and 5 in table 4.4. For locations 2 and 3 this can not be directly deduced since a possible magnetisation in the y-direction also directly influences the B_x-field at these locations. A quantitative interpretation of these numbers is difficult, but a preliminary conclusion that can be drawn is:

- The assumption that the test specimens exhibit uniform magnetisation is likely to be incorrect.

As mentioned in the beginning of this chapter this makes the inversion process more complicated. In the following section, a method is proposed in order to describe non-uniform permanent magnetisation in a square plate.

4.3. Non-uniform distribution functions

Based on the results of the previous section, all specimens are from here on treated as exhibiting non-uniform magnetisation. One of the reasons for conducting experiments on a spheroid is the expectation that, due to its shape and size, it is magnetised uniformly since for spheroids of a linearly reacting material it is known that they magnetise uniformly when subjected to a uniform background field [42]. The discovery in the previous section that this is not the case means that this clear expected advantage of testing a spheroid over sheet metal plates no longer upholds. For this reason, from now on, plate material only will be tested since this is the material that will be used in construction of marine vessels, as well as the fact that it is much more convenient to use sheet metal when applying tension in order to capture the Villari effect which will be discussed in chapter 6. Another change in approach is made by shifting the measuring equipment from the fluxgate sensor to the sensor array. Please refer to appendix B.2.1 for a more detailed description of the array. The individual sensors are less accurate than the fluxgate sensor, but the entire array is able to measure three components of the magnetic induction field with 112 sensors in a 750×300 mm plane instead of a three component measurement at a single location.

In this section an attempt is be made to translate a set of magnetic induction field measurements obtained with the sensor array at a distance from the specimen to the magnetisation within the object. An example of magnetic induction field measurements below a metal plate when the Earth's magnetic field is lifted is shown in figure 4.5.

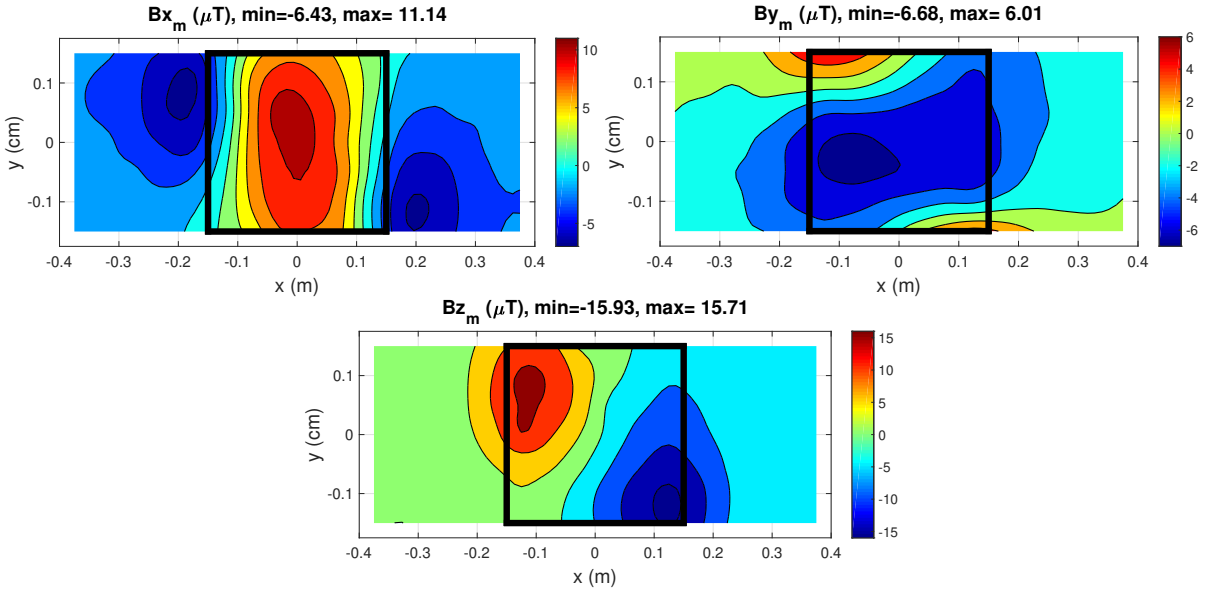

Figure 4.5: Measured induction field in an xy-plane at z = 71 mm due to remnant magnetisation of a 300×300×5 mm metal plate with its centre at (0,0,0), Background field 0 in all directions.

The goal is to find a non-uniform expression which describes the M_x, M_y and M_z distributions over the plate that produce the magnetic induction field components as measured in, for example, figure 4.5.

4.3.1. Global and local functions

Since for a metal plate the width and length are much larger than the thickness, variance in magnetisation over the thickness is neglected. When assuming variance in x and y-directions only, two methods are proposed initially through which non-uniform magnetisation can be described in a square plate:

- Global functions that provide a single equation which exists on the entire domain of the plate;
- Local functions that describe the magnetisation on a discrete domain, for which the entire domain consists of multiple of these discrete domains.

Assume metal plate specimen 1 (300×300×5 mm) from the previous section with its centre at the origin. Global functions describing the magnetisation that depend on both x and y can be defined by taking a polynomial expansion in both directions up to the second order. For each separate component (M_x, M_y, M_z) this yields the following set of expressions:

$$\begin{aligned} M_x(x,y) &= A_1 + A_2\left(\frac{x}{w}\right) + A_3\left(\frac{y}{w}\right) + A_4\left(\frac{x}{w}\right)\left(\frac{y}{w}\right) + A_5\left(\frac{x}{w}\right)^2 + A_6\left(\frac{y}{w}\right)^2 \\ M_y(x,y) &= A_7 + A_8\left(\frac{x}{w}\right) + A_9\left(\frac{y}{w}\right) + A_{10}\left(\frac{x}{w}\right)\left(\frac{y}{w}\right) + A_{11}\left(\frac{x}{w}\right)^2 + A_{12}\left(\frac{y}{w}\right)^2 \\ M_z(x,y) &= A_{13} + A_{14}\left(\frac{x}{w}\right) + A_{15}\left(\frac{y}{w}\right) + A_{16}\left(\frac{x}{w}\right)\left(\frac{y}{w}\right) + A_{17}\left(\frac{x}{w}\right)^2 + A_{18}\left(\frac{y}{w}\right)^2 \end{aligned} \tag{4.1}$$

in which w equals half the width of the plate, 150 mm. Some random magnetisation distributions obtained using expressions (4.1) and random parameters between -1000 and 1000 are presented in figure 4.6.

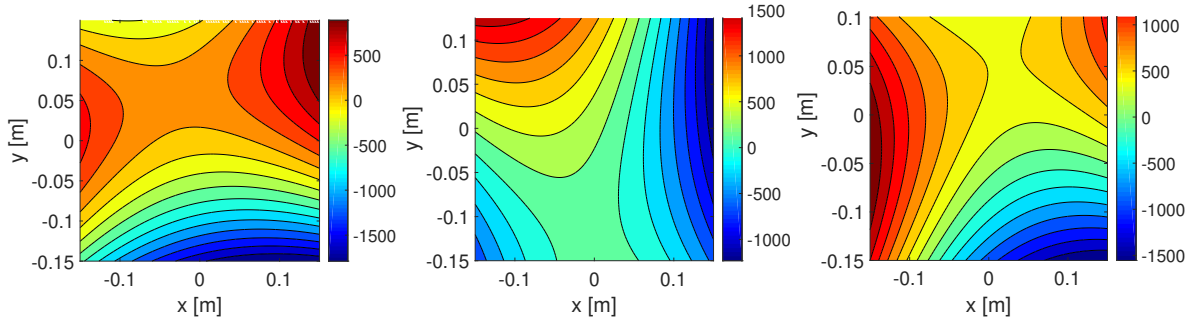

Figure 4.6: Random $M_{x,y,z}$-distributions [A/m] in a 300×300×5 mm plate obtained with second order polynomials.

As can be seen from equations (4.1), the magnetisation distribution within the plate is described using 18 parameters: $A_1, A_2 \ldots A_{18}$. This could be extended to higher order terms in order to capture a higher order of non-uniformity. Below, an extension using third order global functions is given:

$$\begin{aligned} M_x(x,y) = {} & A_1 + A_2\left(\frac{x}{w}\right) + A_3\left(\frac{y}{w}\right) + A_4\left(\frac{x}{w}\right)\left(\frac{y}{w}\right) + A_5\left(\frac{x}{w}\right)^2 + A_6\left(\frac{y}{w}\right)^2 + \\ & A_7\left(\frac{x}{w}\right)^2\left(\frac{y}{w}\right) + A_8\left(\frac{x}{w}\right)\left(\frac{y}{w}\right)^2 + A_9\left(\frac{x}{w}\right)^3 + A_{10}\left(\frac{y}{w}\right)^3 \\ M_y(x,y) = {} & A_{11} + A_{12}\left(\frac{x}{w}\right) + A_{13}\left(\frac{y}{w}\right) + A_{14}\left(\frac{x}{w}\right)\left(\frac{y}{w}\right) + A_{15}\left(\frac{x}{w}\right)^2 + A_{16}\left(\frac{y}{w}\right)^2 + \\ & A_{17}\left(\frac{x}{w}\right)^2\left(\frac{y}{w}\right) + A_{18}\left(\frac{x}{w}\right)\left(\frac{y}{w}\right)^2 + A_{19}\left(\frac{x}{w}\right)^3 + A_{20}\left(\frac{y}{w}\right)^3 \\ M_z(x,y) = {} & A_{21} + A_{22}\left(\frac{x}{w}\right) + A_{23}\left(\frac{y}{w}\right) + A_{24}\left(\frac{x}{w}\right)\left(\frac{y}{w}\right) + A_{25}\left(\frac{x}{w}\right)^2 + A_{26}\left(\frac{y}{w}\right)^2 + \\ & A_{27}\left(\frac{x}{w}\right)^2\left(\frac{y}{w}\right) + A_{28}\left(\frac{x}{w}\right)\left(\frac{y}{w}\right)^2 + A_{29}\left(\frac{x}{w}\right)^3 + A_{30}\left(\frac{y}{w}\right)^3 . \end{aligned} \tag{4.2}$$

It can be seen from equations (4.1) and (4.2) that increasing the global functions by one order significantly increases the amount of parameters used to describe the magnetisation to a total of 30. Random magnetisation distributions, which are obtained using third order polynomials and random parameters between -1000 and 1000 are presented in figure 4.7.

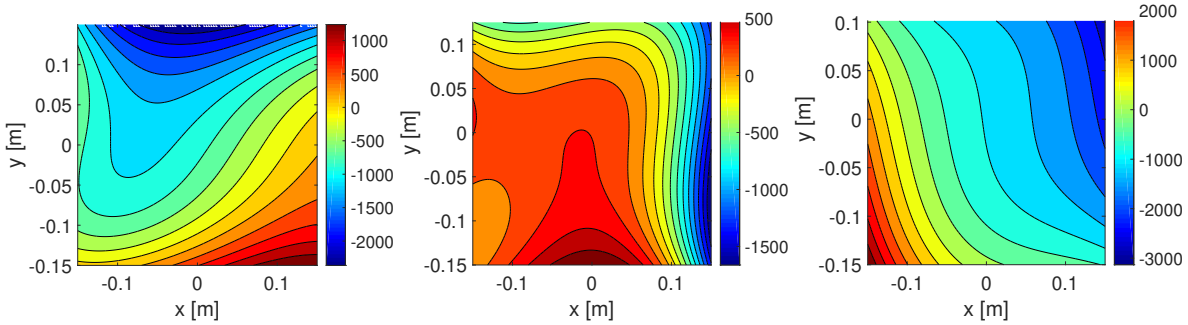

Figure 4.7: Random $M_{x,y,z}$-distributions [A/m] obtained with third order polynomials.

When comparing figures 4.6 and 4.7 it can be seen that increasing the order of the global functions allows for an increase in the possible non-uniformity over the surface of the domain.

Using local instead of global functions, the plate is subdivided into smaller domains in which the magnetisation is uniform. The amount of parameters describing the magnetisation then depends on the amount of squares that the plate is discretized into. For each domain, three parameters are required to describe the, locally uniform, M_x, M_y and M_z components. Assuming a discretization into square domains, the order of discretization can be described by n in which n^2 is the total amount of discretized domains. The total amount of parameters used to describe non-uniformity is then given by $3n^2$ when considering the three components (M_x, M_y, M_z). For n = 2 and n = 3, the M-distribution within the plate could look similar to figure 4.8 when using random parameters between -1000 and +1000 A/m.

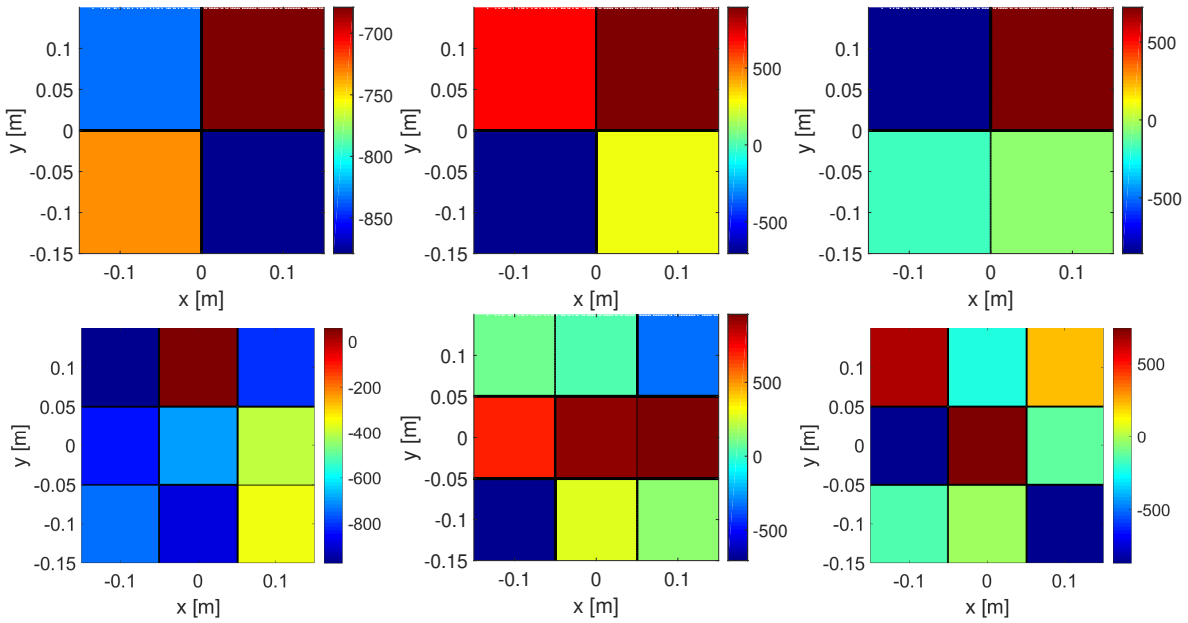

Figure 4.8: Random $M_{x,y,z}$-distributions [A/m] with $n = 2$ (top) and $n = 3$ (bottom).

4.3.2. Two-dimensional Gaussian distributions

A drawback of the local functions is that the magnetisation is not continuous over the domain of the plate, as can be seen in figure 4.8. Eventually, a chosen distribution is projected onto a mesh in the finite element simulation. For each element in this mesh the magnetisation is linearised over the domain

of that element. When using these local functions it is found that these locally steep gradients caused difficulties within COMSOL in finding a solution compared to when the distribution is smooth. Another drawback is the fact that incorporating these separate domains would come with extra implementational burden in COMSOL when combined with the Jiles-Atherton model which will be discussed in the following chapter. This gave rise to the idea to look for functions which act locally but live on a global domain. These were found in the shape of higher order two-dimensional Gaussian functions which are given by

$$f(x,y) = A\exp\left(-\left(\frac{(x-x_0)^2}{2s_x^2} + \frac{(y-y_0)^2}{2s_y^2}\right)^P\right). \tag{4.3}$$

In equation 4.3, A is the amplitude or peak height, x_0 and y_0 the coordinates of the centrepoint, s_x and s_y the standard deviation in x and y directions and P the higher order power. A three-dimensional view of this function is given on the left side of figure 4.9 for A = 1, x_0 = y_0 = 0, s_x = s_y = 0.05, and P = 1. By increasing the value of the higher order term P, the transition zone between zero and the peak value A can be decreased as shown in the right figure, where P = 3.

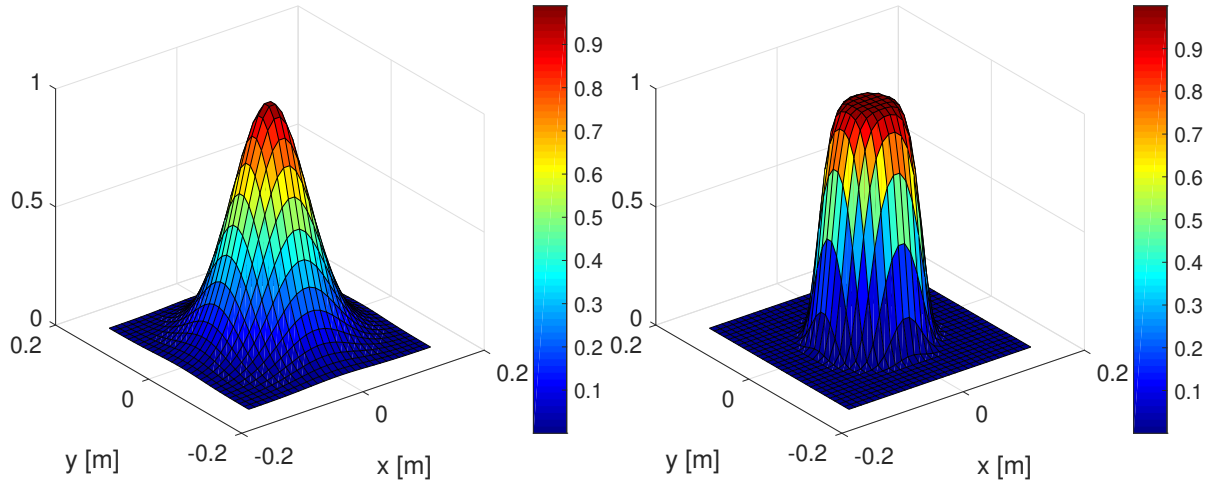

Figure 4.9: Two-dimensional higher order Gaussian distribution functions, P = 1 (left) and P = 3 (right).

A contour plot of both distributions is provided in figure 4.10. From this figure it can be clearly seen how the higher order Gaussian functions can be used to describe magnetisation locally while existing on the entire domain of the plate.

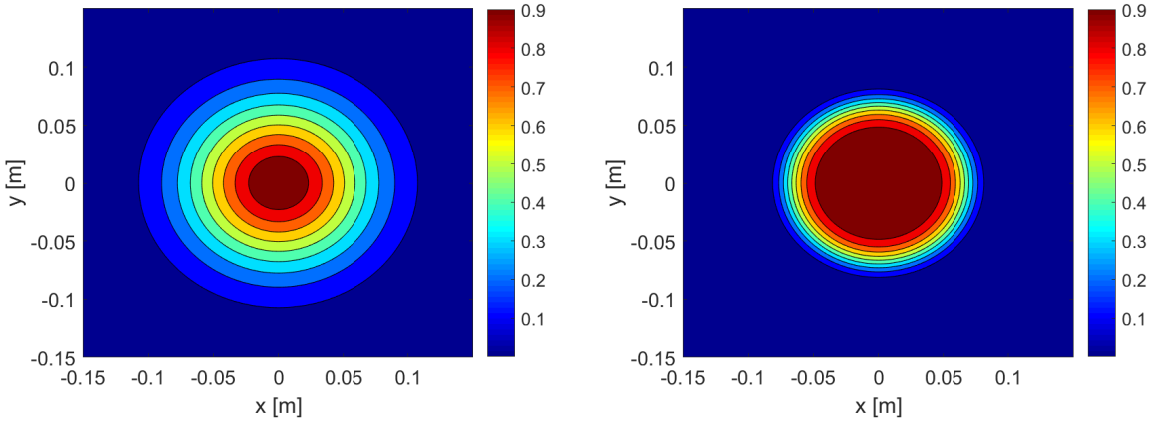

Figure 4.10: Two-dimensional higher order Gaussian distribution functions, P = 1 (left) and P = 3 (right).

A drawback of these functions is their radial symmetry which conflicts with the rectangular shapes of the test specimens. On the left of figure 4.11, nine higher order Gaussian terms with A = 1, a small standard

deviation $s_{x,y}$ = 0.02, and P = 3 are placed in a grid-like shape on the surface of the plate. In order to cover the entire plate, the standard deviation in both directions can be increased. This results in some areas of the plate being over-represented, which means that they feel the effect of two neighbouring Gaussian functions. These areas are dark red and have values >>1. Other areas that are under-represented appear at locations further removed from the centre-points and do not feel the effect of any Gaussian distribution function, which are dark blue and <<1. This effect is visualised on the right side of figure 4.11.

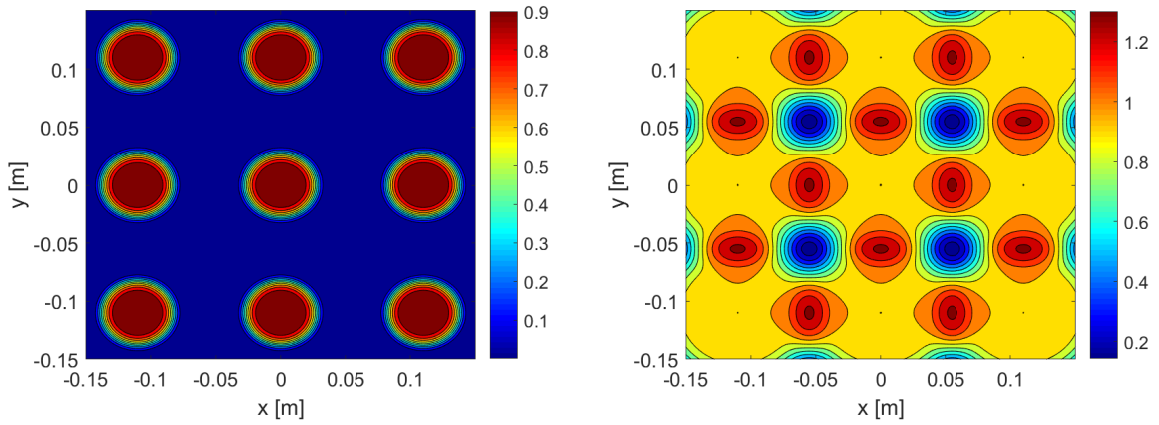

Figure 4.11: Two-dimensional higher-order Gaussian functions distributed in a grid, A =1, P = 3 and $s_{x,y}$ = 0.02 (left), $s_{x,y}$ = 0.046 (right).

The effect from figure 4.11 is caused by the grid-like placement which conflicts with the radial shape of the Gaussian distributions. This can be overcome by ensuring that the distances between centrepoints of neighbouring Gaussian functions is kept identical over the surface. Keeping angles between the centerpoints of the Gaussian functions at 60°, which is a known property of equilateral triangles, results in a hexagonal distribution. The effect of this hexagonal placement versus grid-shaped rectangular placements is shown in figure 4.12. On the left, a hexagonal placement of 7 Gaussian functions with A = 1, a small standard deviation $s_{x,y}$ = 0.03 and P = 2 is shown. On the right, the standard deviation is increased to $s_{x,y}$ = 0.067, resulting in a much better approximation which evenly capturies the entire field compared with the grid-shape from figure 4.11. This is best deduced from the considerable difference in the colourbar range of the right-hand side of figures 4.11 and 4.12.

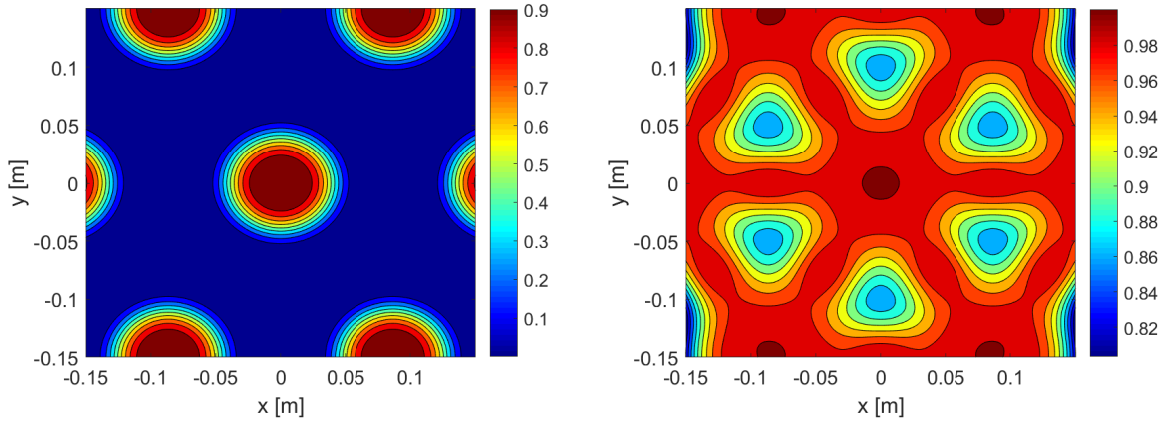

Figure 4.12: Two-dimensional higher-order Gaussian functions in a hexagonal pattern, A =1, P = 3 and $s_{x,y}$ = 0.02 (left), $s_{x,y}$ = 0.067 (right).

The abovementioned hexagonal distribution is a good way to describe non-uniform magnetisation on surfaces of any geometric shape. However, in this research project all test specimens used from here

on are rectangular. For these special cases, a rectangular higher order Gaussian distribution function is used which is slightly different from equation 4.3:

$$f(x,y) = A\exp\left(-\left(\frac{(x-x_0)^2}{2s_x^2}\right)^{P_x} - \left(\frac{(y-y_0)^2}{2s_y^2}\right)^{P_y}\right). \tag{4.4}$$

With expression (4.4), the local functions as used in figure 4.8 are incorporated in one global function. The parameter $P = P_x = P_y$, is varied to smoothen the transition zone in order to prevent discontinuities when incorporated into COMSOL. For P = 1, the ordinary two-dimensional Gaussian function is obtained, while increasing the value of P steepens the transition zone from A (dark red) to 0 (dark blue). Contour plots of the the square higher order Gaussian functions for P = 1.5 and P = 3 are given in figure 4.13.

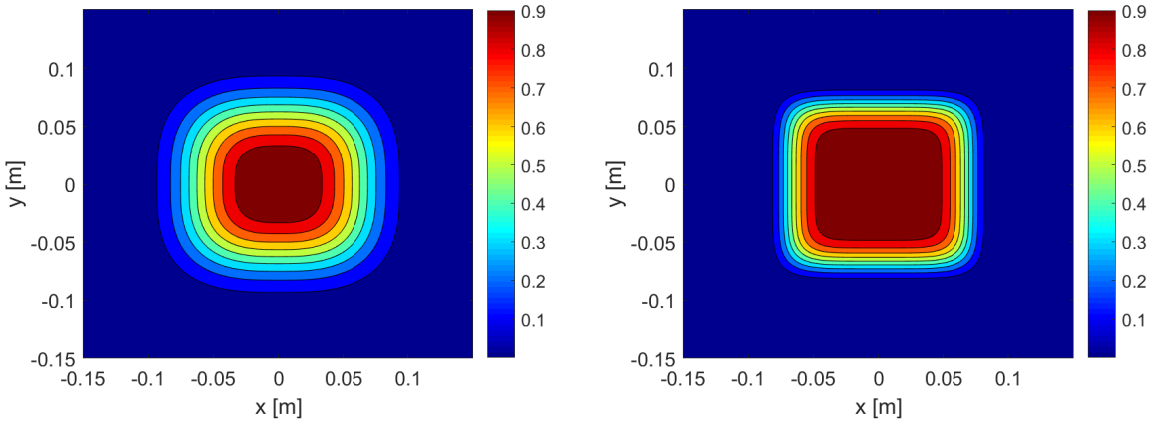

Figure 4.13: Two-dimensional higher-order square Gaussian functions, A =1, $s_{x,y}$ = 0.05 and P = 1.5 (left), P = 3 (right).

As these distirubtions will be implemented in COMSOL, it is important to keep in mind that this expression will be projected onto a meshed surface. For each element on the mesh the magnetisation is then linearised over the element. In order to prevent steep discontinuities which are found to be problemtic, it is decided to look for the optimal distribution in a shape which does not allow for steep local variations from a numerical perspective. On the left side of figure 4.14, a contour plot with nine higher order square Gaussian functions placed in a similar grid-like pattern as figure 4.11 is shown. The parameters used for the distribution functions are: A = 1, P = 1.5 and $s_{x,y}$ = 0.05. This shows how multiple square Gaussian distribution functions are capable of reproducing a more or less uniform field when A is set to 1 for all terms in the expression. For comparative reasons, the figure on the right shows the same distribution as on the left but now with one parameter A = 0 while the others remain unchanged. This shows how this summation of Gaussian distributions is capable of locally varying the field in a global function, while keeping steep discontinuities to a minimum.

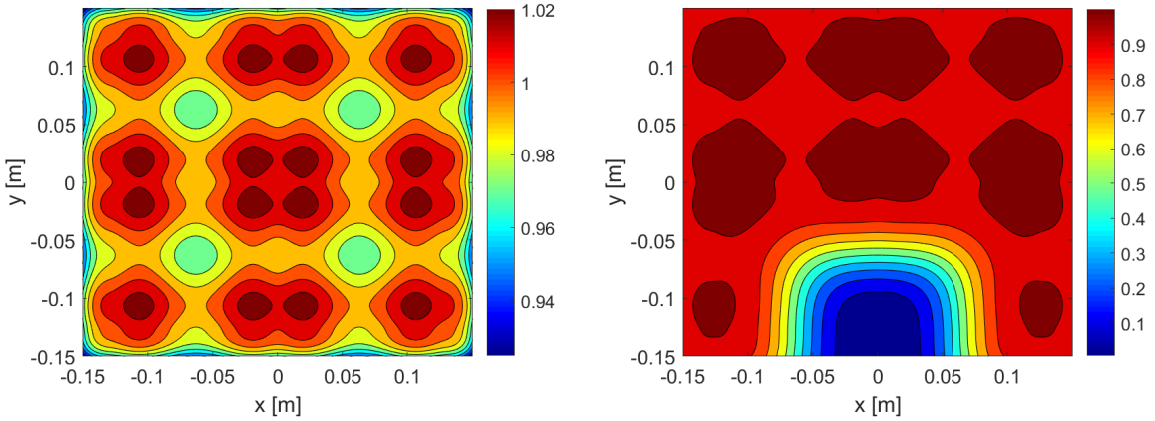

Figure 4.14: Nine two-dimensional higher order square Gaussian functions in a grid-like pattern, $s_{x,y}$ = 0.05, P = 1.5 and A_i = 1 for all i (left), $A_{\{i|i\neq 2\}}$ = 1, A_2 = 0 (right).

4.3.3. Matrix condition

The goal is to find a set of parameters that describes the non-uniform magnetisation in the plate. It is important to note that magnetisation can be described by a linear superposition of separate functions. This implies that when looking at the global and local functions above, the effect of varying each parameter can be investigated separately when these parameters do not directly influence each other. This is the case for the terms describing the amplitude of the Gaussian distirubtion functions $A_1, A_2 \ldots A_n$, since changing one of these parameters does not alter the resulting outcome of changing one of the other amplitudes. For the standard deviation s_x, s_y or the power terms P_x, P_y this is not the case since these terms also directly influence all of the amplitude parameters. For this reason, the power term and standard deviation are fixed. The outcome of the fit is then given by a combination of amplitudes for each Gaussian distribution function given by the terms $A_1, A_2 \ldots A_n$. In order to find a magnetisation that fits with the measured induction field, a parameter sensitivity matrix $\underline{\underline{M}}$ is constructed using the process outlined below which is visualised in the flowchart in figure 4.15:

1. The magnetisation in COMSOL is expressed using a set of functions as described at the beginning of this section;
2. All parameters $A_1, A_2 \ldots A_n$ are set to 0;
3. The *first* parameter, A_1, is set to 1;
4. The corresponding induction field at the location of the sensor array is calculated;
5. The calculated B-field is stored in a vector in the *first* column of matrix $\underline{\underline{M}}$;
6. All parameters $A_1, A_2 \ldots A_n$ are set to 0;
7. The *second* parameter, A_2, is set to 1;
8. etc.

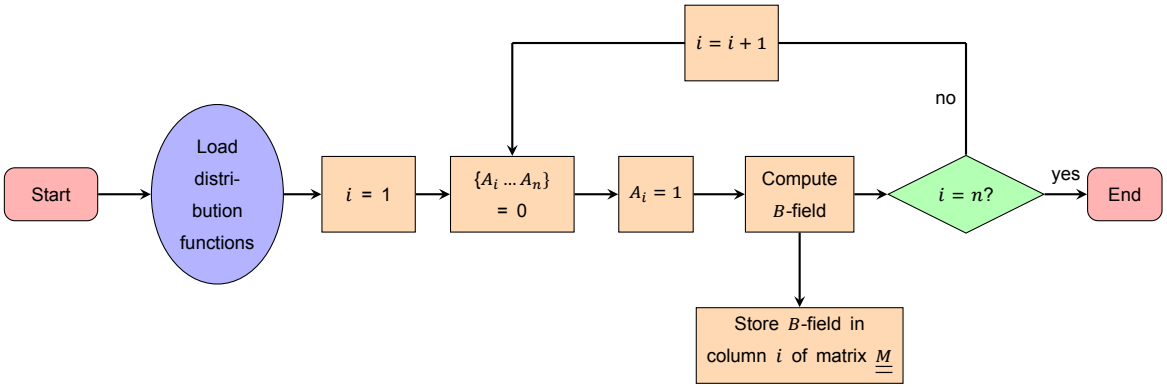

Figure 4.15: Parameter sensitivity matrix creation flowchart.

Upon storing the solution for each parameter in a separate column, the matrix in equation (4.5) appears. The first index indicates the component and sensor number, so x, y, z for the direction of the induction field and a number between 1 and 112 which corresponds with the location of the sensor. The second index is the parameter A for which this induction field is calculated. For a total of n parameters, a parameter sensitivity matrix $\underline{\underline{M}}$ of size 336×n is created. The 336 rows in the matrix correspond with the 112 sensors which measure three components each.

$$\underline{\underline{M}} = \begin{bmatrix} B_{x_1, A_1} & B_{x_1, A_2} & \dots & B_{x_1, A_n} \\ B_{x_2, A_1} & B_{x_2, A_2} & \dots & B_{x_2, A_n} \\ \vdots & \vdots & & \vdots \\ B_{x_{112}, A_1} & B_{x_{112}, A_2} & \dots & B_{x_{112}, A_n} \\ B_{y_1, A_1} & B_{y_1, A_2} & \dots & B_{y_1, A_n} \\ B_{y_2, A_1} & B_{y_2, A_2} & \dots & B_{y_2, A_n} \\ \vdots & \vdots & & \vdots \\ B_{y_{112}, A_1} & B_{y_{112}, A_2} & \dots & B_{y_{112}, A_n} \\ B_{z_1, A_1} & B_{z_1, A_2} & \dots & B_{z_1, A_n} \\ B_{z_2, A_1} & B_{z_2, A_2} & \dots & B_{z_2, A_n} \\ \vdots & \vdots & & \vdots \\ B_{z_{112}, A_1} & B_{z_{112}, A_2} & \dots & B_{z_{112}, A_n} \end{bmatrix}. \tag{4.5}$$

The goal is to find the set of parameters which describes the magnetisation that has the optimal fit with the measured B-field data. When the induction field measurements from the array are stored in a vector, and another vector **A** is defined which contains all parameters $A_1, A_2 \dots A_n$, the following expression can be formulated:

$$\underline{\underline{M}} \begin{bmatrix} A_1 \\ A_2 \\ \vdots \\ \vdots \\ \vdots \\ \vdots \\ \vdots \\ A_n \end{bmatrix} = \begin{bmatrix} B_{x_1, \text{measured}} \\ B_{x_2, \text{measured}} \\ \vdots \\ \vdots \\ \vdots \\ \vdots \\ \vdots \\ B_{z_{112}, \text{measured}} \end{bmatrix}. \tag{4.6}$$

A system like the one described in equation (4.6) can be solved for **A** using `MATLAB`'s direct solver which is built in using the backslash operator '\'. This quickly computes the least squares solution to the above-mentioned problem, see [20], or the best 'fit' of the parameters in the **A**-vector that connects $\underline{\underline{M}}$ with the solution on the right-hand side. This operator can only be used if $\underline{\underline{M}}$ is well-conditioned. The *condition number* of matrix $\underline{\underline{M}}$ qualitatively describes how the solution **A** varies when the right-hand side of equation (4.6) is changed. If a small alteration of the measured signal leads to a large change in

the solution **A** it is said that $\underline{\underline{M}}$ is ill-conditioned. A well-conditioned matrix will translate a change in the induction field into a change in **A** of the same order of magnitude. Another topic of importance is the stability of the solution and trustworthiness of its results. This can be tested using twin-experiments that will be further elaborated in the following section. A more in-depth analysis of condition numbers and matrix stability can be found in the master's thesis by Vijn [56]. For the purpose of this research it suffices to keep in mind that, as a rule of thumb, the base logarithm of the condition number can be seen as a measure of the worst-case loss of precision in terms of significant digits lost in the solution [35].

4.4. Model verification

In the previous section, methods are introduced through which non-uniform magnetisation in a surface can be described. In order to verify the applicability of these methods so-called twin experiments are conducted. Initially, an identical twin experiment is performed, where the inversion is applied to a fictitious B-field measurement which is created using the original distribution function. The second step involves a twin experiment in which the fictitious B-field is subjected to various levels of noise. A stable expression should reproduce the original M-distribution when inversion is applied. Eventually the applicability to measured data is checked and the effectiveness of different functions is compared.

4.4.1. Identical twin

The methodology behind the identical twin experiment is outlined below.

1. A distribution for $M_{x,y,z}$ is chosen following the approach outlined in section 4.3. When using Gaussian functions, fixed values are used for $\sigma_{x,y}$ and $P_{x,y}$. Each value $A_1, A_2 \dots A_n$ is a separate parameter that can be varied in order to find the best M-distribution;
2. An M-distribution is created using the function defined in step 1 with random parameters for $A_1 \dots A_n$. This M-distribution is entered in `COMSOL` and the corresponding B-field in a plane below the plate is stored in a vector B_{true};
3. The parameter sensitivity matrix $\underline{\underline{M}}$ is created for the chosen distribution, as described in section 4.3;
4. `MATLAB`'s direct solver is used to compute the least-squares fit of parameters (values for A) that corresponds with B_{true};
5. The calculated values for $A_1, A_2 \dots A_n$ are compared with the random input values for $A_1, A_2 \dots A_n$ from step 2.

In general, the matrix condition number is a good indicator of the outcome of the identical twin experiment. Well-conditioned matrices will always lead to a calculated fit which corresponds correctly with the randomly chosen A-values. As the matrix condition number increases it is found that the direct solver fails to correctly reproduce the input values which should be avoided. A substantial amount of functions has been analysed following the methodology above. The results of the identical twin experiment for a selection of these functions are presented table 4.5. This selection consists of

- f_1: Second order global functions as described in equations (4.1): 6 parameters per M-component, 18 parameters in total;
- f_2: Third order global functions as described in equations (4.2): 10 parameters per M-component, 30 parameters in total;
- f_3: Circular higher order Gaussian functions in a hexagonal pattern: 23 parameters per M-component, 69 parameters in total. $\sigma_x = \sigma_y = 0.031$ and $P_x = P_y = 1.5$;
- f_4: Square higher order Gaussian functions in a grid: 9 for M_x, 9 for M_y and a constant, location independent parameter describing M_z, 19 parameters in total. $\sigma_x = \sigma_y = 0.05$ and $P_x = P_y = 1.5$.

The choice of the latter function demands some explanation. While trying out different sets of functions to describe the magnetisation it was found from time to time that the components of the magnetisation in z-direction became very small compared to the x and y components when trying to fit the functions to measured data. When the z-component of the magnetisation was taken as uniform over the surface, the resulting fit would always find a value close to zero compared to the x and y-components of the magnetisation. It is only when more freedom in z-direction is allowed that the maximum and minimum M_z start to deviate from 0, but the average z-component was still found to be equal to 0 in all testcases which can be observed further in this report. In order to not completely neglect the possibility of magnetisation in z-direction, a single uniform term is used to describe M_z in f_4. Even so, this term turned out to provide an irrelevant contribution to the B-field in all calculated fits on measured data compared to its x and y counterparts when fit to actual data. In order to improve the stability of the system which will be investigated further in this section the choice was made to allow for only uniform magnetisation in z-direction.

		$f_1(x,y)$	$f_2(x,y)$	$f_3(x,y)$	$f_4(x,y)$
Condition no. of $\underline{\underline{M}}$		5.4×10^1	5.7×10^6	4.3×10^2	4.9×10^1
Parameter	True input				
A_1	1	1.000	1.000	1.000	1.000
A_2	3	3.000	3.000	3.000	3.000
A_3	0	0.000	-0.525	0.000	3.000
A_4	-1	-1.000	-1.000	-1.000	-1.000
A_5	-2	-2.000	-2.000	-2.000	2.000
A_6	1	1.000	1.000	1.000	1.000
A_7	2	2.000	2.525	2.000	2.000
A_8	0	0.000	-0.000	0.000	0.000
A_9	-2	-2.000	-2.000	-2.000	-2.000
A_{10}	-1	-1.000	-1.000	-1.000	-1.000
A_{11}	-2	-2.000	-2.000	-2.000	-2.000
A_{12}	-1	-1.000	0.475	-1.000	-1.000
A_{13}	0	0.000	0.000	0.000	0.000
A_{14}	0	0.000	0.000	0.000	0.000
A_{15}	0	0.000	0.000	0.000	0.000
A_{16}	2	2.000	2.000	2.000	2.000
A_{17}	0	0.000	0.000	0.000	0.000
A_{18}	3	3.000	2.475	3.000	3.000
A_{19}	1		1.000	1.000	1.000
A_{20}	3		3.000	3.000	
⋮	⋮		⋮	⋮	

Table 4.5: Identical twin experiment comparison.

The following conclusions can be drawn from table 4.5:

- The condition number is an indicator of the stability of $\underline{\underline{M}}$;
- It is unclear for which value of the condition number the system becomes unstable, but it is lower than 5.7×10^6;
- The amount of parameters and the condition of the matrix are not necessarily related. Function f_3 uses 69 parameters compared to 30 parameters in f_2, while maintaining a much lower condition number;
- The use of higher order Gaussian functions leads to an abundance of freedom to describe the M-distribution without capitalising on matrix condition.

A visualisation of the true M and B-values from table 4.5 is provided in figure 4.16 for f_2. It is important to keep in mind that the B-fields on the right are created due to a superposition of the magnetisation

components on the left, i.e. the M_x distribution by itself creates a B-field with components in all three directions, which also holds for the M_y and M_z components. The B-fields on the right-hand side consist of superpositions of the B-fields due to the three magnetisation components on the left, please refer to chapter 2.

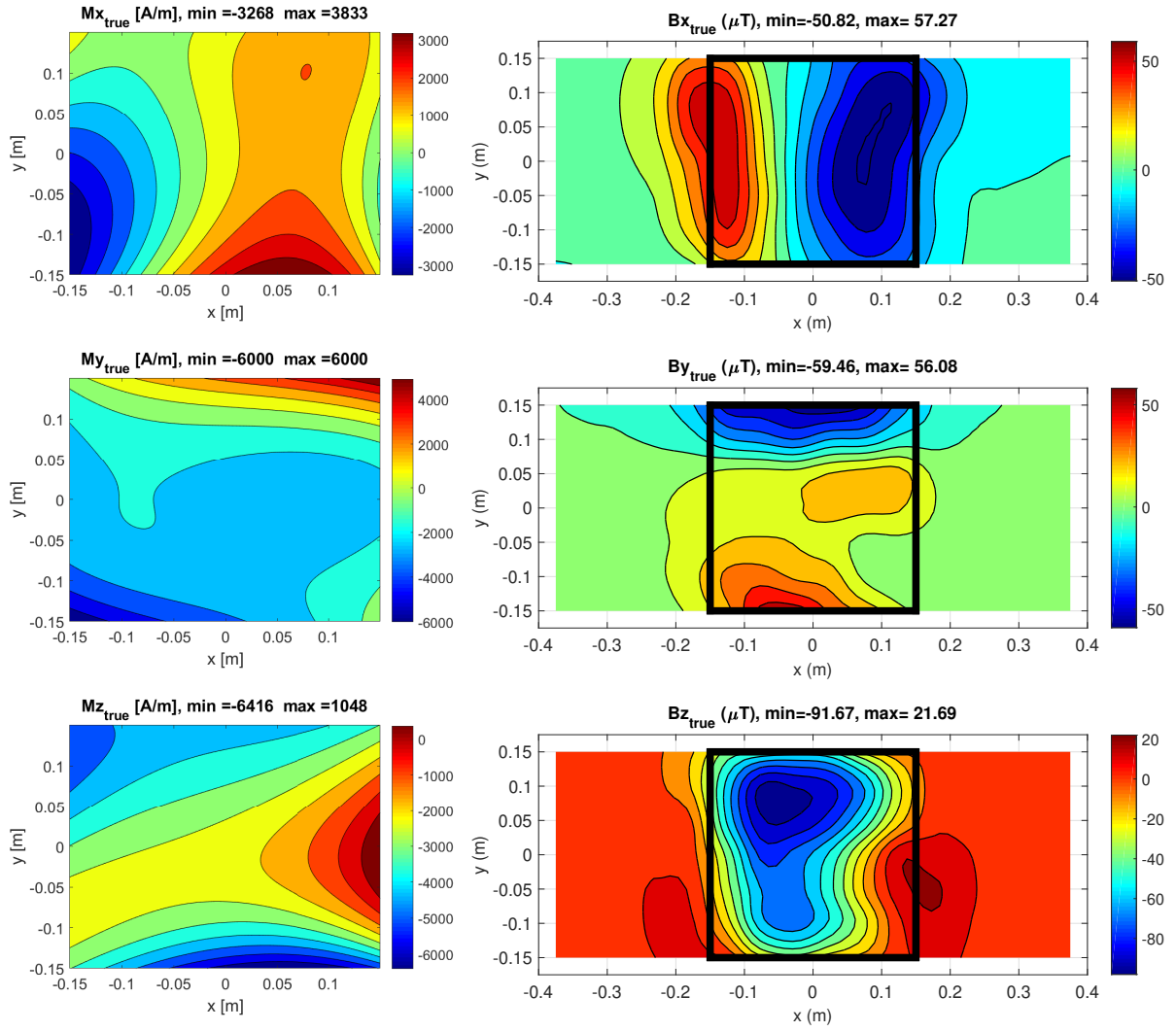

Figure 4.16: True M_x, M_y and M_z distributions and the corresponding B-fields in a plane below the plate corresponding with f_2 and the true parameters from table 4.5.

The optimal fit calculated for f_2 uses a slightly different set of parameters to describe the magnetisation than the original input. In figure 4.17 the fit magnetisation and corresponding B-field component plots are provided. From these figures it is seen that the third order global description for the magnetisation f_3 allows for too much freedom in the M-distribution to coincide with the measured B-field below. In other words, there are multiple combinations of M possible that produce an identical B-field at a distance below the plate, which is clearly an unwanted result when trying to fit a model to experimental data.

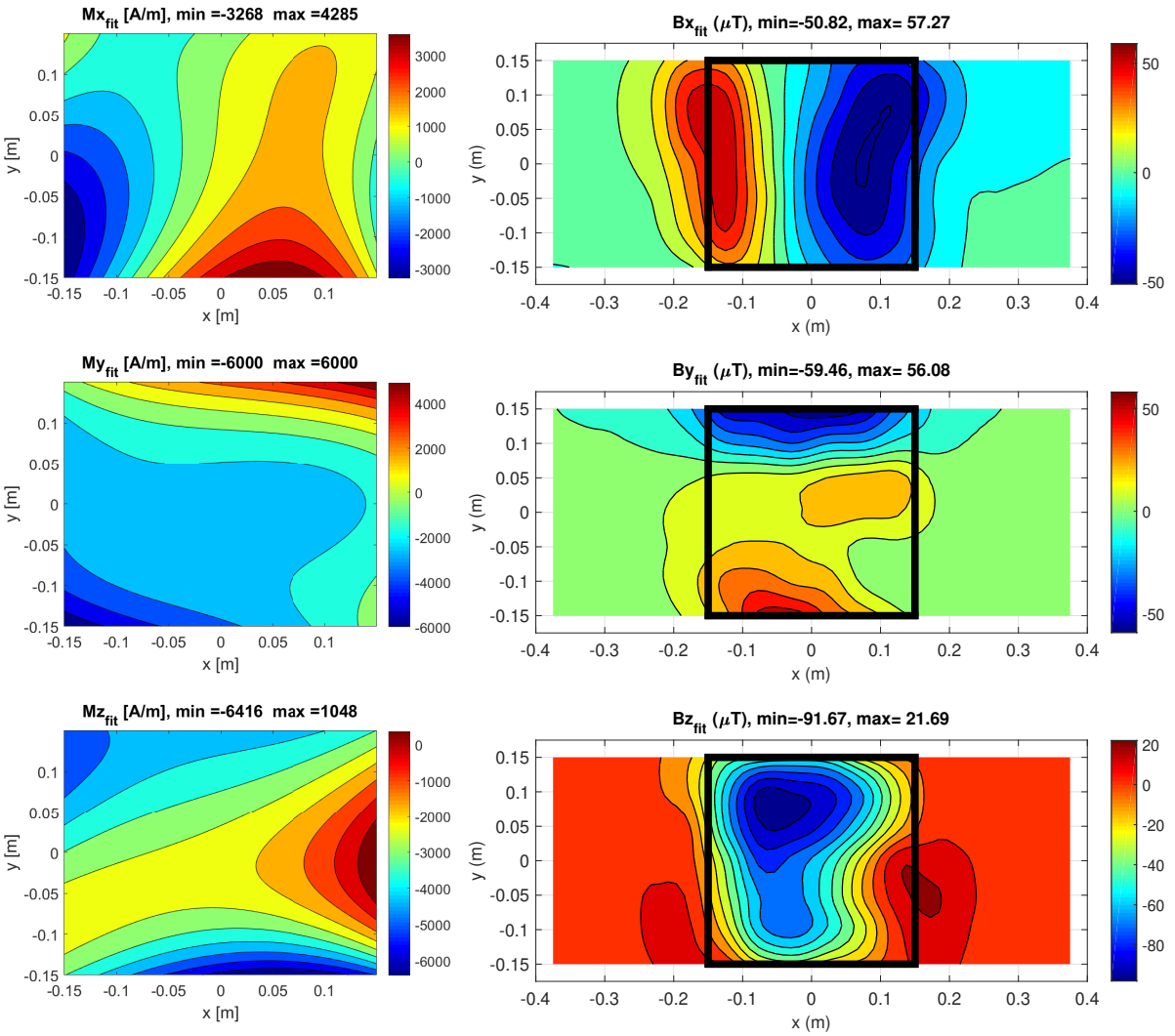

Figure 4.17: Calculated M_x, M_y and M_z distributions and the corresponding B-fields in a plane below the plate corresponding with f_2 and the true parameters from table 4.5.

4.4.2. Twin experiment

When performing real-world experiments the measured B-field will, in all likelihood, not be formed due to a magnetisation that perfectly fits the distribution functions as described in section 4.3. Even if this was the case, the corresponding measured B-field will be affected by noise due to inaccuracy of the sensors in the array. For this reason it is important to investigate the stability of the distribution functions when the output is affected by noise. The methodology of the twin experiment is outlined below.

1. A distribution for $M_{x,y,z}$ is chosen following the approach outlined in section 4.3. When using Gaussian functions, fixed values for $\sigma_{x,y}$ and $P_{x,y}$ are used. Each value for A is a separate parameter that can be varied in order to find the best M-distribution;
2. An M-distribution is created using the function defined in step 1 with random parameters for $A_1, A_2 \ldots A_N$. This M-distribution is entered in `COMSOL` and the corresponding B-field in a plane below the plate is calculated;
3. Various levels of normally distributed noise are added to the B-field calculated in step 2. These noise-affected B-fields are stored in separate columns in a matrix B_{true}. Each column of B_{true} is a separate 'solution' of the system, with increasing amounts of noise added;
4. `MATLAB`'s direct solver is used to compute the least-squares fit of parameters (values for A) that correspond with B_{true} for each noise level;

5. The calculated values for $A_1, A_2 \ldots A_N$ are compared for each noise level with the input for $A_1, A_2 \ldots A_N$ from step 2.

For each of the functions f_{1-4}, the average total strength of the measured B-field is calculated using

$$A_{\text{signal}} = \frac{\sum_{i=1}^{112} \sqrt{B_{x,i}^2 + B_{y,i}^2 + B_{z,i}^2}}{112} . \tag{4.7}$$

The signal-to-noise ratio, or SNR, can be expressed by

$$SNR = \frac{A_{\text{noise}}}{A_{\text{signal}}} \tag{4.8}$$

in which A stands for amplitude. The corresponding noise is calculated as a percentage of the average measured field. The noise is added in five different levels of magnitude:

- L1: 2.5% SNR;
- L2: 5% SNR;
- L3: 10% SNR;
- L4: 20% SNR;
- L5: 40% SNR.

The noise is added to the B-field using an ordinary Gaussian distributed function with a mean of 0 and a standard deviation equalling one third of A_{noise} in order to ascertain that 99.7% of the noise is equal to or lower than the noise amplitude. A visualisation of the noise classes is provided using COMSOL output in figure 4.18.

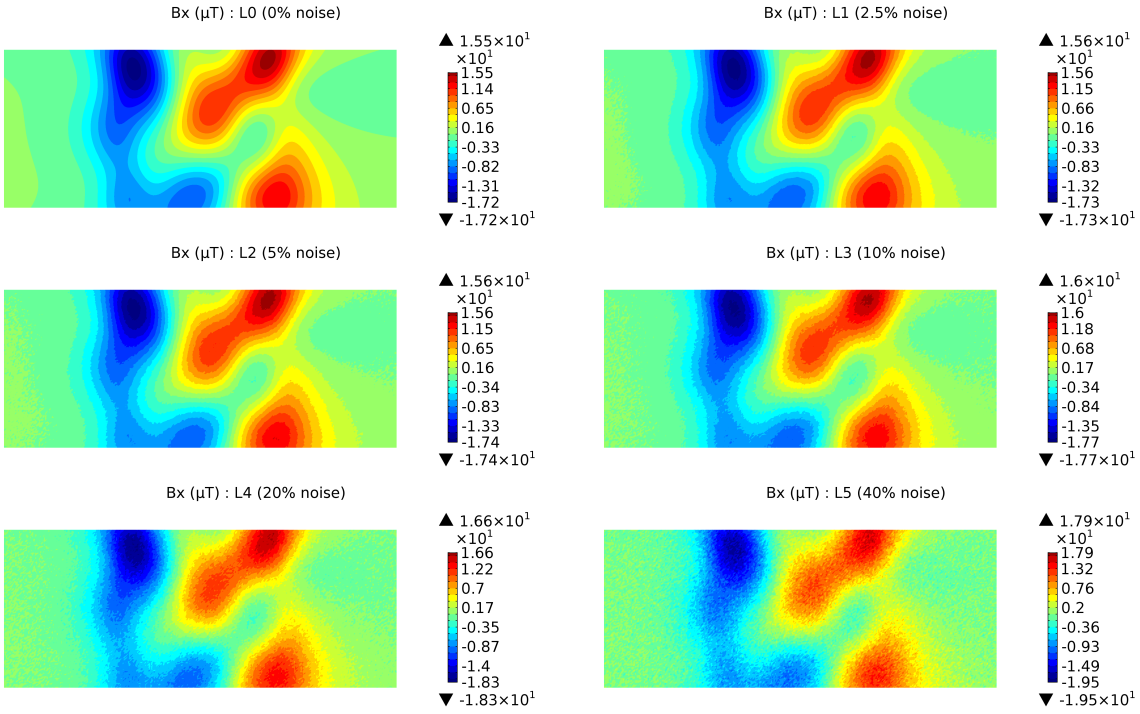

Figure 4.18: The x-components of a B-field with various levels of added noise.

The error between the input and the calculated parameters is calculated through

$$\eta = \frac{\sum_{i=1}^{n} \left| A_{i,\text{input}} - A_{i,\text{calculated}} \right|}{\sum_{i=1}^{n} \left| A_{i,\text{calculated}} \right|} \tag{4.9}$$

which calculates the relative difference between the input and the calculated fit parameter vectors.The results of the twin experiment for f_1 and f_2 in combination with the noise levels mentioned above are given in table 4.6.

		$f_1(x,y)$, A_{signal} =16.76 μT				
Level		L1	L2	L3	L4	L5
St. dev. noise		0.14 μT	0.28 μT	0.56 μT	1.11 μT	2.22 μT
Parameter	Input	Calculated fit value				
A_1	1	1.001	1.001	1.088	1.087	1.217
A_2	3	3.006	2.978	3.027	3.004	2.903
A_3	0	0.004	0.019	0.023	0.094	-0.072
A_4	-1	-1.028	-1.026	-1.072	-0.939	-1.253
A_5	-2	-1.999	-1.977	-2.052	-2.014	-2.289
A_6	1	0.986	0.952	0.784	0.645	1.095
$A_7, A_8 \ldots A_{18}$	⋮	⋮	⋮	⋮	⋮	⋮
η		**0.89 %**	**2.85 %**	**4.21 %**	**7.01 %**	**17.35 %**

		$f_2(x,y)$, A_{signal} =31.6 μT				
Level		L1	L2	L3	L4	L5
St. dev. noise		0.26 μT	0.53 μT	1.05 μT	2.11 μT	4.21 μT
Parameter	Input	Calculated fit value				
A_1	1	1.055	0.942	0.498	1.216	2.807
A_2	3	2.963	2.963	2.635	3.509	2.930
A_3	0	1.07×10^4	4.23×10^3	-2.67×10^4	-4.58×10^4	3.60×10^4
A_4	-1	-0.984	-1.026	-1.030	-1.032	-1.838
A_5	-2	-2.095	-1.977	-1.975	-2.322	-5.684
A_6	1	0.947	0.952	1.134	0.807	0.592
$A_7, A_8 \ldots A_{30}$	⋮	⋮	⋮	⋮	⋮	□
η		**» 100 %**	**» 100 %**	**» 100 %**	**» 100 %**	**» 100 %**

Table 4.6: Twin experiment results for f_1 and f_2.

The contrast with respect to noise sensitivity of the two functions is large. f_1 shows that even with a significant amount of noise, the relative error between the input and the inversely calculated parameters remains small. This proves that f_1 returns a stable solution when confronted with output blurred by a certain amount of noise. The contrary can be said for f_2, for which the error becomes huge when the output is subjected to the smallest amount of noise. Based on figure 4.17, one could argue that even though the parameters returned in the *identical* twin experiment were different than the input values, the resulting M-distribution and corresponding B-field are still nearly identical. However, the M-distributions that follow from table 4.6 show that certain calculated parameters become extraordinarily large. These parameters are linked to the following terms from equations (4.2):

In the expression for M_x : $A_3\left(\frac{y}{w}\right)$ and $A_7\left(\frac{x}{w}\right)^2\left(\frac{y}{w}\right)$;
In the expression for M_y : $A_{12}\left(\frac{x}{w}\right)$ and $A_{18}\left(\frac{y}{w}\right)^2\left(\frac{x}{w}\right)$.

Upon investigation it was found that these four terms, in a certain configuration, are capable of cancelling out each others' effect on the B-field in a plane below the plate. Therefore, it can be said that f_2 allows for too much freedom in the solution in order to be reliable and stable.

The results of the twin experiment for f_3 and f_4 are shown in table 4.7.

		$f_3(x,y)$, $A_{\text{signal}} = 8.9$ µT				
Level		L1	L2	L3	L4	L5
St. dev. noise		0.07 µT	0.15 µT	0.30 µT	0.59 µT	1.19 µT
Parameter	Input	Calculated fit value				
A_1	1	1.170	1.115	-0.292	0.923	-0.527
A_2	3	2.986	2.921	3.106	2.208	3.469
A_3	0	-0.048	0.167	0.189	0.587	0.388
A_4	-1	-0.983	-0.944	-0.770	-0.483	-2.277
A_5	-2	-2.039	-2.234	-2.125	-1.752	-0.696
A_6	1	1.221	0.748	-0.401	1.128	-0.193
$A_7, A_8 \dots A_{69}$	⋮	⋮	⋮	⋮	⋮	⋮
η		**7.00 %**	**16.55 %**	**38.06 %**	**61.71 %**	**124.63 %**

		$f_4(x,y)$, $A_{\text{signal}} = 8.5$ µT				
Level		L1	L2	L3	L4	L5
St. dev. noise		0.07 µT	0.14 µT	0.28 µT	0.57 µT	1.14 µT
Parameter	Input	Calculated fit value				
A_1	1	0.995	1.015	0.961	0.972	1.195
A_2	3	2.996	3.041	2.999	2.997	3.340
A_3	0	-0.002	0.014	0.022	0.001	0.101
A_4	-1	-1.000	-1.007	-0.971	-1.022	-1.105
A_5	-2	-2.008	-1.985	-1.960	-2.090	-1.951
A_6	1	0.995	0.993	1.021	0.948	1.195
$A_7, A_8 \dots A_{30}$	⋮	⋮	⋮	⋮	⋮	⋮
η		**0.34 %**	**1.59 %**	**2.18 %**	**3.07 %**	**14.87 %**

Table 4.7: Twin experiment results for f_3 and f_4.

Table 4.7 shows that expression f_4 allows for a very stable reproduction of the input values when the output is subjected to noise. The error in f_3 is considerable and grows rapidly for increasing noise levels, which can be explained by the fact that this expression uses 69 parameters compared to only 19 parameters in f_4. From these results it can be stated that the use of higher order Gaussian global functions is a good way to describe non-uniform magnetisation. A trade-off is always made between the amount of freedom available to apply local variations (the amount of parameters) and the robustness of the function (the error).

4.4.3. Application to measurements

The final step in the model verification process consists of applying the functions proposed in this chapter to actual measurements and see how well they are capable of finding an M-distribution that reproduces the measured data. Based on the results of the (identical) twin experiments it was found that only f_1 and f_4 prove to be reliable functions. Their applicability to real-world measurements is investigated below, which implicates that from here on M_{true} is unknown. This implies that only B-field measurements can be compared with B-fields that follow from the magnetisation calculated through inversion using the functions above. Since f_1 and f_4 provide a substantially different approach when describing the magnetisation, it is interesting to investigate the differences between the magnetisation obtained when using both functions on the same dataset as a method of verifying them.

The Earth's magnetic field is lifted within the Helmholtz cage (see appendix B.1) and a zero measurement is taken without an object present. Then, a steel plate (300×300×5 mm) is placed in the centre of the cage. The B-field is measured and the zero measurement is subtracted. This yields the B-field due to the remnant magnetisation within the steel plate. The result of this measurement for each separate component are shown on the left side of figures 4.19 & 4.20. Based on these measurements, an attempt is made to find the M-distribution using f_1 and f_4. For both functions, the obtained M-distributions are given in figure 4.21. The B-fields obtained using f_1, and the difference between the fit B-field and the original measurement are shown in the centre and right side of figure 4.19. For the fit obtained using

f_4, these are given in the centre and right side of figure 4.20. The experiment above was repeated for a different metal plate with identical dimensions (300×300×5 mm). The results of this second experiment are given in figures 4.22 - 4.24.

From figures 4.19-4.24 it can be observed that both f_1 and f_4 are capable of producing an M-distribution that produces a B-field which fits properly with the measured data. The difference fields show that the error between the measured and calculated fields rarely exceeds 1 µT, which is roughly the same magnitude of error known for the sensors mounted in the sensor array used to measure the B-field. To conclude this chapter it is decided to continue with the higher order square Gaussian function, f_4, instead of f_1 for the remainder of this project due to the reasons outlined here:

1. Higher order Gaussian functions can be easily adapted to other (irregular) geometric shapes. This is more complicated for the global functions from f_1;
2. The specimens above are found to be relatively uniformly magnetised. If future specimens are encountered with larger local variations, f_4 provides a more intuitive approach to vary the magnetisation locally;
3. Function f_4 can be easily scaled to include more degrees of freedom by refining the grid (adding more Gaussian terms to the equation). Adding additional terms to f_1 (essentially transforming f_1 into f_2) is found to destabilise the solution;
4. The noise-effected inversion error in f_4 is smaller than in f_1 which implies a more robust approach;
5. The extreme values of the magnetisation produced by f_4 are smaller than in f_1.

At this point it is decided to continue with these functions in order to describe an initial magnetisation which acts as a starting magnetisation, M_0, for the hysteresis and Villari experiments. This does not stipulate that this methodology or the functions derived in this chapter will always provide both the optimal and a unique solution to the inverse problem. Defining this optimal expression, and guaranteeing this solution is unique, will require a signifcant amount of time and someone who is skilled in the field of *regularisation*, please refer to chapter 7.

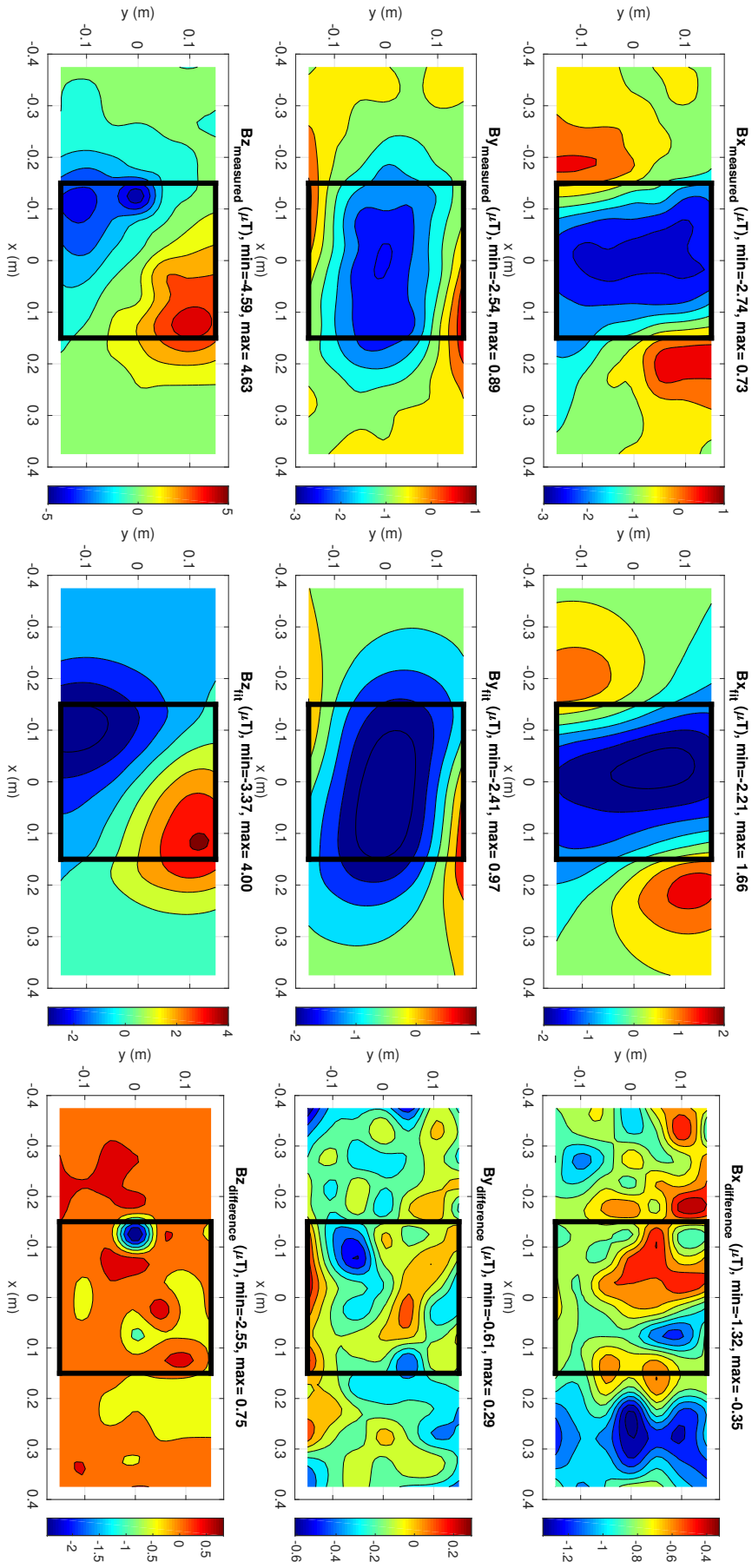

Figure 4.19: Measurement 1: B-field 1 (left), B-field corresponding with the calculated fit using f_1 (centre), difference between B_{measured} and B_{fit} (right).

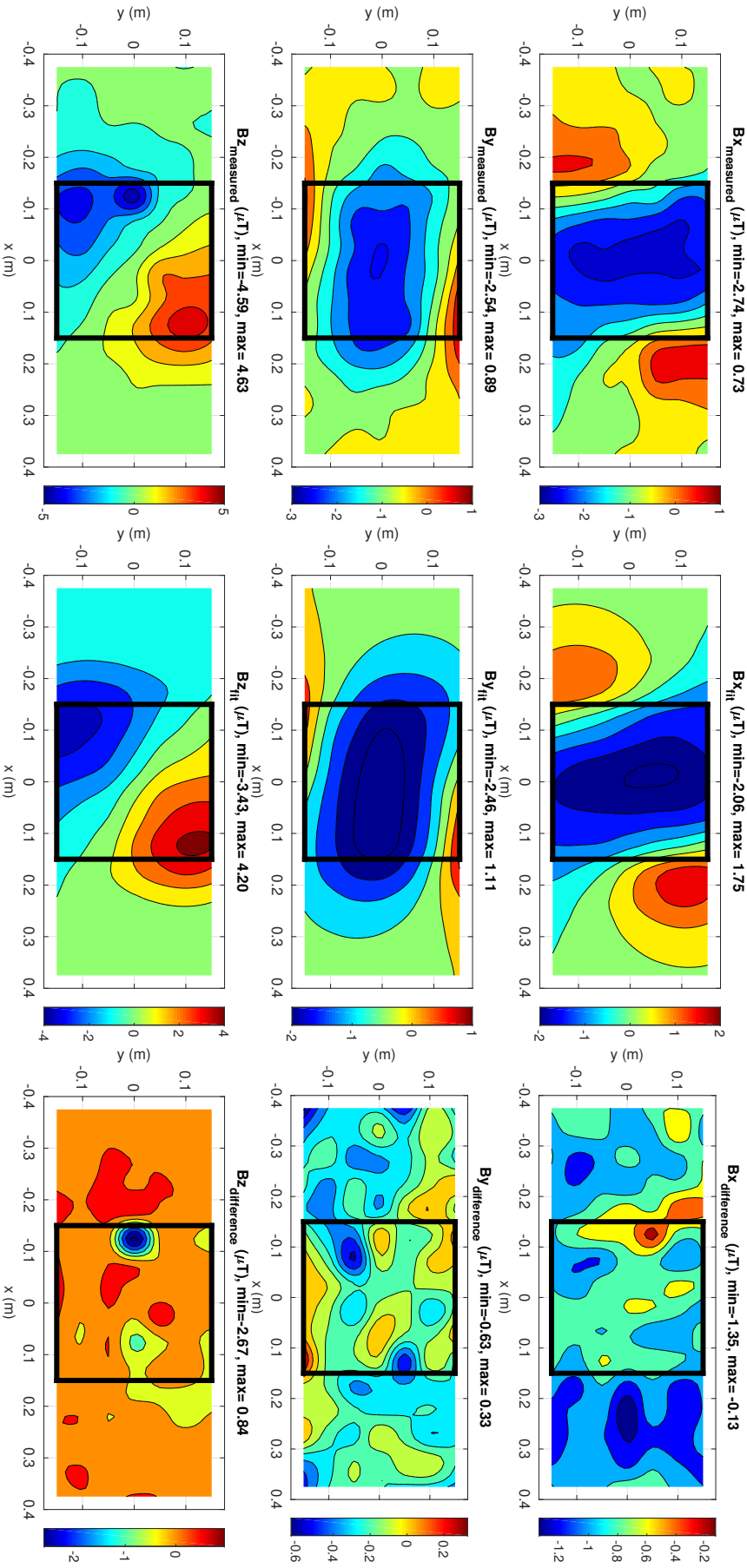

Figure 4.20: Measurement 1: B-field 1 (left), B-field corresponding with the calculated fit using f_4 (centre), difference between B_{measured} and B_{fit} (right).

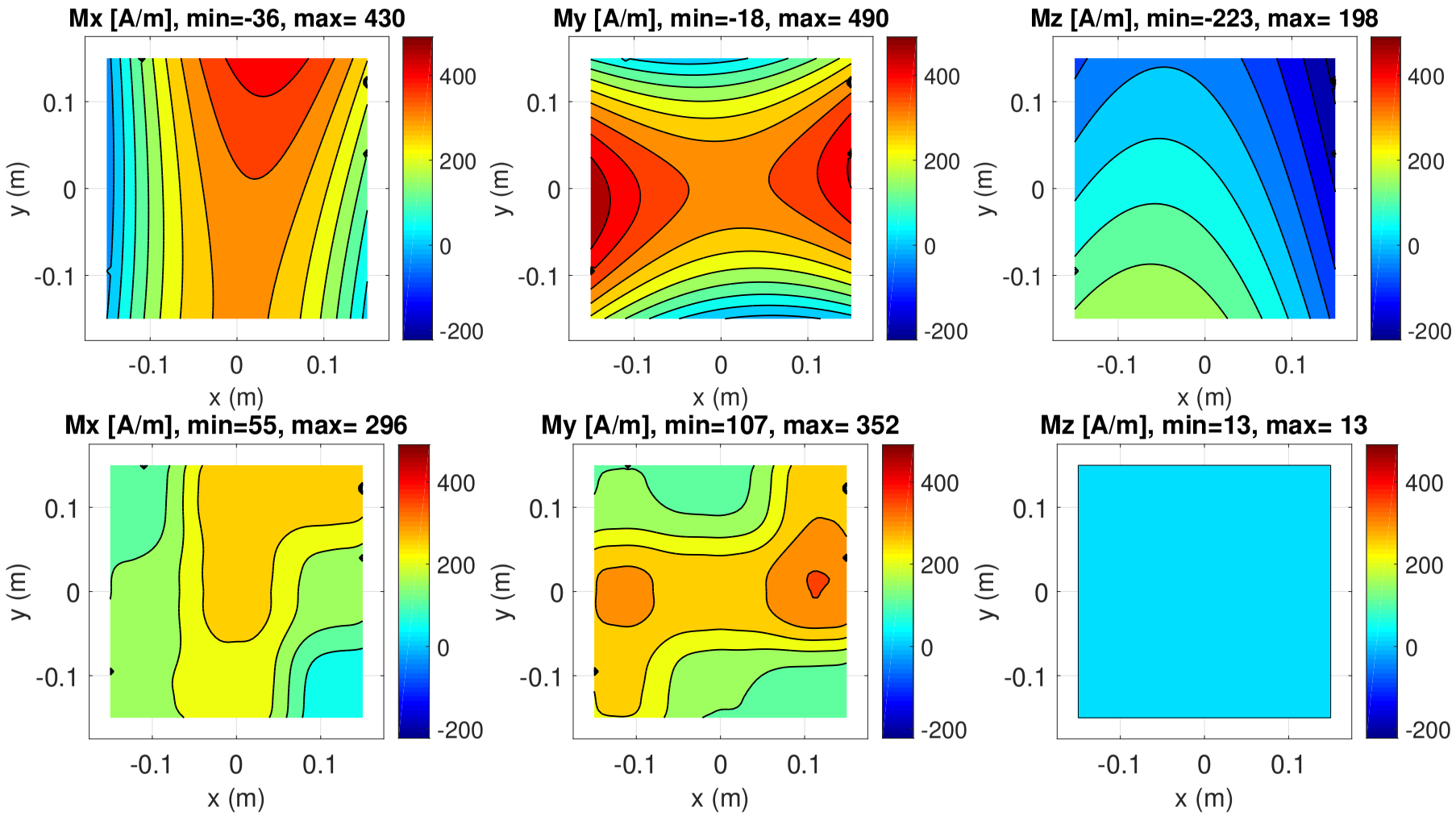

Figure 4.21: Measurement 1: M-distributions using f_1, see figure 4.19 (top) and using f_4, see figure 4.20 (bottom).

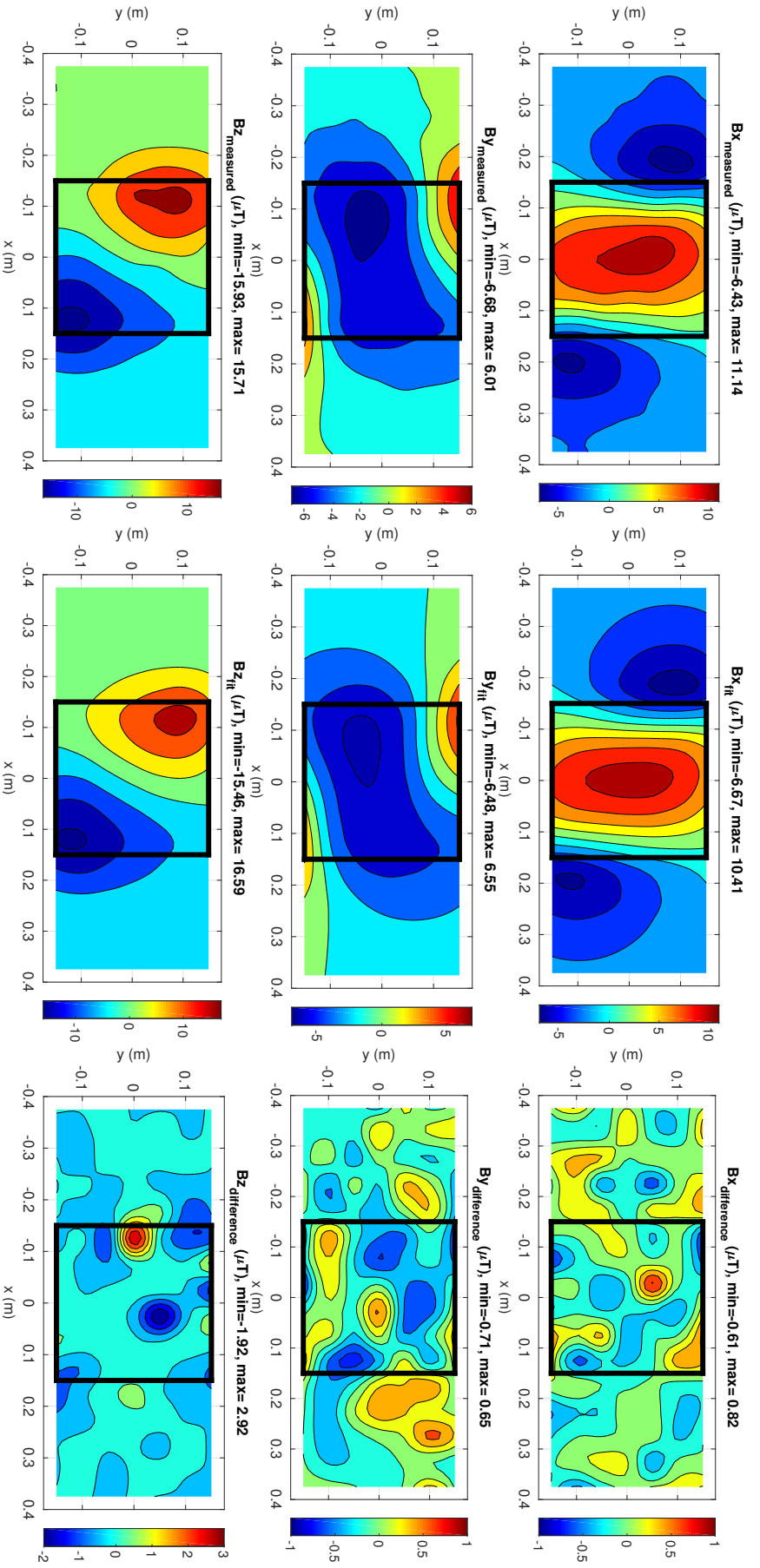

Figure 4.22: Measurement 2: B-field (left), B-field corresponding with the calculated fit using f_1 (centre), difference between B_{measured} and B_{fit} (right).

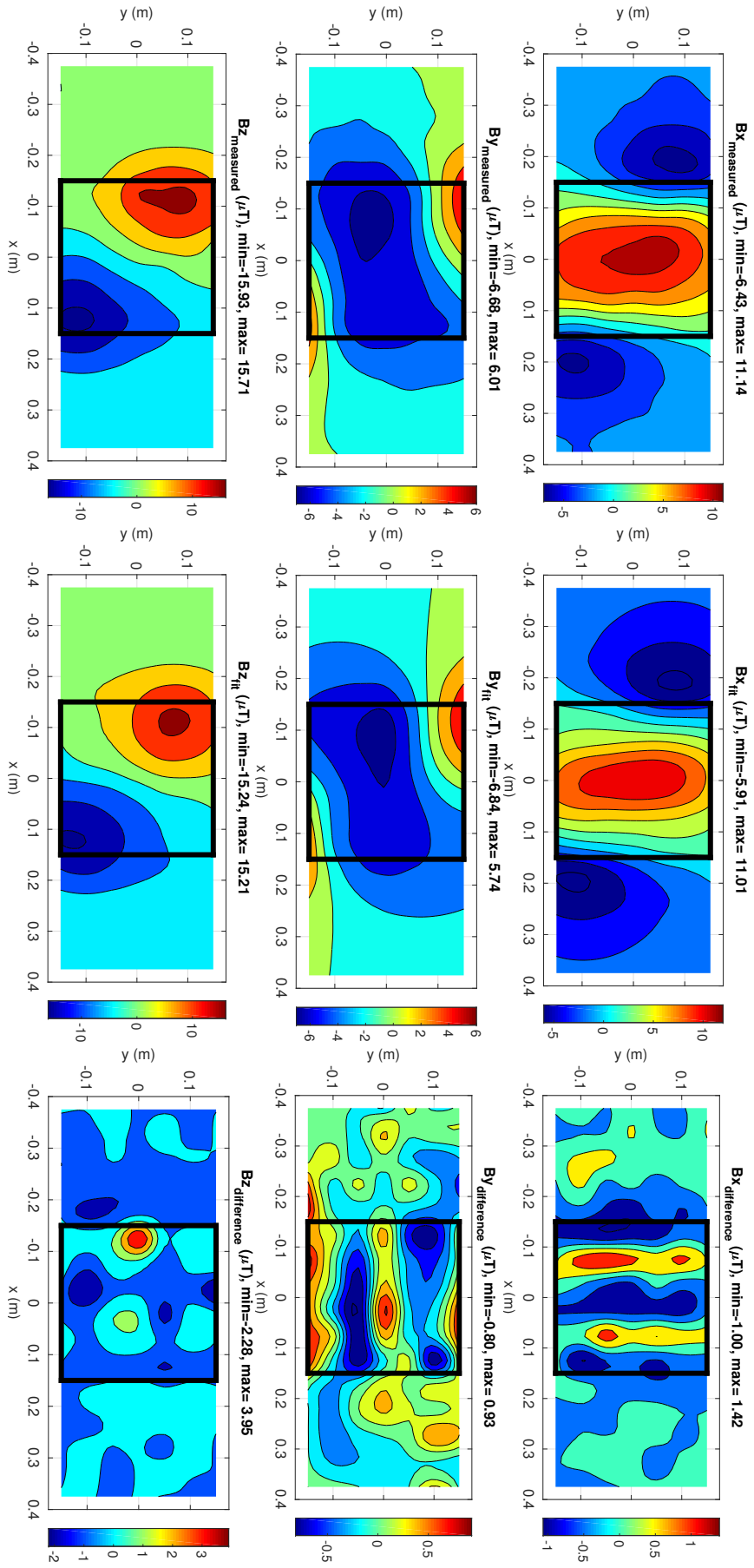

Figure 4.23: Measurement 2: B-field 1 (left), B-field corresponding with the calculated fit using f_4 (centre), difference between B_{measured} and B_{fit} (right).

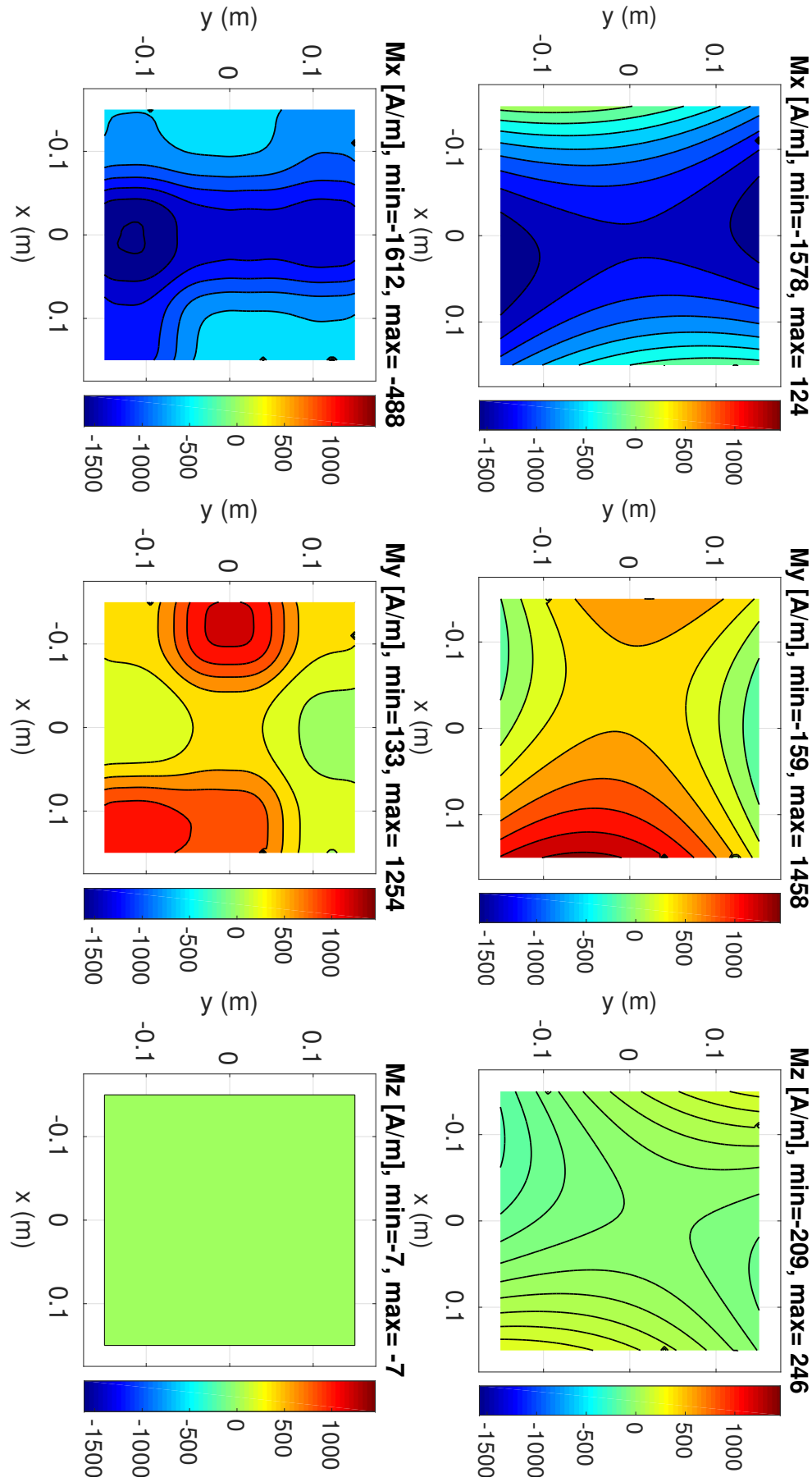

Figure 4.24: Measurement 2: M-distributions using f_1, see figure 4.22 (top) and using f_4, see figure 4.23 (bottom).

5

Hysteresis

5.1. Introduction

The origin of the word hysteresis traces back to the the ancient Greek *hysteros* which means 'later', 'second' or 'after', and was later incorporated in the English language as 'lagging behind' or 'shortcoming'. It was coined around 1890 by Sir James Alfred Ewing to describe the behaviour of magnetic materials [26]. Magnetic hysteresis implicates that magnetisation is not only a result of the applied background field at this moment, but also depends on the history of the magnetic background field that preceded this moment. This history-dependent aspect causes hysteresis to be an equally intriguing and complex phenomenon to describe.

While magnetic hysteresis has been studied extensively up until now, consensus in the academic world as to which model best describes magnetic hysteretic behaviour has not been reached. As mentioned above, this is mainly due to the overall complexity of describing hysteretic behaviour which takes into account the history of magnetic fields applied to the ferromagnetic material in order to be complete. Several models based on different assumptions have been made over the years, of which the Jiles-Atherton and Preisach models are well regarded as the most adequate modelling techniques to date. A preliminary analysis and comparison of these models was performed by Berkman [3]. A short summary of his comparison is provided in this section, as well as an explanation for why the model developed by Jiles & Atherton is the most suitable for this research project.

Magnetic hysteretic behaviour is dependent on many different material properties of the magnetisable material. Besides properties that describe the internal crystallogrpahic structure of the material, other properties such as temperature-dependence [28], frequency of alternating fields [25], and applied stress [5] are important. Since the scope of this project is about investigating hysteresis from a quasi static standpoint, with fields alternating at a relatively low frequency of 0.1 Hz, frequency dependence is not accounted for in the model. The same goes for temperature; it is known that magnetic materials demagnetise when the Curie temperature is reached, as described by Oguchi [41]. Since testing is performed at room temperature of around 293 K with negligible variations over time, temperature dependence is left out of the scope of this research as well. Stress-induced magnetisation, also known as the magneto-mechanical effect, will be studied separately in chapter 6.

In the previous chapter it was discovered that the distribution of the magnetisation was not uniform. This chapter aims to find the material parameters, for which the variance over the domain is described using the term *homogeneity*. It is assumed that the material parameters do not vary over the domain of the specimens, i.e. the test specimens are all homogeneous. The material is also assumed to be *isotropic* which implies that the material is rotationally independent and behaves similarly in all directions.

5.1.1. Jiles-Atherton

The theory by Jiles and Atherton (JA) [26] describes ferromagnetic hysteresis from a physical point of view by means of subdividing the materials into a finite amount of separate domains of microscopic size (10^{-4} - 10^{-6} m), see Coey [9]. Within each domain, the magnetisation is said to be orientated in a certain direction. When a background field is applied, the magnetisation within these individual domains rotate into a direction aligned with the background field. If the direction of the background field is changed, the magnetisation within the grains follow the direction of the background field. Domains that are aligned with the background field might increase in size due to the fact the the domain walls bend without permanently altering the size of the domains, see Subrahmanjam [48]. The magnetic orientation, as well as the position of the domain walls, return to their original states when the background field is removed. This is called *reversible magnetisation* and is shown schematically in figure 5.1.

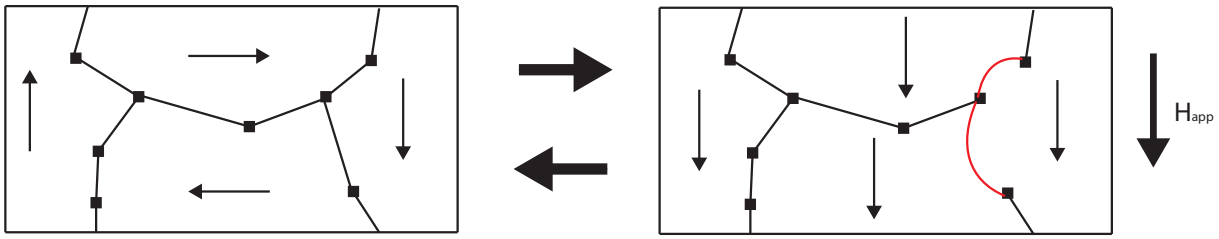

Figure 5.1: Reversible Magnetisation.

Besides changing orientation of the grains, it is also possible that the domains permanently deform under the applied magnetic field, with domains that are aligned with the background field increasing in size. This effect causes the boundaries and shapes of the grains to deform around the 'pinning sites'. Pinning sites can be seen as small anomalies in the material along which the edges of the domain walls are formed. Upon removing the background field, the domains remain deformed and hence this effect is known as *irreversible magnetisation*, see figure 5.2. Please note that these two effects are shown separately here for clarity, but in reality happen simultaneously. This section's explanation is derived from the paper by Melo [37].

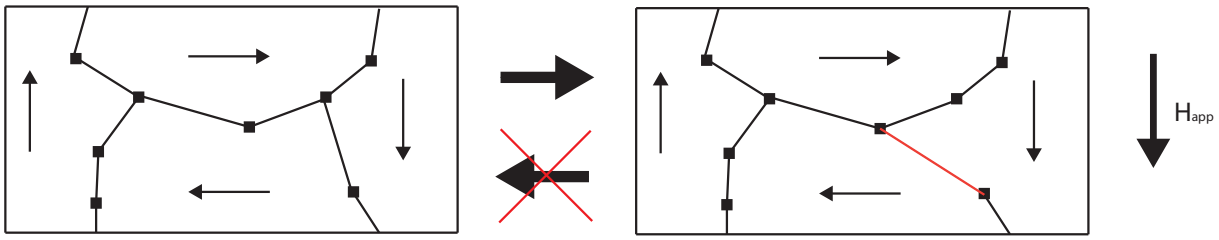

Figure 5.2: Irreversible magnetisation.

In a magnetic material without hysteresis, there is only fully reversible magnetisation, which is usually modelled with a relative permeability μ_r. A full hysteresis model includes a nonlinear relationship between the change in magnetic field **H**, magnetisation **M** and magnetic flux density **B**. Only a relationship between two of these three parameters must be found since it was seen in chapter 2 that the following relationship always holds:

$$\mathbf{B} = \mu_0(\mathbf{H} + \mathbf{M}) \, . \tag{5.1}$$

The prevalent way of visualising magnetic hysteresis is plotting the internal magnetic field **H** against the magnetisation **M**. While magnetisation and magnetic fields exist in three dimensions, for now only uniaxial hysteresis is considered. When the applied magnetic background field in x-direction is plotted on the x-axis and the magnetisation in x-direction on the y-axis a typical sigmoid-shaped curve is obtained as shown in figure 5.3.

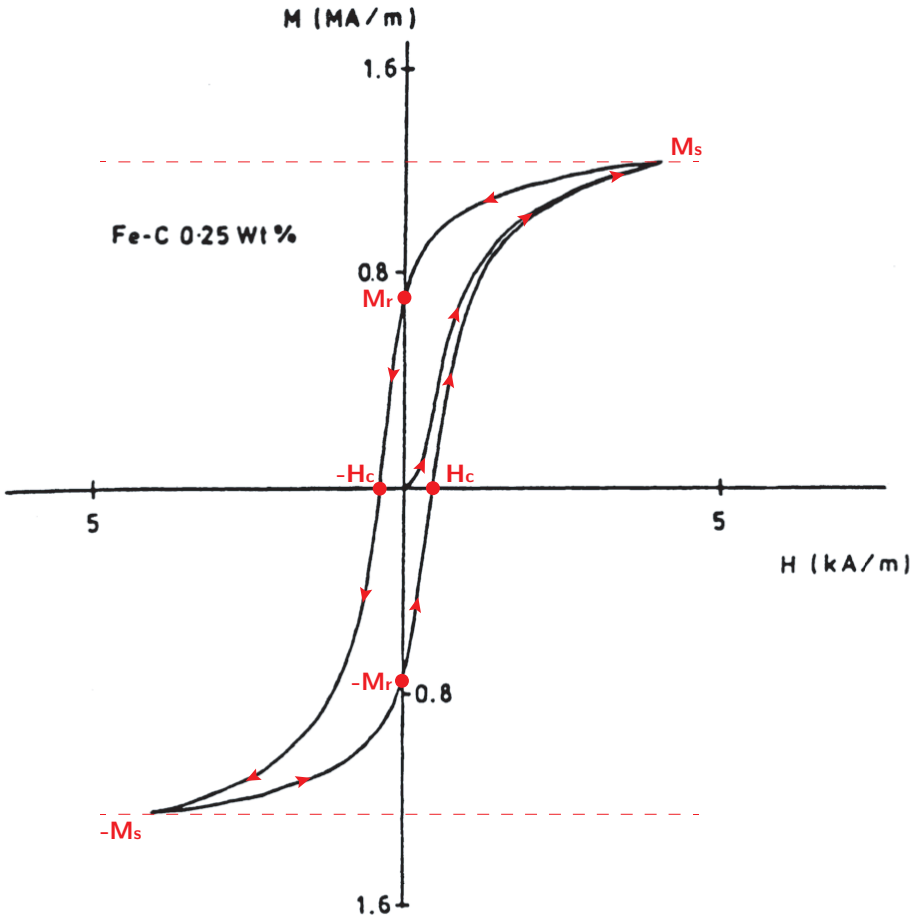

Figure 5.3: Major hysteresis loop of a specimen of iron containing 0.25% wt carbon, from Jiles [22].

Figure 5.3 shows a typical magnetic hysteresis curve for a ferromagnetic material that is subjected to strong magnetic fields. In this example a hysteretic material is chosen which has zero initial magnetisation. As the applied magnetic field H_a increases, the magnetisation increases nonlinearly in the same direction, rapidly at first, and slower as H_x increases. For large H_x, asymptotical behaviour is observed. The magnetisation corresponding to these H-values is known as the saturation magnetisation M_s which is one of the parameters in the JA-model. The physical interpretation of this parameter is that all of the separate domains have been rotated in alignment with the background field and further amplification of the background field will not cause more changes in the domain wall structure. An additional increase of the background field strength will therefore not change the magnetic orientation of the domains causing the material to reach a certain saturation level. When the external field is reduced, the magnetisation decreases less rapidly than the H-field is dropping since the pinning sites prevent deformation into its original shape, resulting in a remnant magnetisation M_r when H_a = 0. In order to return the material to zero magnetisation, a magnetic field in the opposite direction is required which is called the coercive force H_c. When the field is further reduced the material again reaches saturation but now in the opposite direction. From there on the process repeats itself, revealing another remnant magnetisation and coercive force at mirrored locations. Such a loop, in which the material reaches saturation level on sides of the H-spectrum is called a major loop. Major loops are always symmetrical with respect to the origin, and for a certain ferromagnetic object only one major loop exists.

It is important to note that major loops occur under very strong applied magnetic fields in the order of 1-2 T, which is comparable with the strength of magnetic fields used in medical MRI scans. The field strengths that will be applied during this research project are of a much smaller magnitude of around 400 µT. This means that magnetic saturation will not occur, which alters the shape of the hysteresis curve. If a weaker field is applied, different curves may appear. These curves can have many shapes depending on material

parameters, starting magnetisation and applied field range, but always lie between the ascending and descending branches of the major loop from figure 5.3. In figure 5.4, some possible minor loops for an arbitrary material are displayed. Figure 5.4 is a good example of how a certain material can have an infinite amount of minor loops depending on the starting magnetisation and applied background field. This shows how for a certain known background field the material can exhibit any magnetisation in a vertical line between the ascending and the descending branch of the major loop of the hysteresis curve.

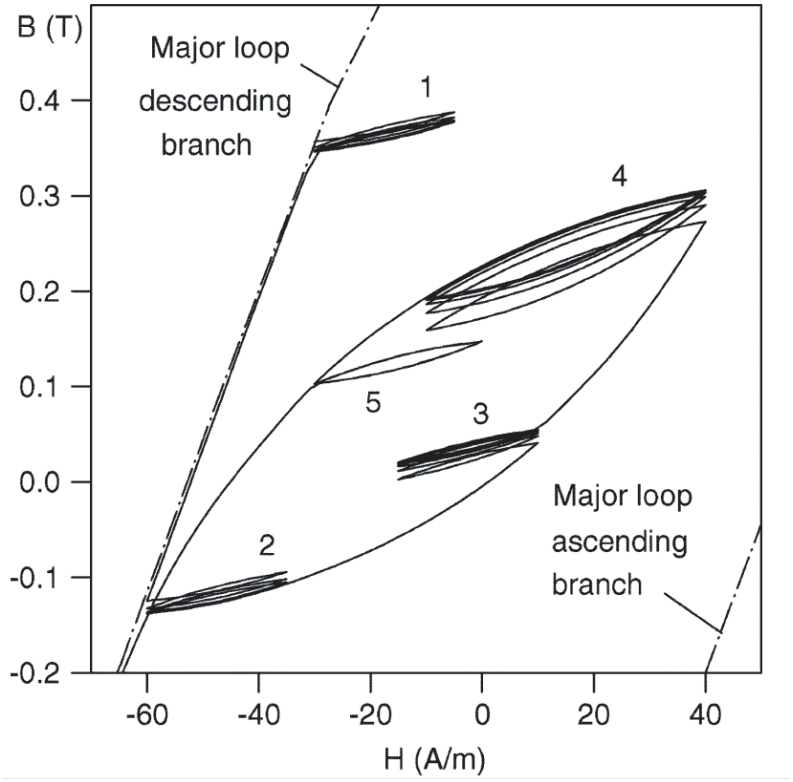

Figure 5.4: Minor hysteresis loops, from Zirka [62].

The magnitude of hysteresis, or the amount of energy dissipated with each loop, can be related to the area under the curve of the hysteresis loop. When a material is not hysteretic, but does get magnetised under an external field, the graph would take the shape of a line crossing the (0,0) intersection in both directions thus having zero residual magnetisation or coercive force. In terms of mathematical formulation, the anhysteretic curve M_{an} was derived by Cullity and Graham [11]. The original Langevin function is given by:

$$M_{an}(H_a) = M_s\left(\coth\left(\frac{H_a}{a}\right) - \frac{a}{H_a}\right) \tag{5.2}$$

in which $a = k_B T/m$, k_B is Boltzmann's constant, T is the temperature in Kelvin, m the magnitude of the magnetic dipole in the material, and H_a the applied field. The magnetic dipole moment m can be seen as the net magnetic moment of a certain domain. If a domain is bound by the volume V the dipole moment is given by

$$\mathbf{m} = \iiint_V \mathbf{M}(\mathbf{r}')\, dV \tag{5.3}$$

where the triple integral denotes integration over the entire volume of the domain. The Langevin approach assumes no interaction between the individual magnetic moments in the material, accounting only for

changes due to the applied field and thermal agitation. For ferromagnetic materials this approach is no longer suitable. There is a strong interaction between the domains, especially at room temperature. In order to account for these, Weiss developed the concept of the mean field H_m [59]. He suggested that a fictitious internal field H_m exists within the material that is directly related to the magnetisation M, which, in turn, also adds to H_a. The resulting field H_r is then given by

$$H_r = H_a + H_m = H_a + \alpha M(H_a) \, . \tag{5.4}$$

This H_r then replaces the original H_a in equation (5.2), resulting in the modified Langevin expression

$$M_{an}(H_a) = M_s \left(\coth\left(\frac{H_a + \alpha M(H_a)}{k_B T} \right) - \frac{k_B T}{H_a + \alpha M(H_a)} \right) \, . \tag{5.5}$$

This describes the saturation of the material, but not the hysteresis as this still only accounts for the reversible part of the magnetisation, i.e. domain rotation. Irreversible magnetic phenomena, like domain wall bending, are not included, and it was concluded earlier that it is due to these specific irreversible aspects that hysteresis occurs. The expression used to model hysteresis eventually follows from an energy equilibrium condition between the magnetic energy supplied by an external source (M_s) the change in stored magnetostatic energy (A) and the hysteresis loss (B) which is directly related to the irreversible magnetisation M_{irr}, as described by Jiles [26]. This energy relation is given by:

$$\mu_0 \int M_{an} \cdot dH_r = \underbrace{\mu_0 \int M \, dH_r}_{\text{A}} + \underbrace{\mu_0 k(1-c) \int \delta \frac{dM_{irr}}{dH_r} \, dH_r}_{\text{B}} \, . \tag{5.6}$$

In this equation k is the pinning parameter, which is related to the energy dissipated due to hysteresis, i.e. the average amount of energy that is required to 'break' a pinning site. The δ makes sure that the energy dissipated is always positive, ensuring that hysteresis is always paired with a loss of energy i.e. $\frac{dM_{irr}}{dH_r} > 0$. The coefficient c depicts a measure of the reversible change in magnetisation which lies between 0 and 1. If c = 0, the magnetisation change is irreversible, and for c = 1 the change in magnetisation is fully reversible. From equation (5.6) it can be seen that energy losses only occur due to irreversible magnetisation changes. Considering that the magnetisation consists of

$$M = M_{rev} + M_{irr} \tag{5.7}$$

both eq (5.6) and eq (5.7) can be rewritten, see Melo [37]:

$$M_{an} = M_{rev} + M_{irr} + k(1-c)\delta \frac{dM_{irr}}{dH_r} \, . \tag{5.8}$$

If the entire process is irreversible, c = 0 and $M_{rev} = 0$, the irreversible magnetisation can be written as

$$M_{an} = M_{rev} + M_{irr} + (1-c)(M_{an} - M_{irr}) \, . \tag{5.9}$$

which can be rewritten as

$$M_{rev} = c(M_{an} - M_{irr}) \, . \tag{5.10}$$

Combining these expressions, an overall rate of change in magnetisation with the applied field can be expressed as

$$\frac{dM}{dH_a} = \frac{ck\delta \cdot dM_{an}/dH_a + (M_{an} - M)}{k\delta - \alpha(M_{an} - M)} \tag{5.11}$$

see Vijn [56]. Equation (5.11) is shaped as a displacement from the original anhysteretic curve. This equation models the magnetic hysteretic behaviour in the JA-model. Together with the original Langevin expression this model has five parameters that are summarised below.

- a, domain wall density [A/m];
- α, interdomain coupling [-];
- c, reversibility of the change in magnetisation [-];
- k, domain wall pinning parameter [A/m];
- M_s, saturation magnetisation [A/m].

There is plenty of discussion on this model due to the fact that it does not correctly incorporate the first law of thermodynamics [63], and due to the employment of non-physical considerations such as the δ which ensures that the hysteresis is a phenomenon which consistently dissipates energy. Even so, the Jiles-Atherton model has shown to represent major hysteresis loops very accurately. For minor loops however, behaviour is observed that does not always coincide with measurements. Modifications have to be made in order for minor loops to be properly represented by the JA-model. The issue at hand is the fact that minor loops in the original JA model do not close properly. Minor loop closure dictates that, when the background field is varied at a constant amplitude, after a few loops the change in magnetisation keeps following the same path, i.e. the M-loops are identical to each other, see Zirka [62]. Without modifications to the original JA-model this is not accounted for properly, which means that the magnetisation changes with every loop iteration. The foregoing does not coincide with real-world measurements.

In figure 5.5 two minor loops are shown. The left-hand side shows a minor loop which closes at the top. This coincides with real-world measurements that invariably show that, after a number of cycles, hysteresis loops stabilise when the amplitude of the background field variation is kept constant. The figure on the right-hand side shows a non-closing minor loop which is the result of a flaw in the Jiles-Atherton model when describing hysteresis in small minor loops. It can be clearly seen that for multiple loop cycles the minor loop on the right-hand side starts to run-off to the right which is an unwanted effect known as *accommodation* which is further described by Zirka [62]. For the figure on the left it can be seen that, since the loop is closed, any new full loop will be identical to the previous loop.

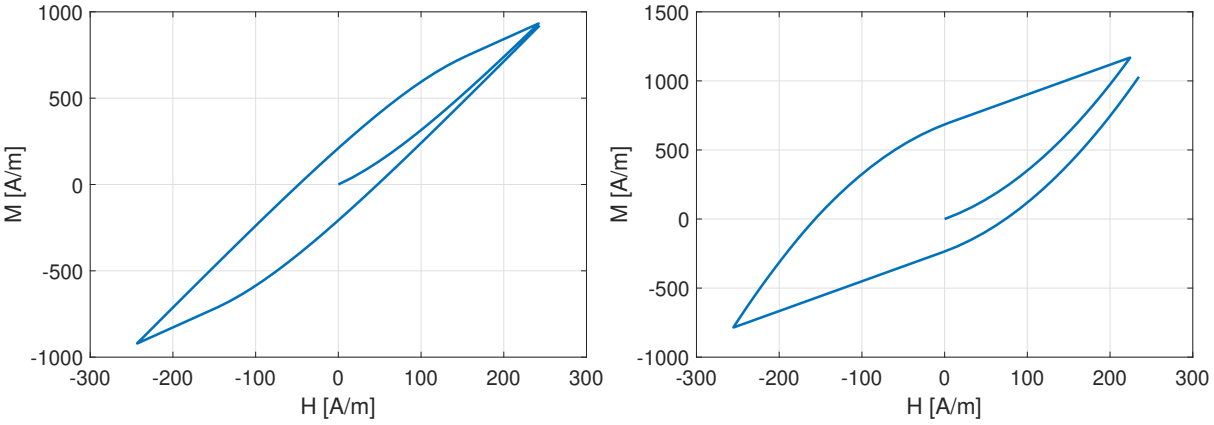

Figure 5.5: Closed minor loop (left), non-closing minor loop (right).

Modifications to the JA model that prevent this run-off of minor loops are more thoroughly discussed by Carpenter, Chwastek and Leite [7][8][32]. The latter suggests an introduction of an additional dissipative factor in the description for the irreversible magnetisation which is implemented by Vijn [56]. In short, the dissipative factor R is introduced in the description for the irreversible magnetisation

$$dM_{irr} = \frac{1}{k\delta}\left[(M_{an} - RM_{irr})dH_e\right]^+ . \tag{5.12}$$

Note that for $R = 1$, the extended model coincides with the original JA model. Two factors are important to keep in mind when introducing this factor:

1. The loop has to be approximately symmetric with respect to the magnetisation (the internal H-field changes sign approximately halfway);
2. The parameter R is a function of the *turning point* of the loop, so it is not a single value.

If a parameter γ is defined as a function of both R and c

$$\gamma(c,R) = 1 + c(R-1) \tag{5.13}$$

the relation for the rate of change in magnetisation with the applied field, equation (5.11) becomes:

$$\frac{dM}{dH_a} = \frac{ck\delta \cdot dM_{an}/dH_a + (\gamma M_{an} - RM)}{k\delta - \alpha(\gamma M_{an} - RM)} \,. \tag{5.14}$$

5.1.2. Preisach

The model developed by Preisach in 1935 [43] can be used to describe any hysteretic effect, including magnetic hysteresis, without considering the physical mechanics behind it. For magnetic hysteresis, a material that is subjected to a unidirectional magnetic field $H(t)$ is subdivided into a large set of identical small dipoles called hysterons. These hysterons can be either positively or negatively magnetised ($\pm m_s$, with the same absolute magnitude for all dipoles). For each hysteron, two threshold levels α and β are defined. α corresponds to the background field that is required in order to flip the magnetisation within the hysteron from $-m_s$ to $+m_s$, and β is the threshold level that must be reached in order to do the reverse. These boundaries only have a meaning when they are approached from a certain direction. This means that if a hysteron already exhibits a positive magnetisation $+m_s$, crossing the α boundary has no effect on the dipoles' magnetisation. The same applies for β if the hysteron already exhibits negative magnetisation. This is best described in figure 5.6. It's important to note that because of this definition $\alpha > \beta$. If $H > \alpha$ the hysteron is positively charged, if $H < \beta$ the hysteron has a negative magnetisation, and if $\beta < H < \alpha$, the magnetisation of the hysteron depends on the history of the path taken, i.e. the history of the background field. This is how the memory aspect of hsyteresis is being accounted for in the Preisach model. Each individual hysteron is then multiplied with the Preisach function $p(\alpha,\beta)$, which is a hysteron weight function which has specific characteristic for different materials. The general formula which calculates the magnetisation is defined as

$$M(t) = \int_{-\infty}^{+\infty} d\alpha \int_{-\infty}^{\alpha} p(\alpha,\beta) f_{\alpha,\beta}(H(t))\, d\beta \,. \tag{5.15}$$

A schematic representation of this formula is given in figure 5.6.

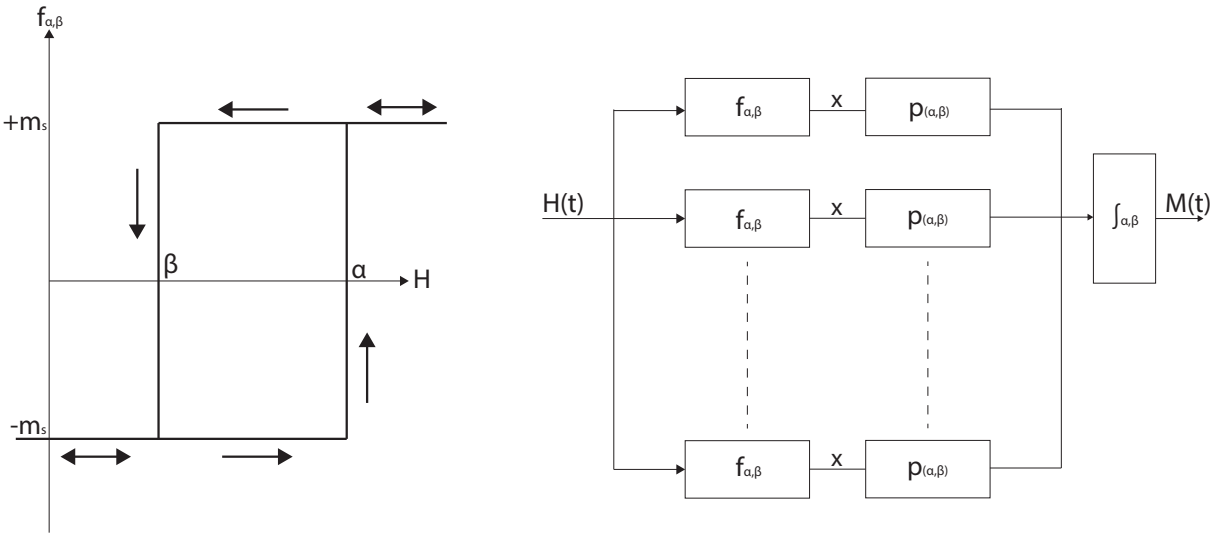

Figure 5.6: Preisach Hysteron and a schematic representation of the Preisach model, from Melo [37].

The mathematical structure of the Preisach model has two fundamental properties:

- *Wiping-Out property*: this is related to the memory process. The sequence of local maximum and minimum values of $H(t)$ can be redundant, since Preisach only stores the dominant extreme values of $H(t)$. All local maxima and minima between these extreme values are erased from the memory;
- *Congruency property*: this addresses the creation of minor loops due to periodic field variations. If two different external fields $H_a(t)$ and $H_b(t)$ are considered to cycle between two values H_1 and H_2 for $t > t_c$, they would both create similar-shaped loops. However, these loops will lie on a different position in the M-H plane if the history of these fields was different for $H_a(t)$ and $H_b(t)$ when $t < t_c$. They will then be shifted along the M-axis (up or down in figure 5.4).

These properties are essential for modelling this physical process with the Preisach formulation. However, the correlation between parameters and the magnetisation process is not always clear as described by Visintin [58]. On top of that, a complex parameter identification is demanded in order to find the correct Preisach weight function which comes with a heavy computational burden. For the purpose of this research, it is important to note that an accurate history of the applied background field is required. Therefore, the Preisach model is very hard to implement in this project. The Jiles-Atherton model also has the benefit that it can be easily extended to account for a stress induced magnetisation component. For these reasons, the Jiles-Atherton model is implemented together with some modifications in order to correctly represent the minor loops that will be measured in experiments.

5.1.3. Approach

In this chapter an attempt is made to find the Jiles-Atherton parameters that describe minor-loop hysteresis in structural steel specimens. When observing a minor hysteresis loop, it is possible to point out five key points of interest which are given by the time instants $t1, t2 \ldots t5$ in figure 5.7.

Time instant	$B_{\text{background}}$	M_x
$t1$	0	$-M_r$
$t2$	$+B_{\text{amplitude}}$	$+M_{\text{max}}$
$t3$	0	$+M_r$
$t4$	$-B_{\text{amplitude}}$	$-M_{\text{max}}$
$t5$	0	$-M_r$

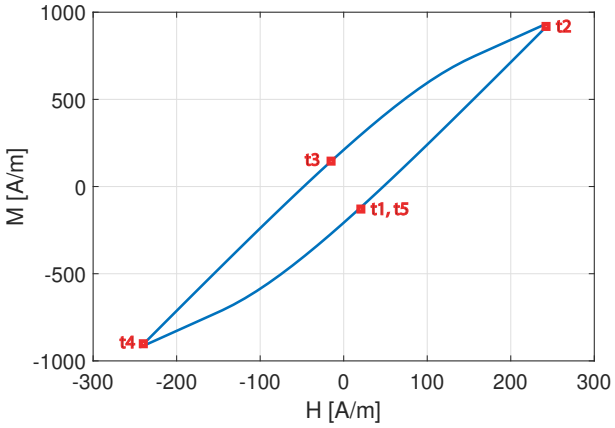

Figure 5.7: Time instants.

The starting point of the loop is taken as the remnant magnetisation on the ascending branch $-M_r$, which is given by $t1$ in figure 5.7. The fact that $t1$ does not lie on the origin implies that the material exhibits a certain starting magnetisation M_0, for which a description was provided in chapter 4. The first turning point of the loop is at $t2$ where the background field, internal field, and the magnetisation find their maximum value. The time instant $t3$ (halfway the loop) yields the remnant magnetisation on the descending branch $+M_r$. At $t4$, the background field and the magnetisation find their minimum after which at $t5$ one re-obtains the remnant magnetisation on the ascending branch $-M_r$. Please note that in figure 5.7 the time instants $t1$, $t3$ and $t5$ are not located exactly on the y-axis. This would be the case when the x-axis depicts the applied background field. In figure the internal total H-field is shown on the x-axis as is common for hysteresis curves. It is known that when an object exhibits a magnetisation in a certain direction, in this case the remnant magnetisation, this is accompanied with an internal magnetic field which points in the opposite direction, as described in chapter 2.

An example of hysteresis measured using the sensor array is given in figure 5.8. This figure shows the B_x-field 71 mm below a metal plate (300×300×5 mm) subjected to a sinusoidally varying background

field with an amplitude of $B_{x,\max}$ = 400 µT at the time instants from figure 5.7. Please note that in these figures the applied background field, shown in the title with B_a, is subtracted from the total measurement. The black lines represent the edges of the square steel specimen.

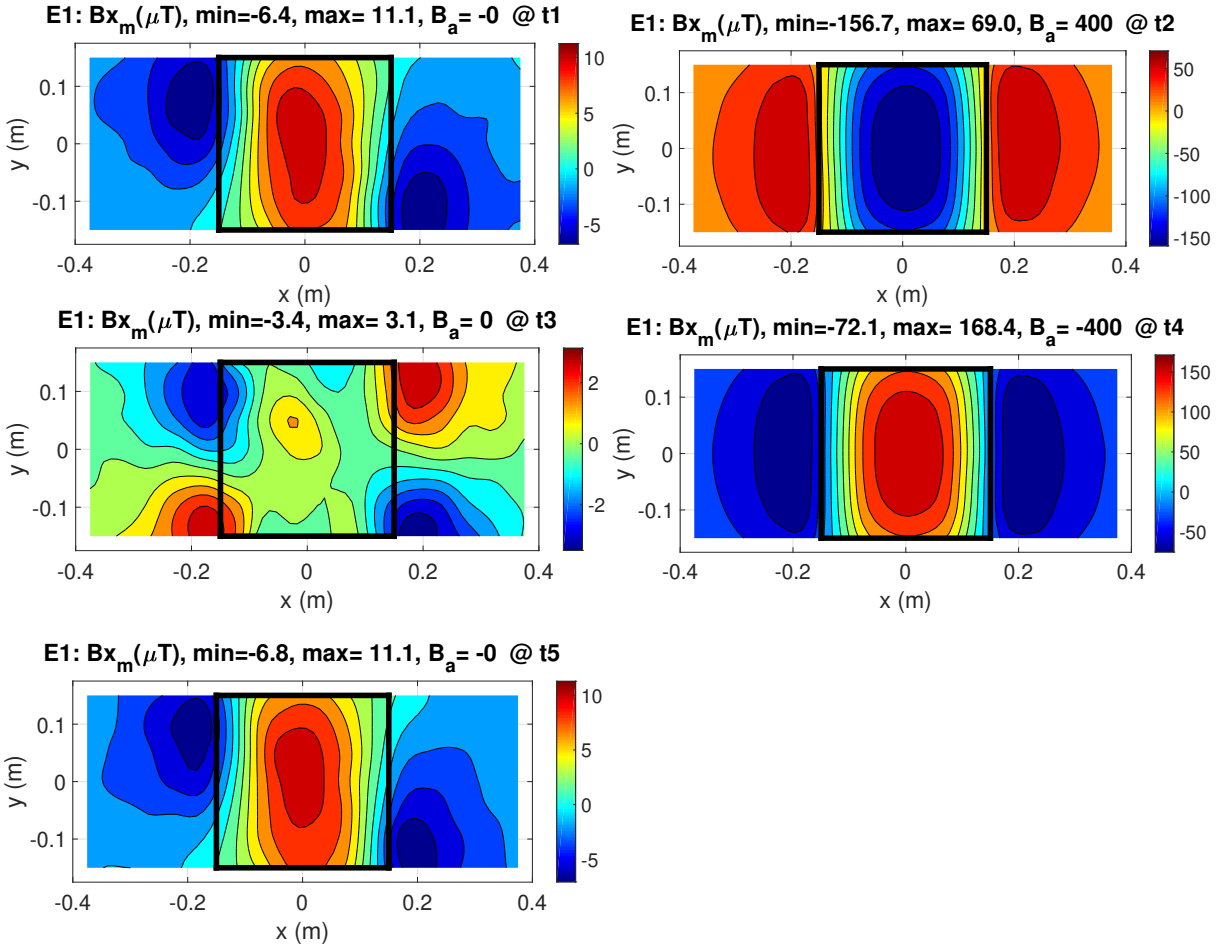

Figure 5.8: Magnetic induction field below a metal plate (300×300×5 mm) subjected to a varying background field with an amplitude of 400 µT at the time instants from figure 5.7.

The hysteretic effect is represented by the difference between the B_x-field at the first, third and fifth time instant. The background field at these instants is zero, but $t3$ is clearly different from $t1$ and $t5$. When pointing back at figure 5.7 this makes sense since the Magnetisation at $t1$ and $t5$ coincide with the remnant magnetisation on the ascending branch of the hysteresis curve. The measurement at $t3$ shows the remnant magnetisation on the descending branch. Looking at figure 5.7 this implies that the specimen inhabits a more positive, or less negative, M_x at $t3$ than at $t1$ and $t5$.

The B-field at $t1$ and $t5$ shows large similarity with the inverse of figure 2.11, which implies that the specimen exhibits a possible negative magnetisation in x-direction. Following that analogy, the B-field at $t3$ shows the B-field below a plate which is less negatively magnetised in x-direction than at $t1$ and $t5$, which corresponds with figure 5.7. When the background field has its extreme values at $t2$ and $t4$ in figure 5.8, the field of a uniformly magnetised plate in x-direction appears, resembling great similarity with figure 2.11. This shows that the effect of the initial magnetisation almost disappears when the background field is strong, and the induced component of the magnetisation is dominant. Even so, it can be seen that $t2$ and $t4$ are still slightly skewed with respect to the symmetry axis at $x = 0$ due to the non-uniform initial magnetisation. Figure 5.8 shows the two-dimensional B_x fields below a metal plate at $t1, t2 \ldots t5$ for one full hysteresis loop. Increasing the size of the measured dataset subsequently increases the chance of finding a good fit of the Jiles-Atherton parameters. Therefore, each test specimen was subjected to multiple symmetrical hysteresis loops of different loop amplitudes. In this project this was done using

four loops with $B_{\text{amplitude}}$ of 100, 200, 300 and 400 µT. Using a numerical model in combination with a parameter optimisation tool, an attempt is made to recreate the measured hysteresis loop through forward modelling using many different sets of Jiles-Atherton parameters until a proper fit is obtained, which is a technique known as forward modelling.

5.2. Forward implementation in COMSOL

This section aims to explain how the theory from section 5.1 is implemented in COMSOL, since this is the software that will be used to model a plate which is subjected to a varying background field. When following the main storyline of this report, it will not be essential to read or understand the following section completely. It may however serve as a guideline for anyone who wishes to replicate the results through the use of FEM software. The most convenient way to follow this section is by reading the methodology below while simultaneously having the model *JA_Model_Plate.mph* open in COMSOL.

5.2.1. Model builder setup

Within COMSOL the ”AC/DC” module is used in combination with a stationary study, which implies that the physics do not include time-derivative components (since the effects are assumed to be quasi-static). The geometry consists of a square air box with sides of 3 m and its centre at (0,0,0), another box which represents a metal plate 300×300×5 mm) with its centre at (0,0,0) and a rectangular plane which represents the sensor array, at a certain z-distance from the plate (which is the distance between the centre of the test specimen and the array, in this case 71 mm). The air domain and the metal plate are shown in the top left and right of figure 5.9. The rectangular shaped plane is shown on the bottom left of figure 5.9 and the resulting combined geometry on the bottom right-hand side.

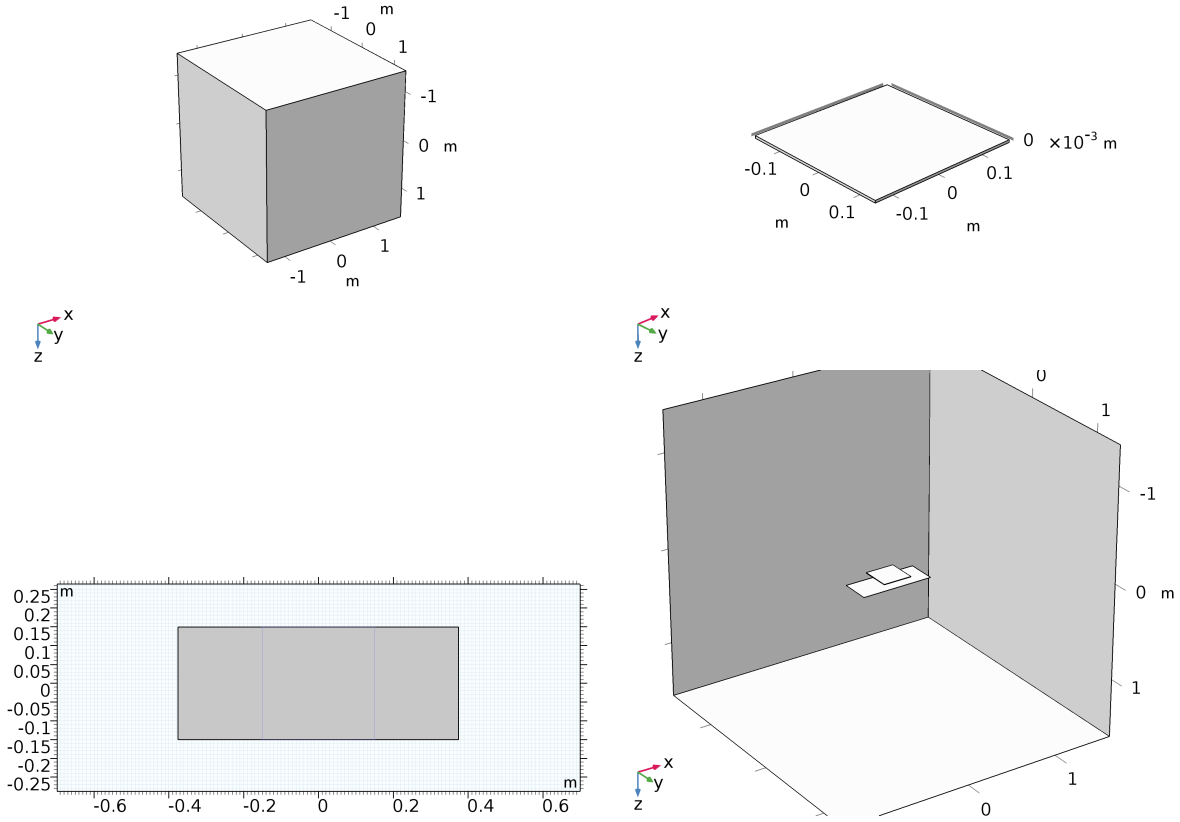

Figure 5.9: Air domain (top left), plate domain (top right), rectangular plane (bottom left), resulting combined geometry (bottom right).

5.2.2. Physics

The ”Magnetic Fields, No Currents” package is used (see chapter 2). For the air domain, the relative permeability is defined as the domain where $\mu_r = 1$. Regarding the Jiles-Atherton model the following nodes in COMSOL are of importance:

1. JA Variables;
2. JA Parameters;
3. Langevin function;
4. Weak form PDE M;
5. Weak form PDE B;
6. JA model (within the ”Magnetic Fields, No Currents” interface).

Within the *Equation View* of the *JA Model* node, the original B-components are replaced with the dependent variables $B1$, $B2$, and $B3$. These dependent variables, together with the dependent variables $M1$, $M2$ and $M3$ refer to the weak form partial differential equations that are defined on the domain of the plate which describe the relations for B and M that hold within the hysteretic domain. These dependent variables, together with the *JA Variables* and *JA Parameters* nodes provide an implementation of the Jiles-Atherton model with full access to all of the expressions used to calculate the hysteresis. This is unique since COMSOL originally provided a basic hysteresis model in which the Jiles-Atherton expressions were inaccessible and therefore locked. In this modified version, each of the expressions from section 5.1 are accessable and alterable. These alterations include the previously discussed minor loop closing parameter R and a possible stress induced component of the magnetisation. For this project, an isotropic material is assumed for which the parameters in xyz-directions are all identical. However, the model does provide the ability to vary the JA-parameters per direction. The local variables section uses local parameters to calculate the Jiles-Atherton equations (5.4-5.11). An analytical expression for the Langevin function (5.2) is programmed separately which is being called upon from within the JA variables section.

Finally, a scalar potential is defined on the edges of the air domain:

$$V_{m0} = -x\frac{B}{\mu_0}\sin(2\pi t)\ . \tag{5.16}$$

With the relation between the scalar potential and the magnetic field given by

$$\mathbf{H} = -\nabla V_{m0} \tag{5.17}$$

through which the background field is varied sinusoidally in x-direction with an amplitude of B Tesla and a period of 1 second.

5.2.3. Mesh and results

The plate is meshed by creating a mapped two-dimensional grid mesh using a fixed element size on the surface of the plate, and sweeping the mesh with one element over the thickness. On the left of figure 5.10 this is shown for a 300×300×5 mm plate with a mapped mesh of 10×10 mm grid size. The same mapped grid is used for the plane which resembles the sensor array in order to obtain an accurate solution in the region which is of interest. The remaining three-dimensional air domain is meshed using free tetrahedral elements set to a predefined size named ”Extra Coarse” which entails that element edges grow with a maximum growth rate of 85% to a minimum size of 162 mm.

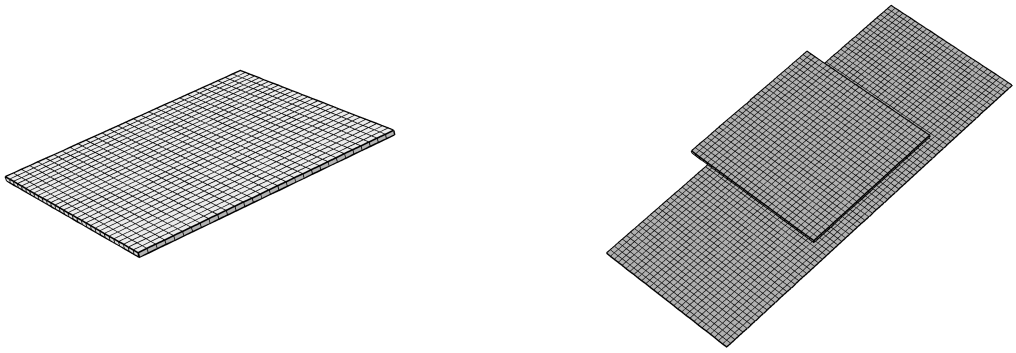

Figure 5.10: Meshed plate (left), Meshed plate and plane (right).

It is important to note that mesh size is of great influence on both the accuracy of the results as well as the computation time. In figure 5.10 a grid size of 10×10 mm is adopted for both the plate and the plane, which is the size that was used during the optimisation process described in section 5.3. If accuracy does not have the highest priority one could change the mesh to a 25×25 mm grid for both the plate and the plane. This reduces computation time by roughly 80%. For final comparisons with actual measurements, the opposite can be done by refining the grid to a 5×5 mm mesh for accurate results, which was was done for the figures in section 5.4. The results are exported at the time instants from figure 5.7. At these tinstants, the following results are exported:

- The B-field in the finely meshed plane below the plate (the xyz-components each in a separate column) at the coordinates which coincide with the sensor array locations (see appendix B.2.1) in order to provide a comparison with measurements;
- The M_x-distribution within the plate.

For examples of these exported datasets, please refer to the results in section 5.4

5.3. Inverse modelling

5.3.1. General model structure

In the previous section a forward COMSOL model was introduced which is capable of capturing hysteresis by placing a metal plate coupled with a Jiles-Atherton hysteresis model in an air domain and varying the background field. The results of this hysteresis loop, the magnetisation distribution and the magnetic induction field at a distance below the plate, are then exported at different time instants in the hysteresis curve. This process is then repeated until a proper fit with the measured dataset is obtained.

These calculated B-fields can be compared with real-world measurements of plate samples that are tested within the Helmholtz cage. The optimal combination of JA parameters used in the COMSOL model reproduces a set of induction field measurements that fits with the measured data. This section outlines the complete procedure, which also implements the non-uniform magnetisation description from chapter 4. A schematic overview of the model is presented in figure 5.11. During initialisation, the measured dataset is loaded and the appropriate non-uniform magnetisation distribution is created that produces the correct B-field at $t1$ as discussed in chapter 4. This chapter will focus on finding the right parameters to describe hysteresis, which is given by the optimisation box in figure 5.11. This is done by defining an objective function which should in an ideal situation, a perfect fit, become zero. A perfect fit means in this case that the output of the model returns the same B-fields as were measured in, for example, figure 5.8. The method of finding the right parameters is then performed by the *shuffled frog leaping algorithm* or SFLA. These two elements are discussed separately in the sections below.

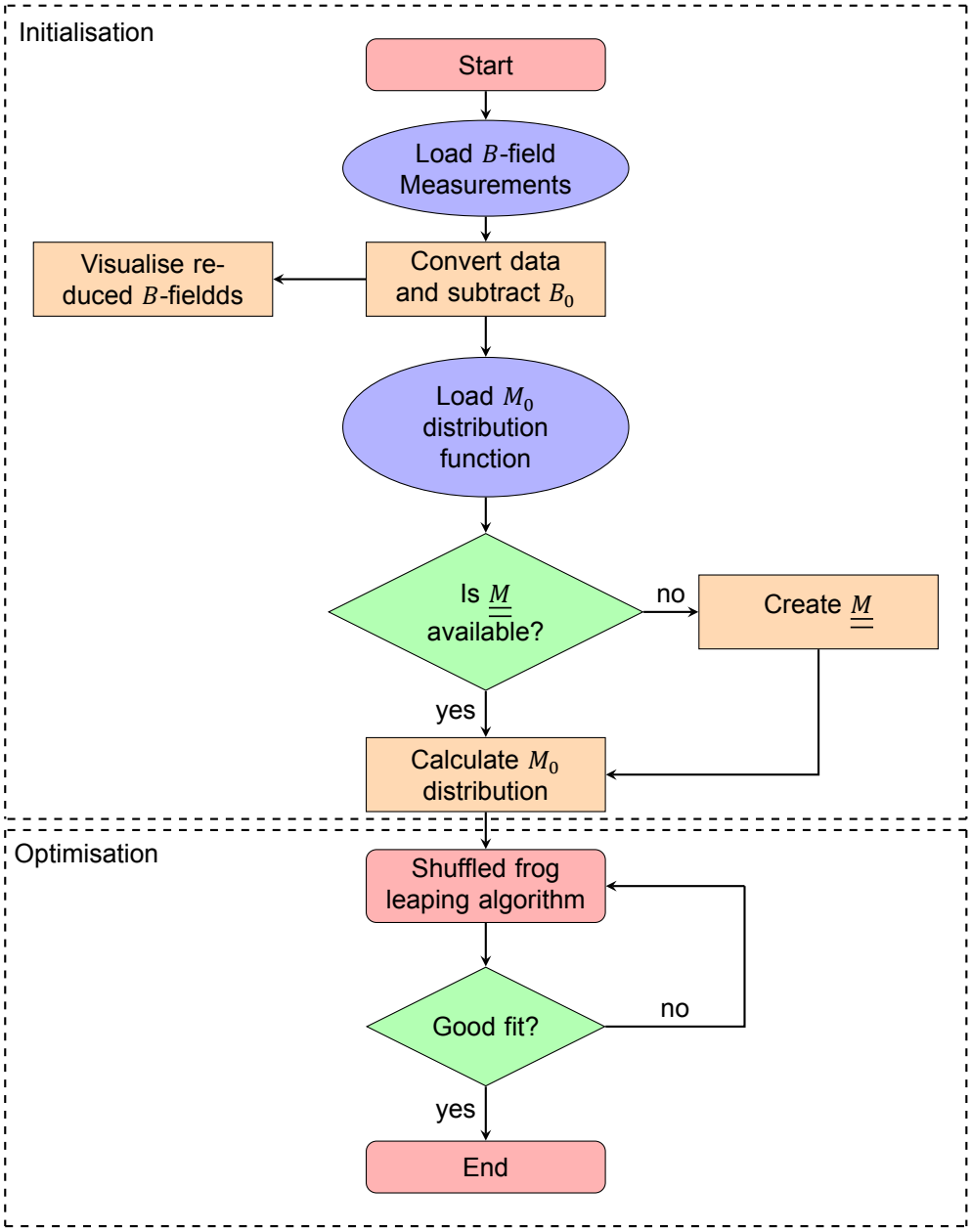

Figure 5.11: Algorithm flowchart (B_0 = background field, M_0 = initial magnetisation distribution, $\underline{\underline{M}}$ = parameter sensitivity matrix).

5.3.2. The objective function

As the optimisation algorithm aims to find a combination of parameters that makes an objective function zero, this function needs to be constructed appropriately. The procedure of the objective function which is used to calculate the fit between the measured and the calculated hysteresis data is visualised in a flowchart in figure 5.12. Initially the measured dataset should be examined. As mentioned before, multiple hysteresis loops were measured for a certain test specimen for varying background field amplitudes. The amount of different loop amplitudes, $i_{\max} = 4$ during these experiments. For each loop size there is a set of B_x, B_y and B_z-fields at the time intervals $t1, t2 \ldots t5$ that acts as the target data for the objective function.

The arguments of the objective function are:

- The M_0 distribution parameters for each i;
- A set of JA parameters S;

- A separate R for each loop i;
- The amplitudes of the background field B_a for each loop i;

for

- i_1 = 100 µT background induction field amplitude;
- i_2 = 200 µT background induction field amplitude;
- i_3 = 300 µT background induction field amplitude;
- i_4 = 400 µT background induction field amplitude.

It is important to note that, when optimising this function, the arguments that vary for each objective function evaluation are the Jiles-Atherton parameters in S and the dissipative factors R. The initial M_0 and loop amplitudes are both known values after the algorithm initialization and therefore do not change during the iterative procedure.

The COMSOL file from section 5.2 is saved as a MATLAB m-file, which means that it can be called as a function from within MATLAB. The function returns a text file with the B-field at $t1, t2 \dots t5$ for a certain combination of JA-R parameters (S,R). On the first call, it runs the hysteresis loop for the first amplitude of the background field (B_1) in combination with the magnetisation distribution of the first loop at ($M_{0,1}$) and the corresponding dissipative factor (R_1). Since the combination of JA-R parameters is chosen by the optimisation algorithm, it is beforehand unknown what the result of the computation in COMSOL will yield. Occasionally a combination of parameters is chosen, within the pre-defined boundaries of the possible JA-R values, for which the solver does not converge. When this occurs the function *JA_model.mph* returns an error within this script. If this happens, the objective function returns an infinite value for the fit and the computation is stopped. This sends a message to the SFLA algorithm that the parameters should be sought in a different combination.

Another unwanted event which sporadically occurs is that the COMSOL function takes extraordinarily long to find a solution. When the function goes through trouble finding a solution it reduces the size of the timestep, since the model uses free time-stepping. This can lead to tedious computations without returning an error. For this reason, a *stop condition* is added to the COMSOL model which quits the computation early when the timestep becames smaller than 10^{-5}s. If this happens, the computation is cancelled before the full hysteresis loop is completed. This is an unwanted event since it shows that the solver has too much trouble finding a solution for the full hysteresis loop. To check if this is the case, the size of the output is investigated. If the output does not contain the $B_{x,y,z}$ values for all five time intervals, but fewer, the fit value is set to infinite and the objective function is aborted similarly to when a convergence error occurs. Upon completion the relative error between the output solution and the measurements is calculated at $t2$ using the expression

$$\eta_{\text{rel},i,t2} = \frac{\sum_{j=1}^{N} \left| B_{\text{measured},t2,j} - B_{\text{computed},t2,j} \right|}{\sum_{j=1}^{N} \left| B_{\text{measured},t2,j} \right|} . \tag{5.18}$$

This is repeated for $t3$, $t4$ and $t5$. The error in $t1$ is not used as a measure for finding the optimal fit since this was already done during the non-uniform mangetisation description in chapter 4 and captured in the parameter set $M_{0,i}$, which obviously does not change for different JA parameters. The relative error at each time interval $t2, t3 \dots t5$ is calculated separately in order to make sure that the fitting algorithm treats each of the time intervals as an equal measure for finding the right fit. One could argue that equation 5.18 could be modified to compute the relative error between the measurements at all time intervals in one summation, but this will lead to a good fit at the extreme values (where the absolute error is large) while the error at $t3$ and $t5$ is underrepresented. In order to clarify this, please regard the strength of the measurements in figure 5.8. The absolute value of the measurements at $t2$ and $t4$ is much larger than those at $t3$ and $t5$, which would significantly reduce the relative error at the latter time intervals when the

error is computed in one calculation.The relative error at $t2, t3 \ldots t5$ is now calculated for the first loop size with a 100 µT background field, $i = 1$. This process is repeated until $i = i_{\text{max}}$. For $i_{\text{max}} = 4$ this leads to table 5.1.

i	$t2$	$t3$	$t4$	$t5$
1	$\eta_{\text{rel},1,t2}$	$\eta_{\text{rel},1,t3}$	$\eta_{\text{rel},1,t4}$	$\eta_{\text{rel},1,t5}$
2	$\eta_{\text{rel},2,t2}$	$\eta_{\text{rel},2,t3}$	$\eta_{\text{rel},2,t4}$	$\eta_{\text{rel},2,t5}$
3	$\eta_{\text{rel},3,t2}$	$\eta_{\text{rel},3,t3}$	$\eta_{\text{rel},3,t4}$	$\eta_{\text{rel},3,t5}$
4	$\eta_{\text{rel},4,t2}$	$\eta_{\text{rel},4,t3}$	$\eta_{\text{rel},4,t4}$	$\eta_{\text{rel},4,t5}$

Table 5.1: Relative error table after one full function evaluation of the objective function for $i_{\text{max}} = 4$.

The overall fit, the scalar output from the objective function, is calculated as the mean of all values in table 5.1. All the elements of the objective function discussed in the previous paragraphs can be retraced to the visualisation in figure 5.12. The next paragraph will explain how this objective function is used within the optimisation algorithm in order to swiftly calculate the optimal fit. In order to find the optimal fit, this objective function is evaluated around 1000 times for each specimen. This means that all diferent loop amplitudes are evaluated 1000 times each with the total computation time (using a high-end pc) at around 24 hours.

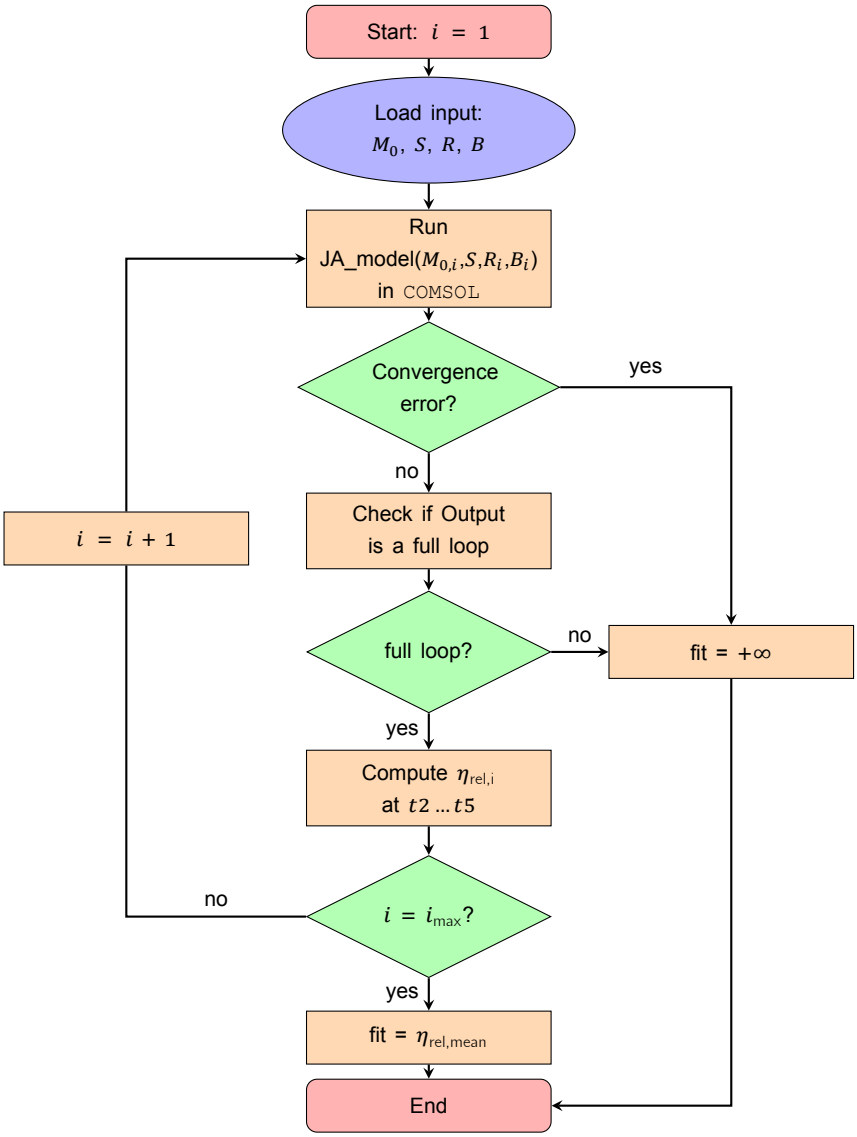

Figure 5.12: Objective function flowchart.

5.3.3. Shuffled Leaping Frog Algorithm

Various methods can be adopted in order to find the minimum of a function. For functions with a clear global minimum without an abundance of local minima, the *Fminsearch* algorithm in MATLAB can be used. This requires the user to enter a starting value for each parameter, after which the algorithm varies each parameter separately in order to find the nearest local minimum value. For this situation such an algorithm is not suitable because during earlier parameter fitting tests conducted on experiments, which are not included in this report, it was found that there are many different combinations of parameters which can produce similar results. Besides that, because of the high nonlinearity of the Jiles-Atherton expressions, the balance between parameters is delicate. Certain combinations of parameters from the Jiles-Atherton equations produce bad results or cause non-convergence, while different compositions of identical parameters might produce a good fit. For this reason a global search algorithm is required which looks for the optimal solution in the entire parameter space when the boundaries for each parameter are defined.

The effective solution time for finding the right JA parameters with different optimisation models has been studied, and a comparison has been made between SFLA, the Genetic Algorithm, Artificial Neural Networks, Fuzzy Logic, Partical Swarm Optimisation and Differential Evolution by Naghizadeh [39]. The SFLA showed the best results in terms of convergence, speed and accuracy. In many applications that are different from the JA-model, the SFLA and modified versions have shown to produce the most efficient results with the least computing power when compared with different optimisation algorithms, see Samuel, Eghbal, Yue [46][14][61]. It is for this reason that the SFLA model was adopted as the optimisation algorithm of choice.

The algorithm requires that the boundaries for each parameter are known. In order to define a set of boundaries for each of the JA parameters, literature was studied (Jiles [27] [24], Leite [31] [32], and Toman [50]). The maximum and minimum boundaries obtained are given in table 5.2.

Parameter	Minimum value	Maximum value	Unit
M_s	1.50×10^6	1.80×10^6	A/m
a	0	5000	A/m
k	0	5000	A/m
c	0.05	0.5	-
α	1.0×10^{-5}	1.0×10^{-2}	-
$R_1, R_2 \ldots R_{i,\max}$	1	20	-

Table 5.2: Jiles-Atherton parameter boundaries.

The SLFA algorithm was originally introduced by Eusuff for the optimal design of a water distribution network [15]. It starts with creating a population P of hypothetical frogs that are created randomly within the space allowed by table 5.2. For each frog, or random combination of parameters, the fitness is evaluated using the objective function. The solutions are stored and sorted from best to worst fit. Then, the population is sorted into m memeplexes each containing n frogs (i.e. $P = m \times n$). The frogs are divided equally over the different memeplexes, which implies that the top n frogs each go in a different memeplex, then the $(n+1\text{th})$ frog goes in the first memeplex, and so on. From that point the local search starts.

In each memeplex, the worst frog leaps towards the best frog in order to improve the worst frog's fit. If the fit is better than it was, the new frog replaces the worst frog. If the fit did not improve, the frog tries to leap towards the best global frog (so the best of all frogs, not just the best in this specific memeplex). If the fit still did not improve, a new random frog is created. A leap implies that, for each parameter, a new random value between the worst frog and the best frog's parameter value is chosen. This is repeated for each memeplex, and after a predefined number of steps within each memeplex the evolved memexplexes are once more mixed together in the shuffling process. Then, the memeplexes are re-created and the process starts over. For a more detailed overview of the SFLA and the corresponding equations, please refer to Naghizadeh [39]. The complete algorithm flowchart is given in appendix C.

The original SFLA algorithm was programmed to quit the optimisation process after a fixed number of

iterations. For the application in this project the code was modified in order to quit when the fit did not change sufficiently for three iterations in a row. In this case the threshold for convergence was set at one tenth of a percentage point. Three iterations in a row which, in total, improve the fit by less than 0.1% was taken as a measure for sufficient convergence.

5.4. Results

The results of the parameter optimisation process are provided in this section. Specimens 1-4 (see appendix B.4) were each subjected to background fields of various amplitudes. The parameters that were found to provide the best fit for each separate experiment are given in table 5.3. For specimen 1 the results of the fit are presented in figures 5.14 - 5.17. For specimens 2, 3 and 4 the results are given in appendix D. The assumptions of homogeneity and isotropy imply that one set of parameters describes the material behaviour for each test specimen. In order to quantify the results of the fit, the relative error as well as the root mean squared error (RMSE) were computed for each loop at each time interval $t1, t2 \ldots t5$ as well as some time intervals in between. The relative error was calculated using expression (5.18) in the previous section, and the RMSE is calculated through

$$RMSE = \sqrt{\frac{\sum_{i=1}^{i=n} (B_{i,\text{computed}} - B_{i,\text{measured}})^2}{n}} \tag{5.19}$$

in which n is the total amount of measurements at one time instant, wich is equal to 112 (sensors) × 3 (components) = 336.

Parameter	Specimen 1	Specimen 2	Specimen 3	Specimen 4	Unit
M_s	1.52×10^6	1.67×10^6	1.52×10^6	1.66×10^6	A/m
a	379	270	295	323	A/m
k	2656	1256	1763	379	A/m
c	0.1344	0.0974	0.1139	0.1194	-
α	1.790×10^{-3}	9.929×10^{-4}	9.884×10^{-4}	7.777×10^{-4}	-
R_1	1.5	1.7	2.9	8.0	-
R_2	1.2	1.0	2.5	1.0	-
R_3	1.1	1.0	1.1	8.3	-
R_4	1.0	8.6	1.1	6.6	-

Table 5.3: JA-R parameters obtained for Specimens 1-4.

An R-value of 1 means that there was no additional dissipative factor necessary in order to make sure that the measurment at $t5$ would be close to the measurement at $t1$ (closing of the minor loop). Increasing R-values show that more of this dissipation is needed in order for the loop to fit better with the measurements. From the table it can be observed that these R-values vary wildly for different specimens. This is likely due to the fact that only one hysteresis loop was simulated for each loop amplitude. In order to find a combination of parameters that fits perfectly it would be better to simulate 2 or 3 hysteresis loops that all have to fit the measured field at $t1, t2 \ldots t5$ each time in order to verify minor loop closure.

The result of these error calculations for the first specimen are given in figure 5.13, and for the remaining specimens these can be found in appendix D. It can be observed that, as expected, the relative error becomes rather large when the background field is zero since the measurements are much closer to 0 µT then when the background field is nonzero. This is also shown by the fact that the peaks disappear almost immediately for the measurements that are directly before or after a measurement where the background field is zero. As for the RMSE, it is seen that this error barely exceeds 2 µT when the background field is zero,which can be seen as a reasonable fit when regarding all measuring uncertainties in the setup, please refer to chapter 7.

For larger background fields the RMSE increases. This can be explained by the fact that for different ranges of measurements the sensors are programmed at a different gain level. The gain is a measure of the precision of the magnetometer. A higher gain allows the sensor to pick up a larger range of

the magnetic induction field at the cost of some precision. The hysteresis loops with larger amplitudes were performed with higher gain levels of the sensors, inherently creating a bigger absolute RMSE in the results. Identical graphs for the relative and RMS error are given for specimens 2-4 in appendix D. A peak in the RMSE is observed for the 400 µT loop. Further investigation showed that one of the sensors malfunctioned during the measuring of the background field at that time interval which resulted in measured x, y and z values that were very different from all the other measurements at that moment in time. The RMSE shows similar peaks for specimens 2-4 as shown in appendix D, which makes sense since the same background field was subtracted from each specimens. This measurement was not used in the fitting algorithm so it did not interfere with the optimisation procedure. For other time instants, peaks can sometimes be observed which also corresponds with several additional cases of sensor malfunctioning. Overall, the RMSE is 10% of the average measured field strength which indicates a good fit.

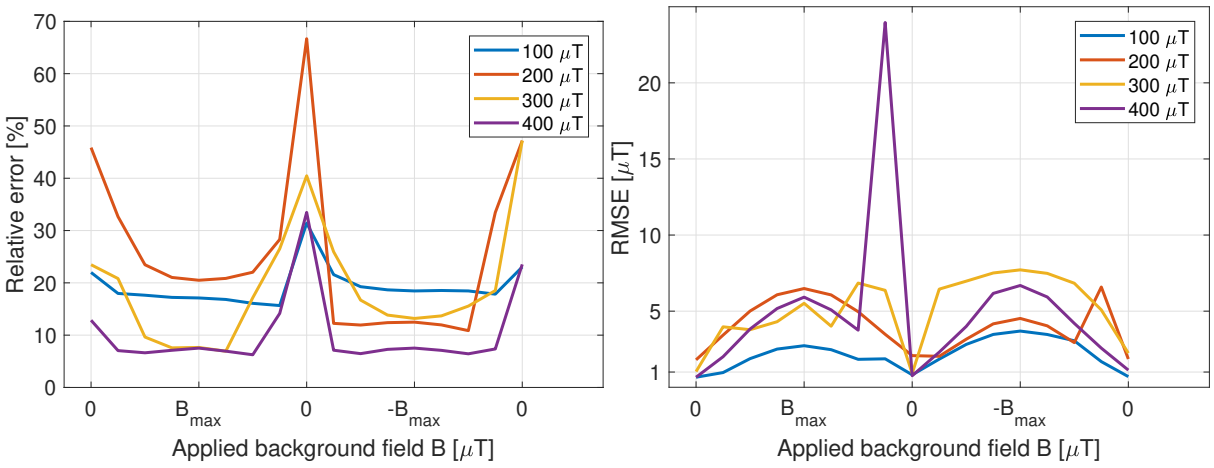

Figure 5.13: Specimen 1. Relative and Root Mean Squared Error.

When observing the magnetisation in figure 5.18 it is interesting to see how the influence of the initial magnetisation disappers for increasing loop amplitude. The initial magnetisation distribution's influence disappears for increasing loop amplitudes. In order to provide a good comparison, the colourbar scales of $t1$ and $t5$ have been made identical since theory suggests that at these time intervals, the magnetisation should be similar.

When comparing the RMSEs and fit results in appendix D it can be seen that reasonable fits can be found, but the results are not perfect yet. Upon investigation it is observed that this is mainly due to the fact that the measured dataset with measurements is not perfectly accurate. A number of measured B_x fields, figure D.10 ($t1$, $t3$ and $t5$) and figure (D.15, $t1$ and $t5$), show that both the maximum and minimum observed B_x values are negative, while in chapter 2 it could be seen that this is highly unlikely to occur from a physical point of view. On top of that, sensors that malfunction can be oberserved on numerous occasions, see figure D.11 ($t5$). Please note that only B_x measurements are plotted in this results section. Errors in B_y and B_z occur as well, and these components are also used as a measure to calculate the fit. In general it can also be seen that the fits behave better when the loop amplitude increases. This makes sense since an increased background field will yield in a more clear representation of hysteresis than a weak background field.

Specimen 3 behaves less well than the other specimens which can be partially explained by the fact that this plate was demagnetised during the study regarding non-uniformity in chapter 4. Since the values of the measured B-field when the background field is 0, are very close to 0, it can be stated that there is a lack of permanent magnetisation at the starting point which makes it harder to correctly describe the initial B-field. This error is then translateed through to the calculations at $t3$ and $t5$, showing the importance of correctly describing the initial magnetisation before attempting to find the JA parameters.

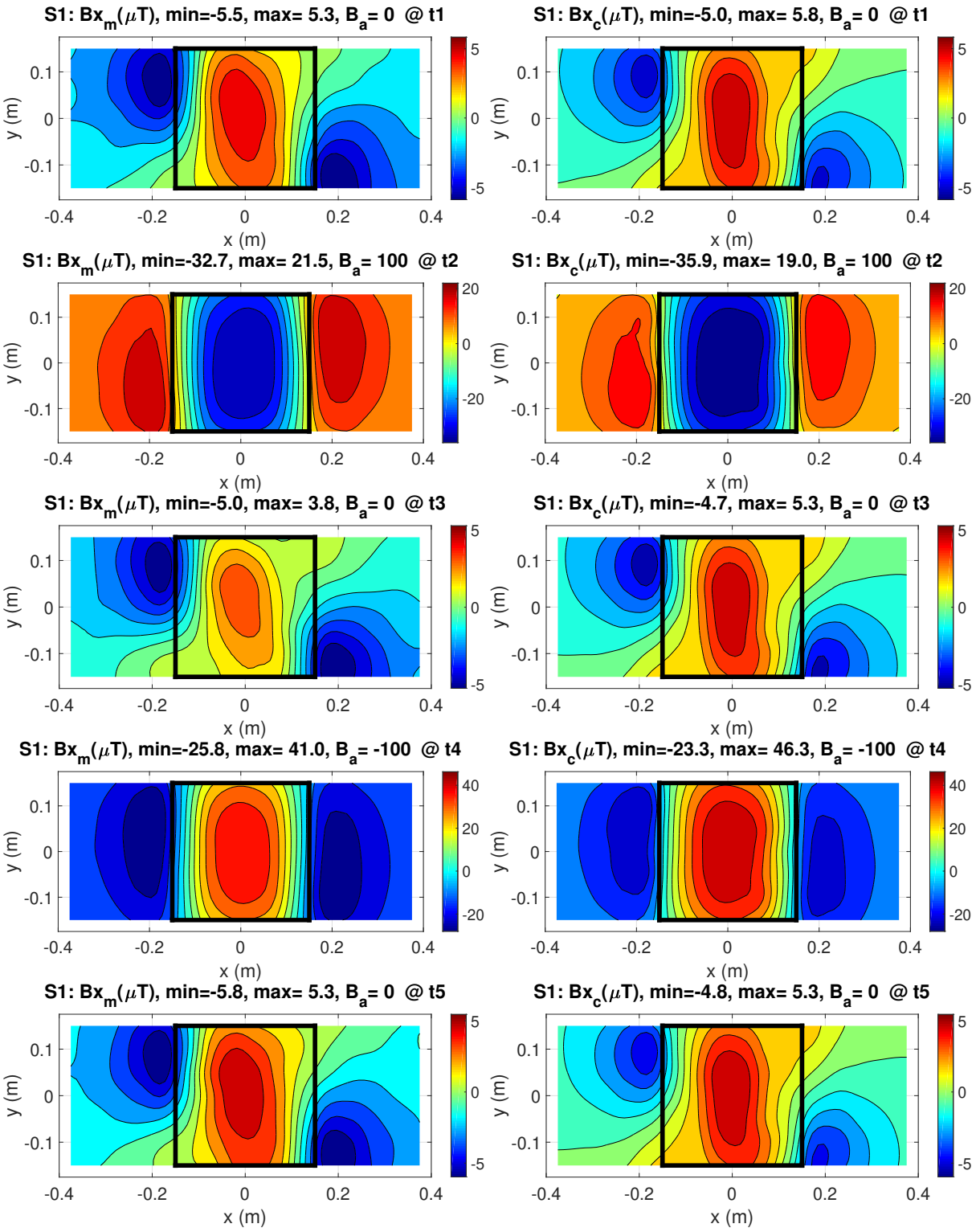

Figure 5.14: Specimen 1. B_x field below a metal plate (300×300×5 mm) subjected to a 100 µT loop, measurements (left) calculated fit (right).

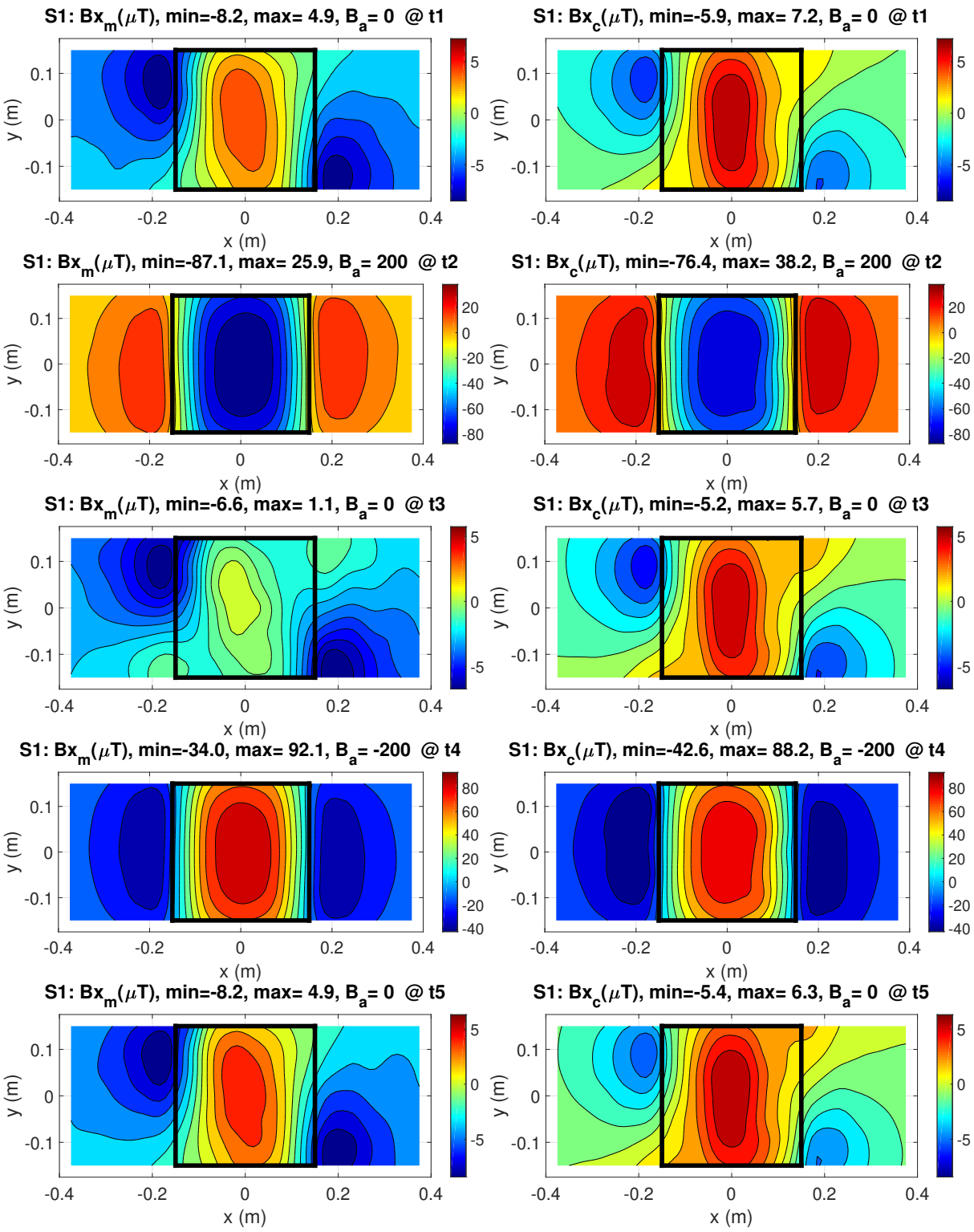

Figure 5.15: Specimen 1. B_x field below a metal plate (300×300×5 mm) subjected to a 200 µT loop, measurements (left) calculated fit (right).

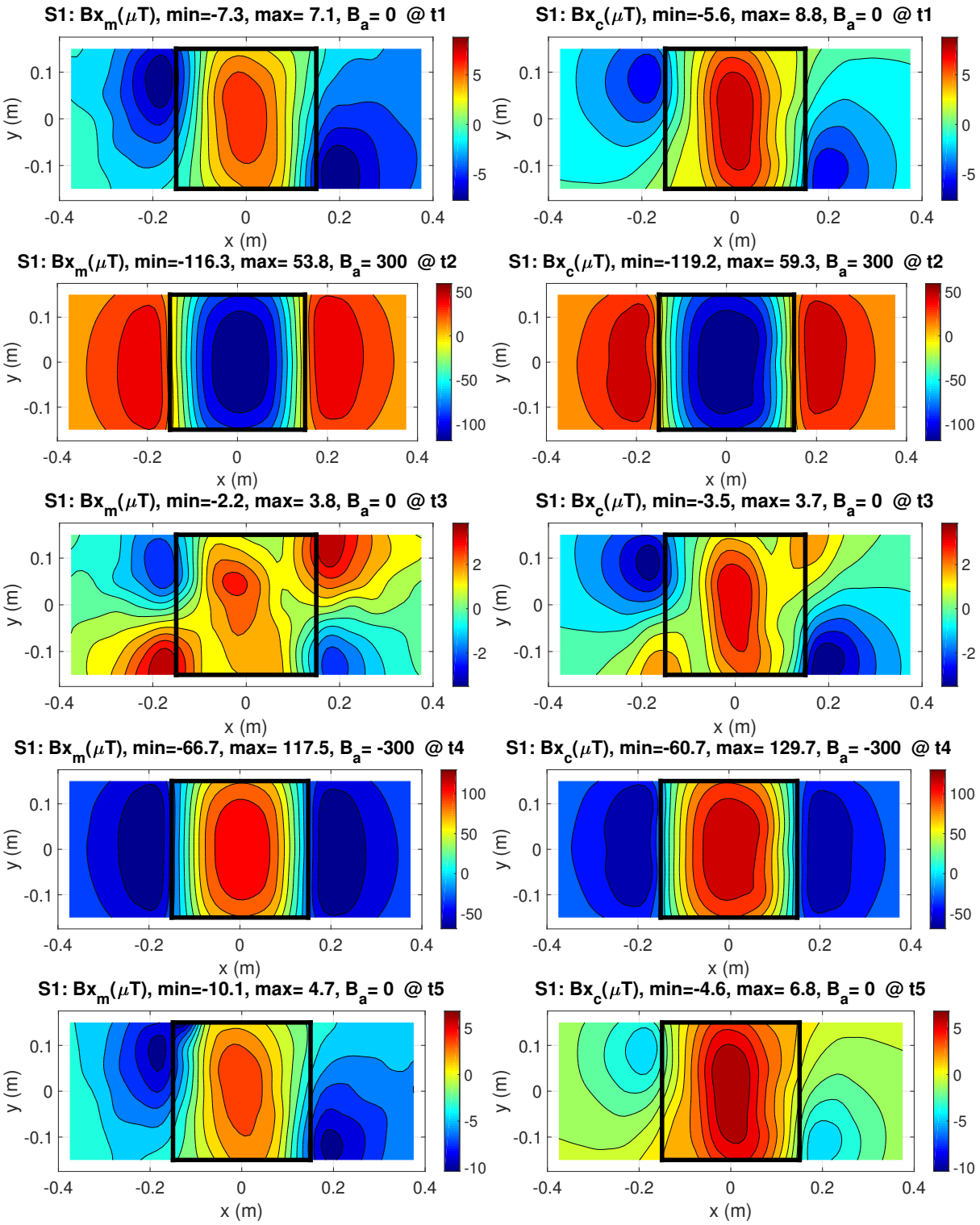

Figure 5.16: Specimen 1. B_x field below a metal plate (300×300×5 mm) subjected to a 300 µT loop, measurements (left) calculated fit (right).

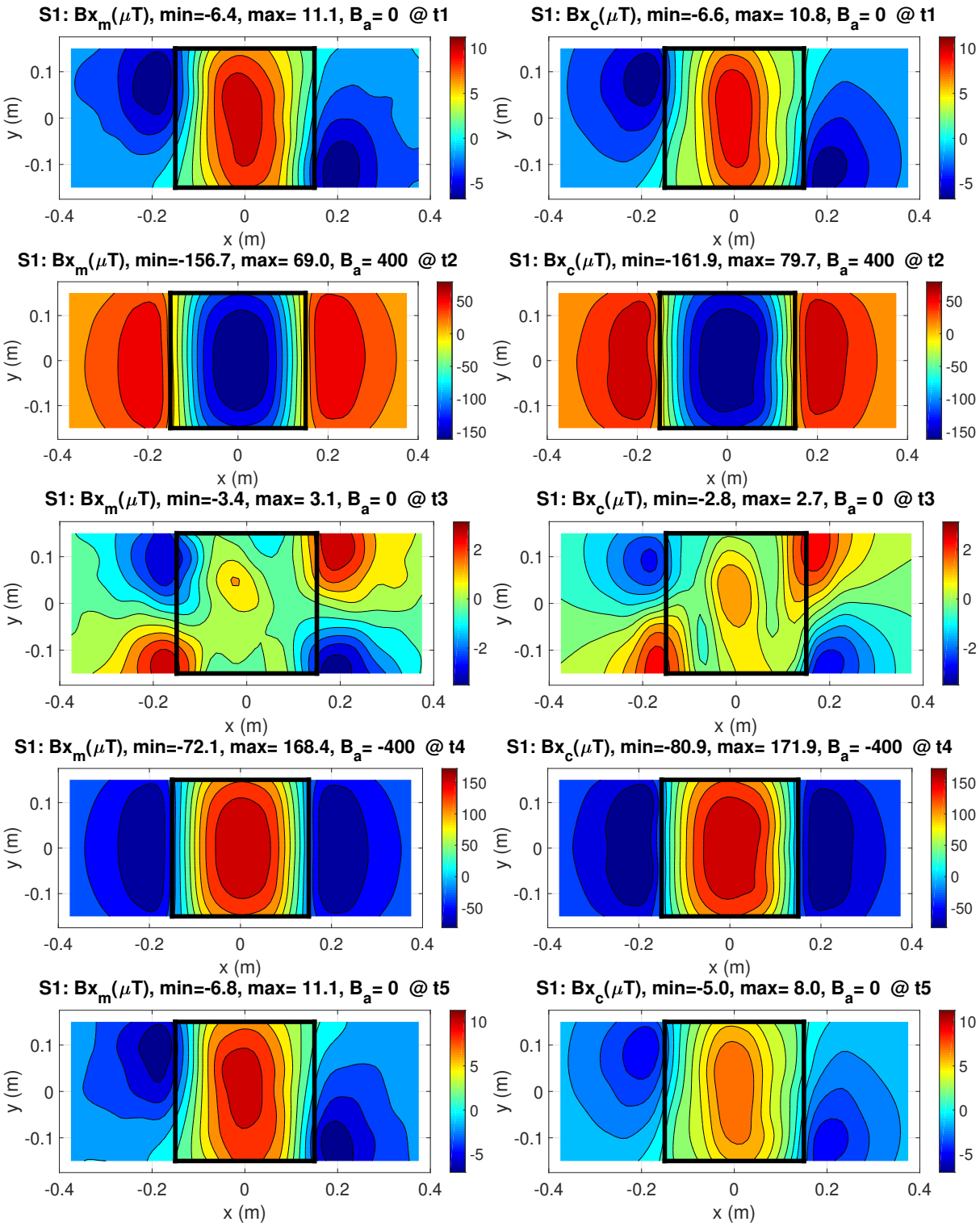

Figure 5.17: Specimen 1. B_x field below a metal plate 300×300×5 mm) subjected to a 400 µT loop, measurements (left) calculated fit (right).

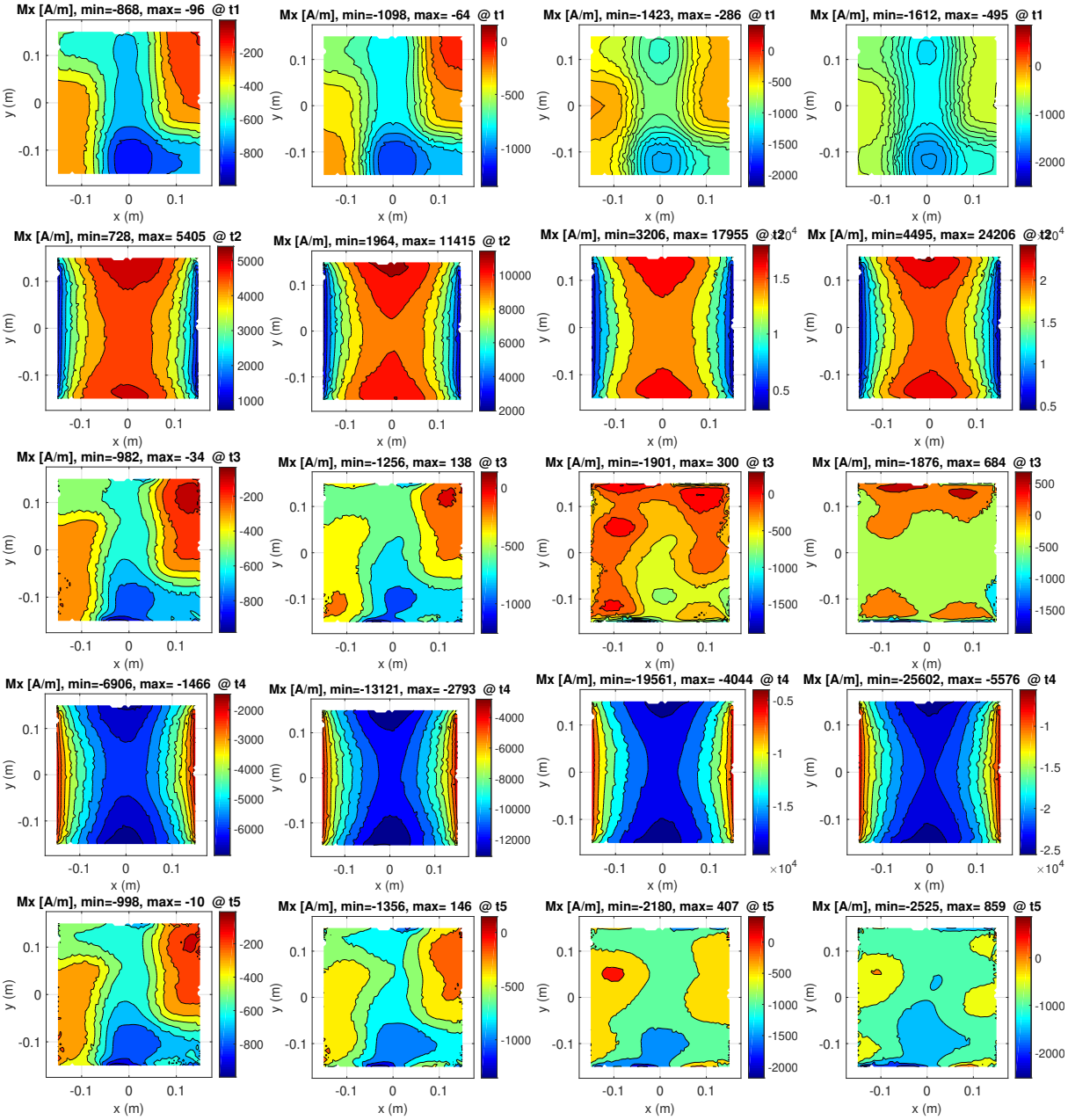

Figure 5.18: Specimen 1. M_x distribution in a metal plate (300×300×5 mm) for four hysteresis loops: 100 μT (left), 200 μT (centre left), 300 μT (centre right), 400 μT (right).

6

The Villari Effect

6.1. Introduction

James Prescott Joule discovered in 1842 how a ferromagnetic object changes length when magnetised, as described by Lee [29]. Using an iron rod and a system of mechanical levers he was able to show that iron expands along the direction of magnetisation in weak magnetic fields, while the rod would shrink for stronger magnetic fields, introducing the term *magnetostriction*. Later, he investigated the effect of external stresses on the magnetostriction of iron and showed that, while under tension, iron would contract further when subjected to external fields. Little over two decades passed until in 1865 the italian physicist Emilio Villari [57] characterised the inverse relation between changes in flux density **B** (achieved for a given value of the magnetic field **H**) in the material subjected to mechanical stress σ, see Szewczyk [49]. This *inverse magnetostriction* or *magneto-mechanical effect* is from there on also known as the *Villari effect*.

In his paper on the magnetomechanical effect Jiles described how originally it was assumed that the process of (inverse) magnetostriction was fully reversible. Jiles concluded that this approach is misleading since the magnetisation process is in itself hysteretic and therefore inherently irreversible by nature. He therefore sought a method of implementing a description for the magnetomechanical effect which is connected with the concepts of irreversibility and hysteresis [23]. Jiles worked on earlier proposed theories for changes in hysteresis curves due to constant applied stress, see Sablik [45] as well as changes in magnetisation due to varying stress levels, see Craik [10]. Based on these findings, Naus developed a formalism which described the magnetisation in ferromagnets when subjected to both constant and varying applied stress levels and background fields which builds on the original Jiles-Atherton framework [40]. His paper leads to the mean field H_e from equation (5.4) being modified to accommodate an additional stress-induced magnetic field term which is expressed in terms of the magnetostriction λ:

$$H_r = H_a + \alpha M(H_a) + \frac{3\sigma}{2\mu_0}\frac{\partial\lambda}{\partial M} \,. \tag{6.1}$$

The magnetostriciton λ is a function which depends on both the magnetisation and the stress, that is $\lambda = \lambda(M, \sigma)$ which is given as a double expansion

$$\lambda(M, \sigma) = \sum_{i=0}^{\infty} \gamma_i(\sigma) M^{2i} \tag{6.2}$$

with $\gamma_i(\sigma)$ expanded as a Taylor series about the origin

$$\gamma_i(\sigma) = \gamma_i(0) + \sum_{n=1}^{\infty} \frac{\sigma^n}{n!}\gamma_i(0)^{[n]} \,. \tag{6.3}$$

In equation (6.3), $\gamma_i^{[n]}$ is the nth derivative of γ_i. In his paper, Naus implements this series up to $i = 2$ and $n = 1$. The derative of $\lambda(M, \sigma)$ leads to the expression derived by Vijn [56]:

$$\frac{\partial \lambda}{\partial M} = \left(\frac{2\mu_0}{3}\right) M\,(\gamma_1 + \gamma_2 \sigma) \tag{6.4}$$

which leads to the expression of the stress field

$$H_\sigma = M\left(\gamma_1 \sigma + \gamma_2 \sigma^2\right) . \tag{6.5}$$

With this addition, the stress in the material gives a contribution to the magnetic field which is incorporated in the JA model in order to capture the hysteretic effect. The addition to the original JA equations is implemented in the COMSOL model from section 5.2. Previous experiments that show the implementation and verification of these γ_1 and γ_2 have not been performed to date. Qualitative assessment of the concept of inverse magnetostriction has been done, and an example of such an experiment is given in figure 6.1 below. On the left the test setup is shown, that consists of a ferromagnetic rod which has been *annealed* in order to remove residual stress and magnetisation. This rod is placed between base plates of non-magnetic material. Compression is applied through these base plates in a cyclical motion and, using a series of coils wrapped around the specimen, a magnetic field is applied while simultaneously measuring the induction field. The resulting internal B_x-field is then displayed on the right-hand side.

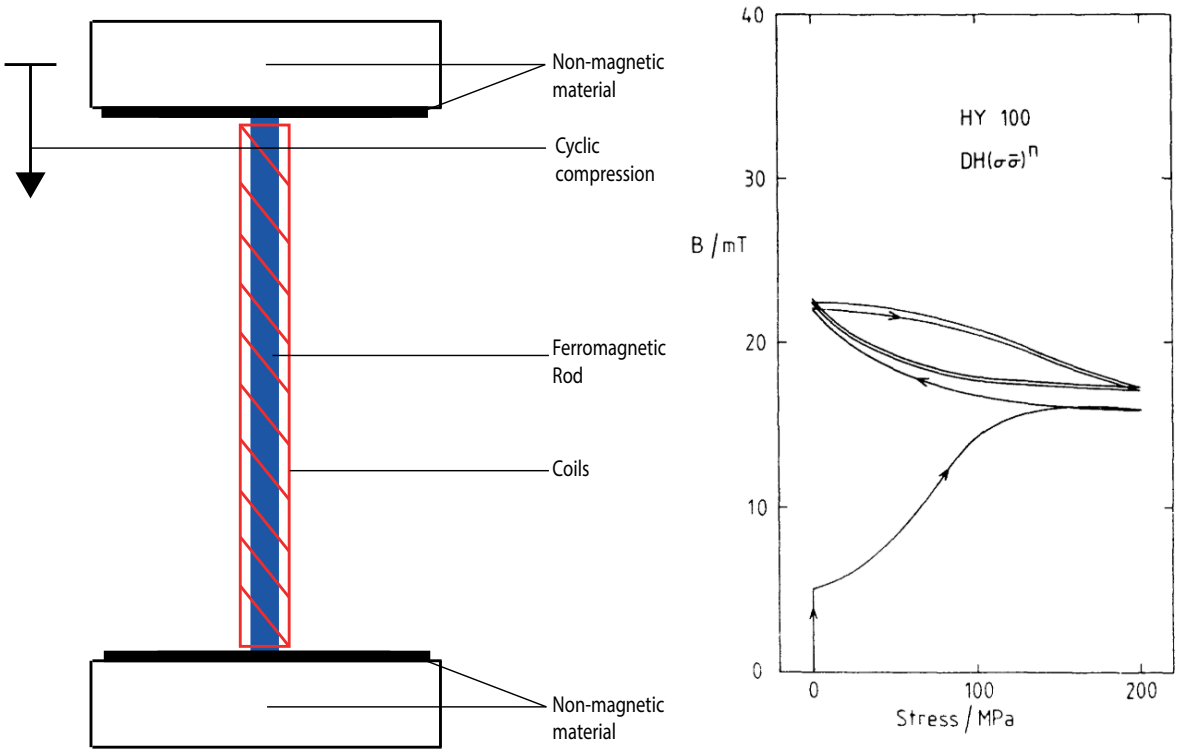

Figure 6.1: Villari testing setup (left) and resulting B-field inside the specimen during three load cycles (right), from Robertson [44].

On the bottom of the right-hand side of figure 6.1 the experiment starts, with an annealed specimen, exhibiting no magnetisation and therefore no internal B-field. A background field of H_a = 50 A/m is applied which results in a B-field within the specimen due to the induced magnetisation as shown by the initial vertical section of the graph. Following this, compressive stress is applied which corresponds with a nonlinear increase in internal B-field. Intriguingly as the compression is relieved, the measured induction field keeps increasing and when this process is repeated a hysteretic effect is observed during the following two load cycles.

6.2. Test setup

In order to measure the Villari effect a custom-made test setup is created which enables the user to apply homogeneous tensile stress to a rectangular steel sheet metal specimen. An important consideration that causes the necessity of building a custom setup is the fact that the entire setup, excluding the specimen, must be made made from non-magnetic material in order to not disrupt the measurements. Besides that, it should be sufficiently small to be conveniently placed in and removed from the Helmholtz cage. This is realised by glueing the test specimen into a block of aluminium on either side. These blocks of aluminium are then locked in an aluminium frame which encapsulates the entire specimen. The specimen is then tensioned using a set of titanium bolts which go through the outer frame into the aluminium block which was glued to the specimen. This is shown schematically in figure 6.2.

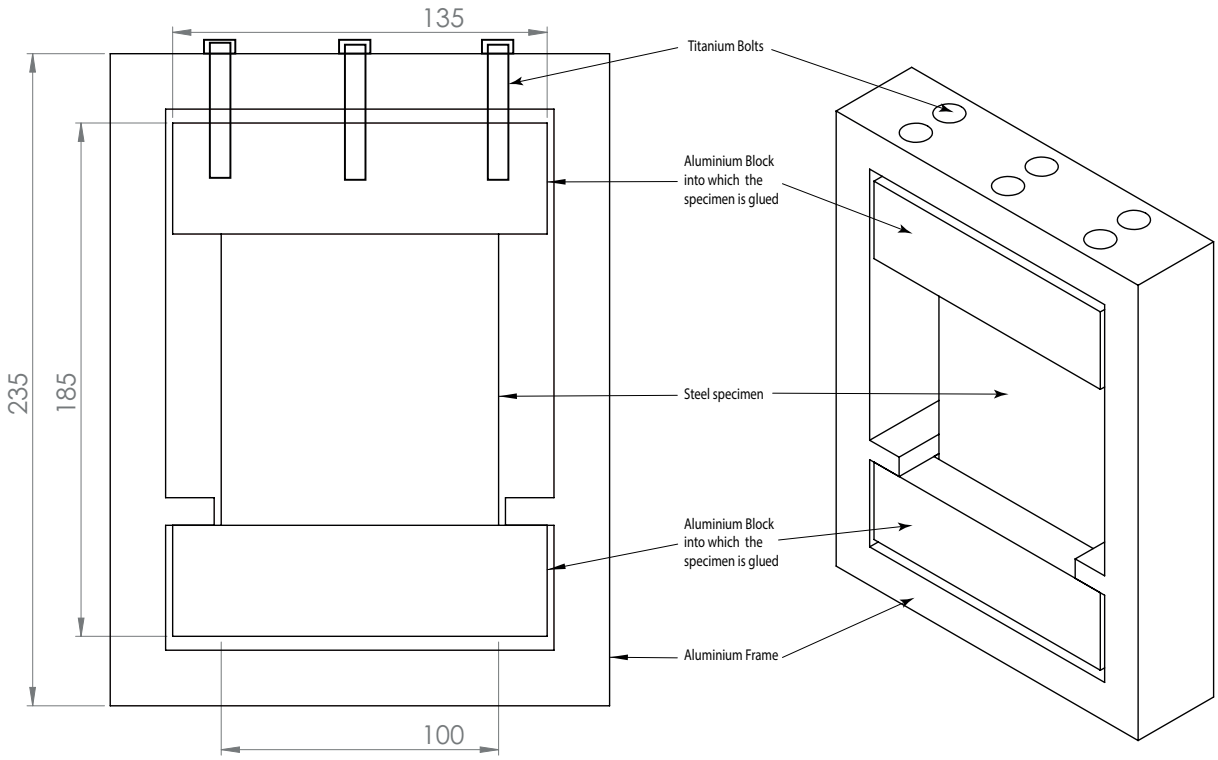

Figure 6.2: The Villari testing setup as used in this project. Top view with measurements in mm (left) three-dimensional view (right).

Two strain gauges are mounted on top of the specimen in order to measure the strain applied by tightening the bolts. For photographs of the setup with the attached strain gauges, please refer to appendix B.5. It is known that below the yield stress σ_y, the relation between stress and strain is given by Hooke's law

$$\sigma = \epsilon E \tag{6.6}$$

in which ϵ is the strain in m/m and E is the young's modulus which is around 210 GPa for most types of structural steel [6]. A small problem which occurs with the setup from figure 6.2 is that in order to tension the specimen the apparatus has to be taken out of the Helmholtz cage in order to tighten the bolts using a spanner. It is not possible to perfectly control the background field and the stress independently as removing it from the cage causes the specimen to be subjected to a background field represented by the Earth's magnetic field. This means that any change in stress goes hand in hand with a minor hysteresis loop of some shape due to the rotation in the Earth's magnetic field. An attempt is made to deminish this effect by subjecting the specimen to a couple of 400 µT hysteresis loops after each alteration of the stress level. In figure 6.3, the variations in stress and background field during the experiments performed are shown.

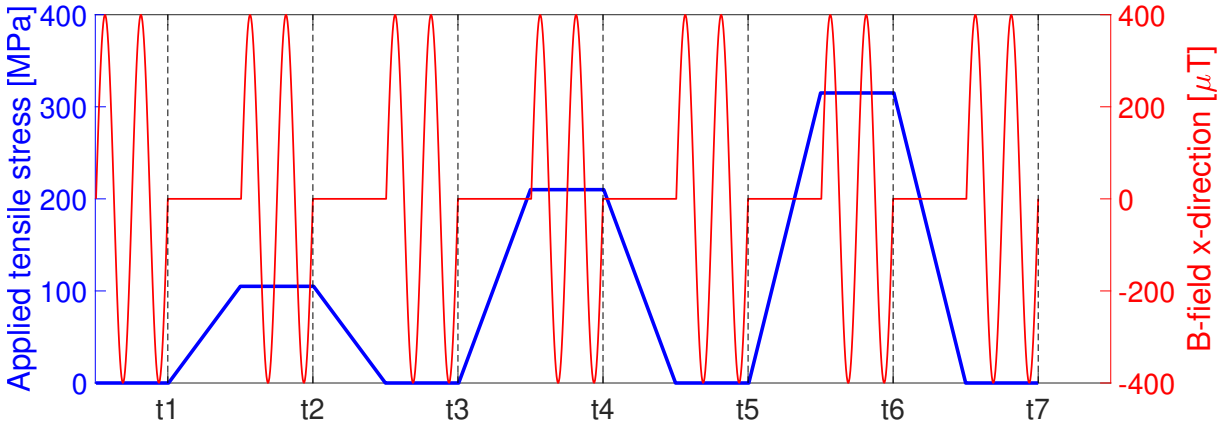

Figure 6.3: The applied stress and the applied induction field during the Villari experiments.

In this case, the B-field was measured at the time instants $t1, t2 \ldots t7$. If this experiment is performed without any stress it is known that the exported B-fields are identical at $t1, t2 \ldots t7$ since minor loops close, see chapter 5. When stress is applied, these induction field measurements will be different, which can be contributed to the magnetomechanical effect. For the numerical simulation it was chosen to only model the stress and assume that there was a constant background field $B_a = 0$ in combination with in initial magnetisation distribution M_0, calculated according to chapter 4. Now it is likely that a small error is made here, because the background field variations will also influence the magnetisation of the steel as was concluded in the previous chapter. However, for this moment it is assumed that these hysteretic effects are significantly smaller than the stress-induced magnetisational changes and therefore negligible.

6.3. Algorithm

The algorithm used to find the parameters is nearly identical to the algorithm used in chapter 5, with a few modifications which are discussed here. The specimen is glued into two aluminium blocks. A problem that occurs is that the part of the specimen glued into the aluminium blocks, which is roughly 30 mm on either side, does not experience the same stress levels as the part of the specimen which is in the middle, which is 105 mm long. Therefore, the specimen has been split up in three regions as shown in figure 6.4. The small strips on the side are taken into account when regarding the initial magnetisation, but the stress remains zero throughout the numerical simulation. The middle section has a homogeneous stress distribution which is calculated directly from the strain gauges. A small error is made since the stress in the sections of the specimen which are glued within the aluminium blocks is technically not zero, but due to the large size of the aluminium blocks compared to the volume of the encapsulated steel strips this is neglected in the simulation.

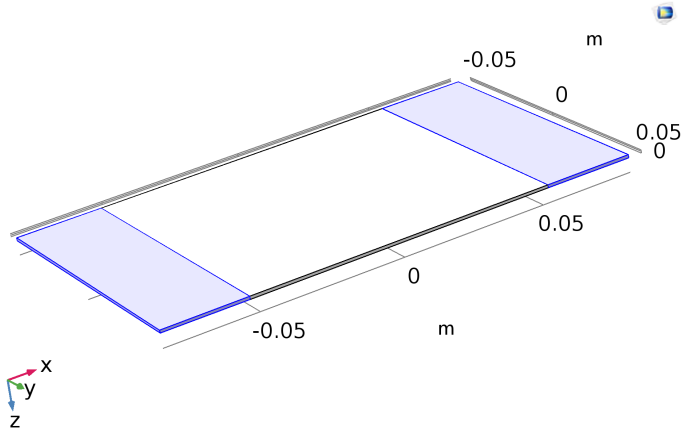

Figure 6.4: Villari specimen 5 and 6 modelled in COMSOL. The stress follows figure 6.3 (white area), stress is zero (blue areas).

Another difference in the algorithm is the definition of the fit. This definition is changed for two main reasons:

1. The starting magnetisation of specimen 5 was found to be large and somewhat oddly distributed (see the B-field in figure 6.5 and the corresponding M-distribution in figure 7.1);
2. Specimen 5 and 6 are much smaller than the plates tested in chapter 5, therefore only the sensors located near the centre of the array measured significant differences in B-field.

For these reasons the time instants at $t2, t3 \ldots t7$ are compared relative to $t1$, i.e. the B-field at $t1$ is subtracted from the remaining measurements. This gives a better and more intuitive insight into the magnitude of the Villari effect than when comparing measured and computed B-fields directly, which resulted in very similar looking graphs at all time instants (reason 1). Another modification in the algorithm is that it compares maximum and minimum values of these difference fields instead of the entire field (reason 2).

6.4. Results

Two specimens were tested according to figure 6.3:

- A 165 × 100 × 1 mm plate made out of high yield steel with σ_y = 700 MPa (specimen 5);
- A 165 × 100 × 2 mm plate made out of structural steel with σ_y = 355 MPa (specimen 6).

Specimen 5 was successfully tested at all time instants. During the loading of specimen 6 from $t3$ towards $t4$ (towards 210 MPa) the glue between the specimen and the aluminium support block gave way. This resulted in the data being limited to $t1, t2$ and $t3$ only. The Jiles-Atherton-Naus parameters obtained using the fitting algorithm are summarised in table 6.1.

Parameter	Specimen 5	Specimen 6	Unit
M_s	1.61×10^{6}	1.72×10^{6}	A/m
a	155	1165	A/m
k	709	52	A/m
c	0.029	0.013	-
α	2.78×10^{-4}	8.08×10^{-5}	-
γ_1	-2.52×10^{-17}	-7.92×10^{-16}	$A^{-2}\cdot m^2$
γ_2	1.82×10^{-29}	-4.70×10^{-27}	$A^{-4}\cdot m^2$

Table 6.1: Jiles-Atherton-Naus parameters obtained for specimen 5 & 6.

In figure 6.5 the B_x-field at $t1$ is shown for specimen 5. From this figure it can be directly observed that the initial magnetisation is large compared to specimens 1-4 from chapter 5 since the extreme values of the B-field are significantly larger while the dimensions of the sample are considerably smaller.

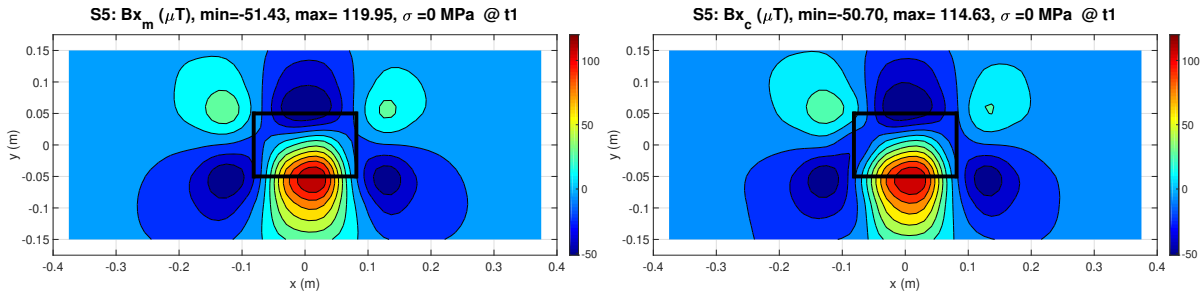

Figure 6.5: Specimen 5. Measured (left) and calculated (right) B_x-field at $t1$ (top left/right).

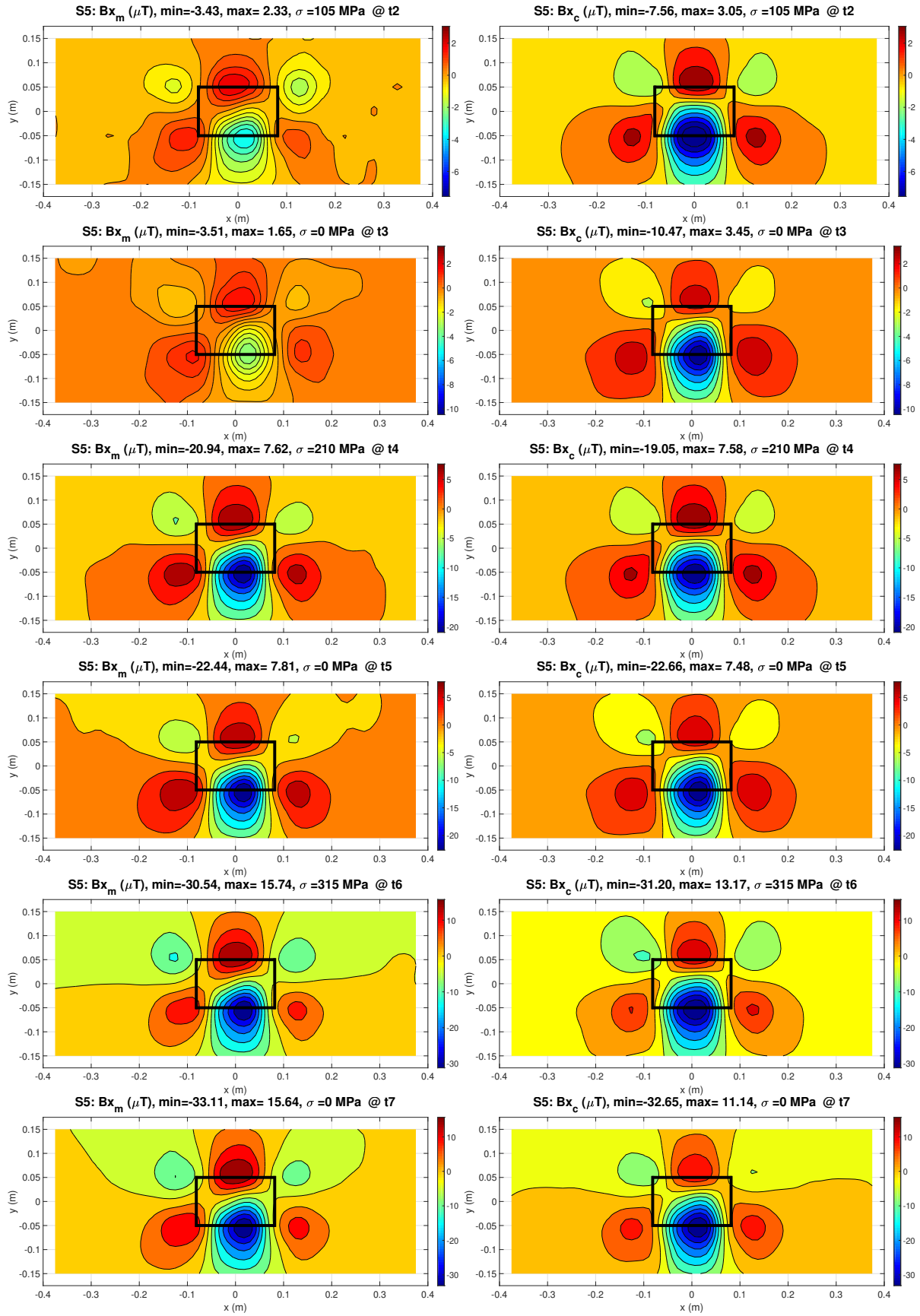

Figure 6.6: Specimen 5. Measured (left) and calculated (right) difference B_x-fields at $t2, t3 \ldots t7$.

For specimen 6 the experiment resulted in the measurements and calculated fit shown in figure 6.7 at time instants $t1, t2$ and $t3$. The B_x-field below this specimen at $t1$ shows more similarity with what was observed during the hysteresis experiments.

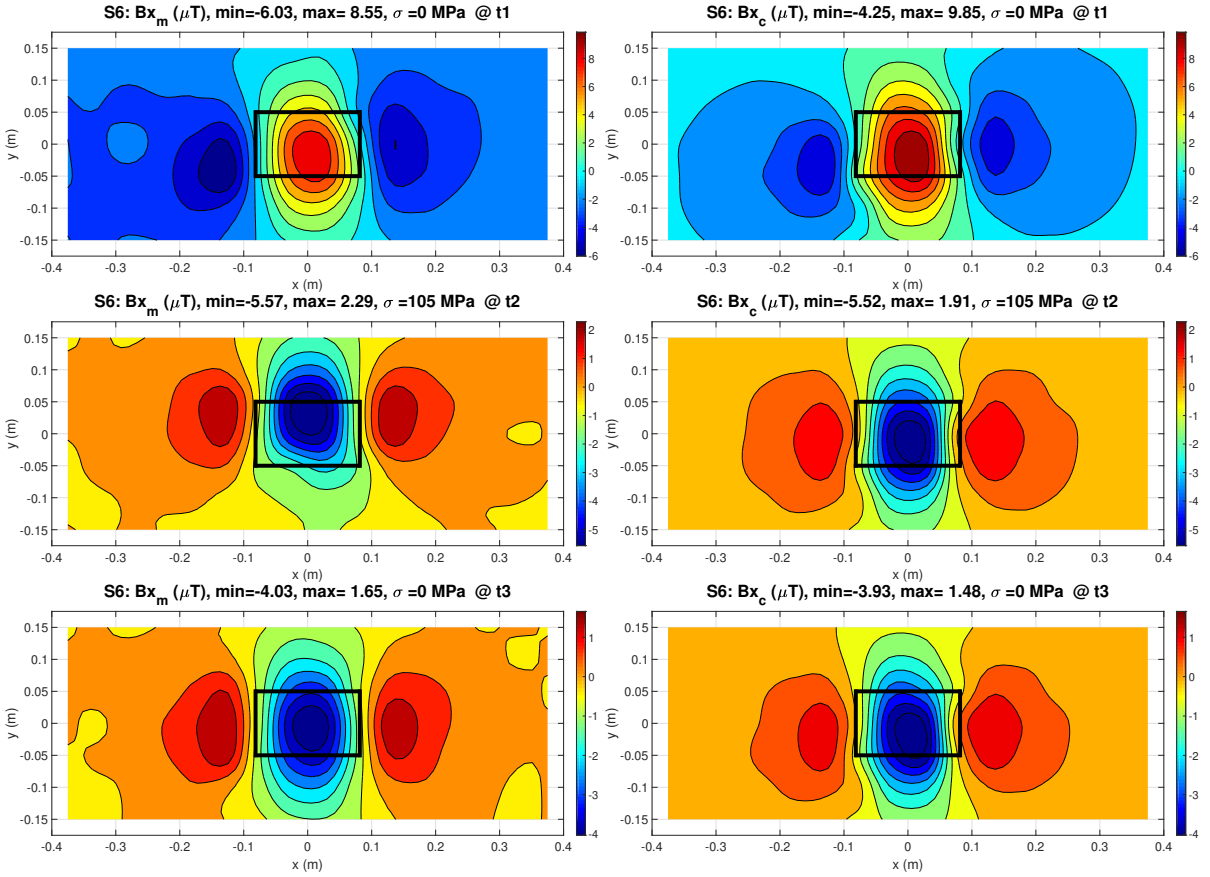

Figure 6.7: Specimen 6. Measured and calculated B_x-field at $t1$ (top left/right), measured and calculated difference fields with respect to $t1$ (remaining left/right).

The fit in figure in figure 6.6 performs well at time instants $t4, t5 \ldots t7$. It seemed difficult for the parameter optimisation algorithm to find a combination of parameters which behaved properly at both $t2$ and $t3$ and the remaining instants. Nonetheless, the overall accuracy is not bad when comparing the minimum and maximum values closely throughout the experiment. A good fit is obtained for specimen 6 in figure 6.7 as well, although the dataset is too limited to adhere any proper conclusions to this fit, especially when regarding the fact that the fitting algorithm had trouble fitting $t2$ and $t3$ with specimen 5. An overview of the absolute error between the minima and maxima for both specimens is given in figure 6.8.

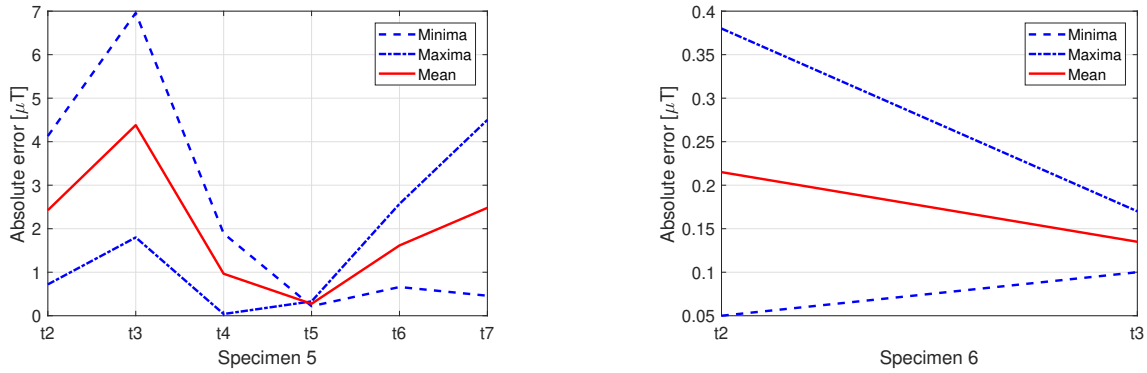

Figure 6.8: Absolute error between the measured and computed minima and maxima at each time instant.

7

Conclusions and Recommendations

7.1. Relaxation

Losses due to short-term magnetic relaxation have been discussed in literature for specimens subjected to strong and rapidly alternating background fields. Since the background field in the Helmholtz cage is neither strong nor rapidly alternating, the effect has not been observed. It is expected that even with better sensoring equipment, the losses due to short-term relaxation will be found to be negligibly small. Further investigation is not recommended due to the fact that for the application of this research such strong and rapidly alternating fields do not occur.

The effect of magnetisational changes due to long-term relaxation can very well be different. It is not unreasonable to expect that when a ferromagnetic object is kept in the same background field for a substantial time, eventually the magnetic orientation in the grains will start to rotate in a direction aligned with the background field. This effect is barely studied since it is hard to measure and possibly of even smaller magnitude than the other effects discussed in this thesis. With a different setup and more time at hand this could and should be studied. A possible test setup used for capturing long-term relaxation is to place a demagnetised ferromagnetic object in a fixed orientation with respect to the Earth's magnetic field. Each month, the specimen is quickly placed within a Helmholtz cage in order to annul the background field and capture the permanent magnetisation. This can be done using inversion performed on the B-field below the object. This process is repeated for several months or even years, and when the measured B-field starts to differentiate this could be the result of magnetic relaxation. Problems that occur with this experiment are the substantial duration of the test as well as the fact that the applied background field has to remain constant. This means that no ferromagnetic objects can be in the vincinity of the test specimen for the duration of the experiment.

7.2. Uniformity

Since literature provided only limited information regarding the description of non-uniform magnetisation it was decided to personally derive an inverse method. Chapter 4 shows a possible way of translating induction field measurements in a plane back to magnetisation within a test specimen with adequate results. Various alternative types of functions could be investigated as well, but this was left out of the scope of this thesis. The main reason for developing this method was that it provides the posibility to define a starting magnetisation M_0 which is a very important aspect of both the Jiles-Atherton hysteresis model and the Jiles-Atherton-Naus model. Without a proper approximation of the initial magnetisation it would be much harder to succesfully obtain the model parameters since, for example, from figure 5.5 it can be clearly seen that the minor loops change size and shape depending on starting magnetisation.

At the end of chapter 4 it was concluded that there are two possible functions to describe initial magnetisation which successfully reproduce the measured B-field, and it was decided that this was a sufficient result in order to continue with the next phase of the research project. However, this does not ascertain that the functions used here provide both the optimal and unique solution to the problem, and more research should be conducted in order to find combinations of functions that describe the magnetisation in

a more scientific approach. This investigation relies heavily on the mathematical field of study known as *regularisation*, and should therefore be conducted by someone with a certain amount of knowledge on this topic.

7.3. Hysteresis

In chapter 5 the JA parameters of ferromagnetic objects were obtained based on minor loops created through weakly varying background fields. This approach is unique since similar experiments were not discovered in literature. The methodology that is proposed in this thesis, which includes the implementation of an extra dissipative factor R in combination with measurements in a plane represented by the sensor array has shown promising results. In literature, the JA parameters are mainly obtained using major loops while the results in this thesis show a viable alternative.

A large peak in the RMSE for all specimens was observed during the 400 µT loops. This happened due to a sensor malfunction while taking the zero measurement. Since this zero measurement (which is subtracted from the actual measurement) is similar for each specimen, this error pops up in each specimen. Other strange peaks in the RMSE are observed which correspond to other occasions of sensor malfunctioning during the experiments.

A closer look at table 5.3 shows that the discovered values of R vary for each test and for each loop, while the original theory by Leite [30] suggests that loops with a smaller amplitude would require a higher R-parameter. The value for R should asymptotically go to 1 for increasing loop size (which coincides with the theory that major loops do not need an extra component to close since major loops always close). This is possibly due to the fact that the JA-parameter identification was conducted on *single* loops in the numerical simulation. In order to check the stability of the solution, multiple loops should be simulated to see if the minor loop is actually as stable as it seems. This can be done relatively straightforward using a similar implementation as used in this thesis, but with a higher computational burden since the numerical simulation will take longer.

Only hysteresis in the longitudinal, or x-direction, of the specimens has been investigated. It would be interesting to measure differences in hysteretic behaviour in x and y-directions since it is known that steel sheet metal is rolled in a certain direction. This will likely cause the crystallographic structure to be different in x and y-directions which inherently results in varying hysteretic behaviour. Another topic of interest would be to investigate the material parameters of different types of steel compared to the structural steel tested within this project. This is preferably a type of steel from a known steel manufacturer for which the JA-parameters are found in literature in order to verify the implementation of the method proposed here.

7.4. The Villari effect

As for the Villari effect, the tests performed have shown that it is possible to find a set of parameters that correctly describes the stress-induced magnetisational changes that were observed during experiments. Testing more specimens succesfully would provide better insight into how the obtained magnetostriction paramers differ between steel types. The failure of specimen 6 before reaching time instant $t4$ renders this experiment less useful than specimen 5 since the fitting is now performed at only two datapoints which is obviously too few for drawing proper conclusions. It would be interesting as well to cycle between two fixed stress points for a number of loops to see if the observed effect from figure 6.1 can be reproduced.

In order to improve the quality of the measurements, it would be interesting to perform the same experiment using annealed samples. This way it can be said with certainty that the stress applied while tightening the titanium bolts is the only stress within the specimen. Another topic of interest are eddy-currents. Due to the changing magnetic background field in the Helmholtz cage, eddy currents will appear in the aluminium frame which create a background field in the opposite direction. However, this would mainly be an issue with applied magnetic background fields in the z-direction which was not the case in this project. Besides this it is expected that the effect of this eddy current-induced magnetic field will be

small since it is based on the derative of the magnetisation with respect to time. With fields alternating at a frequncy of less than 0.1 Hz this is in all likelihood negligible, but this this has not been officially proven.

The importance of finding the right magnetisation distribution before attempting to find JA(N) parameters is best observed in figure 6.5. This B-field corresponds with a rather odd, inversely calculated, magnetisation distribution which is shown in figure 7.1. The z-component of the magnetisation is negligible compared to M_x and M_y and therefore omitted here.

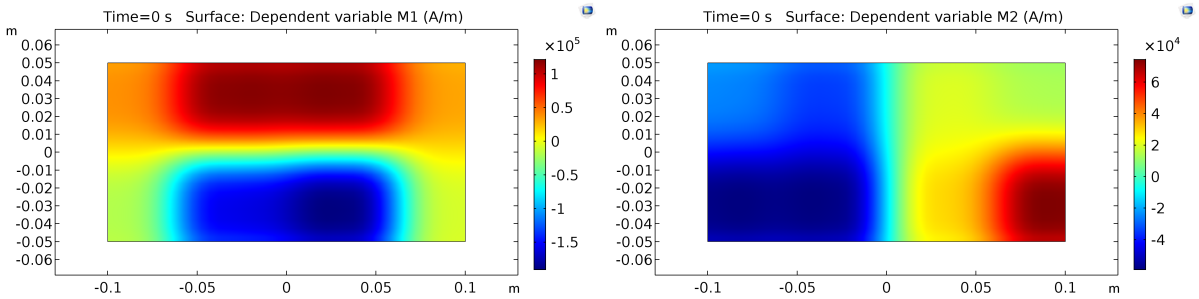

Figure 7.1: Specimen 5. Initial magnetisation in x-direction (left), y-direction (right).

This figure implies that the starting magnetisation in x-direction in the top half of the specimen is positive, while being negative in the bottom half. If one keeps in mind that figure 6.6 consists of difference fields with respect to $t1$ it might seem rather surprising that the difference field shows a similar distribution even though the stress is homogeneous within the specimen. This can only be explained by the fact that the starting magnetisation has a large influence on the stress-induced component of the magnetisation. The homogeneous tensile stress throughout the specimen generates negative x-magnetisation in the top half while simultaneously generating positive x-magnetisation in the bottom half. This effect is captured succesfully by the JA(N) model when regarding the calculated fits on the right hand side of figure 6.6. The reaon why specimen 5 is initially magnetised this way remains rather mysterious. It could be due to production methods or post-processing of the steel sheet. This specimen does however give a very clear insight into how different starting magnetisations lead to different magnetisational changes when tensioned which is definitely a point of interest for future investigation, especially when combined with the question how *compressive* stress influences the magnetisation and how it compares to tension, see Sablik [45].

Continuing on this topic, a proposition is shared which discusses how the results from chapter 6 can be implemented in the monitoring of elliptical crack growth. Assume a slender rectangular steel plate of 70 mm wide, 700 mm tall and 10 mm thickness, see Van der Horst and Van Kreveld [51][55]. These dimensions are chosen in such a way that when one of the short edges of the plate is loaded perpendicularly, the stress distribution in the cross section at y = 0 will be approximately homogeneous when there are no defects present. A semi-elliptical crack is created in the centre of the plate, at the surface. This is modelled as a semi-spheroidal dent with width 10 mm, height 2 mm, and depth 1 mm. The geometry is shown in figure 7.2. This plate is loaded with a tensile stress of 100 MPa at the bottom of the plate (so a force in negative y-direction) while the top edge is fixed. This results in a homogeneous stress distribution of 100 MPa in the middle of the plate at a distance from the elliptical crack. When zooming in on the crack from the top, an increase in stress is observed at the crack tips. A cross section in the xz-plane at y = 0 shows that this increase in stress propagates along the edge of the semi-elliptical crack, with the stress locally reaching a maximum of 270 MPa as is shown in figure 7.3. It can be stated that, hypothetically, this plate is made out of regular steel with a yield stress of σ_y = 235 MPa. Due to a 100 MPa loading at the edge, far below σ_y, it could occur that locally a certain amount of plastic deformation occurs which subsequently results in crack growth.

With the theory from chapter 6 it can be stated that near such a crack tip the permanent magnetisation of the steel is different due to the Villari effect. It is therefore thinkable to use the stress distribution from the structural model shown in figure 7.3 as input for a magnetic model which computes the corresponding B-field distribution around this elliptical crack. Eventually, a measured B-field can be translated back to

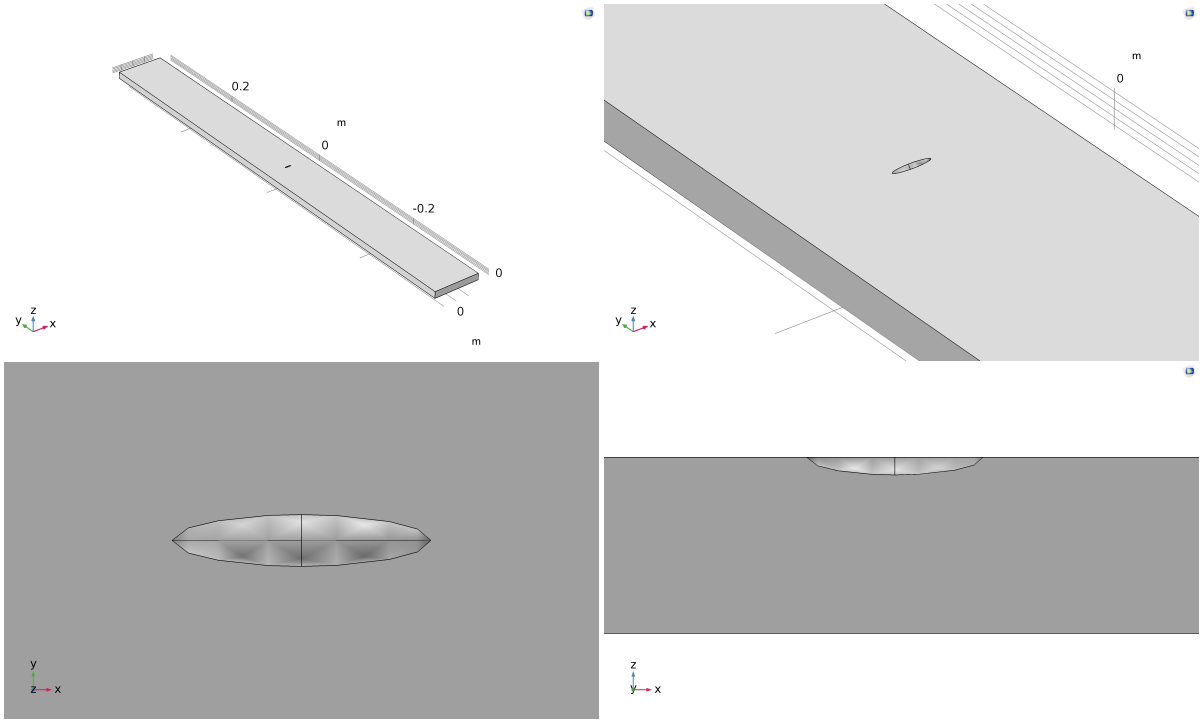

Figure 7.2: Full geometry (top left), close up of full geometry (top right), top view close-up of semi-ellipsoidal crack (bottom left), cross section close-up xz-plane of crack (bottom right).

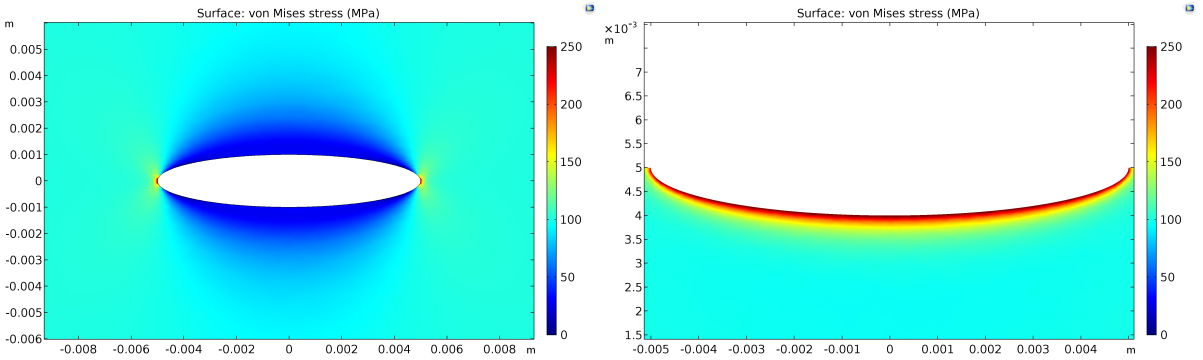

Figure 7.3: Stress distribution around the semi-ellipsoidal crack due to a 100 MPA loading, top view (left), cross section (right).

crack propagation using the methodology outlined in chapter 6. Going one step further, a FEM model can be contructed which has disappearing finite elements as is studied by Bijleveld [4]. Using this methodolgy it is possible to let elements within the steel disappear, i.e. become air elements, when a certain treshhold is reached. This could be, for instance, that during cyclic loading the yield stress is reached a predefined number of times. This illustrates how crack propagation can be modelled using a combination of structural and magnetic FEM models, possibly using the `Multiphysics` toolbox in `COMSOL`.

A

Magnetic field expression derivations

A.1. Uniformly magnetised sphere

Presented here is the derivation of the magnetic field **H** of a sphere with radius a which isuniformly magnetised in z-direction with a magnetisation **M**. A two-dimensional sketch is presented in figure A.1, with the y-axis pointing out of the paper.

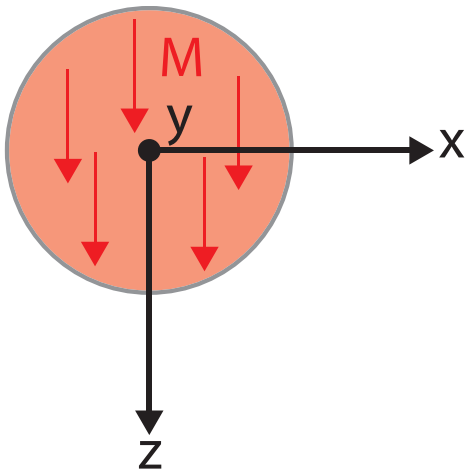

Figure A.1: Two-dimensional view of a uniformly magnetised sphere.

Uniform magnetisation in z-direction implies that for every point within the sphere the magnetisation is given by the vector

$$\mathbf{M} = M \begin{bmatrix} 0 \\ 0 \\ 1 \end{bmatrix} \tag{A.1}$$

assuming no magnetisation in y and x-directions. When combining equations (2.2) and (2.3), it follows that

$$\nabla \cdot \mathbf{B} = \mu_0 \nabla \cdot (\mathbf{H} + \mathbf{M}) = 0 \,. \tag{A.2}$$

in which μ_0 drops out so the following relation is obtained:

$$\nabla \cdot \mathbf{H} = -\nabla \cdot \mathbf{M} \,. \tag{A.3}$$

It can be stated that based on equation (2.1), a magnetic scalar potential Φ can be introduced (see Jackson [21] and Griffiths [18]) such that

$$\mathbf{H} = -\nabla\Phi \,. \tag{A.4}$$

Substituting this in equation (A.3) yields

$$\nabla^2\Phi = \nabla \cdot \mathbf{M} \,. \tag{A.5}$$

This can be mathematically solved since it is known that for a potential function Φ the solution of

$$\nabla^2\Phi(\mathbf{r}) = f(\mathbf{r}) \tag{A.6}$$

can be found in the shape of

$$\Phi(\mathbf{r}) = \frac{-1}{4\pi} \iiint\limits_{\Omega} \frac{f(\mathbf{r}')}{|\mathbf{r} - \mathbf{r}'|} \, d^3r' \tag{A.7}$$

if $f(\mathbf{r})$ is bounded and non-vanishing in a bounded volume Ω. When describing magnetostatics, $f(\mathbf{r})$ equals $\nabla \cdot \mathbf{M}$ such that

$$\Phi(\mathbf{r}) = \frac{-1}{4\pi} \iiint\limits_{\Omega} \frac{(\nabla' \cdot \mathbf{M})(\mathbf{r}')}{|\mathbf{r} - \mathbf{r}'|} \, d^3r' \,. \tag{A.8}$$

To obtain a solution to this potential equation it is necessary to define an expression for $\nabla \cdot \mathbf{M}$. In order to do so the vector $\mathbf{r}$ is projected into a spherical coordinate system as shown in figure A.2. Only the coordinate system is shown here, the magnetised sphere has its centre at the origin as shown in figure A.1.

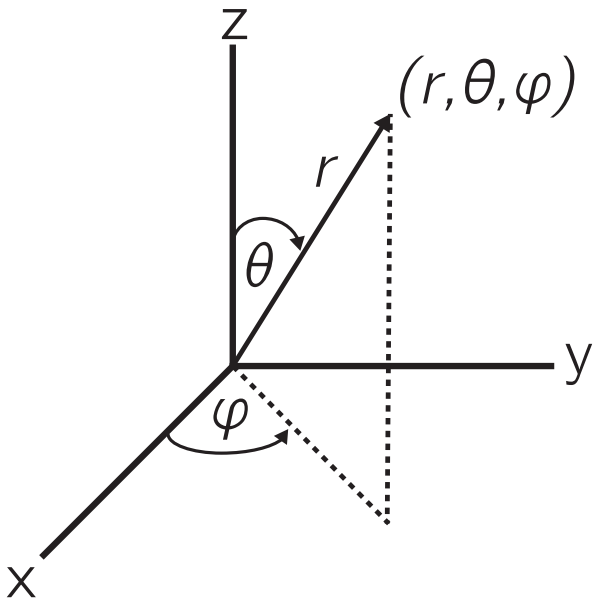

Figure A.2: Spherical coordinate system.

In vector notation, $\mathbf{r}$ is given by

$$\mathbf{r} = \begin{pmatrix} x \\ y \\ z \end{pmatrix} = \begin{pmatrix} r\sin\theta\cos\phi \\ r\sin\theta\sin\phi \\ r\cos\theta \end{pmatrix} = r\sin\theta\cos\phi\ \mathbf{u}_x + r\sin\theta\sin\phi\ \mathbf{u}_y + r\cos\theta\ \mathbf{u}_z \,. \tag{A.9}$$

The magnetisation **M** is uniform in z-direction within the sphere and zero outside of the sphere. This can be written in a single equation using the Heaviside step function which returns 0 if its argument is negative but yields 1 for positive arguments:

$$H(x) = \begin{cases} 0 & \text{if } x < 0 \\ 1 & \text{if } x > 0 \end{cases} . \tag{A.10}$$

The equation for **M** then becomes

$$\mathbf{M} = \mathrm{H}(a - r) M_0 \mathbf{u}_z . \tag{A.11}$$

The goal is to find an expression for the divergence of **M**:

$$\nabla \cdot \mathbf{M} = \begin{pmatrix} \partial_x \\ \partial_y \\ \partial_z \end{pmatrix} \cdot \begin{pmatrix} M_x \\ M_y \\ M_z \end{pmatrix} = \partial_z M_z = M_0 \partial_z \mathrm{H}(a - r) . \tag{A.12}$$

To differentiate in z-direction, the spherical coordinates need to be rewritten to Cartesian coordinates. The mathematical knowledge used is that the derative of the Heaviside step function is 0 for all arguments except when the argument is 0, where the derative is infinite. This is described by the Dirac delta function δ:

$$H'(x) = \delta(x) = \begin{cases} \infty & \text{if } x = 0 \\ 0 & \text{if } x \neq 0 \end{cases} \tag{A.13}$$

such that the integral of the Dirac-delta function is given by

$$\int_{-\infty}^{\infty} \delta(x)\, dx = 1 . \tag{A.14}$$

From the above it is important to observe that equation (A.8) only returns nonzero values exactly at the surface of the sphere, where $a = r$, since this is the only location where the derative of the Heaviside step function is not 0. The area around the surface of the sphere, where the Magnetisation abruptly drops from $M_0 \mathbf{u}_z$ to **0**, can be seen as the source of the magnetic field. Writing out equation (A.12) using the chain rule shows that

$$M_0 \partial_z \mathrm{H}(a - r) = M_0 \delta(a - r) \cdot \frac{\partial r}{\partial z} = M_0 \delta(a - r) \cdot -\frac{1}{2}(x^2 + y^2 + z^2)^{-\frac{1}{2}} \cdot 2z = -M_0 \delta(a - r) \frac{z}{r} . \tag{A.15}$$

Rewriting this to spherical coordinates using equation (A.9) gives

$$\nabla \cdot \mathbf{M} = -M_0 \delta(a - r) \frac{z}{r} = -M_0 \delta(a - r) \cos\theta . \tag{A.16}$$

With the above, equation (A.8) can be rewritten as

$$\Phi(\mathbf{r}) = \frac{M_0}{4\pi} \int_{r'=0}^{\infty} \int_{\theta'=0}^{\pi} \int_{\phi'=0}^{2\pi} \frac{\delta(a - r') \cos\theta' r'^2 \sin\theta'}{|\mathbf{r} - \mathbf{r}'|}\, dr' d\theta' d\phi' . \tag{A.17}$$

Please note that in equation (A.17) a factor $r'^2 \sin\theta'$ has been added which is the multiplication of three scale factors: $h_r = 1$, $h_\theta = r \sin\phi$ and $h_\phi = r$. This is a mathematical necessity while converting from

Cartesian to spherical coordinates while integrating. In order to solve this, it is required to rewrite the denominator using a *Legendre polynomial*:

$$\frac{1}{|\mathbf{r}-\mathbf{r}'|} = \frac{1}{r_>}\sum_{\ell=0}^{\infty}\left(\frac{r_<}{r_>}\right)^{\ell} P_\ell(\cos\gamma)\ . \tag{A.18}$$

In this equation the following symbols are introduced:

$r_> = \max(|\mathbf{r}|, |\mathbf{r}'|)$;
$r_< = \min(|\mathbf{r}|, |\mathbf{r}'|)$;
$P_\ell =$ Legendre polynomial;
$\gamma =$ The angle between **r** and **r'**.

A visual representation of γ is given in figure A.3.

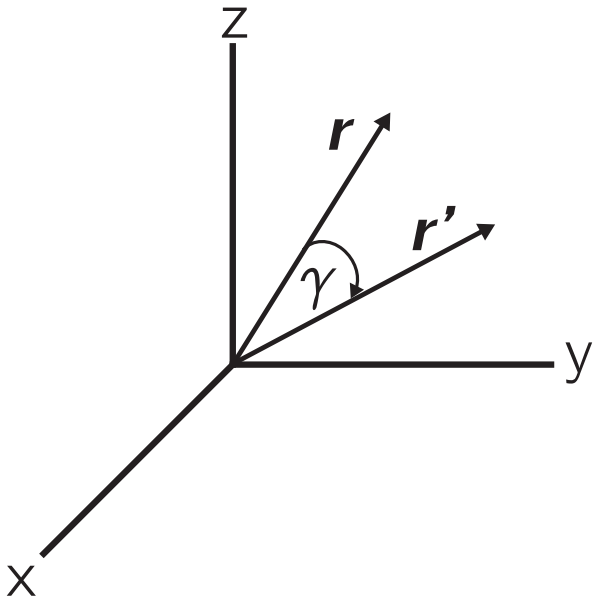

Figure A.3: γ, the angle between **r** and **r**′.

For the purpose of this research it is deemed unnecessary to further discuss Legendre polynomials and their properties, or the mathematical analogy behind equation (A.18). Further explanation of this mathematical topic is extensively described in *Special Functions of Mathematics for Engineers* by Andrews [1]. The final term in equation A.18, $P_\ell(\cos\gamma)$, is given by

$$P_\ell(\cos\gamma) = \frac{4\pi}{2\ell+1}\sum_{m=-\ell}^{\ell} Y^*_{\ell m}(\theta',\phi')Y_{\ell m}(\theta,\phi) \tag{A.19}$$

in which

$$Y_{\ell m}(\theta,\phi) = \sqrt{\frac{2\ell+1}{4\pi}\cdot\frac{(\ell-m)!}{(\ell+m)!}}\cdot P_\ell^m(\cos\theta)\exp(im\phi)\ . \tag{A.20}$$

P_ℓ^m are the *associated Legendre functions* in which Y^*_{lm} is know as the *complex conjugate* of $y_{\ell m}$. Sub-

stituting equation (A.19) in equation (A.17) yields

$$\Phi(\mathbf{r}) = \frac{M_0}{4\pi} \int_{r'=0}^{\infty} \int_{\theta'=0}^{\pi} \int_{\phi'=0}^{2\pi} \delta(a - r') \cos\theta' r'^2 \sin\theta' \frac{1}{r_>} \sum_{\ell=0}^{\infty} \left(\frac{r_<}{r_>}\right)^{\ell} P_\ell(\cos\gamma)\, dr' d\theta' d\phi' \,. \tag{A.21}$$

This function integrates over r and contains the Dirac delta function. It is known that a general form the integral of a Dirac delta function returns

$$\int_{-\infty}^{\infty} f(x)\delta(x - x_0)\, dx = f(x_0) \tag{A.22}$$

which is known as the sifting property. Using this property in equation (A.21) yields

$$\Phi(\mathbf{r}) = \frac{M_0}{4\pi} \int_{\theta'=0}^{\pi} \int_{\phi'=0}^{2\pi} a^2 \cos\theta' \sin\theta' \frac{1}{r_>} \sum_{\ell=0}^{\infty} \left(\frac{r_<}{r_>}\right)^{\ell} P_\ell(\cos\gamma) \quad d\theta' d\phi' \,. \tag{A.23}$$

From here on $r_> = \max(r, a)$ and $r_< = \min(r, a)$. What remains is integration along θ' and ϕ'. It is convenient to start with the integration over ϕ' since ϕ' only appears within $Y^*_{\ell m}$ which is in P^m_ℓ. This means that all other terms can be put in front of the integral (not dependent on ϕ', so constant along the integration) resulting in an integral which has the shape of

$$\int_{\phi'=0}^{2\pi} \exp(im\phi')\, d\phi' = \int_{\phi'=0}^{2\pi} (\cos(m\phi') + i\sin(m\phi'))\, d\phi' = \begin{cases} 2\pi & \text{if} \quad m = 0 \\ 0\pi & \text{otherwise} \end{cases} \,. \tag{A.24}$$

For m = 0 this integral returns 2π, while for all other values of m this integral returns 0, which means that the summation of m can be taken out of the potential equation. The zeroth order of the associated Legendre function P^0_ℓ is the Legendre polynomial P_ℓ, allowing $y_{\ell m}(\theta, \phi)$ to be rewritten to:

$$y_{\ell 0}(\theta, \phi) = \sqrt{\frac{2\ell + 1}{4\pi}} \cdot P_\ell(\cos\theta) \,. \tag{A.25}$$

Substituting this in the expression for the potential equation gives

$$\Phi(\mathbf{r}) = \frac{M_0 a^2}{4\pi} \int_{\theta'=0}^{\pi} \cos\theta' \sin\theta' \frac{1}{r_>} \sum_{\ell=0}^{\infty} \left(\frac{r_<}{r_>}\right)^{l} P_\ell(\cos\theta) P_\ell(\cos\theta')\, d\theta'$$

$$\Phi(\mathbf{r}) = \frac{M_0 a^2}{2} \frac{1}{r_>} \sum_{\ell=0}^{\infty} P_\ell \cos\theta \left(\frac{r_<}{r_>}\right)^{l} \int_{\theta'=0}^{\pi} \cos\theta' \sin\theta' P_l(\cos\theta')\, d\theta' \tag{A.26}$$

which can be solved by renaming some of the terms:

$$\cos\theta' = t \,, \tag{A.27}$$

$$dt = d\cos\theta' = -\sin\theta'\, d\theta' \,, \tag{A.28}$$

$$\int_{\theta'=0}^{\pi} \cos\theta' \sin\theta' P_\ell(\cos\theta')\, d\theta' = \int_{t=-1}^{1} t P_\ell(t)\, dt\,. \tag{A.29}$$

The principle of orthogonality between Legendre polynomials is used (see Andrews [1]):

$$\int_{-1}^{1} P_n(t) P_m(t)\, dt = \frac{2}{2m+1}\delta_{mn} \tag{A.30}$$

in which δ_{mn} is the Kronecker-delta, which returns 1 if $m = n$ and 0 if $m \neq n$. In equation (A.29), t can be rewritten as the first order Legendre polynomial: P_1. From this it follows that only for $\ell = 1$ the solution to the integral is nonzero. Having stated that $\ell = 1$, the solution to equation (A.30) becomes 2/3. The solution to the potential equation can now be written as

$$\Phi(\mathbf{r}) = \frac{M_0 a^2 r_<}{3 r_>^2} \cos\theta\,. \tag{A.31}$$

It can be observed that potential equation (A.31) does not depend on ϕ, which makes sense since ϕ is orthogonal to the direction of the magnetisation. Splitting the potential into two cases, one for inside and one for outside the sphere:

$$\Phi(\mathbf{r}) = \begin{cases} \frac{M_0 r}{3}\cos\theta & \text{if r < a} \\ \frac{M_0 a^3}{3r^2}\cos\theta & \text{if r > a} \end{cases}. \tag{A.32}$$

The magnetic field follows from $\mathbf{H} = -\nabla\Phi$. Using the fact that the gradient of the potential equation can be described by (see Jackson [21])

$$\nabla\Phi = \mathbf{u}_r \frac{\partial\Phi}{\partial r} - \mathbf{u}_\theta \frac{1}{r}\frac{\partial\Phi}{\partial\theta} - \mathbf{u}_\phi \frac{1}{r\sin\theta}\frac{\partial\Phi}{\partial\phi}\,, \tag{A.33}$$

the field **H** can be written as

$$\mathbf{H} = \begin{cases} -\nabla\Phi = \frac{M_0 \cdot r}{3}(\cos\theta\mathbf{u}_r - \sin\theta\mathbf{u}_\theta) = -\frac{M_0}{3}\mathbf{u}_z & \text{if r < a} \\ -\nabla\Phi = \frac{M_0 \cdot a^3}{3r^3}(2\cos\theta\mathbf{u}_\mathbf{r} + \sin\theta\mathbf{u}_\boxtimes) = \frac{M_0 a^3}{3r^3}(3\sin\theta\mathbf{u}_\theta + 2\mathbf{u}_z) & \text{if r > a} \end{cases} \tag{A.34}$$

in which $\mathbf{u}_z = \cos\theta\mathbf{u}_r - \sin\theta\mathbf{u}_\theta$. Using the fact that a sphere's volume is given by $\frac{4}{3}\pi a^3$, for $r > a$ **H** can be rewritten as

$$\mathbf{H} = \frac{V_{\text{sphere}} M_0}{4\pi r^3} \cdot (2\cos\theta\mathbf{u}_r + \sin\theta\mathbf{u}_\theta)\,. \tag{A.35}$$

A.2. Linearly reacting sphere

A sphere with radius a is placed in a uniform background field $\mathbf{H}_0 = H_0\mathbf{u}_z$. Its magnetisation scales linearly with the background field following, as described by Jackson [21] and Griffiths [18]: $\mathbf{H} = H_0\mathbf{u}_z$, and it is stated that the magnetisation inside the sphere is no longer a fixed constant but rather scales linearly with the background field with a relative permeability μ_r. The parameter μ_r describes the magnetic permeability of the material as a multiplication of the magnetic permeability in free space, μ_0. The equation describing the magnetisation within the sphere becomes

$$\mathbf{M} = (\mu_r - 1)\mathbf{H}\,. \tag{A.36}$$

In (A.36), **H** inside the sphere is defined as a superposition of $\mathbf{H}_0$, the background field, and $\mathbf{H}_i$ due to the magnetisation of the sphere itself:

$$\mathbf{H} = \mathbf{H}_0 + \mathbf{H}_i \, . \tag{A.37}$$

Please note that for this example it has been assumed that the magnetic background field points uniformly downwards in the z-direction. Combining equations (A.36) and (A.37) returns the following expression for **M**:

$$\mathbf{M} = (\mu_r - 1)(\mathbf{H}_0 + \mathbf{H}_i) \tag{A.38}$$

In appendix A.1 it iss found that $\mathbf{H}_i$ is equal to $-\frac{1}{3}M_0\mathbf{u_z}$, which means M_0 can be rewritten to

$$\begin{aligned} M_0\mathbf{u}_z &= (\mu_r - 1)(H_0\mathbf{u}_z - \frac{1}{3}M_0\mathbf{u}_z) \\ M_0 &= (\mu_r - 1)(H_0 - \frac{1}{3}M_0) \\ M_0(1 + \frac{1}{3}(\mu_r - 1)) &= (\mu_r - 1)H_0 \\ M_0 &= \frac{\mu_r - 1}{1 + \frac{1}{3}(\mu_r - 1)}H_0 \, . \end{aligned} \tag{A.39}$$

Substituting this into equations (A.35) yields

$$\mathbf{H}_0 + \mathbf{H}_i = H_0\mathbf{u}_z + \frac{V_{\text{sphere}}}{4\pi r^3}(2\cos\theta\mathbf{u}_r + \sin\theta\mathbf{u}_\theta)\frac{\mu_r - 1}{1 + \frac{1}{3}(\mu_r - 1)}H_0 \, . \tag{A.40}$$

To simplify this expression and get rid of the $\mathbf{u}_\theta$ term, the spherical unit vectors $\mathbf{u}_r$, $\mathbf{u}_\phi$ and $\mathbf{u}_\theta$ are rewritten into Cartesian form. The spherical unit vectors are drawn in figure A.4:

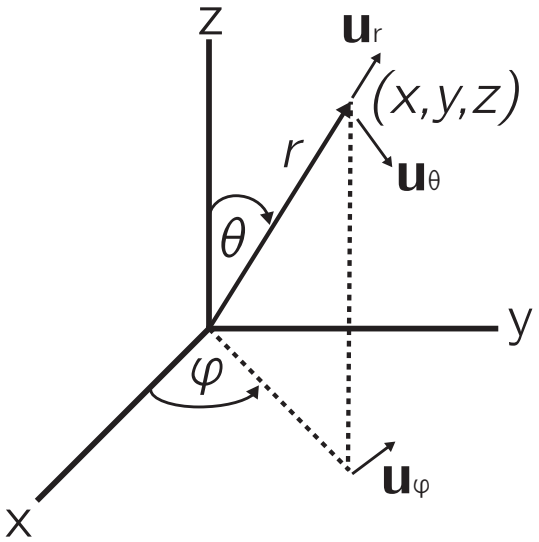

Figure A.4: Spherical unit vectors within the Cartesian coordinate system.

From figure A.4 it can be observed that x, y and z are then given by

$$\begin{aligned} x &= r\sin\theta\cos\phi \\ y &= r\sin\theta\sin\phi \\ z &= r\cos\theta \end{aligned}$$

leading to the following expression for $\mathbf{u}_r$

$$\mathbf{u}_r = \begin{pmatrix} \sin\theta\cos\phi \\ \sin\theta\sin\phi \\ \cos\theta \end{pmatrix}. \tag{A.41}$$

It can be observed that $\mathbf{u}_\phi$ lies in the xy-plane and is therefore independent of z and can be written as

$$\mathbf{u}_\phi = \begin{pmatrix} -\sin\phi \\ \cos\phi \\ 0 \end{pmatrix}. \tag{A.42}$$

In order to find $\mathbf{u}_\theta$, orthogonality between the unit vectors is used:

$$\mathbf{u}_\phi \times \mathbf{u}_r = \mathbf{u}_\theta \tag{A.43}$$

$$\mathbf{u}_\theta = \begin{pmatrix} -\sin\phi \\ \cos\phi \\ 0 \end{pmatrix} \times \begin{pmatrix} \sin\theta\cos\phi \\ \sin\theta\sin\phi \\ \cos\theta \end{pmatrix} = \begin{pmatrix} \cos\phi\cos\theta \\ \sin\phi\cos\theta \\ -\sin\theta \end{pmatrix}. \tag{A.44}$$

Substituting the spherical unit vectors into equation (A.40) yields

$$\mathbf{H} = H_0\mathbf{u}_z + \frac{V_{\text{sphere}}}{4\pi r^3}\left[2\cos\theta\begin{pmatrix} \sin\theta\cos\phi \\ \sin\theta\sin\phi \\ \cos\theta \end{pmatrix} + \sin\theta\begin{pmatrix} \cos\phi\cos\theta \\ \sin\phi\cos\theta \\ -\sin\theta \end{pmatrix}\right]\frac{\mu_r - 1}{1+\frac{1}{3}(\mu_r - 1)}H_0 . \tag{A.45}$$

The part between straight brackets can be rewritten to

$$\begin{pmatrix} 3\cos\theta\sin\theta\cos\phi \\ 3\cos\theta\sin\theta\sin\phi \\ 2\cos^2\theta - \sin^2\theta \end{pmatrix} = \begin{pmatrix} 3\cos\theta\sin\theta\cos\phi \\ 3\cos\theta\sin\theta\sin\phi \\ 3\cos^2\theta - 1 \end{pmatrix} = 3\cos\theta\begin{pmatrix} \sin\theta\cos\phi \\ \sin\theta\sin\phi \\ \cos\theta \end{pmatrix} - \begin{pmatrix} 0 \\ 0 \\ 1 \end{pmatrix}. \tag{A.46}$$

The vectors can then be replaced by $\mathbf{u}_r$ and $\mathbf{u}_z$ and further rewritten to

$$3\cos\theta\mathbf{u}_r - \mathbf{u}_z = \frac{3r\mathbf{u}_r r\cos\theta}{r^2} - \mathbf{u}_z = \frac{3\mathbf{r}z}{r^2} - \mathbf{u}_z = \left(\frac{3\mathbf{r}(\mathbf{m}\cdot\mathbf{r})}{r^2} - \mathbf{m}\right)\frac{1}{M_0 V_{\text{sphere}}}, \tag{A.47}$$

using the knowledge that the magnetic dipole moment $\mathbf{m} = V_{\text{sphere}}M_0\mathbf{u}_z$. Substituting this solution back into equation (A.45) leads to the following equation describing the magnetic field outside a sphere which has a magnetisation that scales linearly with the applied background field:

$$\mathbf{H}(\mathbf{r}) = H_0\mathbf{u}_z + \frac{1}{4\pi r^3}\cdot\frac{H_0(\mu_r - 1)}{1+\frac{1}{3}(\mu_r - 1)}\left(\frac{3\mathbf{r}(\mathbf{m}\cdot\mathbf{r})}{r^2} - \mathbf{m}\right)$$

$$\mathbf{H}(\mathbf{r}) = H_0\mathbf{u}_z + \frac{3H_0(\mu_r - 1)}{4\pi r^3(\mu_r + 2)}\left(\frac{3\mathbf{r}(\mathbf{m}\cdot\mathbf{r})}{r^2} - \mathbf{m}\right). \tag{A.48}$$

A.3. Uniformly magnetised prolate spheroid

In order to describe the magnetic field around a magnetised spheroid, a new coordinate system is introduced, with so-called prolate spheroidal coordinates (ξ, η, ϕ) as introduced by Morse and Feshbach [38]. This is explained further below and illustrated in figure A.5. The derivation provided here follows from

Lepelaars [33].

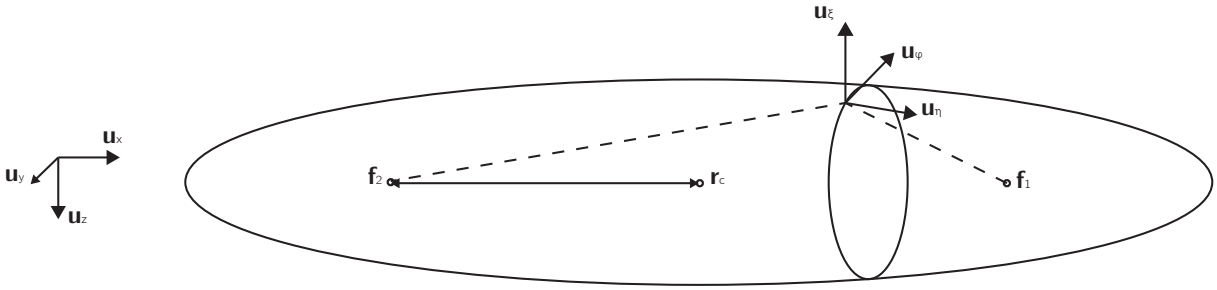

Figure A.5: Prolate spheroid in spherical coordinates.

The centre point of the spheroid is described in Cartesian coordinates by

$$\mathbf{r}_c = \begin{pmatrix} x_0 \\ y_0 \\ z_0 \end{pmatrix} . \tag{A.49}$$

The focal length $2f$ is introduced as the distance (in x-direction) from the centre towards the two focal points:

$$\begin{aligned} \mathbf{f1} &= \mathbf{r}_c + f\mathbf{u}_x \\ \mathbf{f2} &= \mathbf{r}_c - f\mathbf{u}_x . \end{aligned} \tag{A.50}$$

A position vector $\mathbf{r} = (x, y, z)^T$ can now be defined in terms of (ξ, η, ϕ), while using that $r_1 = |\mathbf{r} - \mathbf{f_1}|$ and $r_2 = |\mathbf{r} - \mathbf{f_2}|$:

$$\begin{aligned} \xi &= \frac{r_1 + r_2}{2f} \\ \eta &= \frac{r_1 - r_2}{2f} \\ \cos(\phi) &= \frac{y - y_0}{\sqrt{(y - y_0)^2 + (z - z_0)^2}} \\ \sin(\phi) &= \frac{z - z_0}{\sqrt{(y - y_0)^2 + (z - z_0)^2}} . \end{aligned} \tag{A.51}$$

The surface of the spheroid is defined as $\xi = \xi_0$ so that $\xi < \xi_0$ lies within the spheroid and $\xi > \xi_0$ lies in free space. The uniform magnetisation is then described by:

$$\mathbf{M} = \begin{cases} M_x\mathbf{u}_x + M_y\mathbf{u}_y + M_z\mathbf{u}_z & \text{for} \quad \xi < \xi_0 \\ \mathbf{0} & \text{for} \quad \xi > \xi_0 \end{cases} . \tag{A.52}$$

The spheroid has length $l = 2f\xi_0$, diameter $d = 2f\sqrt{\xi_0^2 - 1}$ and volume $V_{\text{spheroid}} = V_0 = \pi d^2 l/6 = 4\pi f^3 \xi_0(\xi_0^2 - 1)/3$. For further computations, a scalar parameter m is defined as the ratio between the

length and the width as

$$m = \frac{l}{d} = \frac{\xi_0}{\sqrt{\xi_0^2 - 1}} \tag{A.53}$$

so ξ_0 can be defined in terms om m as

$$\xi_0 = \frac{m}{\sqrt{m^2 - 1}} \,. \tag{A.54}$$

Analogous so section 2.2 the magnetic field follows from

$$\mathbf{H} - \nabla\Phi \qquad \& \qquad \nabla^2\Phi = \nabla \cdot \mathbf{M} \tag{A.55}$$

with the magnetic potential

$$\Phi(\mathbf{r}) = \frac{-1}{4\pi} \iiint_{\Omega} \frac{(\nabla' \cdot \mathbf{M})(\mathbf{r}')}{|\mathbf{r} - \mathbf{r}'|} d^3\mathbf{r}' \tag{A.56}$$

in which Ω is the entire domain in which the potential equation is nonzero. Solving $\nabla\cdot\mathbf{M}$ while reintroducing the Heaviside function yields

$$\mathbf{M}(\mathbf{r}) = \mathbf{M}H(\xi_0 - \xi) = (M_x\mathbf{u}_x + M_y\mathbf{u}_y + M_z\mathbf{u}_z)H(\xi_0 - \xi) \tag{A.57}$$

$$\nabla \cdot \mathbf{M} = -\delta(\xi_0 - \xi)\left(M_x\frac{\partial\xi}{\partial x} + M_y\frac{\partial\xi}{\partial y} + M_z\frac{\partial\xi}{\partial z}\right) = -\delta(\xi_0 - \xi)\mathbf{M} \cdot \nabla\xi \,. \tag{A.58}$$

In anticipation of later use the gradients of the spherical coordinates are calculated, and in order to do so some elementary properties are derived. Combining the definitions of ξ and η it is possible to rewrite r_1 and r_2 to

$$r_1 = f(\xi + \eta), \qquad r_2 = f(\xi - \eta) \,. \tag{A.59}$$

The product of f, ξ and η can be simplified to

$$\begin{aligned} f\xi\eta = \tfrac{r_1^2 - r_2^2}{4f} = \tfrac{1}{4}\{&[(x - x_0 - f)^2 + (y - y_0)^2 + (z - z_0)^2] - \\ &[(x - x_0 + f)^2 + (y - y_0)^2 + (z - z_0)^2]\} = -(x - x_0) \,. \end{aligned} \tag{A.60}$$

With these properties, $|\mathbf{r} - \mathbf{f_1}|^2$ can be rewritten in the following manner:

$$\begin{aligned} &|\mathbf{r} - \mathbf{f_1}|^2 = r_1^2 = (f(\xi + \eta))^2 = (x - x_0 - f)^2 + (y - y_0)^2 + (z - z_0)^2 \\ &(f(\xi + \eta))^2 = (-f\xi\eta - f)^2 + (y - y_0)^2 + (z - z_0)^2 \\ &f^2(\xi^2 + \eta^2 + 2\xi\eta) = f^2\xi^2\eta^2 + f^2 + 2f^2\xi\eta + (y - y_0)^2 + (z - z_0)^2 \\ &f^2(\xi^2 + \eta^2 - \xi^2\eta^2 - 1) = (y - y_0)^2 + (z - z_0)^2 \\ &f\sqrt{(\xi^2 - 1)(1 - \eta^2)} = \sqrt{(y - y_0)^2 + (z - z_0)^2} \,. \end{aligned} \tag{A.61}$$

To summarise the above, it can be stated that

$$x - x_0 = -f\xi\eta \tag{A.62}$$

$$y - y_0 = \sqrt{(y - y_0)^2 + (z - z_0)^2}\cos\phi = f\sqrt{(\xi^2 - 1)(1 - \eta^2)}\cos\phi \tag{A.63}$$

$$z - z_0 = \sqrt{(y-y_0)^2 + (z-z_0)^2}\sin\phi = f\sqrt{(\xi^2-1)(1-\eta^2)}\sin\phi\ . \tag{A.64}$$

The following expression for $\nabla\xi$ is obtained:

$$\nabla\xi = \nabla\frac{r_1+r_2}{2f} = \frac{1}{2f}\nabla\Bigg(\sqrt{(x-x_0+f)^2+(y-y_0)^2+(z-z_0)^2}+ \sqrt{(x-x_0-f)^2+(y-y_0)^2+(z-z_0)^2}\Bigg) \tag{A.65}$$

The gradient of $\nabla\xi$ is given by: $\nabla\xi = (\frac{\partial\xi}{\partial x}, \frac{\partial\xi}{\partial y}, \frac{\partial\xi}{\partial z})^T$. Renaming $r_1 = \sqrt{u}$, $r_2 = \sqrt{j}$, $(x - x_0 - f) = w$ and $(x - x_0 + f) = k$ and using the double chain-rule for the gradient in x-direction

$$\nabla_x\xi = \frac{1}{2f}\left(\frac{\partial}{\partial u}u^{\frac{1}{2}}\frac{\partial u}{\partial w}\frac{\partial w}{\partial x} + \frac{\partial}{\partial j}j^{\frac{1}{2}}\frac{\partial j}{\partial k}\frac{\partial k}{\partial x}\right)$$
$$\nabla_x\xi = \frac{1}{2f}\left(\frac{1}{2}u^{-\frac{1}{2}}\cdot 2w\cdot 1 + \frac{1}{2}j^{-\frac{1}{2}}\cdot 2k\cdot 1\right)$$
$$\nabla_x\xi = \frac{1}{2f}\left(\frac{x-x_0-f}{r_1} + \frac{x-x_0+f}{r_1}\right).$$

If this process is repeated for the gradients in y and z-directions, the following relation for the gradient can be obtained:

$$\nabla\xi = \frac{1}{2f}\left(\frac{\mathbf{r}-\mathbf{f_1}}{r_1} + \frac{\mathbf{r}-\mathbf{f_2}}{r_1}\right). \tag{A.66}$$

Substituting the properties derived earlier into equation (A.66) gives the following definitions for $\nabla\xi$:

$$\begin{aligned}\nabla\xi &= \left(\tfrac{\mathbf{r}-\mathbf{f_1}}{r_1} + \tfrac{\mathbf{r}-\mathbf{f_2}}{r_1}\right)\\ &= \tfrac{1}{2f}\Big\{\tfrac{1}{f(\xi+\eta)}\left[f(\xi\eta+1)\mathbf{u}_x + (\cos\phi\mathbf{u}_y + \sin\phi\mathbf{u}_z)f\sqrt{(\xi^2-1)(1-\eta^2)}\right]\\ &\quad + \tfrac{1}{f(\xi-\eta)}\left[f(\xi\eta-1)\mathbf{u}_x + (\cos\phi\mathbf{u}_y + \sin\phi\mathbf{u}_z)f\sqrt{(\xi^2-1)(1-\eta^2)}\right]\Big\}\\ &= \tfrac{1}{f(\xi^2-\eta^2)}\Big\{-(\xi^2-1)\eta\mathbf{u}_x + \xi(\cos\phi\mathbf{u}_y + \sin\phi\mathbf{u}_z)\sqrt{(\xi^2-1)(1-\eta^2)}\Big\}.\end{aligned} \tag{A.67}$$

Analogous to this the gradient of η, $\cos\phi$ and $\sin\phi$ become

$$\nabla\eta = \frac{1}{f(\xi^2-\eta^2)}\left\{-(1-\eta^2)\xi\mathbf{u}_x + \eta(\cos\phi\mathbf{u}_y + \sin\phi\mathbf{u}_z)\sqrt{(\xi^2-1)(1-\eta^2)}\right\} \tag{A.68}$$

$$\nabla\cos\phi = \frac{\sin\phi}{f\sqrt{(\xi^2-1)(1-\eta^2)}}(\sin\phi\mathbf{u}_y - \cos\phi\mathbf{u}_z) \tag{A.69}$$

$$\nabla\sin\phi = \frac{-\cos\phi}{f\sqrt{(\xi^2-1)(1-\eta^2)}}(\sin\phi\mathbf{u}_y - \cos\phi\mathbf{u}_z)\ . \tag{A.70}$$

In order to evaluate the potential function the following expansion is used, as described by Andrews [1]

$$\frac{1}{|\mathbf{r}-\mathbf{r}'|} = \frac{1}{f}\sum_{n=0}^{\infty}\sum_{m=0}^{n}(2n+1)\epsilon_m i^m\left[\frac{(n-m)!}{(n+m)!}\right]\cos[m(\phi-\phi')]\cdot \\ P_n^m(\eta)P_n^m(\eta')\begin{cases} P_n^m(\xi)P_n^m(\xi') & \text{if } \xi<\xi' \\ P_n^m(\eta)P_n^m(\eta') & \text{if } \xi>\xi' \end{cases} \tag{A.71}$$

in which the Neumann factor has been introduced as

$$\epsilon_m = \begin{cases} 1 & m=0 \\ 2 & m=1,\dots \end{cases} \tag{A.72}$$

and where P_n^m and Q_n^m are the associated Legendre functions of the first and second kind, respectively. In order to evaluate the integral, scale factors need to be implemented in the same manner as in appendix A.1. The scale factors in the prolate spherical coordinate system are:

$$h_\xi = f\sqrt{\frac{\xi^2-\eta^2}{\xi^2-1}}, \qquad h_\eta = f\sqrt{\frac{\xi^2-\eta^2}{1-\eta^2}}, \qquad h_\phi = f\sqrt{(\xi^2-1)(1-\eta^2)}\,. \tag{A.73}$$

The potential function can now be rewritten to

$$\Phi(r) = -\frac{1}{4\pi}\int_{\xi'=1}^{\infty}\int_{\eta'=-1}^{1}\int_{\phi'=0}^{2\pi}\frac{-\delta(\xi_0-\xi')\mathbf{M}\cdot\nabla\xi}{|\mathbf{r}-\mathbf{r}'|}h_\xi h_\eta h_\phi\; d\xi' d\eta' d\phi'$$

$$\Phi(r) = -\tfrac{1}{4\pi}\int_{\xi'=1}^{\infty}\int_{\eta'=-1}^{1}\int_{\phi'=0}^{2\pi}\tfrac{-\delta(\xi_0-\xi')}{f(\xi'^2-\eta'^2)}\Big\{-(\xi'^2-1)\eta' M_{0x}+\xi'\cos\phi' M_{0y}+$$

$$\sin\phi' M_{0z})\sqrt{(\xi'^2-1)(1-\eta'^2)}\Big\}\cdot\tfrac{1}{|\mathbf{r}-\mathbf{r}'|}\cdot$$

$$f\sqrt{\tfrac{\xi'^2-\eta'^2}{\xi'^2-1}}\cdot f\sqrt{\tfrac{\xi'^2-\eta'^2}{1-\eta'^2}}\cdot f\sqrt{(\xi^2-1)(1-\eta^2)}\;\; d\xi' d\eta' d\phi'$$

$$\Phi(r) = -\tfrac{1}{4\pi}\int_{\xi'=1}^{\infty}\int_{\eta'=-1}^{1}\int_{\phi'=0}^{2\pi}\tfrac{-\delta(\xi_0-\xi')}{f(\xi'^2-\eta'^2)}\Big\{-(\xi'^2-1)\eta' M_{0x}+\xi'(\cos\phi' M_{0y}+$$

$$\sin\phi' M_{0z})\sqrt{(\xi'^2-1)(1-\eta'^2)}\Big\}\cdot\tfrac{1}{|\mathbf{r}-\mathbf{r}'|}\cdot \tag{A.74}$$

$$f^3(\xi^2-\eta^2)\; d\xi' d\eta' d\phi'\,.$$

At this point, the potential that needs to be evaluated has the following shape:

$$\Phi(r) = \frac{-1}{4\pi}\int_{\xi'=1}^{\infty}\int_{\eta'=-1}^{1}\int_{\phi'=0}^{2\pi} -\delta(\xi_0-\xi')\frac{1}{f(\xi'^2-\eta'^2)}\Big\{-(\xi'^2-1)\eta' M_{0x}+$$
$$\xi'(\cos(\phi')M_{0y}+\sin(\phi')M_{0z})\sqrt{(\xi'^2-1)(1-\eta'^2)}\Big\}$$
$$\frac{1}{f}\sum_{n=0}^{\infty}\sum_{m=0}^{n}(2n+1)\epsilon_m i^m\left[\frac{(n-m)!}{(n+m)!}\right]\cos[m(\phi-\phi')]$$
$$P_n^m(\eta)P_n^m(\eta')P_n^m(\xi_<)Q_n^m(\xi_>)\cdot f^3\ (\xi'^2-\eta'^2)d\xi'\ d\eta' d\phi' \tag{A.75}$$

where $\xi_< = \min(\xi,\xi')$ and $\xi_> = \max(\xi,\xi')$. In the same way as in section 2.2, the fact that the Dirac-delta function's integral only exists while the argument is 0 is used (when $\xi' = \xi_0$), meaning that integrating ξ' over the infinite domain equals getting rid of the delta function and replacing all ξ' terms with ξ_0 terms. The summations (which do not contain integral dependent terms) are moved in front of the integrals and the final term $f^3(\xi'^2-\eta'^2)$ is eliminated to give

$$\Phi(r) = \frac{f}{4\pi}\sum_{n=0}^{\infty}\sum_{m=0}^{n}(2n+1)\epsilon_m i^m\left[\frac{(n-m)!}{(n+m)!}\right]P_n^m(\eta)P_n^m(\xi_<)Q_n^m(\xi_>)$$
$$\int_{\eta'=-1}^{1}\int_{\phi'=0}^{2\pi}\Big\{-(\xi_0-1)\eta' M_{0x}+\xi_0(\cos\phi' M_{0y}+\sin\phi' M_{0z})\cdot \tag{A.76}$$
$$\sqrt{(\xi'^2-1)(1-\eta'^2)}\Big\}\cos[m(\phi-\phi')]P_n^m(\eta')\ d\eta' d\phi'$$

in which $\xi_< = \min(\xi,\xi_0)$ and $\xi_> = \max(\xi,\xi_0)$. When integrating over ϕ' it can be concluded that only the term $m = 0$ for M_{0x} and $m = 1$ for M_{0y} and M_{0z} have a nonzero value. This results in

$$\Phi(r) = \frac{f}{4\pi}\sum_{n=0}^{\infty}(2n+1)\sum_{m=0}^{n}\Big\{-2\pi\delta_{m0}P_n^0(\eta)P_n^0(\xi_<)Q_n^0(\xi_>)(\xi_0^2-1)M_{0x}\cdot$$
$$\int_{\eta'=-1}^{1}\eta' P_n^0(\eta')d\eta' + \frac{2\pi i}{n^2(n+1)^2}\delta_{m1}P_n^1(\eta)P_n^1(\xi_<)Q_n^1(\xi_>)\cdot \tag{A.77}$$
$$\xi_0(\cos\phi' M_{0y}+\sin\phi' M_{0z})\sqrt{\xi_0-1}\int_{\eta'=-1}^{1}\sqrt{1-\eta'^2}P_n^1(\eta')\ d\eta'\Big\}.$$

The Legendre functions for complex arguments are defined by the following expressions, as described by Morse and Feshbach [38]:

$$P_n^m(z) = (1-z^2)^{\frac{m}{2}}\left(\frac{d}{dz}\right)^m P_n(z), \qquad P_n(z) = \frac{1}{2^n n!}\left(\frac{d}{dz}\right)^n (z^2-1)^n, \tag{A.78}$$

$$Q_n^m(z) = (-1)^m(z^2-1)^{\frac{m}{2}}\left(\frac{d}{dz}\right)^m Q_n(z), \tag{A.79}$$

$$Q_n(z) = \frac{1}{2^n n!}\left(\frac{d}{dz}\right)^n\left[(z^2-1)^n)\ln\left(\frac{z+1}{z-1}\right)\right] - \frac{1}{2}P_n(z)\ln\left(\frac{z+1}{z-1}\right), \tag{A.80}$$

from which follows for this particular case that

$$P_1^0(z) = z, \qquad P_1^1(z) = \sqrt{1-z^2},$$
$$Q_1^0(z) = \frac{z}{2}\ln\left(\frac{z+1}{z-1}\right) - 1,\ Q_1^1(z) = \frac{z}{\sqrt{z^2-1}} - \frac{\sqrt{z^2-1}}{2}\ln\left(\frac{z+1}{z-1}\right). \tag{A.81}$$

For real argument, $-1 < \eta > 1$ and $\xi > 1$ it follows that

$$P_1^0(\eta) = \eta, \qquad P_1^1 = \sqrt{1-\eta^2}, \qquad P_1^0(\xi) = \xi P_1^1(\xi) = \sqrt{1-\xi^2}$$
$$Q_1^0(\xi) = \frac{\xi}{2}\ln\left(\frac{\xi+1}{\xi-1}\right) - 1, \qquad Q_1^1(\xi) = \sqrt{xi^2-1}\left[\frac{\xi}{\xi^2-1} - \frac{1}{2}\left(\frac{\xi+1}{\xi-1}\right)\right]. \tag{A.82}$$

For the remaining integrals the orthogonality of the Legendre functions is used, as shown in equation (A.30). This orthogonality simplifies the integrals over η' in equation A.77 to

$$\int_{\eta'=-1}^{1} \eta' P_n^0(\eta')d\eta' = \int_{\eta'=-1}^{1} P_1^0(\eta')P_n^0(\eta')d\eta' = \int_{\eta'=-1}^{1} P_1^0(\eta')P_1^0(\eta')d\eta' =$$
$$\frac{2}{2\cdot 1+1}\cdot\frac{(1+0)!}{(1-0)!} = \frac{2}{3} \tag{A.83}$$

$$\int_{\eta'=-1}^{1} \sqrt{1-\eta'^2}P_n^1(\eta')d\eta' = \int_{\eta'=-1}^{1} P_1^1(\eta')P_n^1(\eta')d\eta' = \int_{\eta'=-1}^{1} P_1^1(\eta')P_1^1(\eta')d\eta' =$$
$$\frac{2}{2\cdot 1+1}\cdot\frac{(1+1)!}{(1-1)!} = \frac{4}{3} \tag{A.84}$$

while discovering that only $n = 1$ survives for the entire solution. Combined with the expressions above $\Phi(r)$ can be rewritten to

$$\Phi(r) = \frac{f}{4\pi}(2\cdot 1+1)\Big\{-2\pi M_{0x}\eta\xi_<(\xi_0^2-1)Q_1^0(\xi_>)\cdot\frac{2}{3} + \frac{2\pi i}{1^2(1+1)^2}\sqrt{1-\eta^2}i\sqrt{\xi^2-1}$$
$$Q_1^1(\xi_>)\xi_0\left(\cos\phi' M_{0y} + \sin\phi' M_{0z}\right)\sqrt{\xi_0^2-1}\cdot\frac{4}{3}\Big\}$$

$$\Phi(r) = -f(\xi_0^2-1)M_{0x}\eta\xi_<Q_1^0(\xi_>) + \frac{f}{2}\xi_0\left(\cos\phi' M_{0y}\cdot\frac{4}{3} + \sin\phi' M_{0z}\right)\cdot$$
$$\sqrt{(xi_0^2-1)(1-\eta'^2)(\xi_<^2-1)}Q_1^1(\xi_>). \tag{A.85}$$

Using the properties derived in equations (A.60) and (A.61) the definition for the potential inside the spheroid, in Cartesian coordinates, becomes

$$\Phi(r) = (\xi_0^2-1)Q_1^0(\xi_0)(x-x_0)M_{0x} + \frac{\xi_0}{2}\sqrt{\xi_0^2-1}Q_1^1(\xi_0)\cdot$$
$$[(y-y_0)M_{0y} + (z-z_0)M_{0z}]. \tag{A.86}$$

In order to find the magnetic field inside the spheroid, **H** is defined as the negative gradient of Φ:

$$\mathbf{H}(\mathbf{r}) = -\nabla\Phi = -(\xi_0 - 1)Q_1^0(\xi_0)M_{0x}\mathbf{u_x} - \frac{\xi_0}{2}\sqrt{\xi_0^2 - 1}Q_1^1(\xi_0)[M_{0y} + M_{0z}] \tag{A.87}$$

From this equation it follows that the H-field inside the spheroid is uniform and in opposite direction to the Magnetisation **M**. If the demagnetisation factors N_x, N_y and N_z are reintroduced $\mathbf{H}(\mathbf{r})$ becomes

$$\mathbf{H}(\mathbf{r}) = -N_x M_{0x}\mathbf{u}_x - N_y M_{0y}\mathbf{u}_y - N_z M_{0z}\mathbf{u}_z \tag{A.88}$$

with

$$N_x = (\xi_0^2 - 1)Q_1^0(\xi_0), \qquad N_y = N_z = \frac{\xi_0}{2}\sqrt{\xi_0 - 1}Q_1^1(\xi_0)\,. \tag{A.89}$$

In order to rewrite the demagnetisation factors in terms of the ratio between length and diameter m:

$$m = \frac{l}{d} = \frac{\xi_0}{\sqrt{\xi_0^2 - 1}} \tag{A.90}$$

from which follows that

$$\xi_0 = \frac{m}{\sqrt{m^2 - 1}}, \qquad \frac{\xi_0 + 1}{\xi_0 - 1} = \left(m + \sqrt{m^2 - 1}\right)^2\,. \tag{A.91}$$

This gives the following equations for the demagnetisation factors in terms of the length/width ratio:

$$N_x = \frac{1}{m^2 - 1}\left[\frac{m}{m^2 - 1}\ln\left(m + \sqrt{m - 1}\right) - 1\right] \tag{A.92}$$

$$N_y = N_z = \frac{m}{2(m^2 - 1)}\left[m - \frac{1}{m^2 - 1}\ln\left(m + \sqrt{m - 1}\right)\right]\,. \tag{A.93}$$

The potential outside of the spheroid is given by

$$\mathbf{H}(\mathbf{r}) = f\xi_0(\xi_0^2 - 1)\nabla\left[-M_{0x}\eta Q_1^0(\xi) + \frac{\sqrt{1 - \eta^2}}{2}(\cos\phi M_{0y} + \sin\phi M_{0z}Q_1^1(\xi)\right]\,. \tag{A.94}$$

In order to solve this, the following derivatives are defined:

$$\begin{aligned} &\partial_\eta\sqrt{1 - \eta^2} = \tfrac{-\eta}{\sqrt{1-\eta^2}}, \qquad \partial_\xi Q_1^0(\xi) = \tfrac{1}{2}\ln\left(\tfrac{\xi+1}{\xi-1}\right), \\ &\partial_\xi Q_1^1(\xi) = \tfrac{-1}{\sqrt{\xi^2-1}}\left[\tfrac{\xi}{2}\ln\left(\tfrac{\xi+1}{\xi-1}\right) - 1 + \tfrac{1}{\xi^2-1}\right]\,. \end{aligned} \tag{A.95}$$

It is found that

$$\mathbf{B} = \mu_0\xi_0(\xi_0^2 - 1)\underline{\underline{A}}\mathbf{M} \tag{A.96}$$

in which

$$\underline{\underline{A}} = \begin{pmatrix} A_{xx} & A_{xy} & A_{xz} \\ A_{yx} & A_{yy} & A_{yz} \\ A_{zx} & A_{zy} & A_{zz} \end{pmatrix} \tag{A.97}$$

with

$$A_{xx} = f\partial_x\left(\eta Q_1^0(\xi)\right) = -\frac{1}{2}\ln\left(\frac{\xi + 1}{\xi - 1}\right) + \frac{\xi}{\xi^2 - \eta^2} \tag{A.98a}$$

$$A_{xy} = -\frac{f}{2}\partial_x\left(\sqrt{1-\eta^2}\cos(\phi)Q_1^1(\xi)\right) = -\frac{\eta\cos(\phi)}{\xi^2-\eta^2}\sqrt{\frac{1-\eta^2}{\xi^2-1}} \tag{A.98b}$$

$$A_{xz} = -\frac{f}{2}\partial_x\left(\sqrt{1-\eta^2}\sin(\phi)Q_1^1(\xi)\right) = -\frac{\eta\sin(\phi)}{\xi^2-\eta^2}\sqrt{\frac{1-\eta^2}{\xi^2-1}} \tag{A.98c}$$

$$A_{yx} = f\partial_y\left(\eta Q_1^0(\xi)\right) = A_{xy} \tag{A.98d}$$

$$\begin{aligned} A_{yy} =& -\tfrac{f}{2}\partial_y\left(\sqrt{1-\eta^2}\cos(\phi)Q_1^1(\xi)\right) = \\ & -\tfrac{1}{4}\ln\left(\tfrac{\xi+1}{\xi-1}\right) + \tfrac{\xi}{\xi^2-1}\left[\tfrac{1-\eta^2}{\xi^2-\eta^2}\cos(\phi)^2 - \tfrac{1}{2}\right] \end{aligned} \tag{A.98e}$$

$$\begin{aligned} A_{yz} =& -\tfrac{f}{2}\partial_y\left(\sqrt{1-\eta^2}\sin(\phi)Q_1^1(\xi)\right) = \\ & \tfrac{\xi(1-\eta^2)}{(\xi^2-1)(\xi^2-\eta^2)}\sin(\phi)\cos(\phi) \end{aligned} \tag{A.98f}$$

$$A_{zx} = f\partial_z\left(\eta Q_1^0(\xi)\right) = A_{xz} \tag{A.98g}$$

$$A_{zy} = -\frac{f}{2}\partial_z\left(\sqrt{1-\eta^2}\cos(\phi)Q_1^1(\xi)\right) = A_{yz} \tag{A.98h}$$

$$\begin{aligned} A_{zz} =& -\tfrac{f}{2}\partial_z\left(\sqrt{1-\eta^2}\sin(\phi)Q_1^1(\xi)\right) = \\ & \tfrac{1}{4}\ln\left(\tfrac{\xi+1}{\xi-1}\right) + \tfrac{\xi}{\xi^2-1}\left[\tfrac{1-\eta^2}{\xi^2-\eta^2}\sin(\phi)^2 - \tfrac{1}{2}\right] . \end{aligned} \tag{A.98i}$$

A.4. Uniformly magnetised plate

A plate with width w, length ℓ, and thickness t in respectively x, y and z-direction exhibits a uniform magnetisation in x-direction, M_0. Using the earlier introduced Heaviside step function H, the magnetisation can be written as

$$\begin{aligned} \mathbf{M} = M_0 \cdot & \left[H\left(x+\tfrac{w}{2}\right) - H\left(x-\tfrac{w}{2}\right)\right] \cdot \left[H\left(y+\tfrac{\ell}{2}\right) - H\left(y-\tfrac{\ell}{2}\right)\right] \cdot \\ & \left[H\left(z+\tfrac{t}{2}\right) - H\left(z-\tfrac{t}{2}\right)\right]\mathbf{u}_x . \end{aligned} \tag{A.99}$$

The three magnetostatic field equations are identical to the sphere and spheroid

$$\nabla \times \mathbf{H} = 0 \,, \tag{A.100}$$

$$\nabla \cdot \mathbf{B} = 0 \,, \tag{A.101}$$

$$\mathbf{B} = \mu_0(\mathbf{H} + \mathbf{M}) \,. \tag{A.102}$$

Similar to previous examples, since $\nabla \times \mathbf{H} = 0$, a scalar potential Φ can be introduced such that

$$\mathbf{H} = -\nabla\Phi \,. \tag{A.103}$$

This results in

$$\nabla \cdot \mathbf{B} = \nabla \cdot \mu_0(\mathbf{H} + \mathbf{M}) = \mu_0(\nabla\mathbf{H} + \nabla\mathbf{M}) = 0 \tag{A.104}$$

from which follows that

$$\nabla \cdot \mathbf{H} = -\nabla \cdot \mathbf{M} \,. \tag{A.105}$$

From this follows the potential equation

$$\begin{aligned} \nabla^2\Phi &= \nabla \cdot \nabla\Phi = -\nabla \cdot \mathbf{H} = \nabla \cdot \mathbf{M} \\ \nabla^2\Phi &= M_0 \cdot \left[\delta\left(x + \frac{w}{2}\right) - \delta\left(x - \frac{w}{2}\right)\right] \cdot \left[U\left(y + \frac{\ell}{2}\right) - U\left(y - \frac{\ell}{2}\right)\right] \cdot \left[U\left(z + \frac{t}{2}\right) - U\left(z - \frac{t}{2}\right)\right] \,. \end{aligned} \tag{A.106}$$

The stepfunctions become Dirac-delta functions after differentiating, similar to appendix A.1. The solution to this potential equation is given by

$$\Phi(\mathbf{r}) = \frac{-1}{4\pi} \iiint_{\Omega} \frac{(\nabla' \cdot \mathbf{M})(\mathbf{r}')}{|\mathbf{r} - \mathbf{r}'|} \, d^3r \tag{A.107}$$

in which Ω represents the entire three-dimensional domain. Substituting the expression for $\nabla \cdot \mathbf{M}$ into equation A.107 yields

$$\Phi(\mathbf{r}) = \frac{-M_0}{4\pi} \int_{y'=-\ell/2}^{\ell/2} \int_{z'=-d/2}^{d/2} \left(\frac{1}{|\mathbf{r} - (-\frac{w}{2}\mathbf{u}_x + y'\mathbf{u}_y + z'\mathbf{u}_z)|} - \frac{1}{|\mathbf{r} - (\frac{w}{2}\mathbf{u}_x + y'\mathbf{u}_y + z'\mathbf{u}_z)|} \right) dy'dz' \,. \tag{A.108}$$

It is assumed that the plate is thin, $t \ll \{w, l\}$. Since the behaviour directly near the edges of the plate is not of great importance to us, equation (A.108) can be simplified to

$$\begin{aligned} \Phi(\mathbf{r}) &\approx \frac{-M_0 t}{4\pi} \int_{y'=-\ell/2}^{\ell/2} \left(\frac{1}{|\mathbf{r} - (-\frac{b}{2}\mathbf{u}_x + y'\mathbf{u}_y + z'\mathbf{u}_z)|} - \frac{1}{|\mathbf{r} - (\frac{w}{2}\mathbf{u}_x + y'\mathbf{u}_y + z'\mathbf{u}_z)|} \right) dy' \\ &= \frac{-M_0 t}{4\pi} \int_{y'=-\ell/2}^{\ell/2} \left(\frac{1}{\sqrt{(x + \frac{w}{2})^2 + (y - y')^2 + z^2}} - \frac{1}{\sqrt{(x - \frac{w}{2})^2 + (y - y')^2 + z^2}} \right) dy' \\ &= \frac{-M_0 t}{4\pi} \int_{\tilde{y}=-\ell/2-y}^{\ell/2-y} \left(\frac{1}{\sqrt{(x + \frac{w}{2})^2 + \tilde{y}^2 + z^2}} - \frac{1}{\sqrt{(x - \frac{w}{2})^2 + \tilde{y}^2 + z^2}} \right) d\tilde{y} \end{aligned} \tag{A.109}$$

in which $\tilde{y} = y' - y$ is substituted. This integral can be solved analytically using the mathematical knowledge that

$$\int \frac{ds}{\sqrt{s^2+p^2}} = \ln\left(\sqrt{s^2+p^2} - s\right) . \tag{A.110}$$

Using equation (A.110), the potential becomes

$$\begin{aligned}\Phi(\mathbf{r}) \approx \frac{-M_0 t}{4\pi}&\left[\ln\left(\sqrt{(x-\tfrac{w}{2})^2+\tilde{y}^2+z^2}-\tilde{y}\right)-\ln\left(\sqrt{(x+\tfrac{w}{2})^2+\tilde{y}^2+z^2}-\tilde{y}\right)\right]_{\tilde{y}=-\ell/2-y}^{\ell/2-y}\\ = \frac{M_0 t}{4\pi}&\left[\ln\left(\sqrt{(x-\tfrac{w}{2})^2+(y-\tfrac{\ell}{2})^2+z^2}+(y-\tfrac{\ell}{2})\right)-\right.\\ &\ln\left(\sqrt{(x-\tfrac{w}{2})^2+(y+\tfrac{\ell}{2})^2+z^2}+(y-\tfrac{\ell}{2})\right)\\ &\ln\left(\sqrt{(x+\tfrac{w}{2})^2+(y-\tfrac{\ell}{2})^2+z^2}+(y-\tfrac{\ell}{2})\right)\\ &\left.\ln\left(\sqrt{(x+\tfrac{w}{2})^2+(y+\tfrac{\ell}{2})^2+z^2}+(y-\tfrac{\ell}{2})\right)\right] .\end{aligned} \tag{A.111}$$

With this expression for the potential known, the magnetic field can be described with

$$\mathbf{H} = \nabla\Phi, \qquad \mathbf{B} = \mu_0(\mathbf{H}+\mathbf{M}) . \tag{A.112}$$

In order to do so, it is first stated that

$$\nabla \ln\left(D^{\pm\pm} + \left(y \pm \frac{l}{2}\right)\right) = \frac{1}{D^{\pm\pm}}\mathbf{u}_y + \frac{1}{(x \pm \frac{w}{2})^2 + z^2}\left(1 - \frac{y \pm \frac{\ell}{2}}{D^{\pm\pm}}\right)\left[x \pm \frac{w}{2}\mathbf{u}_x + z\mathbf{u}_z\right] \tag{A.113}$$

in which

$$D^{\pm\pm} = \sqrt{\left(x \pm \frac{w}{2}\right)^2 + \left(y \pm \frac{\ell}{2}\right)^2 + z^2} \tag{A.114}$$

is the distance from **r** towards one of the corners of the metal plate. The magnetic field is then given by

$$\begin{aligned}\mathbf{H}(\mathbf{r}) = -\nabla\Phi = \frac{M_0 t}{4\pi}\Bigg\{&\frac{1}{D^{--}}\mathbf{u}_y + \frac{1}{(x-\frac{w}{2})^2+z^2}\left(1-\frac{y-\frac{\ell}{2}}{D^{--}}\right)\left[\left(x-\frac{w}{2}\right)\mathbf{u}_x + z\mathbf{u}_z\right]-\\ &\frac{1}{D^{-+}}\mathbf{u}_y + \frac{1}{(x-\frac{w}{2})^2+z^2}\left(1-\frac{y+\frac{\ell}{2}}{D^{-+}}\right)\left[\left(x-\frac{w}{2}\right)\mathbf{u}_x + z\mathbf{u}_z\right]-\\ &\frac{1}{D^{+-}}\mathbf{u}_y + \frac{1}{(x+\frac{w}{2})^2+z^2}\left(1-\frac{y-\frac{\ell}{2}}{D^{+-}}\right)\left[\left(x+\frac{w}{2}\right)\mathbf{u}_x + z\mathbf{u}_z\right]+\\ &\frac{1}{D^{++}}\mathbf{u}_y + \frac{1}{(x+\frac{w}{2})^2+z^2}\left(1-\frac{y+\frac{\ell}{2}}{D^{++}}\right)\left[\left(x+\frac{w}{2}\right)\mathbf{u}_x + z\mathbf{u}_z\right]\Bigg\} .\end{aligned} \tag{A.115}$$

In the middle of the plate, where $\mathbf{r} = \mathbf{0}$, it follows that

$$D^{++} = D^{+-} = D^{-+} = D^{--} = \sqrt{\left(\frac{w}{2}\right)^2 + \left(\frac{\ell}{2}\right)^2} \,. \tag{A.116}$$

The magnetic field in the centre of the plate then simplifies to

$$\mathbf{H}(\mathbf{r} = \mathbf{0}) = -M_0 K \mathbf{u}_x, \qquad \text{with} \qquad K = \frac{2t\ell}{\pi w \sqrt{w^2 + \ell^2}} \,. \tag{A.117}$$

From equation (A.117) it can be observed that the magnetic field inside the plate travels in a direction opposite to the direction of the magnetisation, which is also observed in the sphere and spheroid. The magnetic field increases with magnetisation M_0, thickness t and length ℓ, but reduces with increasing width w. This is due to the fact that the edges of the plate at $w = \pm b/2$ can be seen as the sources of the magnetic field, since this is where $\nabla \cdot \mathbf{M} = 0$. If the plate becomes wider, these sources are separated further, decreasing the strength of the magnetic field. Source strength does increase for larger values of M_0, d and ℓ.

B

Laboratory setup

B.1. Helmholtz cage

A Helmholtz cage was constructed In order to annul the Earth's magnetic field and to be able to subject test specimens to user-controlled, stable and uniform background fields. The principle of Helmholtz coils is that coils carrying an electric current I, which have a spacing R in between them, equal to the radius of the coils, generate a more or less uniform magnetic field in a direction orthogonal to the coils. Two Helmholtz coils and the magnetic field distribution in a plane through the coils' centre line is shown in figure B.1.

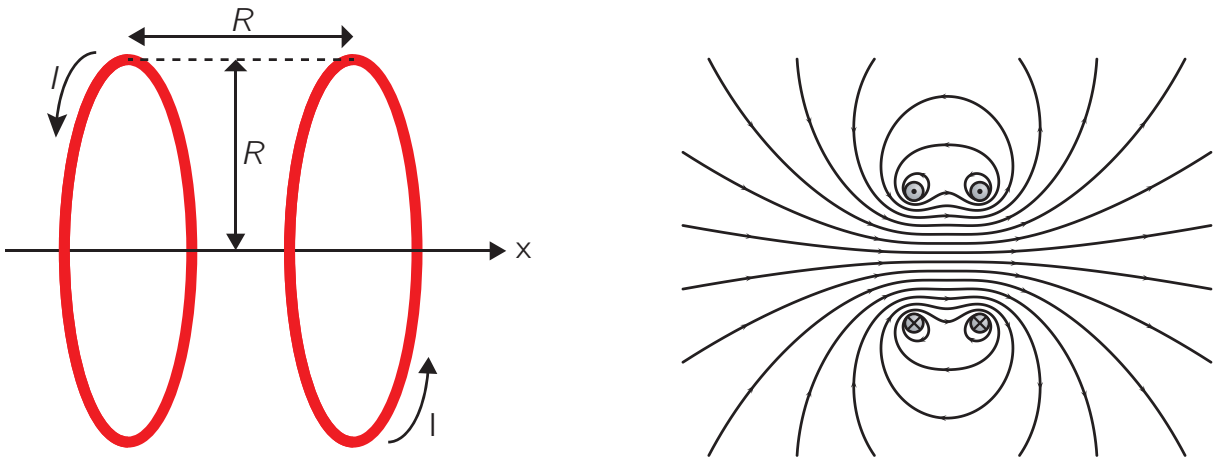

Figure B.1: Helmholtz coils and the magnetic field lines.

Figure B.1 shows how a more or less uniform magnetic field can be generated in x-direction. By placing multiple coils in series, the domain in which this field is generated can be extended. Expanding this system into three dimensions will create an environment in which the magnetic field in x, y and z-directions can be controlled separately. It is known that the strength of the Earth's magnetic field lies around 50 µT depending on the position with respect to the Earth's centre of mass. At the TNO office in where all of the measurements in this report are conducted, this background field can be seperated into three components: $B_{0,x}$ = -16.8 µT, $B_{0,y}$ = -7.5 µT and $B_{0,z}$ = +45.2 µT. In order to nullify this background field, these B-components can be generated in opposite direction within the domain resulting in a net zero magnetic field, using the three coil systems.

In order to simplify construction the testing domain is made cubical with an aluminium frame ($h \times w \times l$ = 679×679×1116 mm), please refer to the Rhino drawing in figure B.2. The x-direction of the frame is defined as the longitudinal axis, the y-direction points sideways and the z-direction points downwards.

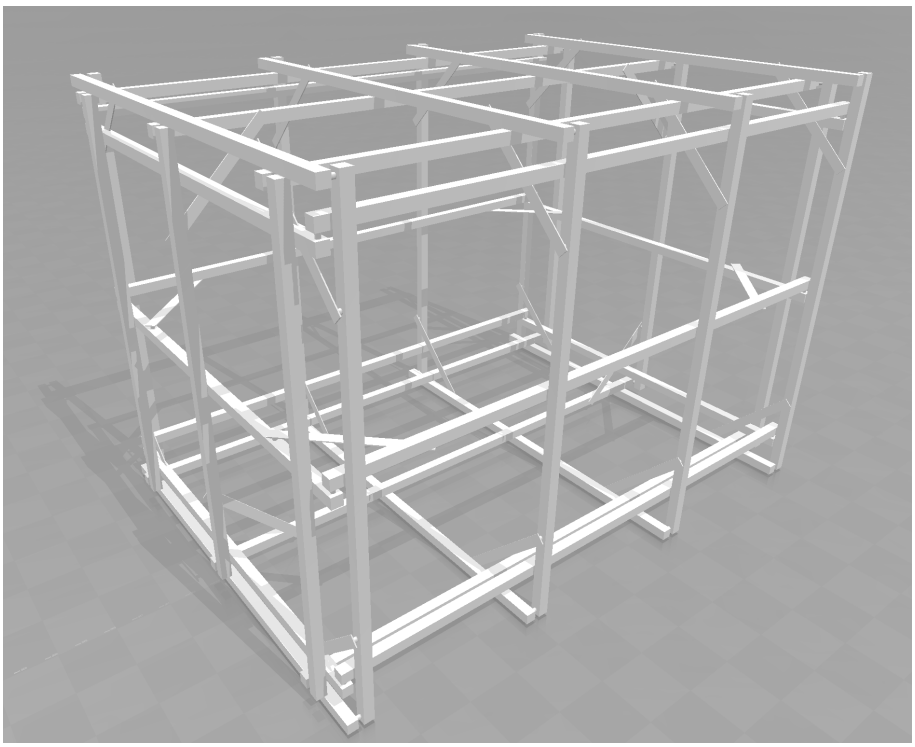

Figure B.2: Aluminium frame 3D drawing.

In x-direction, four coils are mounted along the frame while in y and z-direction three coils each are mounted. For clarity, a schematic overview of the coils for each separate direction is shown in figures B.3 and B.4. Each of these coils consists of a bundle of copper wires which are connected in series. The amount of windings per coil determines the strength of the magnetic field produced by that coil. The magnetic field inside the cage can be calculated by modelling each coil as four separate line currents. The magnetic induction field at a distance r from an infinite wire can be described by

$$B_{\text{tot}} = \frac{\mu_0 I}{2\pi r} \,. \tag{B.1}$$

In this example, an expression is needed for *finite* wires, which is given by Lepelaars [34]:

$$\mathbf{H}(\mathbf{r}) = \frac{I}{4\pi}\left[\left(\frac{\mathbf{r}-\mathbf{r_2}}{|\mathbf{r}-\mathbf{r_2}|} - \frac{\mathbf{r}-\mathbf{r_1}}{|\mathbf{r}-\mathbf{r_1}|}\right)\mathbf{v}\right]\frac{(\mathbf{r}-\mathbf{r_1})\times\mathbf{v}}{|\mathbf{r}-\mathbf{r_1}|^2 - [(\mathbf{r}-\mathbf{r_1})\cdot\mathbf{v}]} \tag{B.2}$$

in which

$$\mathbf{v} = \frac{\mathbf{r_2}-\mathbf{r_1}}{|\mathbf{r_2}-\mathbf{r_1}|} \,. \tag{B.3}$$

In these equations, $\mathbf{r}$ defines the point in three-dimensional space in which the magnetic field is calculated due to a theoretical finite wire with its kathode at $\mathbf{r_1}$ and anode at $\mathbf{r_2}$. For each location in the three-dimensional domain within the cage, the magnetic induction field due to all individual wires of each separate coil can be superpositioned in order to find an analytical expression for the total B-values. The coils that generate a field in a specific direction are linked in series and connected to one amplifier. Three amplifiers (for the three directions) are used which means that for each individual direction the same current flows through all coils while the current in different directions can be varied independently. In order to create a uniform field in each direction, the coils towards the centre of the box carry fewer copper windings than the coils closer to the edges. With this method, a more or less uniform field with three

components can be created with a user-defined magnetic induction field strength. The maximum field strength for this Helmholtz cage is around ±450 µT for each direction.

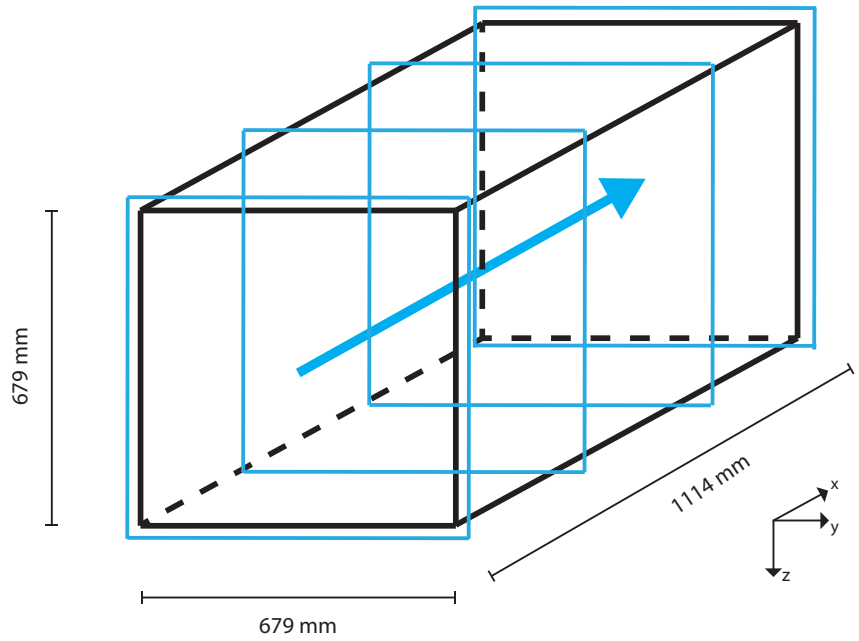

Figure B.3: Frame with measurements and four coils in series in x-direction.

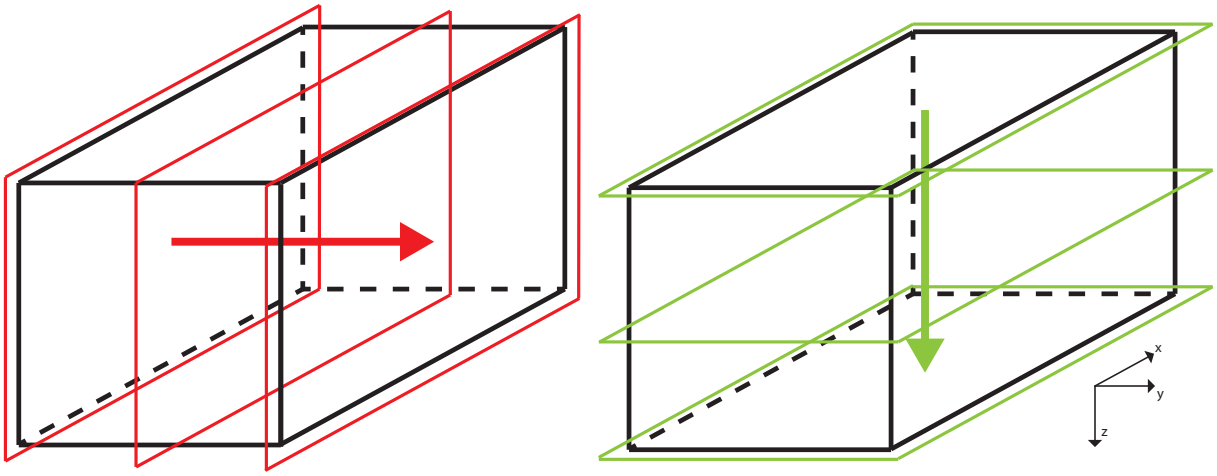

Figure B.4: Three coils in series in y-direction and z-direction.

A photograph of the aluminium frame with the coils installed is shown in figure B.5. Aluminium is chosen as base material for the frame construction since its does not show magnetic behaviour when exposed to weak magnetic field strengths.

When the Earth's background field is present, the current that needs to be sent through the three coil systems in order to counter this field is equal to

$$I = \begin{bmatrix} I_x \\ I_y \\ I_z \end{bmatrix} = \begin{bmatrix} -0.0592 \\ 0.1327 \\ -0.3573 \end{bmatrix} A \,. \tag{B.4}$$

Figure B.5: Aluminium frame with coils in x, y and z-directions.

It is important to note that the above only holds for this Helmholtz cage, positioned at the TNO office, with its orientation fixed. In order to create a uniform field of 100 µT in x-direction, the current in x-direction is increased by 0.789 A to a total amount of 0.7306 A. This yields, analytically, the magnetic flux density distribution in an xy-plane through the centre of the cage shown in figure B.6.

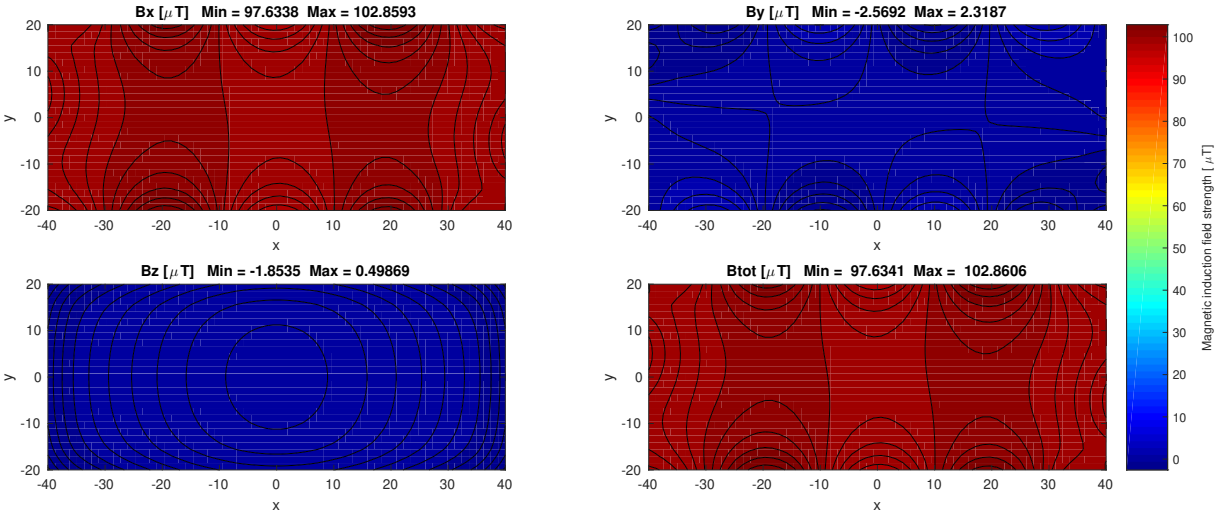

Figure B.6: Magnetic flux density in the xy-plane through the centre of the cage.

From figure B.6 it can be seen that, following the methodology of Helmholtz coils, a more or less uniform

magnetic field can be created. The field in y and z-directions varies between $\pm$2.5 µT over the plane, while in x-direction an error of about 3% is observed. It must be noted that this is an error over a plane through the centre which is 800 mm long and 400 mm wide. Test specimens will be placed in the centre of this plane, where the theoretical error is lower. It is worth noting that by increasing the field strength in a certain direction the relative error stays the same, implying that the absolute error will increase linearly. This means that for a field strength of 400 µT, the absolute error will be around $\pm$12 µT. In this analytical approximation, the following assumptions are made:

- The background field does not vary over time;
- The bundles of wire are modelled as line currents, where in reality they have a cross sectional area of around 10 $\times$ 10 mm;
- When a magnetic field is created in a coil, this also creates an additional field in the neighbouring coil due to an effect known as mutual inductance, see [2]. This effect is assumed to be nonexistent here;
- Instead of a single wire carying a large current, the laboratory setup will consist of many small wires connected in series. Interaction between these wires is assumed to be negligible;
- Resistance of the wires is not accounted for.

When comparing the analytical solution with measurements in the laboratory setup, it was found that there is a relative error between the analytical simulation and the measurments of about 10% due to the abovementioned effects. Zero measurements without an object present are always subracted from measurements with a specimen in order to correctly capture the effect in an attempt to reduce the effect of such errors.

B.2. Sensoring equipment

B.2.1. Sensor array

The first system that measures the B-field in three directions within the cage is the sensor array, which consists of 7×16 sensors placed in the xy-plane at $z \approx 180$ mm from the centre of the cage. The sensors on this array are spaced 50 mm from each other, covering a total area of 750×300 mm. The sensors type is HMC-5983 produced by Honeywell, which measure the magnetic field in three directions with an accuracy of around 0.5 µT. The error of these sensors is relatively high compared with other measuring equipment, but the array provides a good insight into the distribution of a magnetic field over an entire surface compared to single, fixed point measurements. A schematic top view of the array is shown in figure B.7.

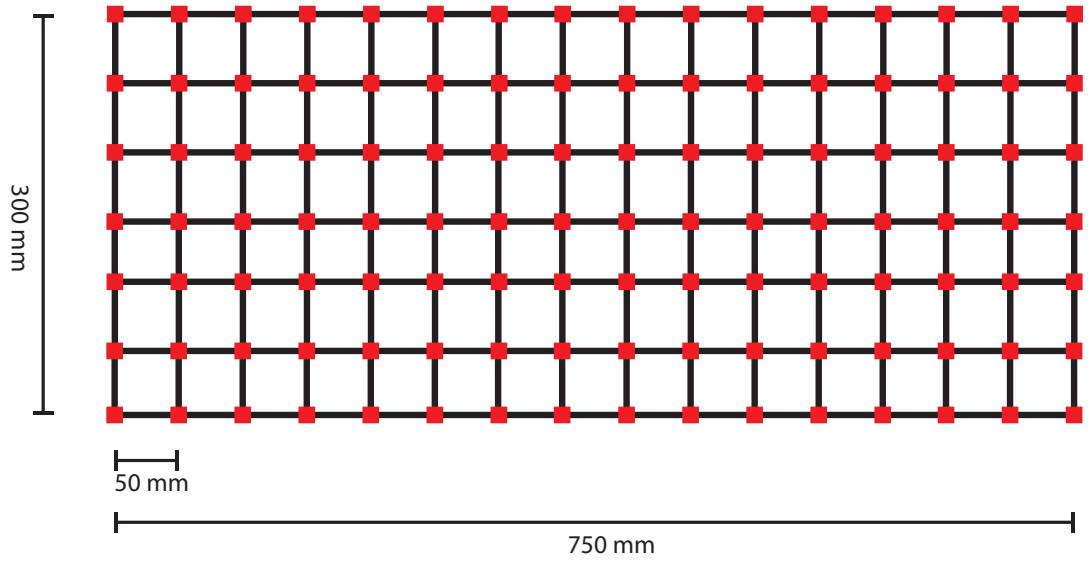

Figure B.7: Sensor array, schematic top view.

The array is placed on a wooden base plate which is located 200 mm below the centre of the cage. In order to protect the array, a perspex casing iss constructed which consists of two vertical walls and a top plate which have a thickness 15 mm. Besides offering protection, the perspex casing allows for convenience in placing objects at a certain z-distance from the array in order to get useful visualisations. A top view photograph of the array with the perspex casing is shown in figure B.8.

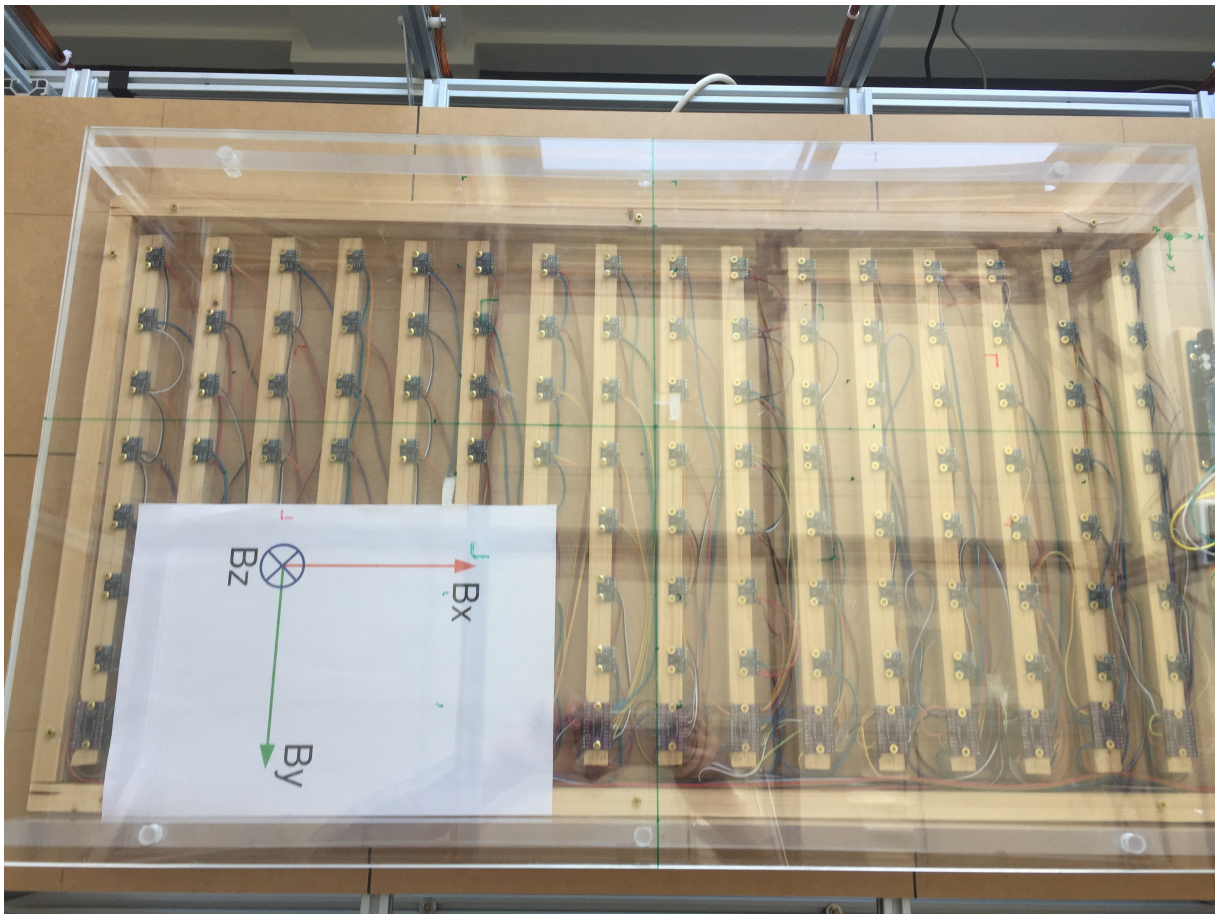

Figure B.8: Sensor array, top view.

A schematic side view of the sensor array with measurements is shown in figure B.9, and a photograph is shown in figure B.10.

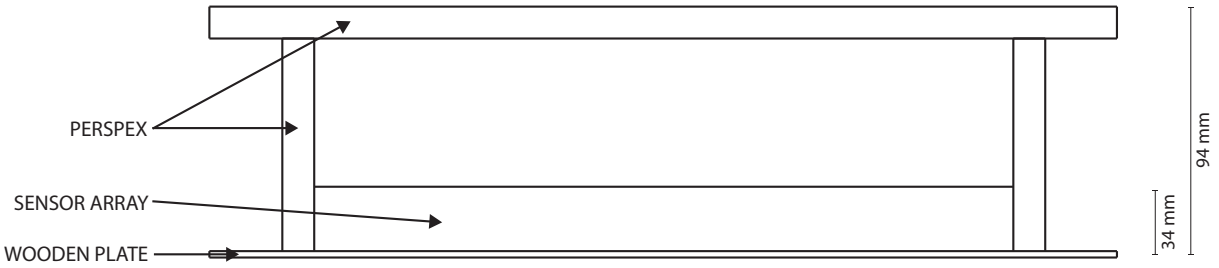

Figure B.9: sensor array with perspex casing, schematic side view.

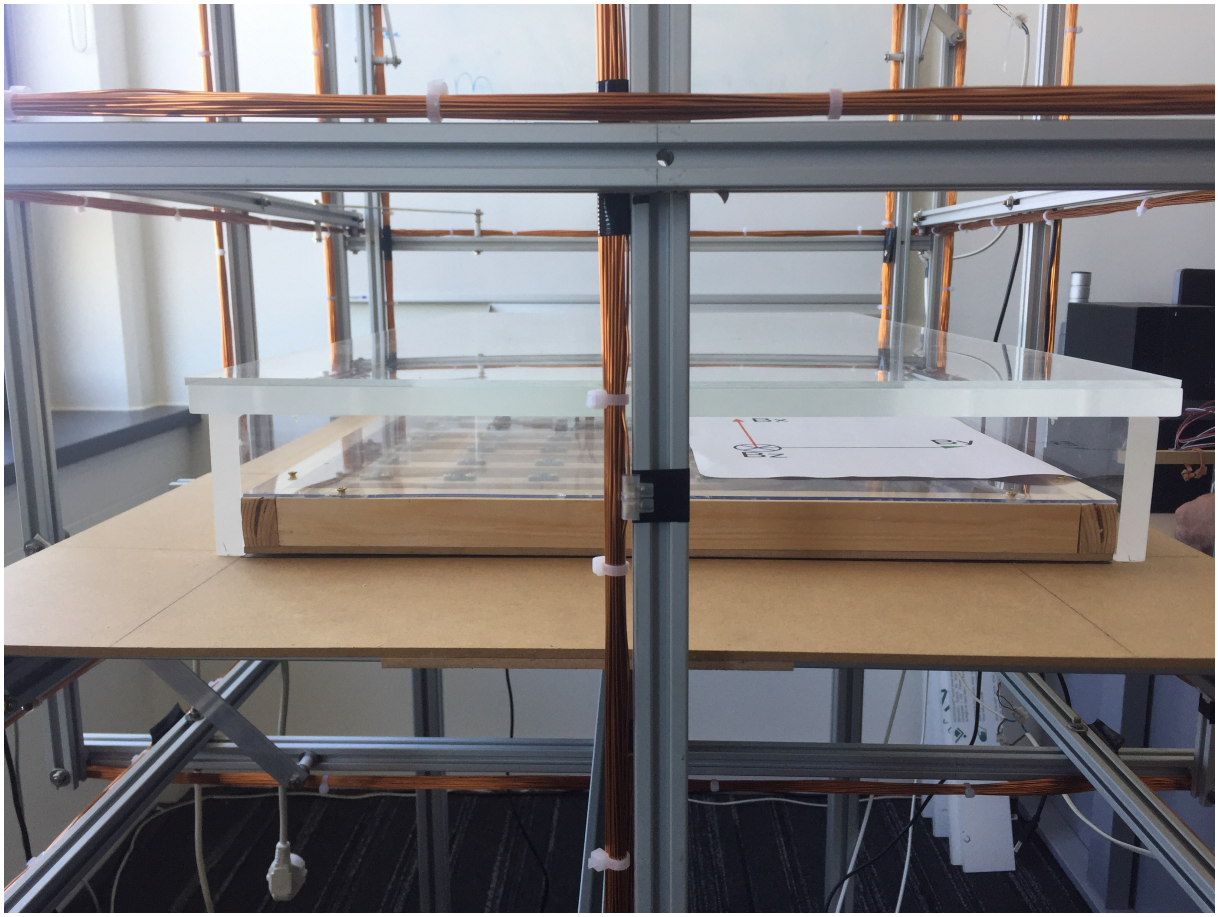

Figure B.10: Sensor array with perspex casing, side view.

During the progress of this thesis, it was decided to move the sensory array closer to the perspex in order to measure a stronger induction field. For the Villari-experiments in chapter 6 the sensor array is lifted up using aluminium bars of 30 mm height. This is shown schematically and with a photograph in figure B.11.

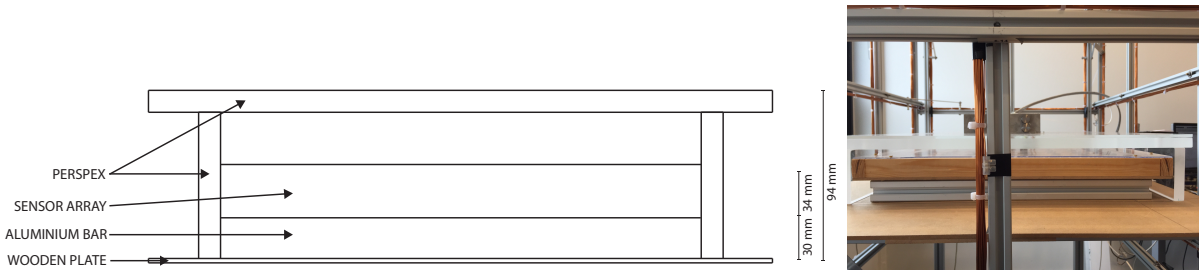

Figure B.11: Sensor array with perspex casing and aluminium bars, side view.

The sensor array is callibrated manually. This means that initially a current is sent through the coil system which lifts the background field. Then, a fixed current is sent in each direction (x, y, z) in turn. For each component, the magnetic field distribution can be calculated manually as shown in figure B.6. These values are then used to callibrate the sensors. It is important to note that a certain error is made here on top of the accuracy of the individual sensors, since there is always a difference between the theoretical magnetic field produced by the Helmholtz cage and the actual field. This is an important reason why, within this report, at certain stage a fit is considered good enough. This means that while theoretically a better comparison between measured and calculated data can be obtained, in practice this means fitting parameters to noise. The precise level of this inaccuracy is not exactly known due to a combination of

sensor inaccuracy, calibration errors and assumptions.

B.2.2. MAG658-fluxgate sensor

Besides the sensory array, a more precise sensor can be used to measure the three-dimensional B-field at one specific location. This sensor consist of a MAG658-fluxgate sensor produced by Bartington Instruments, which is encased into a sturdy black box by TNO in order to prevent it from being damaged. The original circuit board and the box in which it is encased are shown in figure B.12. Contrary to the sensors used in the array, the accuracy of this sensor lies around 10 nT.

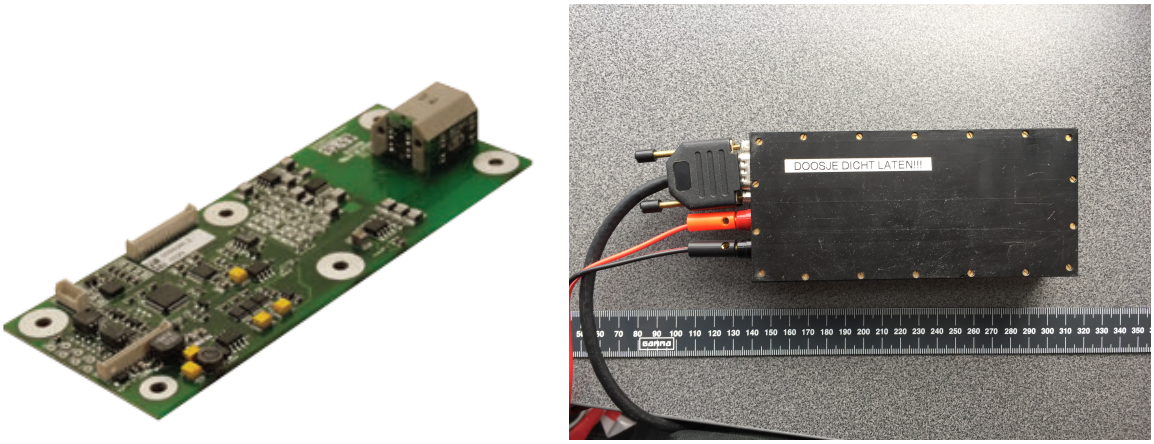

Figure B.12: Mag658 circuit board and casing.

Since the sensor had been encased before the start of this project, it is essential to determine where inside the black box the actual sensor is located. This is done by moving a small magnet along a straight line parallel to the edge of the box. At the location of the sensor, a local maximum or minimum is obtained. The dimensions of the sensor casing were measured to be 154×70×30 mm. The sensor was found to be situated 14 mm from the bottom and 35 mm from the sides as shown in figure B.13.

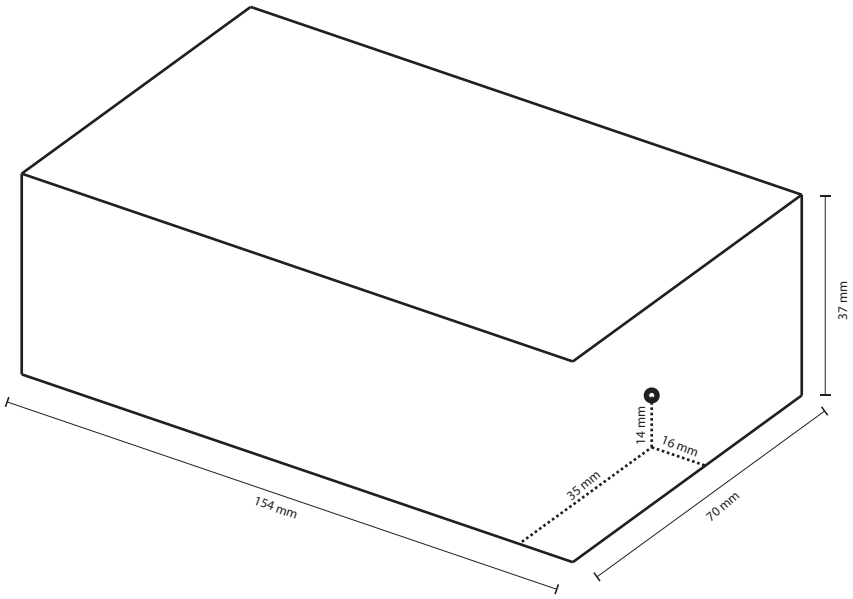

Figure B.13: Schematic drawing of the fluxgate sensor casing with sensor location.

B.3. Demagnetising unit

In order to demagnetise thin ferromagnetic objects, a demagnetising unit produced by `Goudsmit Magnetics` is used. This unit consists of a bar-shaped object that can be connected to a power outlet. When plugged in, the bar starts to produce alternating positive and negative strong magnetic fields at a frequency of 50 Hz. When this bar moves over a thin piece of magnetic steel, the magnetisation in this steel plate alternates simultaneously with the frequency of the demagnetiser. As the bar gradually moves away from the steel, the frequency of the alternating fields is kept constant, while the magnitude decreases. This way, the magnetisation in the objects spirals down to a value close to zero, see the deperming section in the book by Gordon [17]. Top and bottom views of the demagnetising bar are shown in figure B.14.

Figure B.14: Demagnetising bar top and bottom view.

B.4. Steel Specimens

The first specimen that will be used in experiments is a solid steel prolate spheroid, 580 mm long along the main axis and 95 mm diameter along the two minor axes. The prolate spheroid provides an excellent starting point while investigating magnetic hysteresis since a perfect analytical solution for its magnetic field exists, as presented in section 2.3. The characteristic steel properties are unknown, but it can be safely assumed that this spheroid was created by cutting away parts of a steel bar. Steel bars are produced from steel billets, which are soft steel slabs obtained directly after casting steel and are used as a base product for all types of steel products. Figure B.15 shows the prolate spheroid, which is encased in a perspex device that was manufactured in order to safely place and remove the spheroid in the testing area. The distance from the centre of the spheroid to the bottom of the casing is measured at 88 mm.

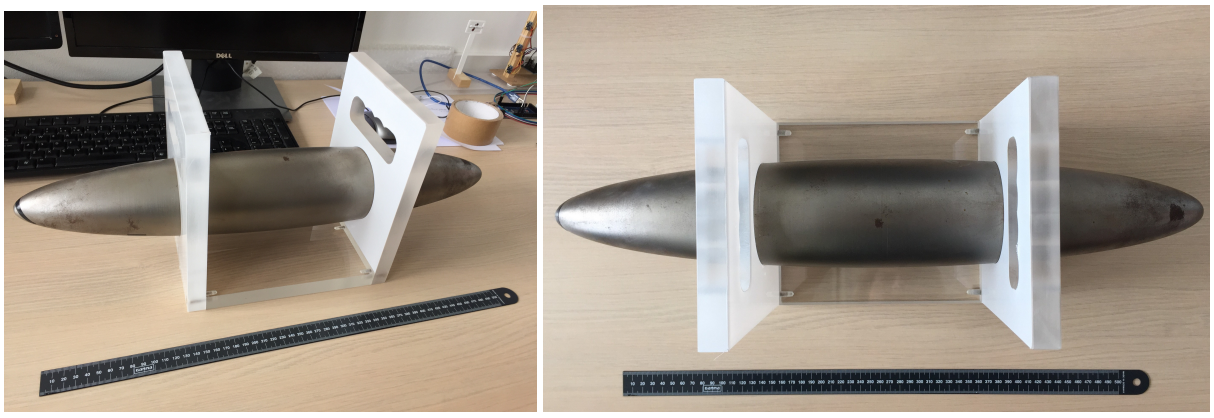

Figure B.15: Prolate spheroid with perspex casing.

Mmetal plates of various dimensions are tested besides the spheroid, since metal plates are compo-

nents commonly used in marine structures. An overview of the test specimens is given in table B.1. All specimens are marked with an arrow pointing in x-direction in order for experiments to be repeatable.

Table B.1: Metal plate specimen overview.

Specimen number	width [mm]	length [mm]	thickness [mm]	Production
1	300	300	5	Ordinarily cut
2	300	300	2	Ordinarily cut
3	300	300	5	Laser cut
4	300	300	2	Laser cut
5	100	165	1	Ordinarily cut, σ_y = 700 MPa
6	100	165	2	Ordinarily cut, σ_y = 355 MPa

Characteristic properties such as carbon or manganese content of these plates are currently unknown, and not particularly relevant since it is expected that two types of steel with the same contents can differ in magnetic behaviour, depending on the way they were produced. Figures of the metal plate specimens 1-4 are given in figure B.16.

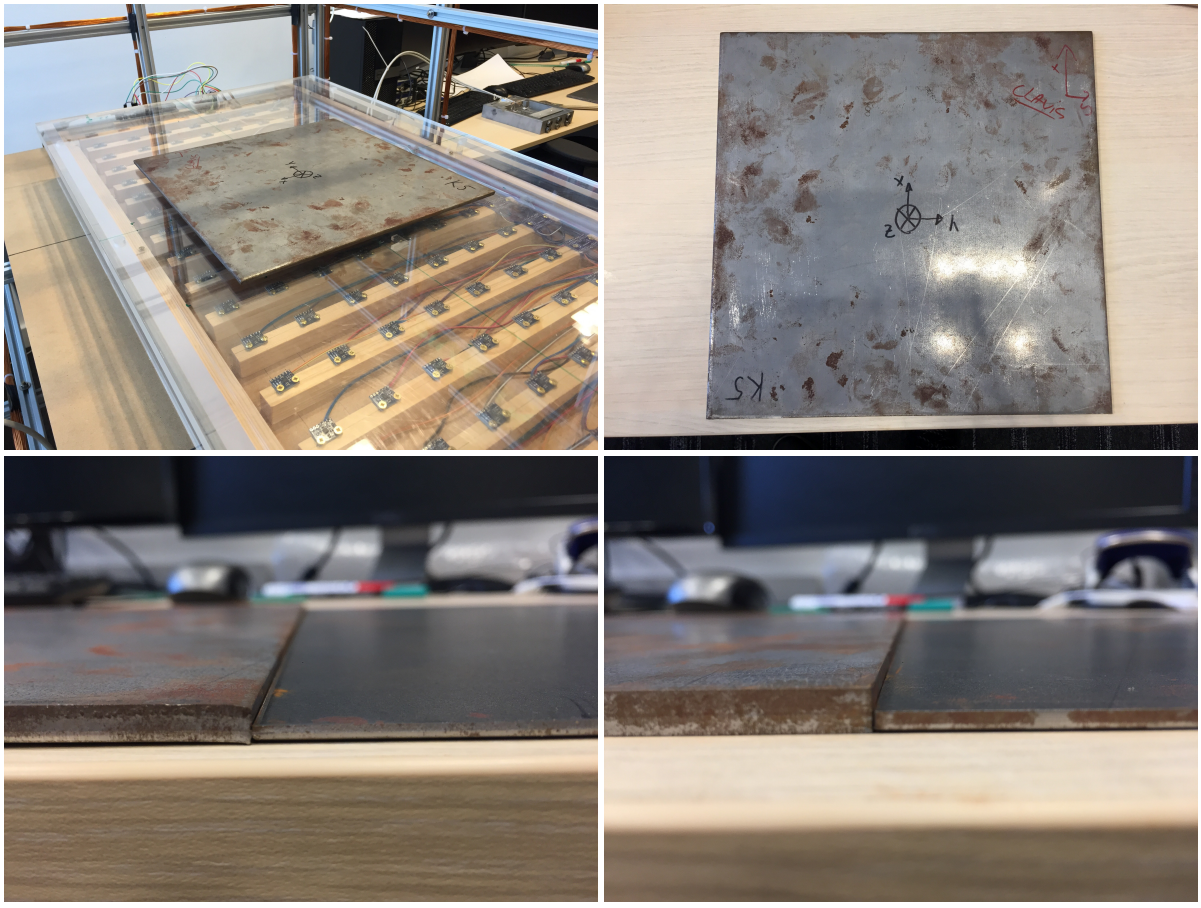

Figure B.16: Photographs of specimen 1 within the Helmholtzcage (top left), top view specimen 1 (top right), side view specimen 1 & 2 (bottom left), side view specimen 3 & 4 (bottom right).

B.5. Villari experiment

A schematic drawing of the Villari experiment setup iss provided in chapter 6. Additional photogaphs of the test setup with the strain gauges mounted on top of the specimen are shown in figure B.17.

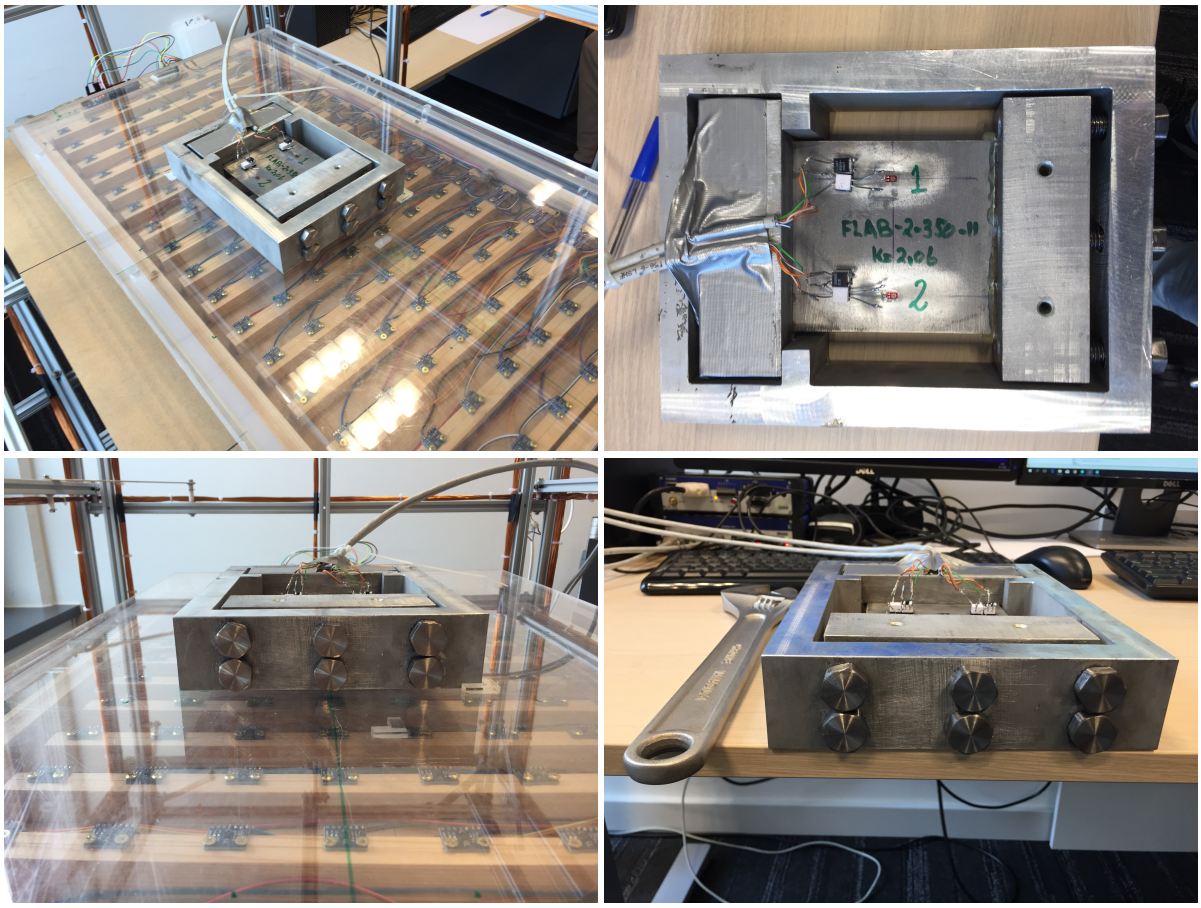

Figure B.17: Photographs of the Villari experiment setup with specimen 6 mounted in the aluminium frame. Within the Helmholtz cage (top left), top view (top right), side view of bolts (bottom left), side view with spanner used for tensioning (bottom right).

C

SFLA Flowchart

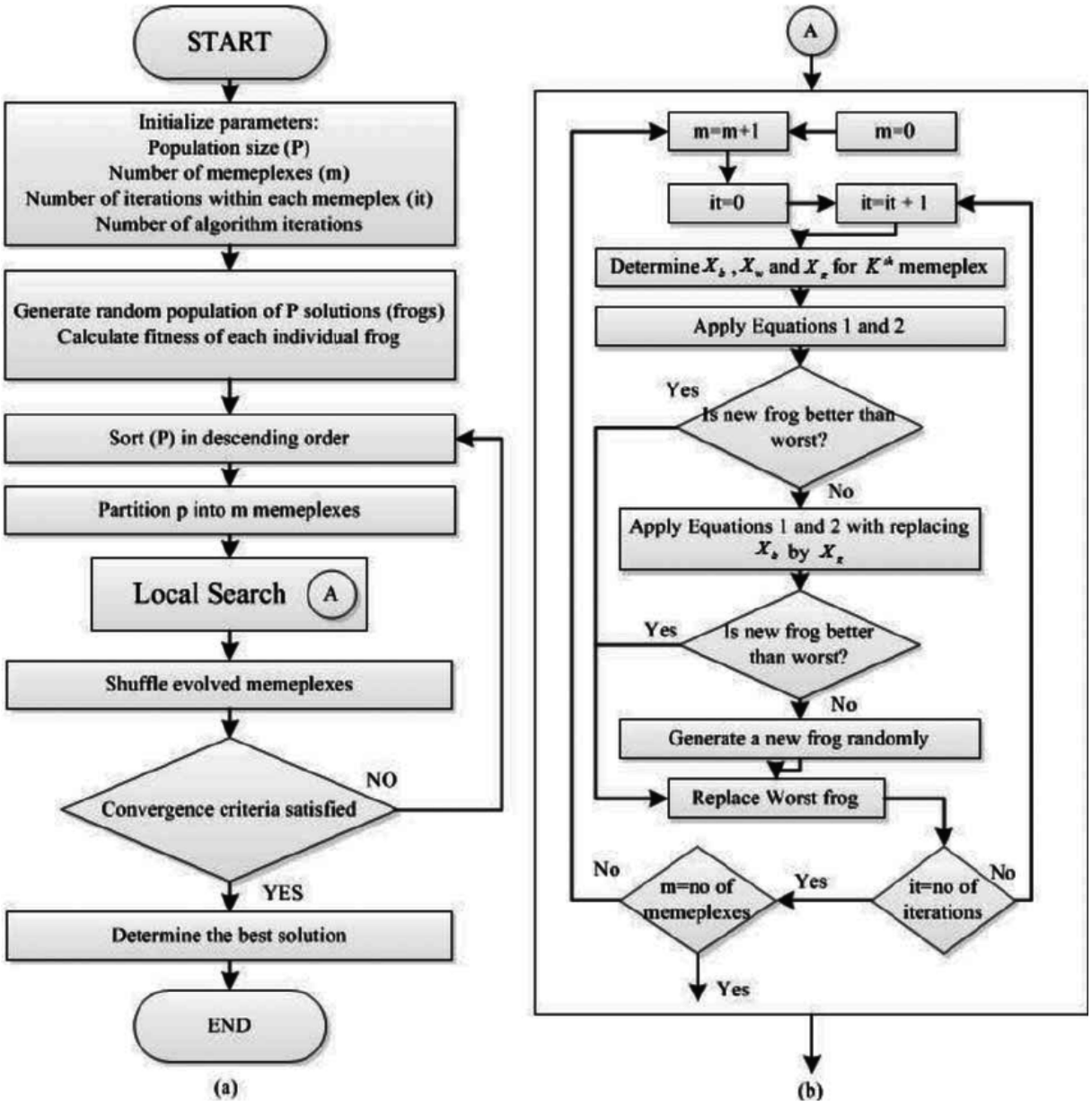

Figure C.1: Shuffled leaping frog algorithm flowchart, from Darabian [12].

D

Hysteresis results

D.1. Specimen 2-4: RMSE & Relative error

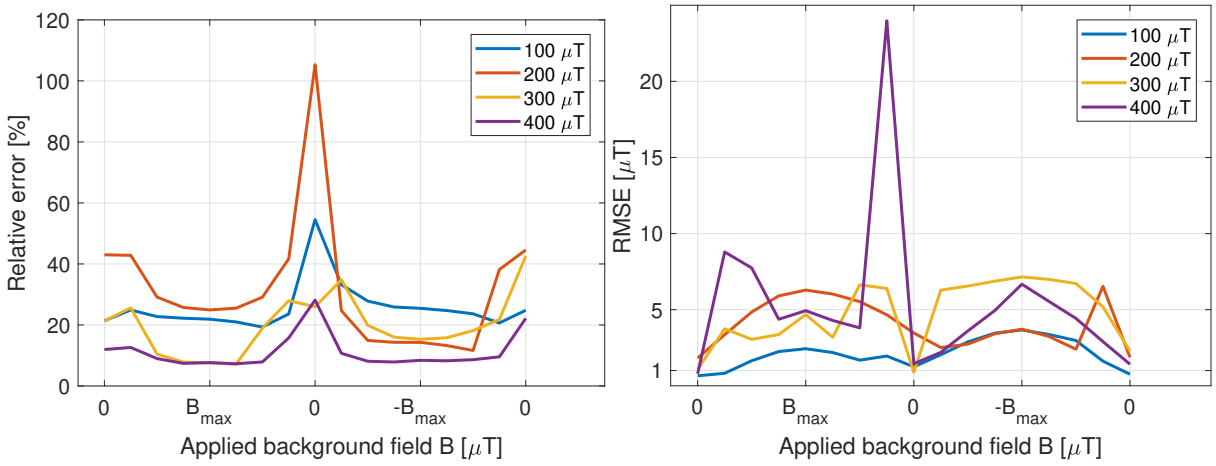

Figure D.1: Specimen 2: Relative and Root Mean Squared Error.

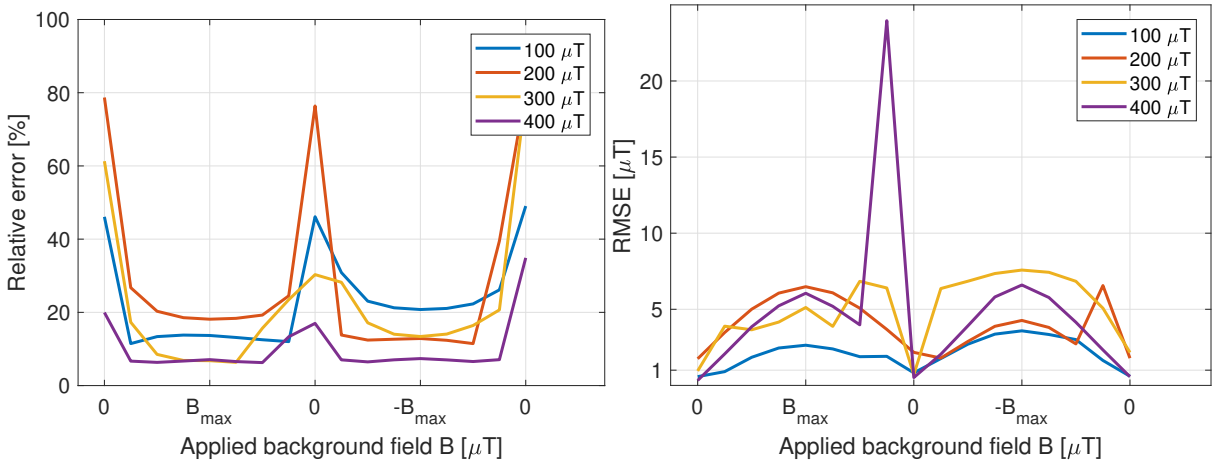

Figure D.2: Specimen 3: Relative and Root Mean Squared Error.

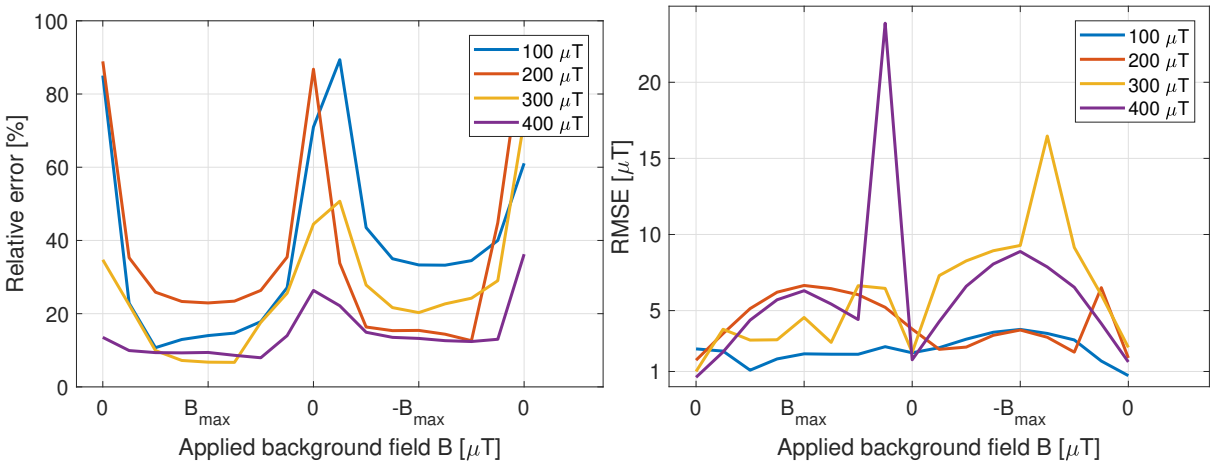

Figure D.3: Specimen 4: Relative and Root Mean Squared Error.

D.2. Specimen 2: Fit

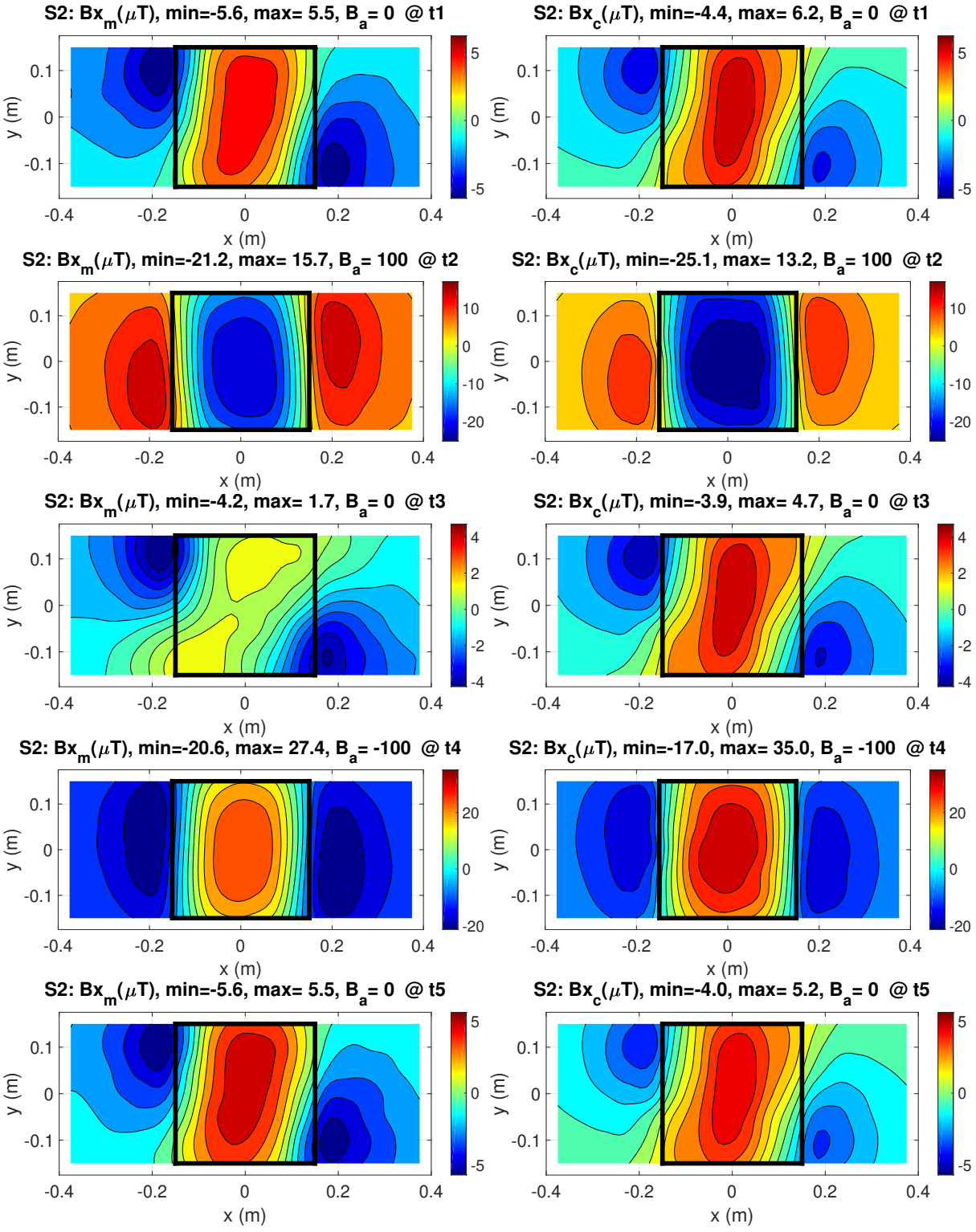

Figure D.4: Specimen 2. B_x field below a metal plate (300×300×2 mm) subjected to a 100 µT loop, measurements (left) calculated fit (right).

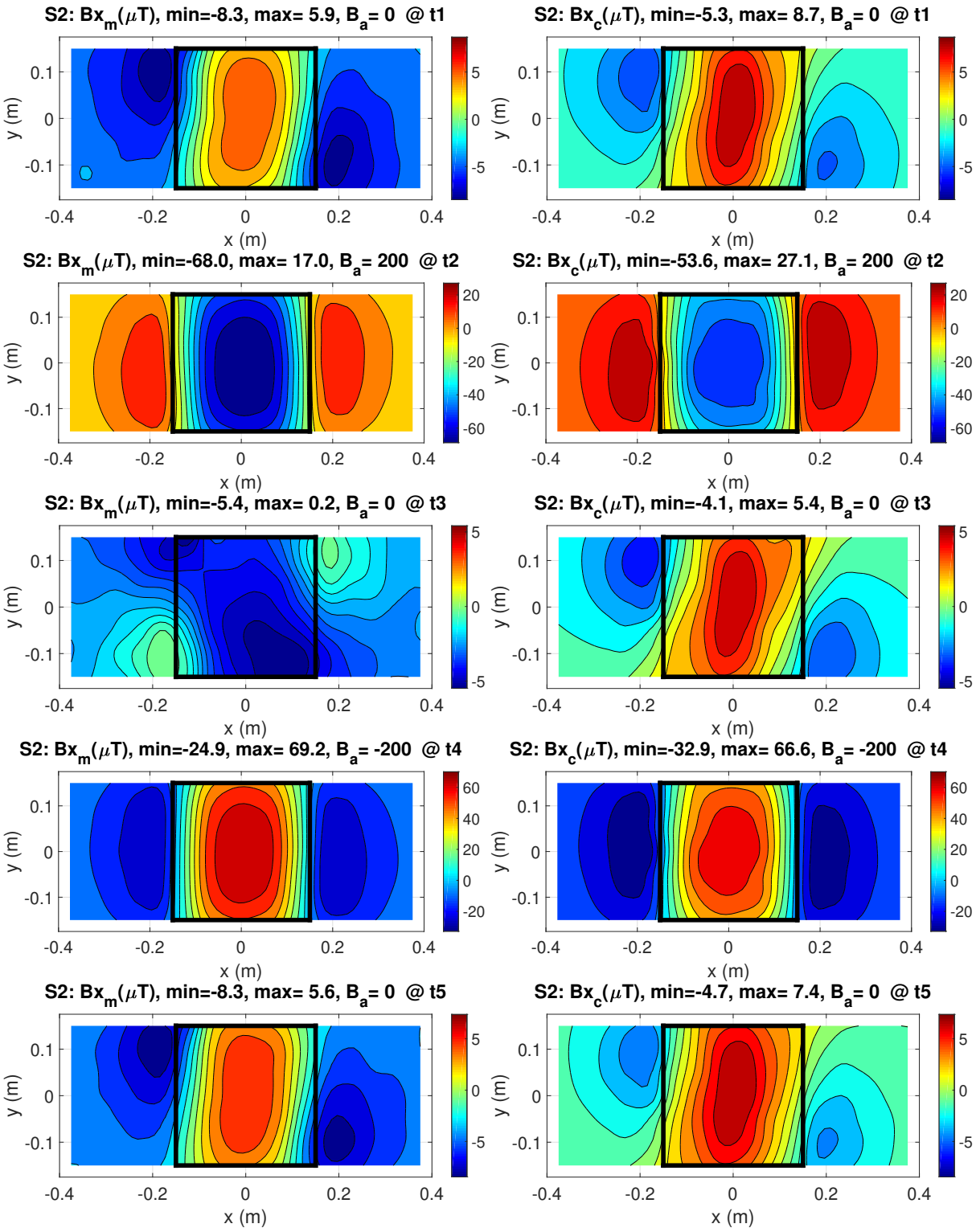

Figure D.5: Specimen 2. B_x field below a metal plate (300×300×2 mm) subjected to a 200 μT loop, measurements (left) calculated fit (right).

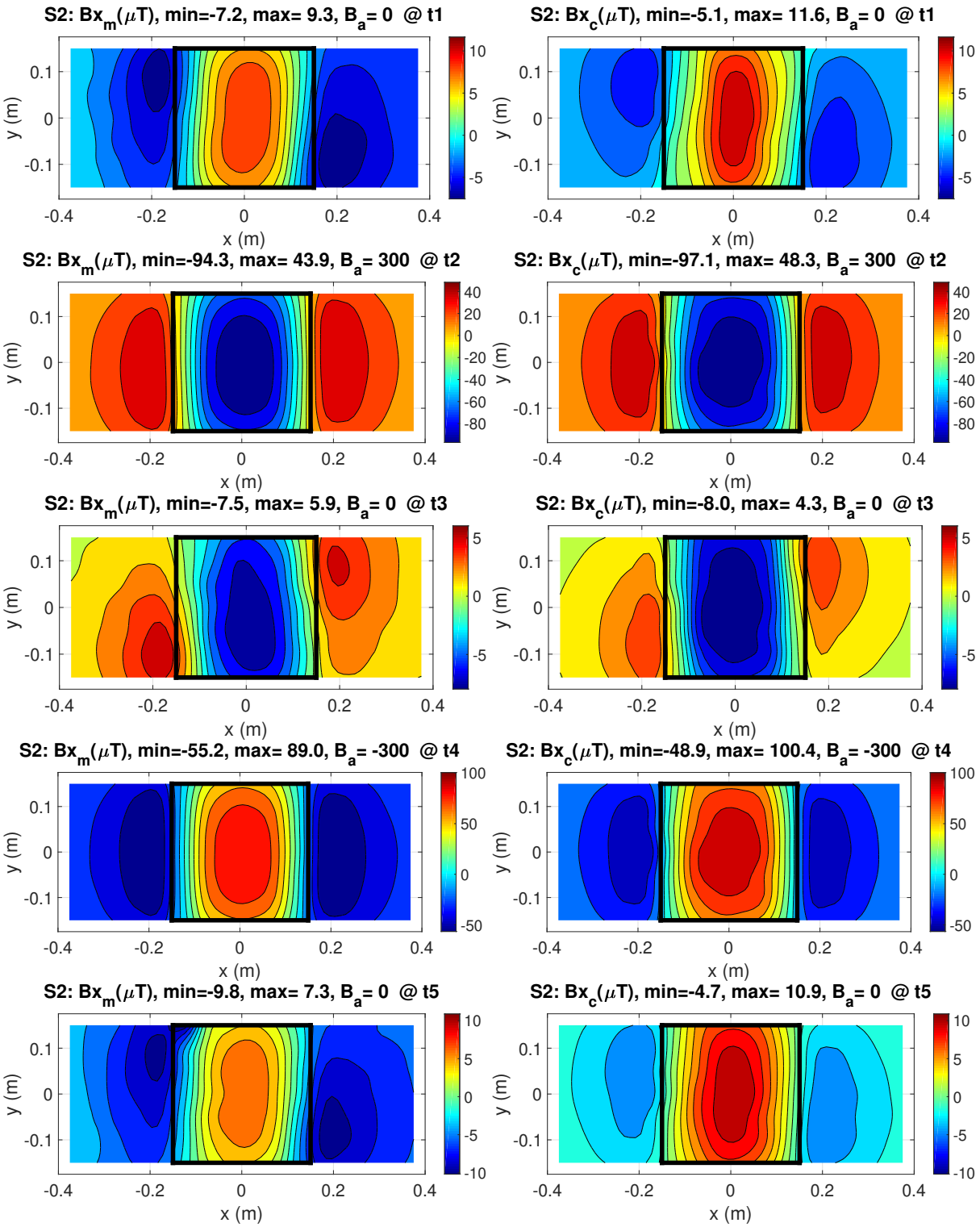

Figure D.6: Specimen 2. B_x field below a metal plate (300×300×2 mm) subjected to a 300 µT loop, measurements (left) calculated fit (right).

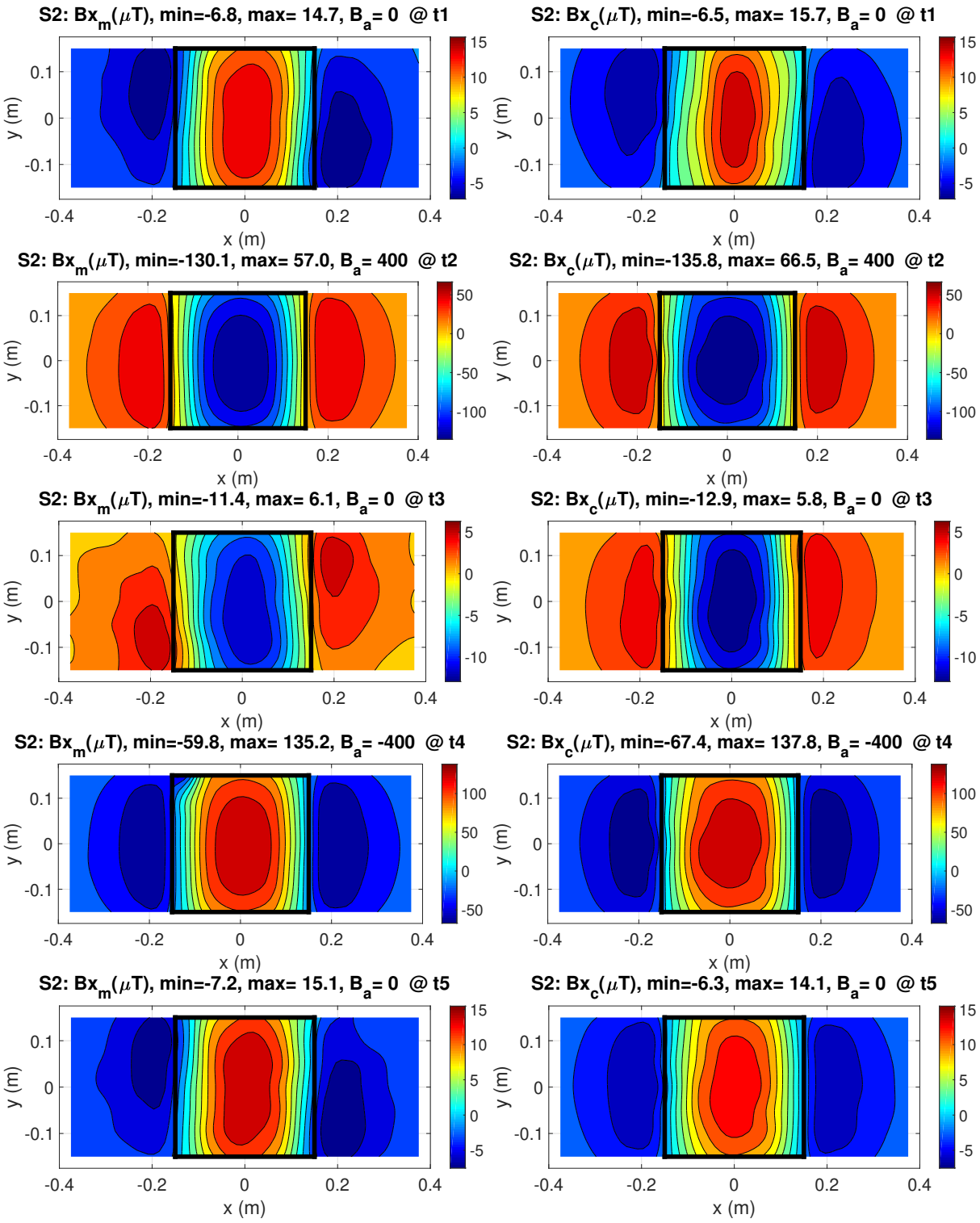

Figure D.7: Specimen 2. B_x field below a metal plate (300×300×2 mm) subjected to a 400 μT loop, measurements (left) calculated fit (right).

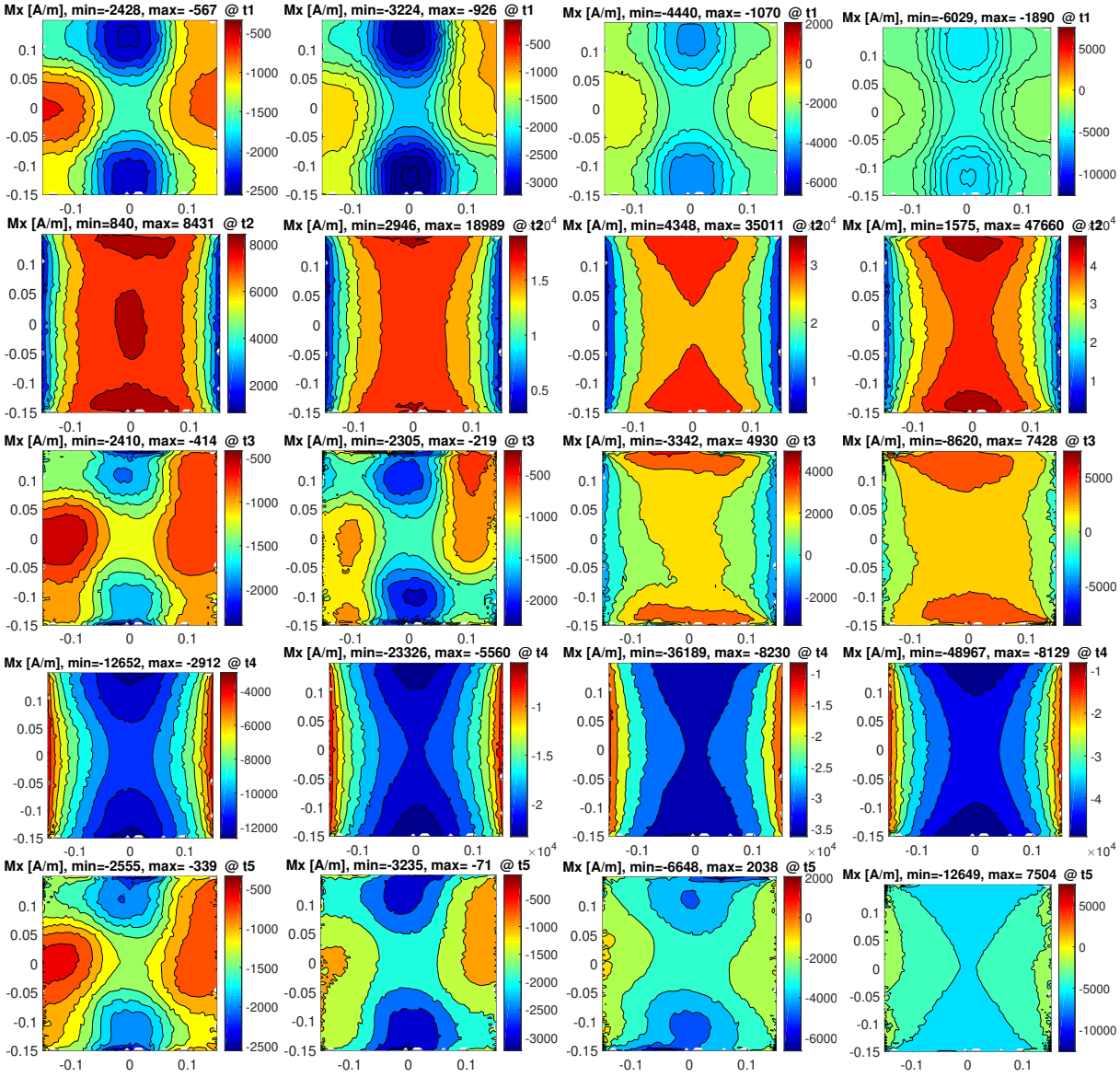

Figure D.8: Specimen 2. M_x distribution in a metal plate (300×300×2 mm) for four hysteresis loops: 100 µT (left), 200 µT (centre left), 300 µT (centre right), 400 µT (right).

D.3. Specimen 3: Fit

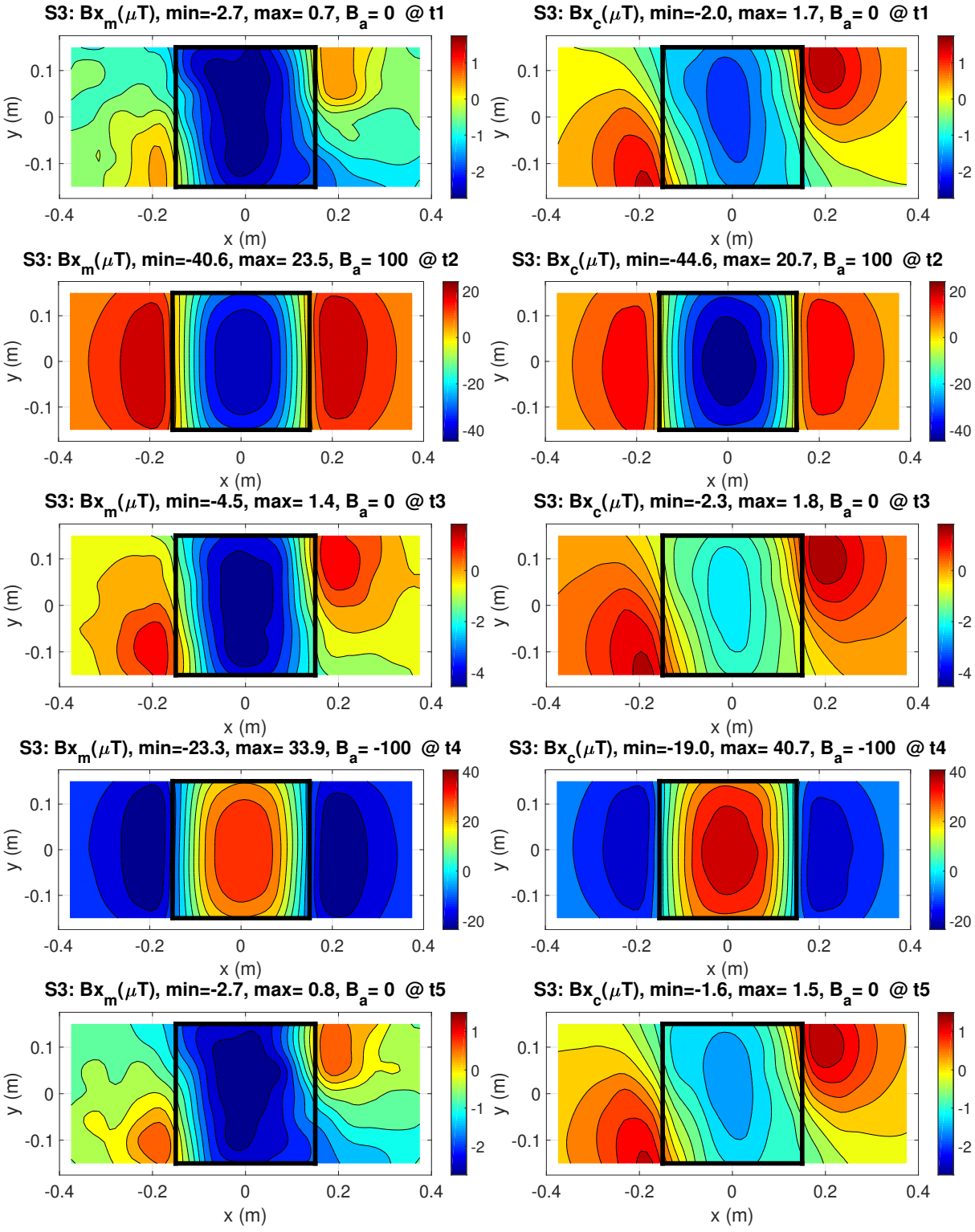

Figure D.9: Specimen 3. B_x field below a metal plate (300×300×5 mm) subjected to a 100 µT loop, measurements (left) calculated fit (right).

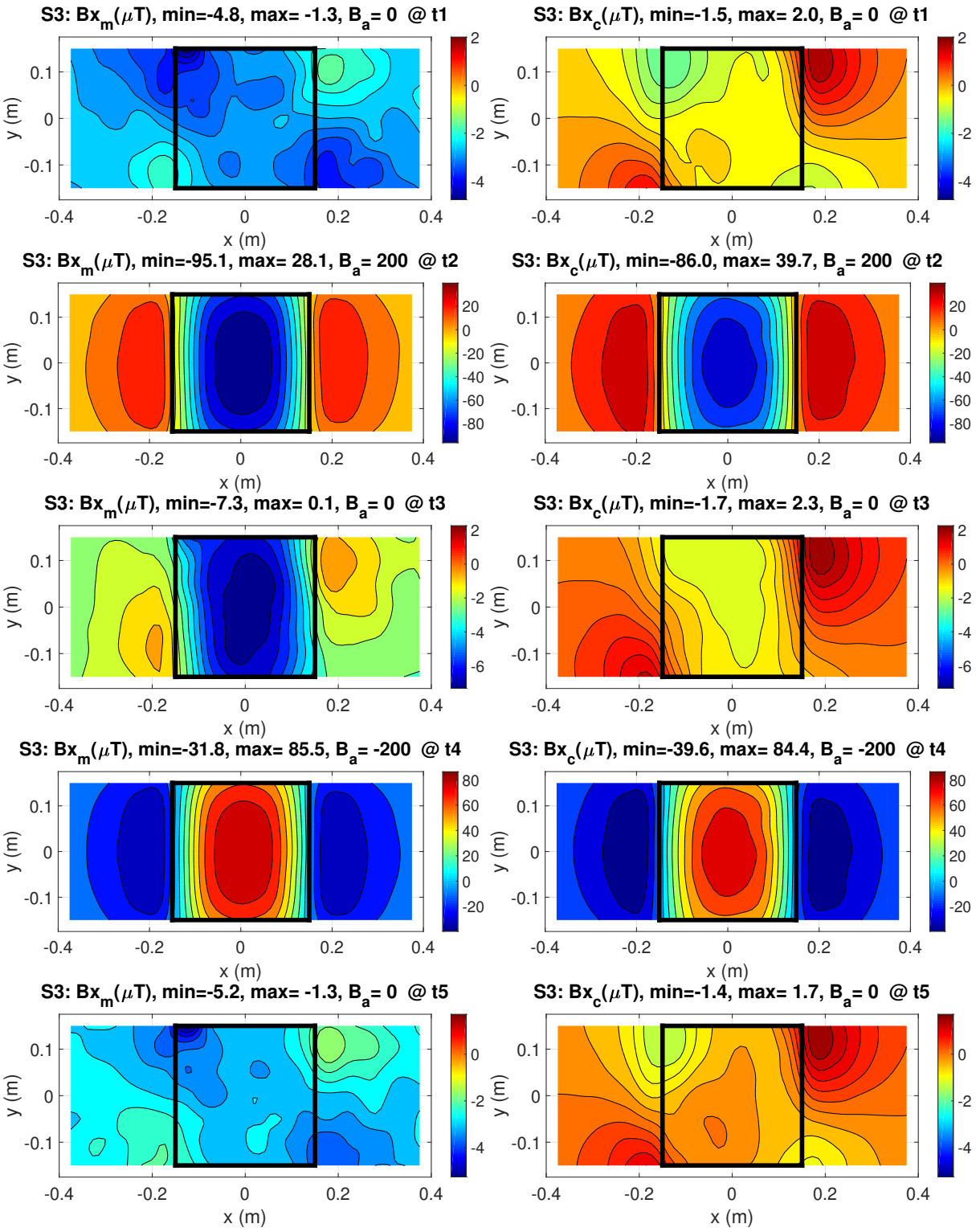

Figure D.10: Specimen 3. B_x field below a metal plate ((300×300×5 mm) subjected to a 200 µT loop, measurements (left) calculated fit (right).

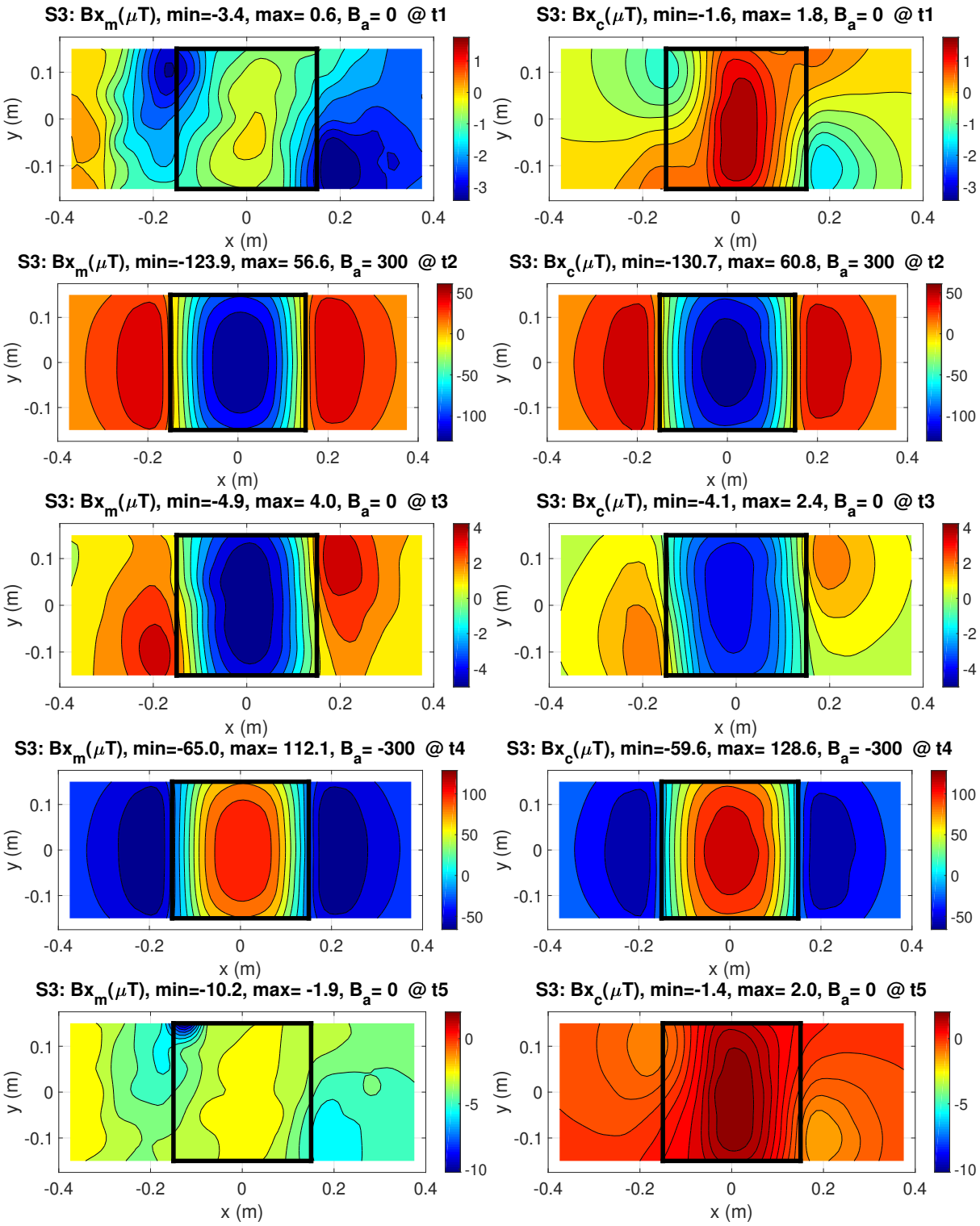

Figure D.11: Specimen 3. B_x field below a metal plate (300×300×5 mm) subjected to a 300 µT loop, measurements (left) calculated fit (right).

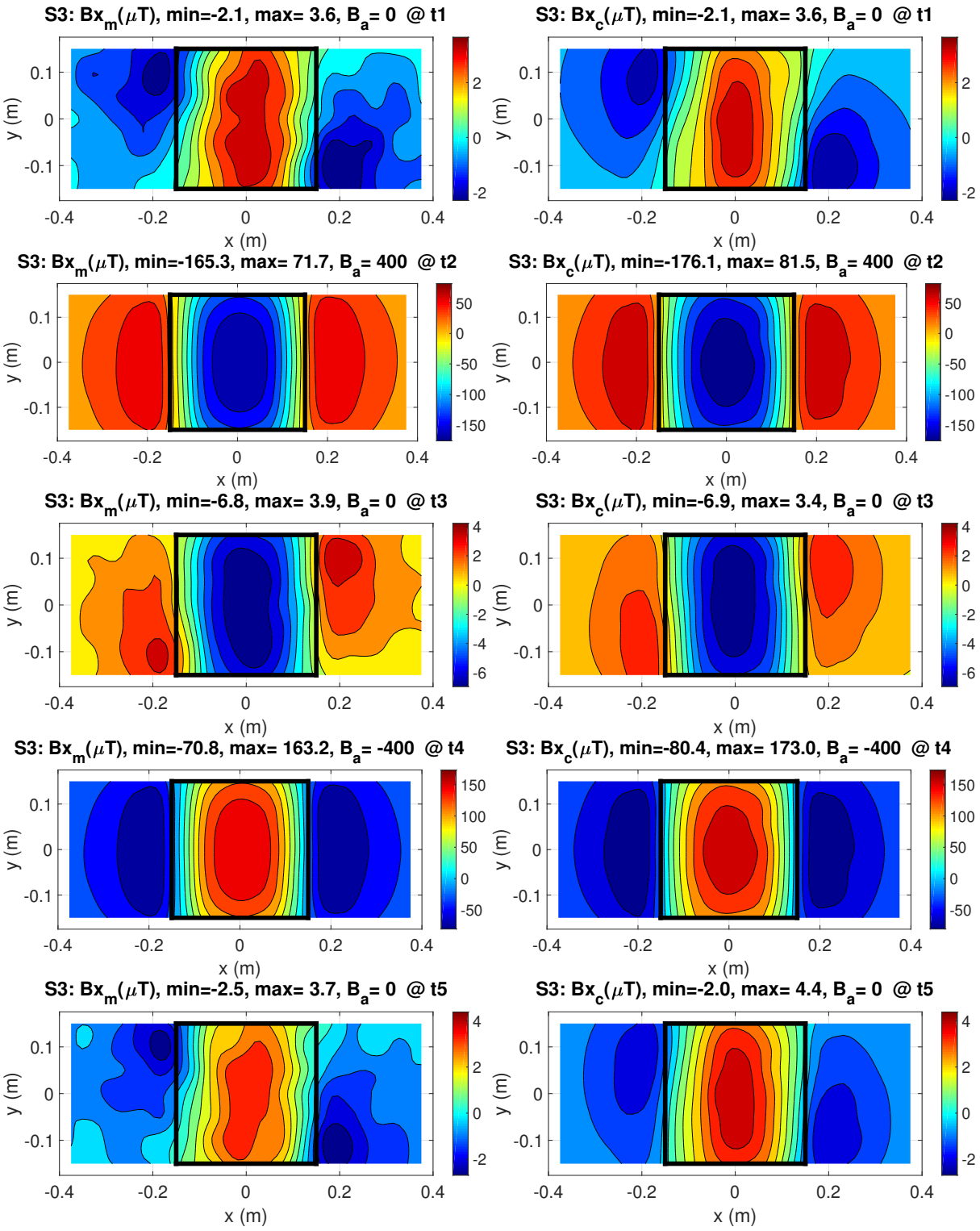

Figure D.12: Specimen 3. B_x field below a metal plate ((300×300×5 mm) subjected to a 400 µT loop, measurements (left) calculated fit (right).

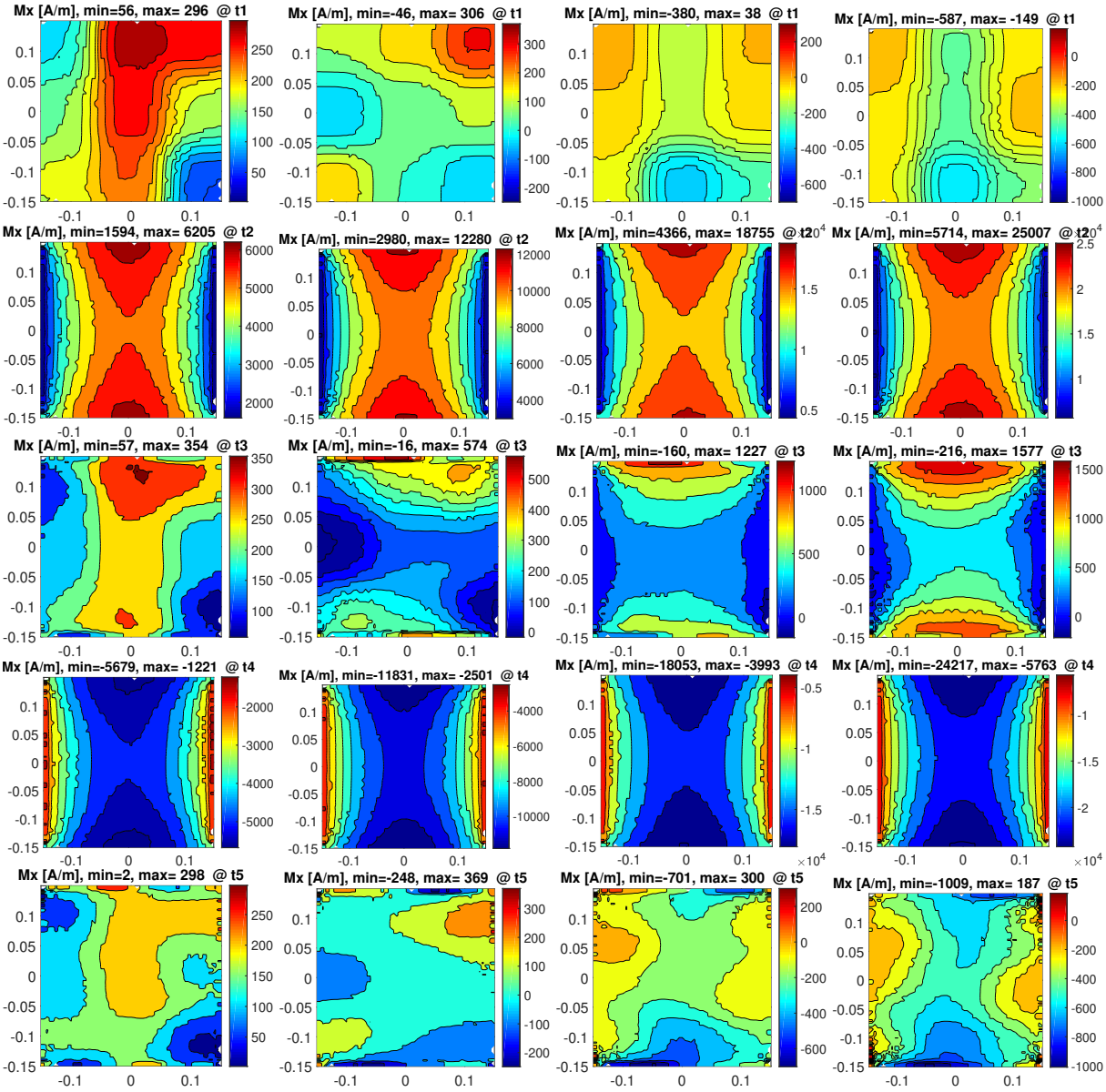

Figure D.13: Specimen 3. M_x distribution in a metal plate (300×300×5 mm) for four hysteresis loops: 100 μT (left), 200 μT (centre left), 300 μT (centre right), 400 μT (right).

D.4. Specimen 4: Fit

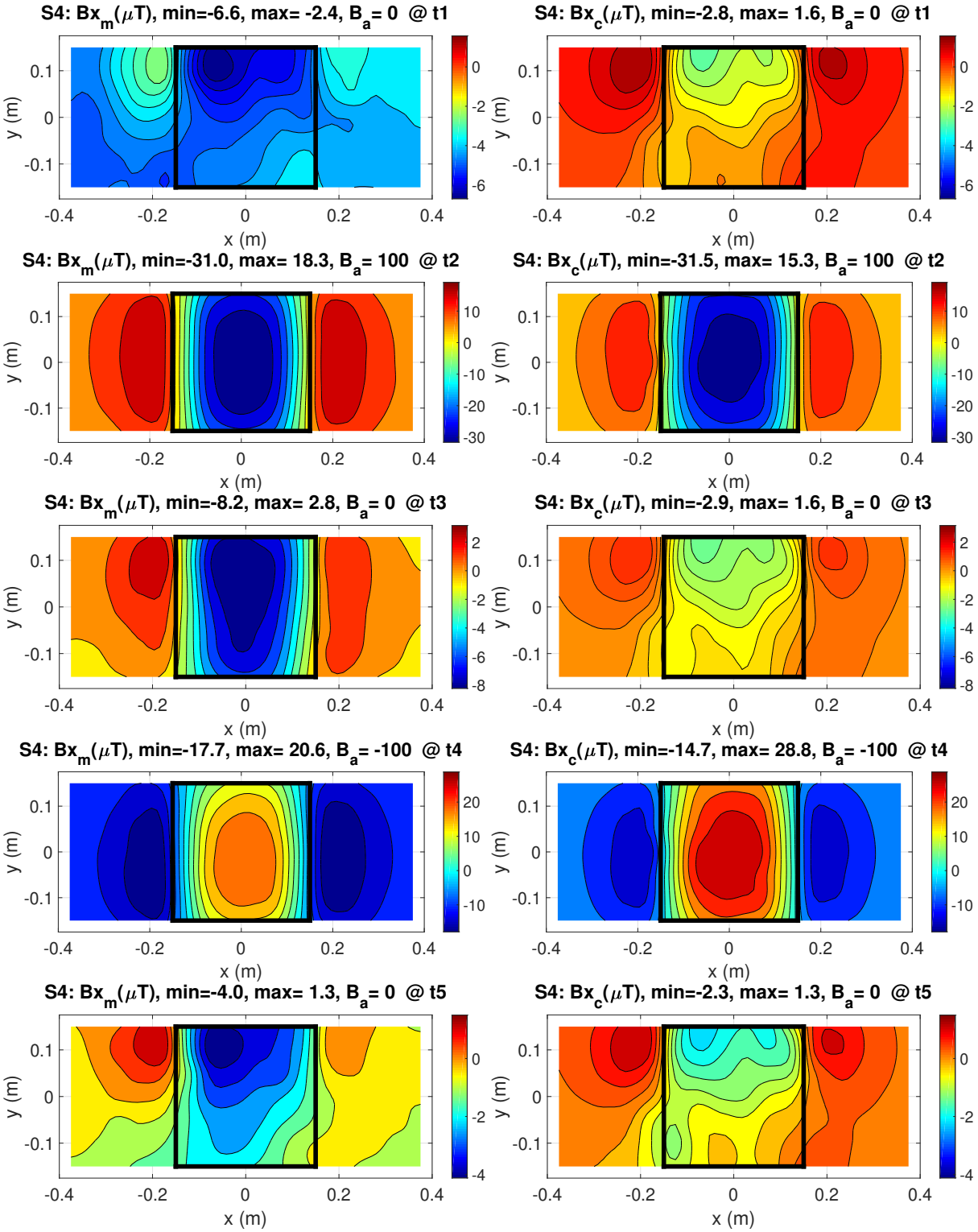

Figure D.14: Specimen 4. B_x field below a metal plate (300×300×2 mm) subjected to a 100 µT loop, measurements (left) calculated fit (right).

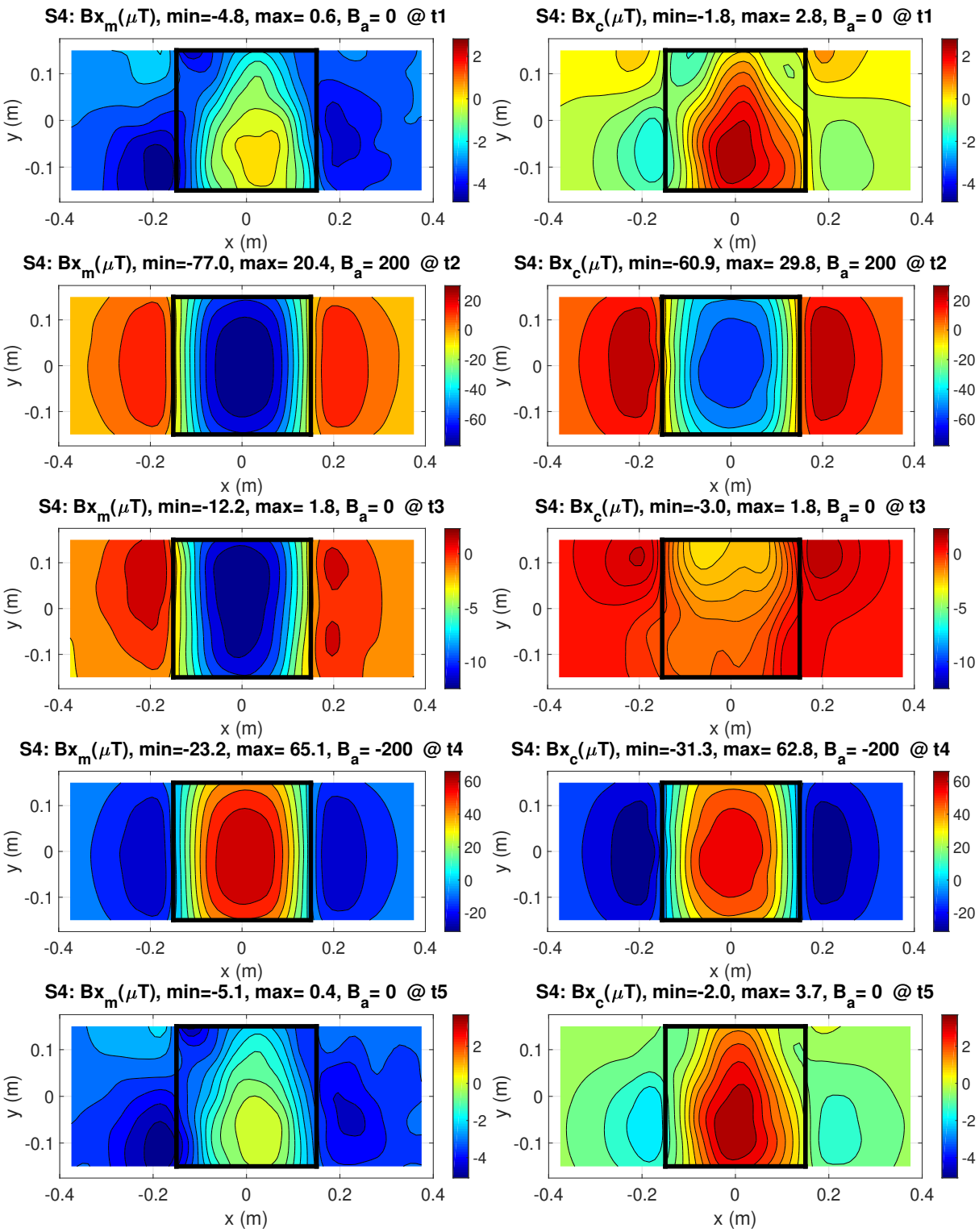

Figure D.15: Specimen 4. B_x field below a metal plate (300×300×2 mm) subjected to a 200 µT loop, measurements (left) calculated fit (right).

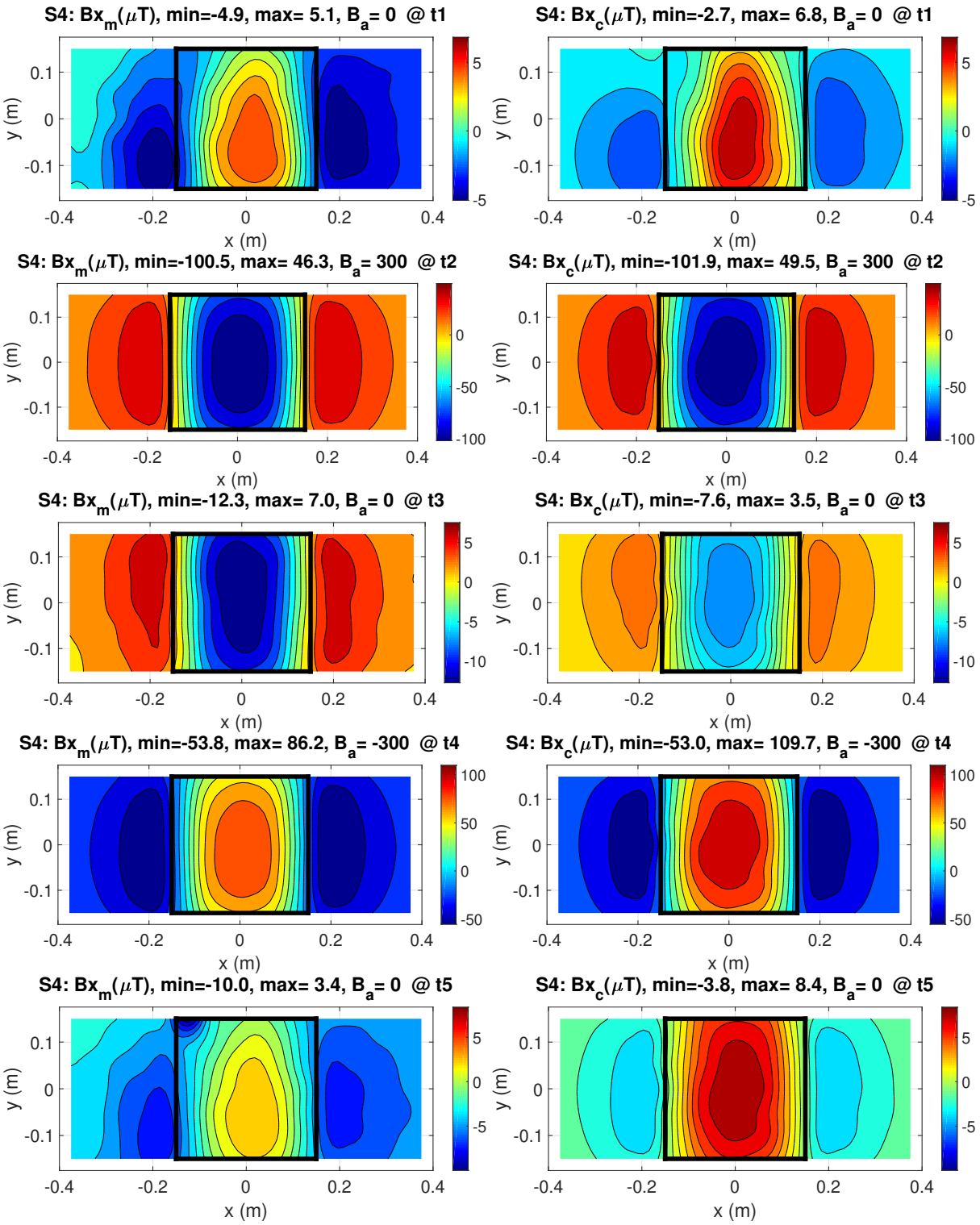

Figure D.16: Specimen 4. B_x field below a metal plate (300×300×2 mm) subjected to a 300 µT loop, measurements (left) calculated fit (right).

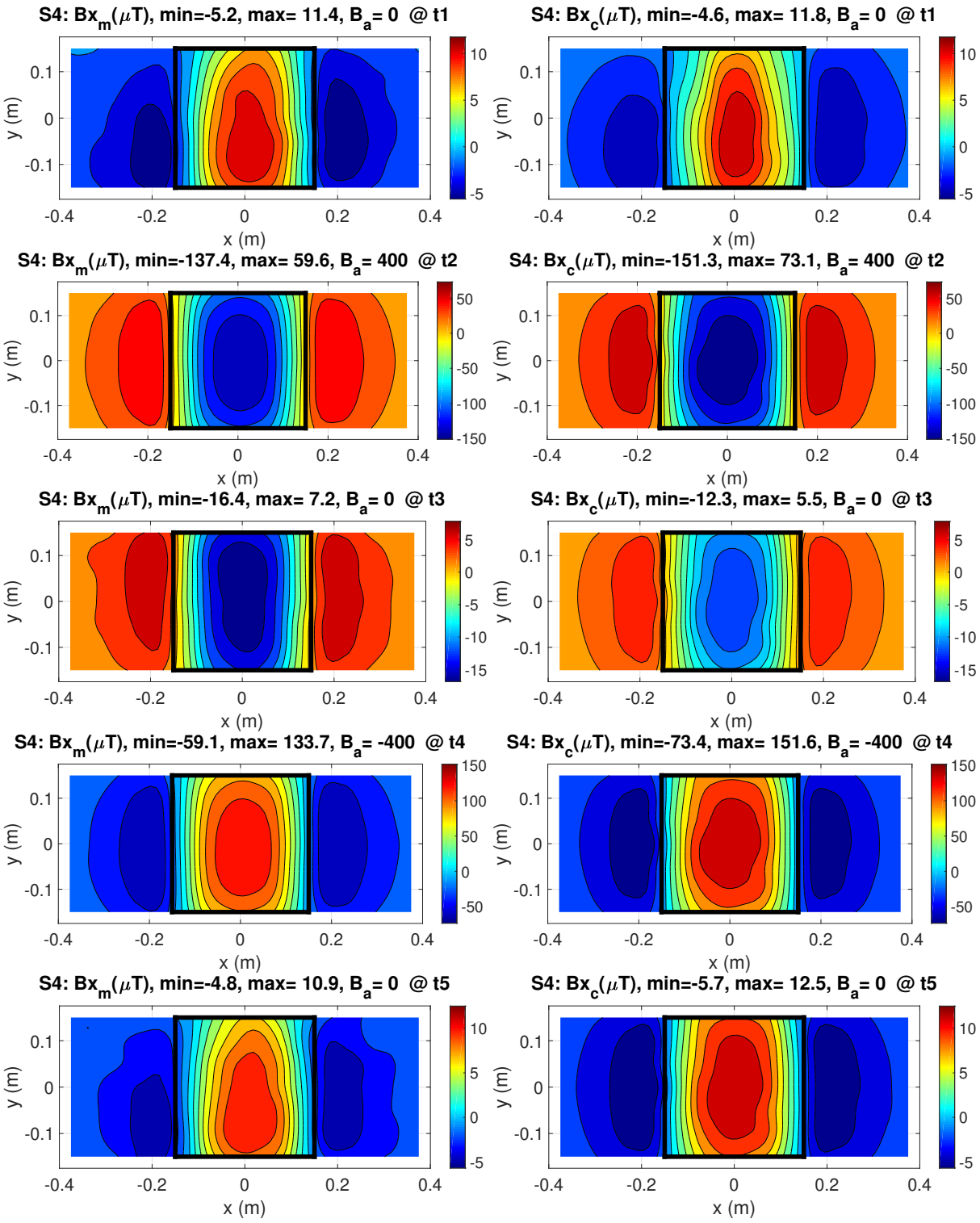

Figure D.17: Specimen 4. B_x field below a metal plate (300×300×2 mm) subjected to a 400 µT loop, measurements (left) calculated fit (right).

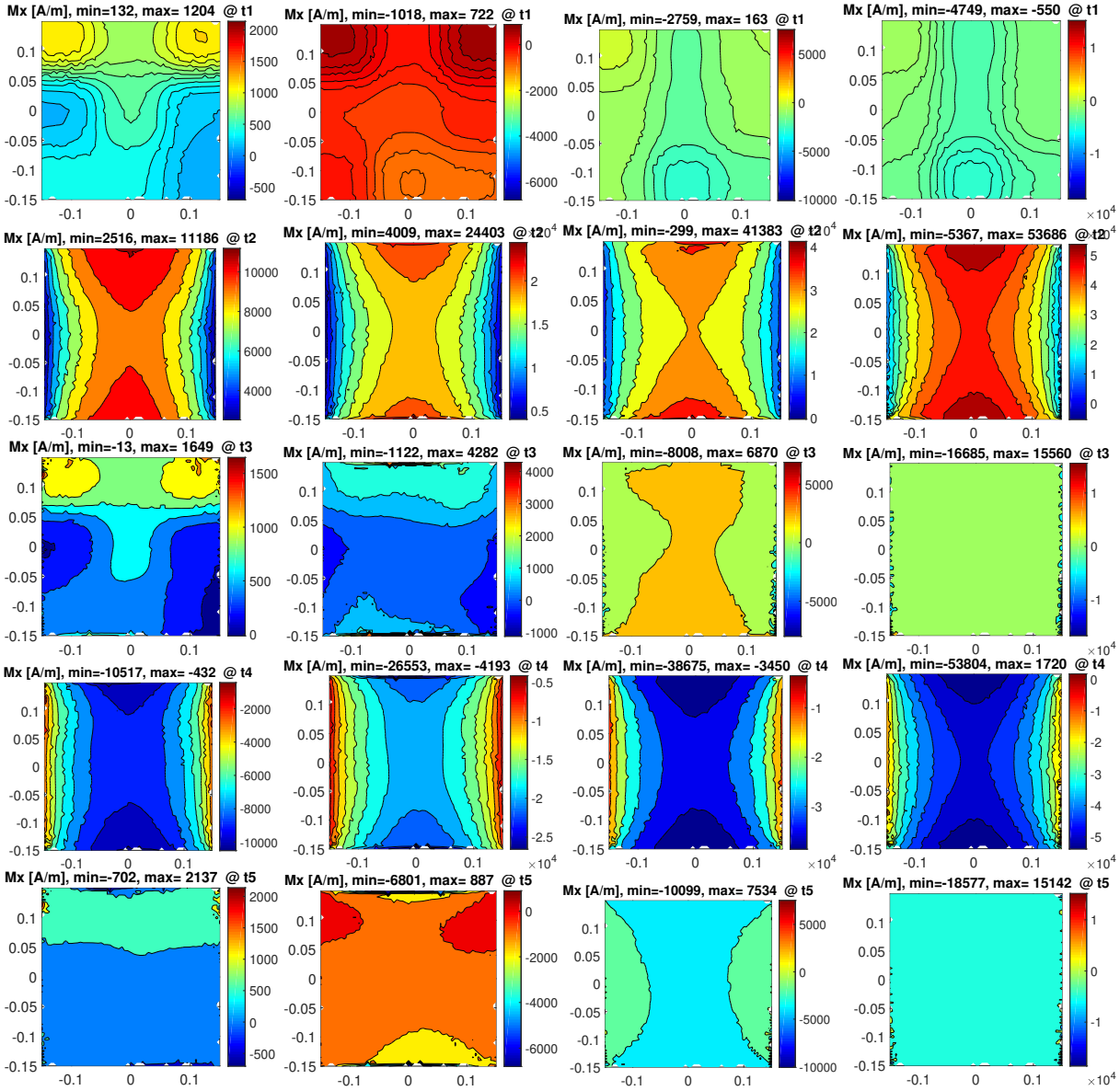

Figure D.18: Specimen 4. M_x distribution in a metal plate (300×300×2 mm) for four hysteresis loops: 100 μT (left), 200 μT (centre left), 300 μT (centre right), 400 μT (right).

Bibliography

[1] L. C. Andrews. *Special Functions of Mathematics for Engineers*. Oxford science publications. SPIE Optical Engineering Press, 1992. ISBN 9780819426161. URL https://books.google.nl/books?id=2CAqsF-RebgC.

[2] S. I. Babic and C. Akyel. Torque calculation between circular coils with inclined axes in air. *International Journal of Numerical Modelling: Electronic Networks, Devices and Fields*, 24(3):230–243, 2011. ISSN 08943370. doi: 10.1002/jnm.773.

[3] I. Berkman. Ferromagnetic hysteresis in ship's steel, analysis of the Preisach and Jiles-Atherton models. *Bsc Thesis TU Delft, unpublished*, December 2017.

[4] F. W. Bijleveld. Stress-State Dependent Fracture Prediction: An Application in Numerical Analysis of Maritime Collision. Master's thesis, 2018.

[5] D. Burgy. Magnetic and Magnetostrictive Characterization and Modeling of High Strength Steel. (May 2008), 2014.

[6] W. D. Callister. *Materials Science and Engineering: An Introduction*. Wiley and Sons Inc., 2007.

[7] K. H. Carpenter. A Differential Equation Approach to Minor Loops in the Jiles-Atherton Hysteresis Model. *IEEE Transactions on Magnetics*, 27(6):4404–4406, 1991. ISSN 19410069. doi: 10.1109/20.278655.

[8] K. Chwastek. Modelling offset minor hysteresis loops with the modified Jiles-Atherton description. *Journal of Physics D: Applied Physics*, 42(16), 2009. ISSN 00223727. doi: 10.1088/0022-3727/42/16/165002.

[9] J. M. D. Coey. *Magnetism and magnetic materials*. Cambridge University Press, 2009. ISBN 9780857090591. doi: 10.1016/0304-8853(84)90352-4.

[10] D. J. Craik and M. J. Wood. Magnetization changes induced by stress in a constant apllied field. *Journal of applied Physics*, 3(1009), 1970.

[11] B. D. Cullity and C. D. Graham. *Introduction to Magnetic Materials*. Wiley-IEEE Press, 2 edition, 2008. ISBN 0471477419, 9780471477419.

[12] M. Darabian, S. M. Mohseni-Bonab, and B. Mohammadi-Ivatloo. Improvement of power system stability by optimal SVC controller design using shuffled frog-leaping algorithm. *IETE Journal of Research*, 61(2):160–169, 2015. ISSN 0974780X. doi: 10.1080/03772063.2014.999830. URL http://dx.doi.org/10.1080/03772063.2014.999830.

[13] L. H. Dong, B. Xu, S. Dong, L. Song, Q. Chen, and D. Wang. Stress dependence of the spontaneous stray field signals of ferromagnetic steel. *NDT and E International*, 42(4):323–327, 2009. ISSN 09638695. doi: 10.1016/j.ndteint.2008.12.005.

[14] M. Eghbal, K. Saha, T, and K. N. Hasan. Transmission expansion planning by meta-heuristic techniques: A comparison of Shuffled Frog Leaping Algorithm, PSO and GA. *IEEE Power and Energy Society General Meeting*, pages 1–8, 2011. ISSN 19449925. doi: 10.1109/PES.2011.6038998.

[15] M. M. Eusuff and K. E. Lansey. Optimization of water distribution network design using the shuffled frog leaping algorithm. *Journal of Water Resources planning and management*, 129(3):210–225, 2003.

[16] J. Glanz. Genoa Bridge Collapse: The Road to Tragedy. https://www.nytimes.com/interactive/2018/09/06/world/europe/genoa-italy-bridge.html, 2018. [Online; accessed 12-10-2018].

[17] B. Gordon. Degaussing: The demagnetisation of ships. *Electronics and Power*, 30(6):473–476, June 1984. doi: 10.1049/ep.1984.0246.

[18] D. J. Griffiths. *Introduction to Electrodynamics*. Upper Saddle River, N.J., 1999.

[19] J. J. Holmes. *Modeling a Ship's Ferromagnetic Signatures*. Number 1. Springer US, 2007. ISBN 9781598292503. doi: 10.2200/S00092ED1V01Y200706CEM016.

[20] Mathworks Inc. Mldivide . http://nl.mathworks.com/help/matlab/ref/mldivide.html, 2018.

[21] W. D. Jackson. *Classical Electrodynamics*. John Wiley and Sons Inc., 1999.

[22] D. Jiles. *Introduction to Magnetism and Magnetic Materials*, volume 1. 1991. ISBN 978-0-412-38640-4. doi: 10.1007/978-1-4615-3868-4. URL http://www.wiley.com/WileyCDA/WileyTitle/productCd-EHEP000803.html{%}5Cnhttp://link.springer.com/10.1007/978-1-4615-3868-4.

[23] D. C. Jiles. Theory of the Magnetomechanical effect. *Journal of Magnetism and Magnetic Materials*, 13(3):283–288, 1979. ISSN 03048853. doi: 10.1016/0304-8853(79)90210-5.

[24] D. C. Jiles. A Self Consistent Generalized Model for the Calculation of Minor Loop Excursions in the Theory of Hysteresis. *IEEE Transactions on Magnetics*, 28(5):2602–2604, 1992. ISSN 19410069. doi: 10.1109/20.179570.

[25] D. C. Jiles. Frequency Dependence of Hysteresis Curves in "Non-Conducting" Magnetic Materials. *IEEE Transactions on Magnetics*, 29(6):3490–3492, 1993. ISSN 19410069. doi: 10.1109/20.281206.

[26] D. C. Jiles and D. L. Atherton. Theory of ferromagnetic hysteresis. *Journal of Magnetism and Magnetic Materials*, 61(1-2):48–60, 1986. ISSN 03048853. doi: 10.1016/0304-8853(86)90066-1.

[27] D. C. Jiles, J. B. Thoelke, and M. K. Devine. Numerical Determination of Hysteresis Parameters for the Modeling of Magnetic Properties Using the Theory of Ferromagnetic Hysteresis. *IEEE Transactions on Magnetics*, 28(1):27–35, 1992. ISSN 19410069. doi: 10.1109/20.119813.

[28] B. Kvasnica and F. Kundracik. Fitting experimental anhysteretic curves of ferromagnetic materials and investigation of the effect of temperature and tensile stress B. *Journal of Magnetism and Magnetic Materials*, 162, 1006. ISSN 1550235X. doi: 10.1103/PhysRevB.91.064402.

[29] E. W. Lee. Magnetostriction and magnetomechanical effects. *Reports on Progress in Physics*, 18 (184), 1955.

[30] J. Leite, N. Sadowski, N. J. Batistela, and J. P. A. Bastos. The Inverse Jiles – Atherton Model Parameters Identification. *IEEE Transactions on Magnetics*, 39(3):1397–1400, 2003. ISSN 0018-9464. doi: 10.1109/TMAG.2003.810216.

[31] J. V. Leite, S. L. Avila, N. J. Batistela, W. P. Carpes, N. Sadowski, P. Kuo-Peng, and J. P. A. Bastos. Real coded genetic algorithm for Jiles-Atherton model parameters identification. *IEEE Transactions on Magnetics*, 40(2 II):888–891, 2004. ISSN 00189464. doi: 10.1109/TMAG.2004.825319.

[32] J. V. Leite, N. Sadowski, and A. Benabou. Accurate minor loops calculation with a modified Jiles-Atherton hysteresis model. *COMPEL - The International Journal for Computation and Mathematics in Electrical and Electronic Engineering*, 28(3):741–749, 2009. ISSN 03321649. doi: 10.1108/03321640910940990.

[33] E. S. A. M. Lepelaars. *Static Magnetic Signature Variation*. TNO_DV A399, restricted, 2010.

[34] E. S. A. M. Lepelaars. *Static electromagnetic field of an electric current segment in a layered media*. Personal communication, 2018.

[35] D. M. Lichtblau and E. W. Weisstein. Condition Number. http://mathworld.wolfram.com/ConditionNumber.html, 2018.

[36] J. López, P. N. Lisboa-Filho, W. A. C. Passos, W. A. Ortiz, and F. M. Araujo-Moreira. Magnetic relaxation and magnetization field dependence measurements in La0.5Ca0.5MnO3. *Journal of Magnetism and Magnetic Materials*, 226-230:500–501, 2001. ISSN 03048853. doi: 10.1016/S0304-8853(00)00987-2.

[37] P. Melo and R. E. Araújo. Technological Innovation for Smart Systems. 499:398–405, 2017. doi: 10.1007/978-3-319-56077-9. URL http://link.springer.com/10.1007/978-3-319-56077-9.

[38] P. M. C. Morse and H. Feshbach. *Methods of theoretical physics*. Number 2 in International series in pure and applied physics. McGraw-Hill, 1953. URL https://books.google.nl/books?id=DvZQAAAAMAAJ.

[39] R. A. Naghizadeh, B. Vahidi, and S. H. Hosseinian. Parameter identification of Jiles-Atherton model using SFLA. *COMPEL - The International Journal for Computation and Mathematics in Electrical and Electronic Engineering*, 31(4):1293–1309, 2012. ISSN 03321649. doi: 10.1108/03321641211227573.

[40] H. W. L. Naus. Theoretical developments in magnetomechanics. *IEEE Transactions on Magnetics*, 47(9):2155–2162, 2011. ISSN 00189464. doi: 10.1109/TMAG.2011.2134863.

[41] T. Oguchi, K. Terakura, and N. Hamada. Magnetism of Iron Above the Curie-Temperature. *Journal of Magnetism and Magnetic Materials*, 31-4:97–98, 1983. URL http://gateway.webofknowledge.com/gateway/Gateway.cgi?GWVersion=2{&}SrcAuth=mekentosj{&}SrcApp=Papers{&}DestLinkType=FullRecord{&}DestApp=WOS{&}KeyUT=A1983QF67700032{%}5Cnpapers2://publication/uuid/EE4CEC6A-4756-4D92-A8C0-D3D506E42DC1.

[42] J. A. Osborn. Demagnetizing Factors of the General Ellipsoid. *Physical Review*, page 7, 1945.

[43] F. Preisach. Uber die magnetische Nachwirkung. *Zeitschrift für Physik*, 94:277–302, 1935.

[44] Ian M. Robertson. Direction of Change of Magnetization of a Ferromagnet Subjected to Stress. *IEEE Transactions on Magnetics*, 29(3):2077–2080, 1993. ISSN 19410069. doi: 10.1109/20.211322.

[45] M. J. Sablik, H. Kwun, G. L. Burkhardt, and D. C. Jiles. Model for the effect of tensile and compressive stress on ferromagnetic hysteresis. *Journal of Applied Physics*, 61(8):3799–3801, 1987. ISSN 00218979. doi: 10.1063/1.338650.

[46] G. Samuel and C. A. Rajan. A Modified Shuffled Frog Leaping Algorithm for Long-Term Generation Maintenance Scheduling. 258, 2014. doi: 10.1007/978-81-322-1771-8. URL http://link.springer.com/10.1007/978-81-322-1771-8.

[47] A. Sophian, G. Y. Tian, and S. Zairi. Pulsed magnetic flux leakage techniques for crack detection and characterisation. *Sensors and Actuators, A: Physical*, 125(2):186–191, 2006. ISSN 09244247. doi: 10.1016/j.sna.2005.07.013.

[48] J. Subrahmanjam. Magnetic materials. Lecture, 2015. URL https://www.slideshare.net/harshaambati9/magnetic-materials-47590107.

[49] R. Szewczyk. Stress-induced anisotropy and stress dependence of saturation magnetostriction in the Jiles-Atherton-Sablik model of the magnetoelastic Villari effect. *Archives of Metallurgy and Materials*, 61(2A):607–612, 2016. ISSN 17333490. doi: 10.1515/amm-2016-0103.

[50] M. Toman, G. Stumberger, and D. Dolinar. Parameter identification of the Jiles-Atherton hysteresis model using differential evolution. *IEEE Transactions on Magnetics*, 44(6):1098–1101, 2008. ISSN 0018-9464. doi: 10.1109/TMAG.2007.915947. URL http://dx.doi.org/10.1109/TMAG.2007.915947{%}5Cnhttp://ieeexplore.ieee.org/ielx5/20/4526781/04527009.pdf?tp={&}arnumber=4527009{&}isnumber=4526781.

[51] M. P. Van der Horst. *On self magnetic flux leakage in support of fatigue crack monitoring in ship and offshore structures: A numerical, experimental, and full-scale application study*. PhD thesis, Delft University of Technology, 2018.

[52] M. P. Van der Horst and M. L. Kaminski. Slit Induced Self Magnetic Flux Leakage in a Square Steel Plate. *Manuscript under review*, 2018.

[53] M. P. Van der Horst, M. L. Kaminski, E. S. A. M Lepelaars, and E. Puik. Methods for Sensing and Monitoring Fatigue Cracks and Their Applicability for Marine Structures. *Proceedings of the International Offshore and Polar Engineering Conference*, pages 455–462, 2013. ISSN 10986189. URL http://www.scopus.com/inward/record.url?eid=2-s2.0-84883662199{&}partnerID=tZOtx3y1.

[54] M. P. Van der Horst, M. L. Kaminski, and E. S. A. M. Lepelaars. Testing and Numerical Simulation of Magnetic Fields Affected by Presence of Fatigue Cracks. *Proceedings of the International Offshore and Polar Engineering Conference*, 3:445–450, 2014. ISSN 15551792. URL http://www.scopus.com/inward/record.url?eid=2-s2.0-84906902858{&}partnerID=tZOtx3y1.

[55] S. Van Kreveld. Effect of stress-induced magnetization on crack monitoring by self magnetic flux leakage method. Master's thesis, Delft University of Technology, 2018.

[56] A. R. P. J. Vijn. Macroscopic Hysteresis Model for the general ellipsoid. *Dissertation, unpublished*, 2018.

[57] E. Villari. Ueber die aenderungen des magnetischen moments, welche der zug und das hindurchleiten eines galvanischen stroms in einem stabe von stahl oder eisen hervorbringen. *Annalen der Physik*, 202(9):87–122, 1865. doi: 10.1002/andp.18652020906. URL https://onlinelibrary.wiley.com/doi/abs/10.1002/andp.18652020906.

[58] A. Visintin. Mathematical Models of Hysteresis. In *The Science of Hysteresis Volume 1*, volume 1, pages 1–123. 2005. ISBN 0124808735. URL http://www.springer.com/us/book/9781461277675.

[59] P. Weiss. L'hypothèse du champ moléculaire et la propriété ferromagnétique. *Journal of Theoretical and Applied Physics.*, 6(1):661–690, 1907. doi: 10.1051/jphystap:019070060066100. URL https://hal.archives-ouvertes.fr/jpa-00241247.

[60] H. P. J. Wijn and H. Van der Heide. A Richter type after-effect in Ferrites containing Ferrous and Ferric Ions. *Review of Modern Physics*, 711(1):2–3, 1948.

[61] M. Yue, T. Hu, B. Guo, and X. Guo. The research of parameters of genetic algorithm and comparison with particle swarm optimization and shuffled frog-leaping algorithm. *PEITS 2009 - 2009 2nd Conference on Power Electronics and Intelligent Transportation System*, 1:77–80, 2009. doi: 10.1109/PEITS.2009.5406960.

[62] S. E. Zirka, Y. I. Moroz, and E. Della Torre. Combination hysteresis model for accommodation magnetization. *IEEE Transactions on Magnetics*, 41(9):2426–2431, 2005. ISSN 00189464. doi: 10.1109/TMAG.2005.854335.

[63] S. E. Zirka, Y. I. Moroz, R. G. Harrison, and K. Chwastek. On physical aspects of the Jiles-Atherton hysteresis models. *Journal of Applied Physics*, 112(4), 2012. ISSN 00218979. doi: 10.1063/1.4747915.